Spatial Estimations of Soil Properties for Physically-based Soil Erosion Modelling in the Three Gorges Reservoir Area, Central China

Dissertation

der Mathematisch-Naturwissenschaftlichen Fakultät
der Eberhard Karls Universität Tübingen
zur Erlangung des Grades eines Doktors
der Naturwissenschaften
(Dr. rer. nat.)

vorgelegt von
Felix Stumpf
aus Eberbach am Neckar

Tübingen 2015

Gedruckt mit Genehmigung der Mathematisch-Naturwissenschaftlichen Fakultät der Eberhard Karls Universität Tübingen.

Tag der mündlichen Qualifikation:	11.02.2016
Dekan:	Prof. Dr. Wolfgang Rosenstiel
1. Berichterstatter:	Prof. Dr. Thomas Scholten
2. Berichterstatter:	Prof. Dr. Volker Hochschild

Contents

List of Figures

List of Tables

1 Summary

Soils present a central medium for processes between the environmental spheres, and therefore play a key role in the functioning of terrestrial ecosystems. However, soil erosion as a natural force of landscape evolution adversely affects the capacity of soils to support ecosystem services. Moreover, inadequate agricultural practices, deforestation, and construction activities amplify natural soil loss rates and transform soil erosion to a major threat for managed ecosystems worldwide. Particularly, the Three Gorges Reservoir Area in China is highly susceptible to soil erosion by water. This is attributable to unfavorable environmental conditions, such as rainfall events of high intensity and steep slope inclinations in areas of extensive, but small-scale crop cultivation. Moreover, in the course of the impoundment of the Yangtze River in the area of the Three Gorges, resettlements and accompanied deforestation reinforced the risk of hazardous soil erosion, which attenuates soil productivity and threatens the functioning of the reservoir. Therefore, conservation measures to stabilize steep sloping surfaces have been implemented to mitigate the hazardous effects of soil erosion. However, to assess the conservation measures an efficient tool is required to identify spatial soil erosion patterns in small, mountainous, and data scarce catchments within the Three Gorges Reservoir Area.

The present thesis aims to provide an efficient modelling framework that facilitates a detailed quantification of sediment reallocations due to erosive rainfall-runoff events. Therefore, Digital Soil Mapping techniques based on Latin Hypercube Sampling and Random Forest regression were applied to derive spatially distributed data on soil properties and to furnish a physically- and event-based soil erosion model. The soil sampling design was optimized to address the difficult terrain, an integrative use of legacy soil samples, and a reduced sample set size. Furthermore, the present thesis introduces a spatial uncertainty measure, which was used to identify areas for additional sampling to further refine initially processed soil property maps. In addition, continuous data on rainfall, runoff, and sediment yields were obtained to identify erosive rainfall-runoff events and to calibrate the physically-based soil erosion model EROSION 3D.

Evaluation of the hypercube sampling design was conducted by comparing it to a simulated Latin Hypercube design without constraints in terms of operability and efficiency

adjustments. Using the optimized sample set size of n = 30, the proposed sample design adequately reproduced the variation of terrain parameters, which served as proxies on the target soil properties of coarse, medium, and fine topsoil sand contents. Furthermore, the validity of the approach was assessed by estimating the spatial distribution of the target soil properties and validating the results independently. The results show convincing accuracies with R^2-values between 0.59 and 0.71.

The adequacy of the uncertainty-guided sampling for refining initial mapping approaches was evaluated by comparing the refined maps of topsoil silt and clay contents to the initial and further mapping approaches that exclusively used random samples from the entire study area. For the comparative analysis, the quality of the approaches was assessed by independent, bootstrap-, and cross-validation. The refined mapping approach performs best, showing a reduced spatial uncertainty of 31% for topsoil silt and 27% for topsoil clay compared to the initial approaches. Using independent validation, the accuracy increases by similar proportions, showing an accuracy of R^2 = 0.59 for silt and R^2 = 0.56 for clay.

The EROSION 3D model runs were evaluated using the measured sediment yields. The model performs well for large events (sediment yield > 1 Mg) with an average individual model error of 7.5%, while small events show an average error of 36.2%. The focus of analysis was led on the large events to evaluate reallocation patterns. Soil losses occur on approximately 11.1% of the study area with an average soil loss rate of 49.9 Mg ha^{-1}. Soil loss mainly occurs on crop rotation areas with a spatial proportion of 69.2% for ‘corn-rapeseed’ and 69.1% for ‘potato-cabbage’. Deposition occurs on 11% of the study area. Forested areas (9.7%), infrastructure (41%), cropland (corn-rapeseed: 13.6%, potato-cabbage: 11.3%), and grassland (18.4%) are affected by deposition. Since the vast majority of annual sediment yields (80.3%) were associated to a few large erosive events, the modelling framework can be recommended to identify sediment reallocations and to assess conservation measures in small catchments in the Three Gorges Reservoir Area.

2 Zusammenfassung

Böden sind ein zentrales Bindeglied für in Wechselwirkung stehende Prozesse zwischen den Umweltsphären und nehmen damit eine Schlüsselrolle in terrestrischen Ökosystemen ein. Auch wenn Bodenerosion eine natürliche physikalische Kraft der Landschaftsentwicklung darstellt, verringert sie die Kapazität des Bodens, Ökosystemdienstleistungen bereitzustellen. Ferner verstärken ungeeignete landwirtschaftliche Praktiken, Entwaldung und Baumaßnahmen natürliche Erosionsraten, sodass Bodenerosion heute weltweit als eine wesentliche Bedrohung bewirtschafteter Ökosysteme wahrgenommen wird. Aufgrund ungünstiger Umweltbedingungen, die sich durch hohe Reliefenergie, Niederschlagsereignisse von hoher Intensität sowie extensiver, kleinbäuerlicher landwirtschaftlicher Strukturen auszeichnen, gilt die Region um das Drei-Schluchten-Reservoir in China als anfällig für Bodenerosion durch Wasser. Darüber hinaus haben Umsiedlungen und Entwaldungen im Zuge der Aufstauung des Yangtze-Flusses zu einem gesteigerten Erosionsrisiko geführt, welches sowohl die landwirtschaftliche Produktivität potenziell vermindert als auch die Funktionsweise des Reservoirs bedroht. Bereits in den 1990er Jahren wurden Maßnahmen zur Stabilisierung stark geneigter Flächen eingeführt, um so die Auswirkungen von Erosionsereignissen zu vermindern. Zur Beurteilung der Schutzmaßnahmen bedarf es eines effizienten Instruments, das räumliche Erosionsmuster in kleinen und gebirgigen Einzugsgebieten der Drei-Schluchten-Region trotz schwacher Datengrundlage identifizieren kann.

Diese Arbeit verfolgt die Entwicklung eines effizienten Modellierungskonzepts zur detaillierten Quantifizierung von Sedimentumlagerungen infolge erosiver Niederschlags-Abfluss-Ereignisse. Methoden der Boden-Landschafts-Modellierung, basierend auf Latin Hypercube Beprobung und Random Forest Regression, wurden angewendet, um ein physikalisches und ereignisbasiertes Erosionsmodell zu parametrisieren. Das Design zur Bodenbeprobung wurde optimiert, um schwer zugängliches Terrain zu kompensieren, Altdaten zu integrieren und die Probenzahl zu reduzieren. Weiterhin wurde ein räumlich verteiltes Maß für Prognoseunsicherheiten in Boden-Landschafts-Modellierungen entwickelt. Dieses wurde verwendet, um Gebiete zur Nachbeprobung auszuweisen und ursprüngliche Modellierungsereignisse zu verbessern. Zusätzlich wurden kontinuierliche Niederschlags-,

Abfluss- und Sedimentaustragsdaten per Monitoring erfasst, um erosive Niederschlags-Abfluss-Ereignisse zu identifizieren und das physikalische, prozessbasierte Bodenerosionsmodell EROSION 3D zu kalibrieren.

Das Hypercube-Bodenbeprobungsdesign wurde mit einem simulierten Latin Hypercube Design ohne einschränkende Anpassungen an Operabilität und Effizienz verglichen. Mit einer optimierten Probenanzahl von n = 30 repräsentiert das modifizierte Beprobungsdesign die Variabilität von Terrainparametern, welche als Proxies für die Zielvariablen Grob-, Mittel- und Feinsand fungieren. Die Gültigkeit des Beprobungsdesigns wurde zusätzlich durch eine unabhängige Validierung der finalen Boden-Landschafts-Modellierung erfasst. Die Ergebnisse zeigten eine überzeugende Prognosegüte mit R^2-Werten zwischen 0.59 und 0.71.

Die Eignung des Nachbeprobungsdesigns wurde mittels eines Vergleiches von verbesserten Karten von Schluff- und Tongehalten des Oberbodens mit den ursprünglichen Modellierungsergebnissen und einem weiteren Kartierungsansatz, ausschließlich basierend auf zufälligen Altdaten im gesamten Untersuchungsgebiet, evaluiert. Für die Vergleichsstudie wurden neben dem räumlichen Unsicherheitsmaß eine unabhängige, eine bootstrap-, sowie eine Kreuzvalidierung herangezogen. Die Modellierungsergebnisse des Nachbeprobungsansatzes zeigen die höchste Genauigkeit, während die räumliche Unsicherheit der Oberbodengehalte von Schluff um 31% und von Ton um 27%, verglichen zu den ursprünglichen Modellierungen, verbessert werden konnten. Für die unabhängige Validierung betragen die R^2-Werte für Schluff 0.59 und für Ton 0.56.

Die EROSION 3D-Modelldurchläufe wurden mithilfe der gemessenen Sedimentaustragsdaten evaluiert. Für stark erosive Ereignisse (Sedimentaustrag > 1Mg) zeigt das Modell eine niedrige mittlere Abweichung von 7.5%, während schwach erosive Ereignisse (Sedimentaustrag < 1Mg) eine hohe mittlere Abweichung von 36.2% erbringen. Aus diesem Grund wurden ausschließlich die starken Erosionsereignisse zur Evaluierung der Sedimentumlagerungen herangezogen. Demnach tritt auf 11.1% des Untersuchungsgebietes Bodenerosion mit einer mittleren Abtragsrate von 49.9 Mg ha^{-1} auf. Während Bodenerosion hauptsächlich auf landwirtschaftlichen Anbauflächen auftritt, sind 69.2% der Fruchtfolgeflächen ‘Mais-Raps’ und 69.1% der ‘Kartoffel-Kohl’-Flächen betroffen. Sedimentablagerungen treten auf 11% des Untersuchungsgebiets auf. Dabei sind bewaldete Gebiete zu 9.7%, Infrastrukturflächen zu 41%, landwirtschaftliche Anbauflächen zu 13.6%

für ‘Mais-Raps’ beziehungsweise zu 11.3% für ‘Kartoffel-Kohl’, und Grasland zu 18.4% von Sedimentablagerungen betroffen. Da der überwiegende Teil des jährlichen Sedimentaustrags auf wenige, aber stark erosive Ereignisse (80.3%) zurückzuführen ist, kann das angewandte Modellierungskonzept zur Identifizierung von Sedimentumlagerungen sowie zur Beurteilung von Erosionsschutzmaßnahmen in kleinen Einzugsgebieten der Drei-Schluchten-Region herangezogen werden.

3 List of Publications in the Thesis

3.1 Assessment of Geo-Hazards in a Rapidly Changing Landscape: The Three Gorges Reservoir Region in China

Manuscript 1, co-author, published in *Environmental Earth Sciences* 2015.

Co-authors: Alexander Strehmel, Sarah Schönbrodt-Sitt, Giovanni Buzzo, Christian Dumperth, Karsten Zimmermann, Katrin Bieger, Thorsten Behrens, Karsten Schmidt, Renneng Bi, Joachim Rohn, Joachim Hill, Thomas Udelhoven, Wei Xiang, Xuezheng Shi, Qinghua Cai, Ton Jiang, Nicola Fohrer, and Thomas Scholten.

The full publication can be found on page 112.

3.2 Incorporating Limited Field Operability and Legacy Samples in a Hypercube Sampling Design for Digital Soil Mapping

Manuscript 2, first author, accepted with major revision in *Journal of Plant Nutrition and Soil Science* 2015.

Co-authors: Karsten Schmidt, Thorsten Behrens, Sarah Schönbrodt-Stitt, Giovanni Buzzo, Christian Dumperth, Alexandre Wadoux, Wei Xiang, and Thomas Scholten.

The full publication can be found on page 160.

3.3 Spatial Uncertainty-Guided Sampling to Improve Digital Soil Maps

Manuscript 3, first author, under review in *Catena* 2015.

Co-authors: Karsten Schmidt, Philipp Goebes, Thorsten Behrens, Sarah Schönbrodt-Stitt, Alexandre Wadoux, Wei Xiang, and Thomas Scholten.

The full publication can be found on page 185.

3.4 Sediment Reallocation due to Erosive Rainfall events in the Three Gorges Reservoir Area, Central China

Manuscript 4, first author, under review in *Land Degradation & Development* 2015.

Co-authors: Philipp Goebes, Marcus Schindewolf, Karsten Schmidt, Sarah Schönbrodt-Stitt, Alexandre Wadoux, Wei Xiang, and Thomas Scholten.

The full publication can be found on page 213.

3.5 Rule-based Analysis of Throughfall Kinetic energy to Evaluate Leaf and Tree Architectural Trait Thresholds to Mitigate Erosive Power

Manuscript 5, co-author, accepted for publication in *Progress in Physical Geography* 2015.

Co-authors: Philipp Goebes, Karsten Schmidt, Werner Härdtle, Steffen Seitz, Goddert von Oheimb and Thomas Scholten.

The full publication can be found on page 253.

4 Introduction

4.1 Soils and Soil Erosion

Soils outline one of the most complex biomaterials on earth that develop and operate at the interface of atmosphere, biosphere, hydrosphere, and lithosphere [Young & Crawford, 2004; White, 2006; Brevik *et al.*, 2015]. In this context, soils present a central medium for processes between the environmental spheres, and therefore play a key role in the functioning of terrestrial ecosystems [Blum, 2005; Wall *et al.*, 2012]. In consequence, soils support the delivery of ecosystem services that are fundamental for human societies, including provisional services (e.g., provision of food, fresh water, raw materials, and gene pools), regulative services (e.g., regulation of climate, water, erosion and floods, and carbon sequestration), cultural services (e.g., storage of geological and archaeological heritage), and supporting services (e.g., provision of habitats and support of nutrient cycling) [Costanza *et al.*, 1997; Daily, 1997; de Vries *et al.*, 2013; Adhikari & Hartemink, 2016]. Regarding the relevance of soils for ecosystem functioning and services that are elementary to sustain human livelihood, the United Nations proclaimed 2015 as the 'Year of Soils' [FAO, 2015].

However, soil erosion as a major geomorphic force of landscape evolution adversely affects the capacity of soils to support ecosystem services [Manuscript 1; Pimentel & Kounang, 1998; Godfray et al., 2010]. Soil erosion is a four-phase process of (i) detachment of individual soil particles from the soil mass, (ii) their breakdown, (iii) their transport and redistribution by water and wind, and (iv) their deposition with declining transport energy [Manuscript 1; Pimentel et al., 1995; Lal, 2003; Morgan, 2005]. In the process of soil erosion, primary soil particles are initially detached from the soil mass by destructing stable soil structures mainly due to raindrop impacts (i.e., splash erosion). Subsequently, the detached soil particles are transported and deposited by runoff or wind [Pimentel *et al.*, 1995; Lal, 2001]. This reallocation of soil particles occurs areally distributed as sheet erosion (i.e., interrill erosion), or linearly when surface runoff concentrates in channels, forming rills (depth < 30 cm) and gullies (depth > 30 cm) [Morgan, 2005]. Although the relative contributions of different erosion agents to the erosion process is not yet quantified across

ecosystems, there is a broad agreement that water outlines the dominant agent [Manuscript 1; Pimentel *et al.*, 1995; Middleton & Thomas, 1997; Verheijen *et al.*, 2009; Zhang *et al.*, 2011].

The magnitude of natural soil erosion by water is strongly related to interacting biophysical factors including climate, soil, topography, and vegetation cover [Morgan, 2005]. In this context, rainfall properties (e.g., raindrop size, amount, distribution, intensity) determine the raindrop energy and the amount of available runoff water [Merz *et al.*, 2006]. Soil properties (e.g., texture, structure, soil organic matter) influence soil erodibility and water infiltration rates that further control runoff generation [Pimentel, 2006]. Topographical properties (e.g., slope gradient, slope length, aspect, and curvature) control the flow velocity and paths of surface runoff [Kateb *et al.*, 2013]. In addition, the vegetation cover forms a biomass layer that comprehensively moderates effects of soil erosion by stabilizing the soil structure, dissipating raindrop energy, and dissecting surface runoff [Lal, 2001; Sun *et al.*, 2013]. Beyond, the magnitude of natural soil erosion is reinforced by human-induced land use changes that are related to inappropriate agricultural practices, deforestation, and construction activities (e.g., expansion and shift of agricultural areas, intensification of cultivation, urban sprawl, mega infrastructure projects) [Manuscript 1; Onyando *et al.*, 2005; Park *et al.*, 2011; Wu *et al.*, 2011; Shi *et al.*, 2012].

On-site effects of soil erosion are associated with nutrient depletion, reduced soil organic matter content, and an alteration of soil physical properties [Kaihura *et al.*, 1999]. This results in declining soil quality (i.e., soil degradation), which is manifested in diminished regulatory capacity of soils in the ecosystem and reduced soil productivity with unfavorable consequences for food security [Pimentel & Kounang, 1998; Lal, 2001; Lal, 2003; Pimentel, 2006]. Off-site effects are mainly associated with amplified sedimentation processes [Morgan, 2005]. Thereby, the risk of floods is reinforced by a reduced water storage capacity in the catchments, and impaired functioning of reservoirs for hydro-electrical and irrigation management [Manuscript 1; Palazón *et al.*, 2014; Ferreira *et al.*, 2015]. Moreover, the sediments are often transported with pollutants, which originate from agro-chemical fertilizers and are attached to the primary soil particles causing eutrophication in the water bodies due to increasing levels of nitrogen and phosphorus [Manuscript 1; Liu *et al.*, 2006; Zhang & Lou, 2011]. In addition, soil erosion fosters climate change, since particle-bound carbon is released

to the atmosphere due to the breakdown of soil aggregates [Lal, 2003; Lal *et al.*, 2004; Morgan, 2005].

Investigations on soil erosion at the landscape scale are commonly based on sparse measurements of statistically extrapolated data on suspended sediments in river systems. Moreover, a high variety of methods to acquire and to extrapolate those data, combined with the singularity of natural and managed ecosystems, produces questionable results [Lal, 2001; Morgan, 2005; Hewawasam *et al.*, 2015]. However, there is a wide agreement on the global estimation of approximately 75 billion Mg a^{-1} of eroded soil from terrestrial ecosystems, of which 82% are attributed to human-induced soil erosion predominantly on agricultural land [Manuscript 1; Oldeman, 1994; Pimentel *et al.*, 1995; Pimentel & Kounang, 1998; Lal, 2003; Morgan, 2005]. Globally, managed ecosystems exhibit average soil loss rates between 13 Mg ha^{-1} a^{-1} and 40 Mg ha^{-1} a^{-1}, while in natural ecosystems average soil loss rates range from 0.005 Mg ha^{-1} a^{-1} to 0.5 Mg ha^{-1} a^{-1} [Pimentel & Kounang, 1998]. In this context, Brantley [2008] argued that human activities increased long-term soil erosion rates by a factor of approximately 30 in a global context. Moreover, average soil erosion is reported to be 10 to 40 times faster than natural soil formation [Pimentel, 2006; Verheijen *et al.*, 2009; Zhao *et al.*, 2013].

Considering this imbalance between unsustainable soil losses and the fundamental role of soils within the earth system and human societies, soil erosion outlines one of the prime environmental problems worldwide [Lal, 2001; Pimentel, 2006; Zhao *et al.*, 2013].

4.2 Soil Erosion in the Three Gorges Reservoir Area

The Three Gorges Reservoir Area (TGRA) in China presents one of the global hotspots of soil erosion. The region shows high susceptibility to hazardous soil erosion due to intense anthropogenic activities and unfavorable environmental conditions [Manuscript 1; Zhang *et al.*, 2009; Schönbrodt-Stitt *et al.*, 2010; Peng *et al.*, 2011; Wu *et al.*, 2011; Kepa Brian Morgan *et al.*, 2012; Shi *et al.*, 2012]. The entire TGRA covers an area of 57,802 km². At the maximum pool level of 175 m a.s.l. at the Three Gorges Dam (TGD), the reservoir expands approximately 660 km westwards from the TGD [Xu *et al.*, 2011]. The TGD project outlines the world`s largest hydroelectric scheme and was designed to increase energy supply, to

control seasonal floods, and to improve navigation on the Yangtze river [Manuscript 1; Zhang & Lou, 2011]. Accompanied by the construction of TGD and the impoundment of the Yangtze River, 1.3 million people were resettled due to the inundation of 431 km² of agricultural land and of 35 km² of residential areas in the TGRA [Manuscript 1; Xu *et al.*, 2011, 2013]. About 42% of the resettlers were moved to previously forested and steep sloping uphill sites for small scale crop cultivation [Cai *et al.*, 2005; Tan & Yao, 2006; Wu *et al.*, 2011; Zhang & Lou, 2011]. In total, 96% of the TGRA exhibits mountainous and hilly terrain with steep slopes [Zhang *et al.*, 2009; Wu *et al.*, 2011; Fang *et al.*, 2013]. It shows a subtropical monsoon climate with an unimodal rainfall regime. The long-term average annual precipitation is 1,146 mm, of which approximately 70% occurs from May to September [CMA, 2012]. Purple soils and Yellow to Yellow-brown soils are dominant in the TGRA. They are considered to be highly vulnerable to soil erosion [Manuscript 1; Zhang *et al.*, 2009; Peng *et al.*, 2011; Schönbrodt-Stitt *et al.*, 2013]. Estimations on the long-term annual soil losses based on empirical modelling amount to 157 million Mg [Lu & Higgitt, 2000]. The soil erosion induces sedimentation of the reservoir, and hence an attenuated ecological functioning of the Yangtze basin, a reduced lifespan of the dam, and a declined capacity to control floods [Manuscript 1; Shi *et al.*, 2004; Zhang & Lou, 2011; Xu *et al.*, 2013]. Since the 1990s, conservation measures were established to mitigate the hazardous effects of soil erosion. The measures include programs to implement conservation farming practices and to stabilize steep sloping surfaces mainly by reforestation and the construction of cropland terraces [Manuscript 1; Xu *et al.*, 2013].

In the TGRA, the major sediment yield caused by soil erosion is attributable to only very few heavy storm events each year [Manuscript 4; Fang *et al.*, 2013]. Thus, to assess conservation measures in detail and to identify areas of hazardous soil erosion, a methodological frame is required that facilitates an event-based, spatial quantification of soil erosion at the catchment scale [Manuscript 4; Cai *et al.*, 2005; Peng *et al.*, 2011; Shi *et al.*, 2012].

4.3 Quantification of Soil Erosion

4.3.1 Measuring Soil Erosion

Soil erosion can be quantified by numerous strategies that cover a wide range of temporal and spatial scales; these include erosion plots, field surveys, soil tracers, and measured sediment yields among others [Boix-Fayos *et al.*, 2006; Matisoff & Whiting, 2013].

Erosion plots enable for accurate measurements of runoff and associated soil losses on event-basis or any other time interval at the hillslope scale [Loughran, 1989]. Standard plots extent 22.13 m in length and 1.83 m in width, while the runoff and sediment from the bounded area is caught in trays and led through pipes to collecting tanks [Morgan, 2005]. Subsequently, the obtained runoff and soil loss data can be analyzed in relation to agricultural practices combined with rainfall properties and seasonal changes of the hydroregime [Bakr *et al.*, 2012; Ha *et al.*, 2012; Maetens et al., 2012]. However, plot-based soil erosion rates only represent the immediate locality, while inferences about the surrounding landscape are invalid [Brazier, 2004; Boardman, 2006]. Moreover, the artificial limitation of the slope length due to the bounding of the plots alters the runoff generation, and therefore introduces a bias to the soil loss data [Wainwright *et al.*, 2000].

Field surveys are based on volumetric measurements of erosion rills and gullies using remote sensed data on topography and in-situ investigations [Betts *et al.*, 2003]. The volumetric data is related to the bulk density of the soil, and thereby converted into soil loss in mass per unit area [Morgan, 2005]. Soil erosion rates can only be derived by relating the soil loss data to an estimated medium- to long-term period, which is assumed to have caused the erosion patterns that are investigated [Brazier, 2004].

Tracer applications to derive soil erosion rates are mainly based on the analysis of the fallout radionuclide caesium-137 (^{137}Cs) that originates from thermonuclear weapon tests between the 1950s and 1970s, from perturbations in fallout until the 1980s, and from the Chernobyl accident in 1986 [Alewell *et al.*, 2014]. Since ^{137}Cs has a strong affinity to clay particles of the soil, the distribution of the isotope is reported to be relatively homogeneous, especially at the field and catchment scale [Matisoff & Whiting, 2011]. Thus, ^{137}Cs serves as an indicator

for spatial patterns of soil loss and deposition that have taken place since the 1950s [Mabit *et al.*, 2013]. However, the ^{137}Cs inventories are only suitable in regions with a generally low spatial variability of rainfall and a spatially uniform distribution of ^{137}Cs [Parsons & Foster, 2011; Mabit *et al.*, 2013].

Measuring sediment yields at the outlet of a catchment provides information on the quantity of sediments that leave the catchment [Brazier, 2004]. The sediment yields can be acquired whether by analyzing water samples that are obtained in specified time intervals, or by continuously monitoring sediment concentrations in the water using turbidity sensors [Anderson, 2005; Shi *et al.*, 2012]. In both cases, sediment yields are estimated by relating the sediment concentrations to the discharge of the runoff channel [Satterland & Adams, 1992]. Particularly, continuous measurements are preferable since the accuracy of the method is determined by the sampling frequency [Morgan, 2005]. Thus, with a low sampling frequency the likelihood to exclude erosive runoff events and therefore underestimating sediment yields, is increased [Duck & McManus, 1994]. Considering that this measure disregards the quantity of sediments that is deposited within the catchment, estimations on total sediment yields and erosion rates are reported to be biased [Fryirs, 2013; Marchamalo *et al.*, 2015]. In addition, outlet data fail to represent spatial details of soil erosion and are therefore difficult to apply in the spatial quantification of soil loss [Manuscript 4; Boardman, 2006]. However, sediment yield data are valuable in revealing long-term trends of sediment fluxes related to soil erosion. They further enable for validating methods that spatially estimate erosion patterns in case of high landscape connectivity [Boardman, 2006; Shi *et al.*, 2012; Fryirs, 2013].

The above methods are suitable to quantify soil erosion rates under specific conditions, whether in high temporal resolution (e.g., erosion plots) or from small spatial scales (e.g., field surveys, soil tracers, and sediment yields). Moreover, some methods are accompanied by extensive field work (e.g., plot studies, field surveys) usually constrained by scarce monetary and temporal resources, while others comprise a limited representation of erosion data, such as sediment yields [Manuscript 4; Boardman, 2006; Keesstra *et al.*, 2009; Marchamalo *et al.*, 2015]. Thus, an efficient method is required that (i) combines a high temporal resolution to capture individual erosive events and (ii) provides a detailed spatial representation of erosion rates at catchment scale. This deficiency might be overcome by soil erosion models, which enable for efficiently quantifying hazardous erosion patterns and for predicting soil loss rates

for different land use scenarios [Manuscript 4; Morgan, 2005; Boardman, 2006]. Several model-based erosion studies have been applied in the TGRA [Manuscript 1; Quine *et al.*, 1999; Lu & Higgit, 2000; Shi *et al.*, 2004; Cai *et al.*, 2005; He *et al.*, 2007; Zhang, 2008; Shen *et al.*, 2010; Shi *et al.*, 2012].

4.3.2 Modelling Soil Erosion in the Three Gorges Reservoir Area

A few studies applied empirical soil erosion models, such as the Universal Soil Loss Equation (USLE) [Wischmeier & Smith, 1981] and the Revised Universal Soil Loss Equation (RUSLE) [Renard *et al.*, 1997] in the TGRA [Manuscript 1; Shi *et al.*, 2004; Yin *et al.*, 2007; Zhou *et al.*, 2008]. The USLE/RUSLE establishes relationships between rainfall, topography, conservation and management practices, soil, and soil vegetative cover to estimate long-term annual averages of sheet and rill erosion [Zhou *et al.*, 2008]. Soil loss is calculated from the product of environmental coefficients, which were derived from field observations in 37 U.S. states at plot scale [Manuscript 1; Zhang *et al.*, 1996; Shen *et al.*, 2009; Terranova *et al.*, 2009]. The USLE/RUSLE predicts an average soil loss for an extended time period, provided that the application remains within the range of conditions for which the model was developed [Grønsten & Lundekvam, 2006]. However, erosive effects of complex topography are not included in the standard USLE/RUSLE model, since the influence of flow convergence and divergence is not adequately regarded [Mitasova *et al.*, 1996; Tarboton, 1997; Capolongo *et al.*, 2008]. Beyond, these approaches are incapable to provide estimations of spatial erosion structures, while deposition is disregarded at all [Zhang *et al.*, 1996].

Other studies applied physically-based erosion and sediment transport models in the TGRA, such as the European Soil Erosion Model (EUROSEM), the Water Erosion Prediction Project (WEPP) and the Water and Tillage Erosion Model (WaTEM) [Manuscript 4; Cai *et al.*, 2005; Shen *et al.*, 2010; Shi *et al.*, 2012]. These models consider the spatial variability of the erosion processes and provide spatially distributed outputs of erosion and deposition. They are based on model routines, which describe the interactive erosion processes by corresponding mass equations [Zhang *et al.*, 1996; Aksoy & Kavvas, 2005]. This implicates a complex model structure and requires high quality input data in terms of spatial and temporal resolution and accuracy [Manuscript 4; Merritt *et al.*, 2003; De Vente & Poesen, 2005; Morgan & Nearing, 2011; De Vente *et al.*, 2013]. Beyond a likely incomplete process description of physically-

based models, the quality of available input data at catchment scale is often insufficient to adequately represent the local heterogeneity [Jetten *et al.*, 2003; Jordan *et al.*, 2005; De Vente *et al.*, 2013]. If the complexity of the model is not in agreement with the data quality, the models underperform due to error propagation [Van Rompaey *et al.*, 1999; Van Rompaey & Govers, 2002]. Hence, a variety of high quality erosion-related input data, such as soil properties, land cover, terrain, and climate is required to parameterize and to apply a physically-based erosion model in a reasonable manner [Manuscript 4; Chaubey *et al.*, 1999; Prosser & Dietrich,1995; Castillo *et al.*, 2003; Nearing *et al.*, 2005; Molina *et al.*, 2007; Immerzeel *et al.*, 2009; Baartman *et al.*, 2011; Bossa *et al.*, 2012; Shen *et al.*, 2012; De Vente *et al.*, 2013]. In addition, physically-based models can be distinguished in (i) event-based models to simulate sediment reallocations of single erosive events and in (ii) continuous models to address a series of events [Manuscript 4; Nearing *et al.*, 2005]. Input data requirements for continuous models are less restrictive compared to event-based models, since an event-specific parameterization is avoided and averaged parameter values may buffer random input errors [Van Rompaey *et al.*, 1999; De Vente *et al.*, 2013]. However, event-based models are preferable in order to investigate erosive responses in areas with few but high-intensity rainfall events such as in the TGRA [Manuscript 4; Cai *et al.*, 2005]. Recent studies in the TGRA using physically-based erosion and deposition models produced acceptable results [Cai *et al.*, 2005; Shen *et al.*, 2009, 2010; Shi *et al.*, 2012]. Most of the studies applied continuous models due to limited data availability at the catchment scale [Shen *et al.*, 2009, 2010; Shi *et al.*, 2012]. By contrast, Cai *et al.* [2005] applied an event- and physically-based model at the plot scale that indeed facilitates parameterization, but is inadequate in assessing spatial organization of conservation measures at the catchment scale [Shi *et al.*, 2012].

Thus, a model is required that provides event-based and spatially representative estimations on erosion rates at catchment scale to assess spatial patterns of hazardous soil erosion in the TGRA [Manuscript 4; Cai *et al.*, 2005; Peng *et al.*, 2011]. This was not accomplished by recent physically-based modelling attempts [Cai *et al.*, 2005; Shen *et al.*, 2010; Shi *et al.*, 2012], mainly due to complex model structures and the associated high input data requirements [Shi *et al.*, 2012]. The problem of overall data scarcity and inaccurate model input data, especially in terms of spatially distributed soil property information, needs to be addressed in the first place [Manuscript 4; Moore *et al.*, 1993; De Vente *et al.*, 2013]. In this

context, the challenge is to set up quantitative and spatially explicit models of the soil-landscape continuum, which enable for deriving detailed soil property information in a cost and time efficient manner [Manuscript 2, 3; Gessler *et al.*, 1995; Cook *et al.*, 1996; Scull *et al.*, 2003; Behrens & Scholten, 2006; Behrens *et al.*, 2010].

4.4 Soil-landscape Modelling

4.4.1 Quantitative Soil-landscape Modelling

A conventional soil survey is based on a conceptual model that describes the strong relationship between landscape features and the spatial distribution of soils [Hudson, 1992; Wysocki *et al.*, 2000]. Thereby, landscape units that show similarities in soil forming factors are delineated based on field observations. Subsequently, representative locations within the typological units are selected to investigate soil characteristics in detail. Based on this, qualitative rules are formulated that describe the soil-landscape relationship and determine the spatial distribution of soils. This procedure results in a soil-class map to represent specific soil types by discrete polygons with abrupt transitions [Wilding, 1985; Bui, 2004]. However, polygon-based maps of soil types are inadequate to furnish complex physically-based models, which require detailed information on the variability of soil properties within the considered landscape [Webster, 1977; Gessler *et al.*, 1995; Cook *et al.*, 1996; Scull *et al.*, 2003]. Moreover, conventional soil surveys are based on the experience of the surveyor, and therefore are criticized as subjective and too qualitative [McSweeney *et al.*, 1994; McBratney *et al.*, 2000]. In addition, elaborate reconnaissance surveys, extensive sampling campaigns, and laboratory analyses of conventional soil surveys are expensive and time consuming [Bishop *et al.*, 2001; Scull *et al.*, 2003; Behrens & Scholten, 2006; Adhikari *et al.*, 2014].

As a response to the deficiencies of conventional soil-class maps and along with technological advances in information technology, a quantitative and cost-efficient approach for soil-landscape modelling has been developed, known as Digital Soil Mapping (DSM) [Gessler *et al.*, 1995, McBratney *et al.*, 2003; Scull *et al.*, 2003]. DSM couples soil property information at distinct points with statistically related, co-located, and area-covering environmental covariates. While conventional soil maps are based on mental inferences to describe soil-landscape relationships, DSM uses (geo-) statistical models or data mining techniques instead.

Applying a DSM model in the area for which the model was built results in a map of continuous or discrete estimations of soil properties. Due to the quantitative character of the DSM procedure, soil-landscape relationships are objectively determined, detailed statistical analyses of related variables are facilitated, and uncertainty measures to evaluate the model predictions can be derived [Manuscript 2, 3; McBratney *et al.*, 2003; Scull *et al.*, 2003; McMillan, 2008].

The DSM concept originates from Jenny`s equation that describes the soil-landscape relationship, where soil (*S*) is a function of climate (*c*), organisms (*o*), topography (*r*), parent material (*p*), and time (*t*) at distinct locations [Jenny, 1941]:

$$S = f(c, o, r, p, t) \quad \text{(Eq. 1)}$$

McBratney *et al.* [2003] extended Jenny`s equation by incorporating the space and related soil properties as further independent variables, resulting in the SCORPAN approach that formulizes DSM:

$$S_{SC} = f(s, c, o, r, p, a, n) \quad \text{(Eq. 2)}$$

where S_{SC} is the soil property or soil category, *s* is the related soil property, *a* is age, respectively, time factor, and *n* is the spatial or geographic position.

DSM presents an established framework for soil mapping that comprises several work stages, including the extraction of environmental covariates, sampling of soil data, model building, and uncertainty analysis of the final prediction map [Padarian *et al.*, 2015]. Environmental covariates are usually extracted from small scale legacy soil maps and remote sensing data [Manuscript 2, 3; Mendonça-Santos et al., 2008]. At the local and landscape scale, one of the key data sources is the topography (*r*), which can be described by digital elevation models (DEM) and associated terrain derivatives [Manuscript 2, 3; Hudson, 1992; McBratney *et al.*, 2003; Grunwald, 2005; Behrens *et al.*, 2010]. Since the acquisition of DEMs is relatively inexpensive and terrain derivatives can be generated straightforwardly by a digital terrain analysis, DEMs are the prime data source to obtain DSM covariates [McKenzie & Ryan, 1999; Behrens *et al.*, 2010]. In this context, Bishop & Minasny [2005] reported that approximately 80% of the DSM applications are predominantly based on DEMs. Moreover, there are various possibilities to numerically describe the relationship between the covariates

and the co-located soil properties [Zheng *et al.*, 1996; Oberthur *et al.*, 1999; Pennock & Corre, 2001; Behrens *et al.*, 2005; Behrens *et al.*, 2010; Dorji *et al.*, 2014]. Machine learning techniques, such as classification and regression trees (e.g., CART) or tree-based ensemble classifiers (e.g., Random Forest) increasingly gain popularity [Manuscript, 2, 3, 5; Quinlan, 1986; Breiman, 2001; Grimm *et al.*, 2008; Ließ *et al.*, 2012; Adhikari *et al.*, 2014; Heung *et al.*, 2014; Schmidt *et al.*, 2014].

DSM has been successfully applied in numerous studies addressing various soil properties, landscapes, and spatial scales [Manuscript 2, 3; Behrens *et al.*, 2005; Wang *et al.*, 2012; Mansuy *et al.*, 2014; Taghizadeh-Mehrjardi *et al.*, 2014]. However, the field sampling of soil data outlines a limiting factor in the DSM procedure. This is attributed to the importance of DSM sampling designs in terms of model performance, adjustments to local conditions, and the incorporation of real field costs [Manuscript 2; Lagacherie, 2008; Kidd *et al.*, 2015]. In addition, there are various error sources in the DSM procedure due to inaccuracies in input data and oversimplification of the models that result in uncertainty [Nelson *et al.*, 2011; Wellmann, 2013]. This raises the question of a comprehensive, thus spatial quality assessment that is still limited [Manuscript 3; Finke, 2007; Krol, 2008; Nelson *et al.*, 2011].

4.4.2 Soil Sampling for Digital Soil Mapping

The sampling design to obtain field soil data should reflect the variation of the target soil property in the study area [Manuscript 2; Heuvelink *et al.*, 2007; Brungard & Boettinger, 2010]. Suggested strategies infer sampling in the geographical space [Brus *et al.*, 2006], in the feature space of covariates [Minasny & McBratney, 2006], or in a combination of both [Dobermann & Simbahan, 2007]. In addition, the sampling design should support field operability in terms of constrained accessibility, particularly due to difficult terrain and restricted areas [Manuscript 2; Kidd *et al.*, 2015]. Few studies addressed this issue by excluding inaccessible areas in the process of sample site selection [Roudier *et al.*, 2012; Mulder *et al.*, 2013; Clifford *et al.*, 2014] or by applying models from accessible areas to inaccessible areas based on similar environmental conditions [Cambule *et al.*, 2013]. Moreover, the sampling design should incorporate available legacy soil information to reduce high labor and monetary costs for sampling and laboratory analysis [Manuscript 2, 3; Lagacherie, 2008]. Therefore, legacy data from soil profiles and existing soil maps in a

disaggregated form served as a data source to calibrate prediction models [Manuscript 2, 3; Carré & Girard, 2002; Hengl *et al.*, 2004; Naumann & Thompson, 2014]. However, a spatial mismatch of statistically predefined sample sites, a lack in harmonization with the target soil property, and different spatial resolutions, formats and objectives remain problematic when incorporating legacy data into specific DSM sampling designs [Manuscript 2; Carré *et al.*, 2007; Krol, 2008; Sulaeman *et al.*, 2013]. A further possibility to increase the efficiency in soil data acquisition comprises an optimized sample set size. Few studies addressed this issue by comparing model results based on different calibration set sizes [Manuscript 2; Brungard & Boettinger, 2010; Ramirez-Lopez *et al.*, 2014; Schmidt *et al.*, 2014].

As a consequence of the aforementioned limitations, most sampling designs were established to solely focus on reflecting the variation of the target soil property in the area of interest. Operability and efficiency improvements in terms of accessibility, the integrative use of legacy samples, and optimization of the sample set size are often disregarded [Manuscript 2; Lagacherie, 2008; Cambule *et al.*, 2013]. Thus, advances in surveying soil data for DSM depend on comprehensively addressing the statistical, operational, and efficiency potentials of sampling designs [Manuscript 2].

4.4.3 Uncertainty in Digital Soil Mapping

Digital soil maps present an approximated description of spatially distributed soil properties that comprise an element of uncertainty [Manuscript 3; Webster & Oliver, 2005; Minasny & Bishop, 2008]. According to Nelson *et al.* [2011], the uncertainty in DSM originates from four error sources, which are (i) covariate error, (ii) model error, (iii) positional error, and (iv) analytical error. The covariate error refers to the error in the DSM covariates. Since data are usually derived from remote sensing devices, the error is sourced in the measurement or in an additional interpolation error if the data requires geostatistical pre-processing [Bishop *et al.*, 2006]. The model error refers to an insufficient understanding, and therefore to an oversimplification of real processes [Minasny & Bishop, 2008]. Depending on the type of model, the error can be ascribed to model specifications, estimations of model parameters or interpolations. McBratney *et al.* [2006] quantified the model error by applying bootstrapping that fits a model to different realizations of a data set to obtain an error variance. The positional error refers to the imprecise localization of spatial data, which is sourced in

measurement errors of the GPS technology [Grimm & Behrens, 2009]. The analytical error refers to measurement errors of soil properties occurring during the process of laboratory analysis. According to Viscarra Rossel & McBratney [1998], the analytical errors are low compared to other DSM error sources and in most cases well documented. In addition, the use of legacy data for DSM prevents monetary and temporal expenditures, such as field sampling and laboratory analyses [Cambule *et al.*, 2013]. However, the increase in practicability is accompanied by additional error sources since the inclusion of legacy data from multiple sources into DSM poses the question of reliability [Carré *et al.*, 2007; Krol, 2008].

The various error sources in the DSM workflow as well as the use of legacy data raises the question of quality assessment. In DSM, this is still limited and primarily related to prediction accuracy [Hengl & Husnjak, 2006; Finke, 2007; Krol, 2008; Grunwald, 2009]. The term 'accuracy' comprises measures on how close a prediction is to the true value [Everitt, 2002]. It is conventionally based on the variance between observed and predicted values at validation sites [Bishop *et al.*, 2001]. Brus *et al.* [2011] reviewed methodologies for validating soil maps and stated the importance of quantifying the accuracy by independent validation using model-free samples.

However, according to Minasny & Bishop [2008] as well as Wellmann [2013], an uncertainty analysis should give response to three questions that may arise from a user`s perspective: (i) How good is the prediction? (ii) Where are the areas of significant uncertainties located? and (iii) Where to spend available resources to reduce uncertainties? In this context, Wellmann [2013] postulated that mapped information necessarily require analysis and visualization of compound errors if it is used for further decision making. Furthermore, Sun *et al.* [2013] emphasized the spatial aspect of uncertainty analyses and stated that mapped uncertainty is inevitable for DSM products and its further applications. In this context, disregarding the relevance of a comprehensive uncertainty assessment weakens the confidence of soil scientists and decision makers in the final DSM product [Fischer, 1999].

Few studies in the field of DSM addressed the issue of a comprehensive, spatially distributed and therefore practicable uncertainty analyses [Manuscript 3; Grunwald, 2009]. If geostatistical methods are applied to map soil properties [Tutmez & Hatipoglu, 2010; Li & Heap, 2011], a spatially distributed error estimate, called kriging variance, is reported along with the predictions [Knotters *et al.*, 1995; Carré & Girard, 2002; Diodato & Ceccarelli, 2006;

Bourennane *et al.*, 2007; Qu *et al.*, 2013; Sun *et al.*, 2013]. These quality maps are restricted to the use of geostatistical interpolation methods and depend on the model-assumptions used for the predictions [Brus *et al.*, 2011]. Besides geostatistical methods, Bishop *et al.* [2015] proclaimed to focus on uncertainty, which is represented by a prediction interval at each location. In this context, Malone *et al.* [2011] adapted a method by Shrestha & Solomatine [2006] for DSM, which spatially quantifies uncertainty by regionalizing prediction intervals (PIs) based on the residuals between predicted and observed data. Though, this method was discussed as statistically complex and thus exhibiting limited practicability.

5 Research Objectives

The present thesis aims to provide a modelling framework that facilitates a detailed assessment of sediment reallocations due to erosive rainfall-runoff events at the catchment scale [Manuscript 1, 4]. The study area is a small, mountainous, and particularly data scarce catchment in the TGRA [Manuscript 1, 2, 3, 4]. DSM based on Random Forest regression has been applied to obtain relevant soil parameters to furnish a physically- and event-based soil erosion model, which requires high quality and spatially distributed soil property input data [Manuscript 2, 3, 4]. The DSM approaches were optimized in terms of operability and efficiency improved soil sampling to overcome difficult terrain and budgetary constraints [Manuscript 2]. Moreover, a spatial uncertainty measure has been developed, which was used for the identification of areas for additional soil sampling to further improve the initial DSM models [Manuscript 3]. Rainfall, runoff, and sediment yield were continuously monitored to determine and characterize erosive events [Manuscript 4]. As a result, spatial estimations on event-related sediment reallocations were derived by calibrating EROSION 3D [Manuscript 4].

In detail, this thesis addresses the following research objectives:

(i) The development of a DSM sampling design, which covers the feature space of relevant DSM covariates, compensates limited field accessibility, and provides efficiency improvements in terms of integrating legacy samples and optimizing the sample set size [Manuscript 2].

(ii) The development of a straightforward method to derive spatially distributed uncertainties of a digital soil property map, and to use the uncertainty information for additional sampling in relevant areas to refine initial maps [Manuscript 3].

(iii) The identification of erosive rainfall-runoff events based on continuously monitored data on rainfall, runoff, and sediment yields [Manuscript 4].

(iv) The calibration of the physically- and event-based soil erosion model EROSION 3D to spatially identify sediment reallocations [Manuscript 4].

The thesis was conducted within the framework of the BMBF-funded (grant no. 03 G 0827A) joint Sino-German project ‘YANGTZE GEO – Land use change, soil erosion, mass

movements, and matter fluxes along the Yangtze River, Three Gorges Reservoir Area', particularly within the sub-project 'Soil Erosion – Mechanisms and control factors of soil erosion by water in the Three Gorges Dam ecosystem' located at the University of Tübingen [Manuscript 1]. Thus, the results of this thesis contribute to the joint research focus of better understanding the dynamics and ecological consequences of large dam projects at the Yangtze River and worldwide.

6 Material and Methods

6.1 Study Area

The studies [Manuscript 2, 3, 4] were conducted in the Upper Badong catchment (Figure 1), located approximately 74 km upstream of the TGD in western Hubei Province (31°1′24″N, 110°20′35″E). The Upper Badong catchment covers an area of 428.7 ha of which 72% are exposed to the north. Elevation ranges from 469 m a.s.l. to 1,483 m a.s.l. with an average elevation of 1,053 m a.s.l. Slope angles amount to an average of 26° and range between 0° and 53°. The lithology of the southern study area exhibits clayed siltstone linked to the middle Triassic formation, while dolomite and microcrystalline limestone from the lower Triassic is dominant in the north. According to the Chinese Soil Taxonomic system, dominant soil groups are Purple soils in the south and Yellow to Yellow-brown soils in the north. Following the World Reference Base for Soil Resources [WRB, 2014], these soils refer to Cambisols and Alisols, respectively. The climate is humid subtropical with an average temperature of 12.9 C° and an average annual precipitation of 1,082 mm [CMA, 2012]. The rainfall regime is governed by the East Asian monsoon, showing a unimodal distribution with 68% of rainfall occurring from May to September. Land use is dominated by secondary forest vegetation (79.4 %) in the steep hillslopes of the mountainous study area [Manuscript 4]. Small agricultural plots (< 0.5 ha) are scattered in the study area, but concentrate to unconsolidated farmland patches in the north at elevations between 500 m a.s.l. and 700 m a.s.l., in the middle-east from 850 m a.s.l.to 1,050 m a.s.l., and in the south from 1,150 m a.s.l. to 1,250 m a.s.l. [Manuscript 4]. Since the climate allows for cropping twice a year, the typical crop rotation is corn and sweet potato in summer, followed by rapeseed and cabbage in winter. Conservation farming practices, such as contour tillage, furrow-ridge tillage or mulching with crop residues after harvest are increasingly implemented.

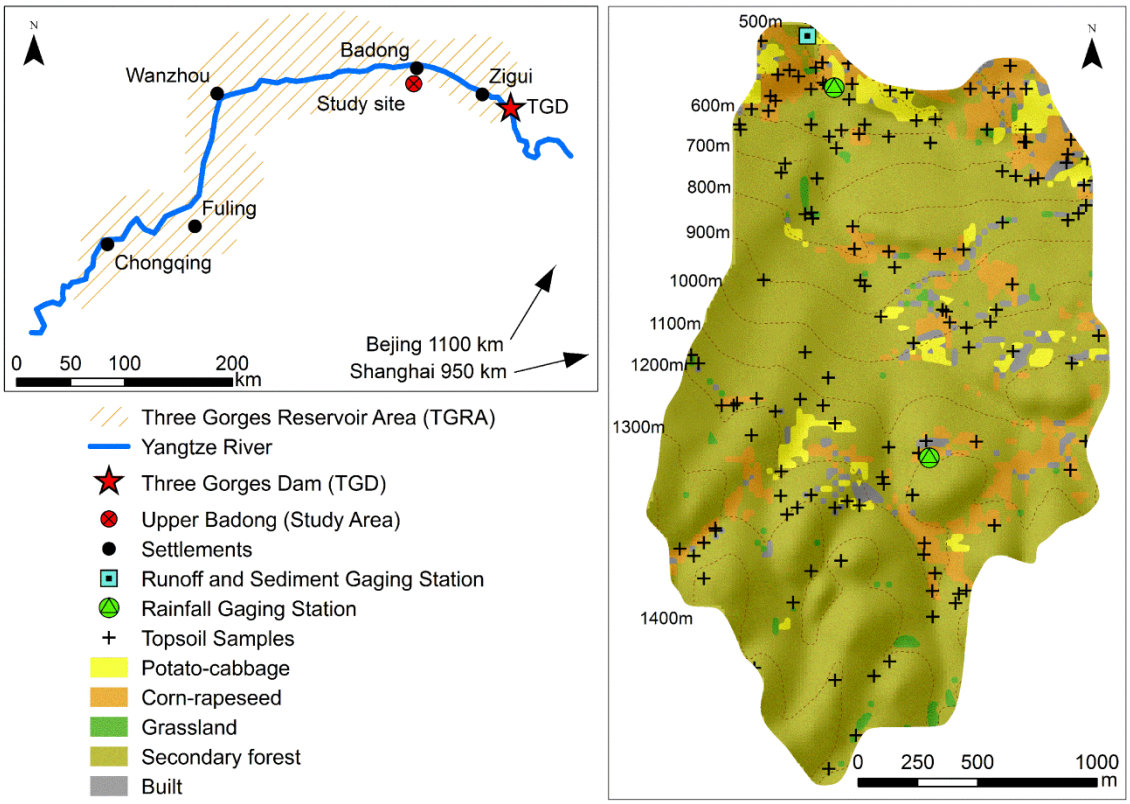

Figure 1: Study area (right) and its location within the Three Gorges Reservoir Area (left).

6.2 Data-base and Processing

6.2.1 Soil Data and Environmental Covariates

From 2012 to 2014, 145 topsoil samples (0 - 25 cm depth) were collected in four sampling campaigns based on the knowledge and results from one reconnaissance survey and three statistical DSM sampling designs (Figures 1 and 2). In October 2012, 55 samples were obtained in qualitatively delineated soil-landscape units using information on land use, topography, and field observations [Manuscript 2]. In April 2013 and March 2014, 90 samples were collected based on simple random sampling in the entire study area (30 samples), based on a modified conditioned Latin Hypercube Sampling (cLHS) design (30 samples), as well as on a modified cLHS design in areas of high DSM uncertainties (30 samples) [Manuscript 3, 4]. The samples were analyzed in terms of particle size distribution,

organic carbon content, and bulk density. At each sampling location five subsamples were pooled from the corners and the center of a 40 cm x 40 cm square in order to obtain composite samples. In addition, three subsamples were pooled, which were randomly taken within this square using a cylindrical core cutter with a defined volume of 100 cm³. Aliquots (50 g) of the homogenized and dried (40°C) composite samples were used to determine the soil organic carbon content (elemental analyzer Vario EL III). The remaining material of the composite samples was used for particle size analysis. Therefore, samples were sieved (< 0.63 mm) to separate sand contents, while silt and clay contents were separated using the Sedigraph III 5120 (micromeritics GmbH). The bulk density was derived from the dry weight (105°C) of the volume defined samples. In addition, topsoil (0-20 cm depth) moisture measurements were conducted at 235 sites randomly distributed over the entire study area using a TDR-sensor ML3 Thetakit by Delta-T Devices. The topsoil moisture measurements were performed within three days of dry weather conditions and after four days of frequent rainfall of low intensity in November 2014.

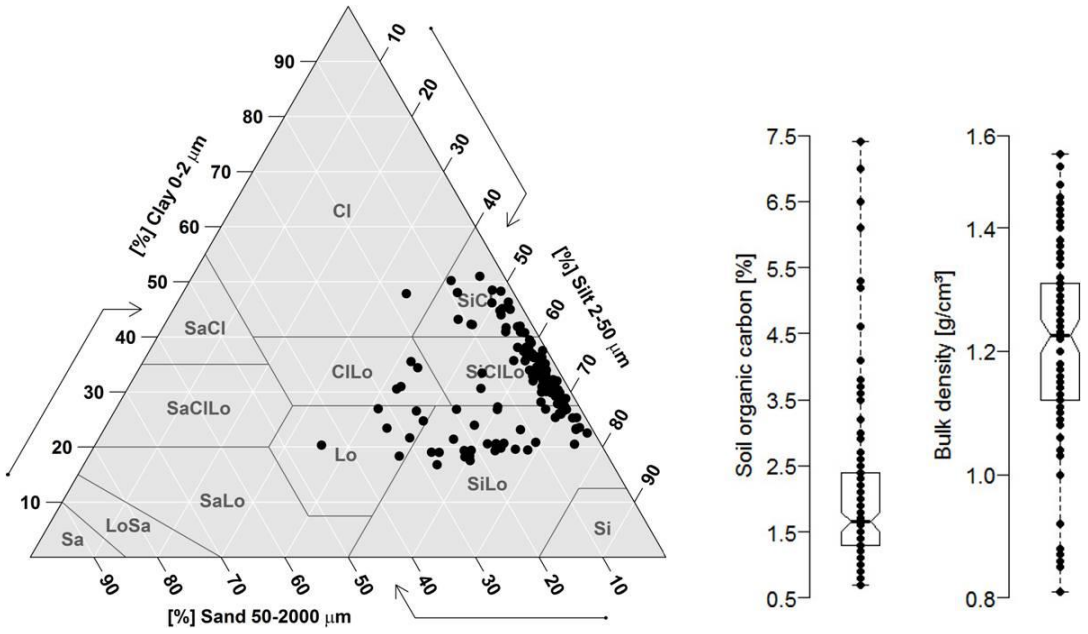

Figure 2: Particle size distribution (left), organic carbon content, and bulk density (right) for the topsoil samples.

Land use information is based on a RapidEye satellite image from September 28th 2012, providing five spectral bands in a spatial resolution of 5 m x 5 m [RapidEye, 2012]. Six land use classes were derived according to ‘cropland’, ‘grassland’, ‘broadleaf’, ‘conifer’, ‘shrub’, ‘woods’, and ‘built’ [Liu *et al.*, 2005]. Based on in-situ observations during the field campaigns in 2013 and 2014, the land use class ‘cropland’ was further refined in terms of a more accurate description of the crop rotations into ‘corn-rapeseed’ and ‘potato-cabbage’ (Figure 1).

A DEM was computed by digitizing a topographical map of the catchment with contour lines at 10 m intervals. The data was rasterized and resampled to a cell size of 25 m x 25 m to buffer potential uncertainties. Subsequently, 21 continuous terrain attributes were derived using a digital terrain analysis [SAGA GIS, 2012]. These DSM covariates present proxies to describe soil properties and repositioning processes of soil particles at a local and regional scale (Table 1).

Table 1: Environmental covariates with summary statistics.

Covariate	Unit	Minimum	Maximum	Average	Standard deviation
Altitude	m a.s.l.	469	1483	1054	255
Northing	-	1.42E-02	1.75E-02	1.62E-02	1.10E-03
Easting	-	0	1.30E-02	4.98E-03	3.74E-03
Wetness Index (SWI)	-	0	14.8	5.9	1.8
Slope angle	degree	0	53.2	26.4	6.9
Slope angle, maximum	degree	0	0.72	0.42	0.13
Slope length	m	0	2854	184	293
Catchment area	m^2 (log)	6.43	15.17	8.66	1.40
Plane curvature	m^{-1}	-1.03E-02	1.09E-02	-4.28E-05	2.82E-03
Profile curvature	m^{-1}	-1.09E-02	1.04E-02	-1.90E-04	2.30E-03
Combined curvature	m^{-1}	-8.80E-01	8.10E-01	-4.90E-03	1.54E-01
Flow accumulation	pixels (log)	2.8	6.1	3.9	0.56
Overland flow distance	m	0	377	91.9	75.1
Vertical flow distance	m	0	135	29.8	26.1
Horizontal flow distance	m (log)	0	2.6	1.5	0.88
Altitude above channel (AAC)	m	0	307	92	62
Terrain ruggedness	-	0.18	17.2	8.4	2.4
Mass balance index	-	-0.79	2.04	0.13	0.52
Convergence index	-	0	28.8	8.7	3.8
Position index	m	-26.9	35.7	0.25	7.2
Protection index	-	0	0.14	0.07	0.02

6.2.2 Hydrological Monitoring

A monitoring network was established to continuously record data on rainfall, runoff, and sediment yields (Figure 1). The data was logged in a temporal resolution of 10 minutes for a period of twelve months, starting in June 2013 (Figure 3).

Rainfall data was obtained by two self-emptying tipping bucket raingauges using the Vantage Pro 2 system by Davis Instruments with a single impulse capacity of 0.2 mm. The calibrated

raingauges were installed at elevations of 501 m a.s.l. and 1,193 m a.s.l. within the study area (Figure 1). The orifices were positioned at 1.5 m above ground to avoid disturbances by vegetation and wind. For further processing, data from both raingauges were averaged. The short-term data are representative, since - compared to long-term monthly records - similar distributions are revealed (Figure 3). The long-term data were recorded between 1960 and 2009 by the China Meteorological Administration [CMA, 2012] at Badong climate station (station ID 57355) in a distance of approximately 7 km from the study area.

Runoff data was obtained using a water pressure sensor (PTM/N/SDI-12 by STS-Sensors) that was positioned at the outlet of the catchment (Figure 1). Primarily, the water level was derived based on the water pressure and the geometry of the flow cross-section, which was measured in-situ. Subsequently, the standard flow rate equation was applied to determine the runoff according to Kirkby [1978]:

$$Q = A * V_q \qquad \text{(Eq. 3)}$$

where Q is the runoff [m^3s^{-1}], A is the flow cross-section [m^2], and V_q is the average flow velocity [ms^{-1}]. V_q was calculated according to the empirical Manning equation for gravity flow in open channels [Kirkby, 1978]:

$$V_q = \frac{1}{n} * \delta^{2/3} s^{1/2} \qquad \text{(Eq. 4)}$$

where n is the Manning coefficient for the hydraulic surface roughness [$sm^{-1/3}$], s is the slope gradient [-], and δ is the flow depth [m].

Data on sediment yield were obtained from the outlet (Figures 1 and 3) using a turbidity sensor (SN-PNEPA by PONSEL).The sensor measures the light intensity with an infrared beam that is scattered due to suspended particles. The measure is expressed in nephelometric turbidity units (NTU) and indicates the clarity, respectively, the turbidity of the water, which is mainly influenced by suspended sediments from eroding soil [Satterland & Adams, 1992; Anderson, 2005]. Since the NTU measure depends on the properties of the suspended sediment, a conversion into mass units [mgl^{-1}] requires a site-specific calibration. Thus, 250 composite sediment samples from the entire study area were progressively added to a defined

water volume of 5 l. By applying stepwise NTU measurements, a calibration curve has been derived to convert NTU values into suspended sediment load in mass units.

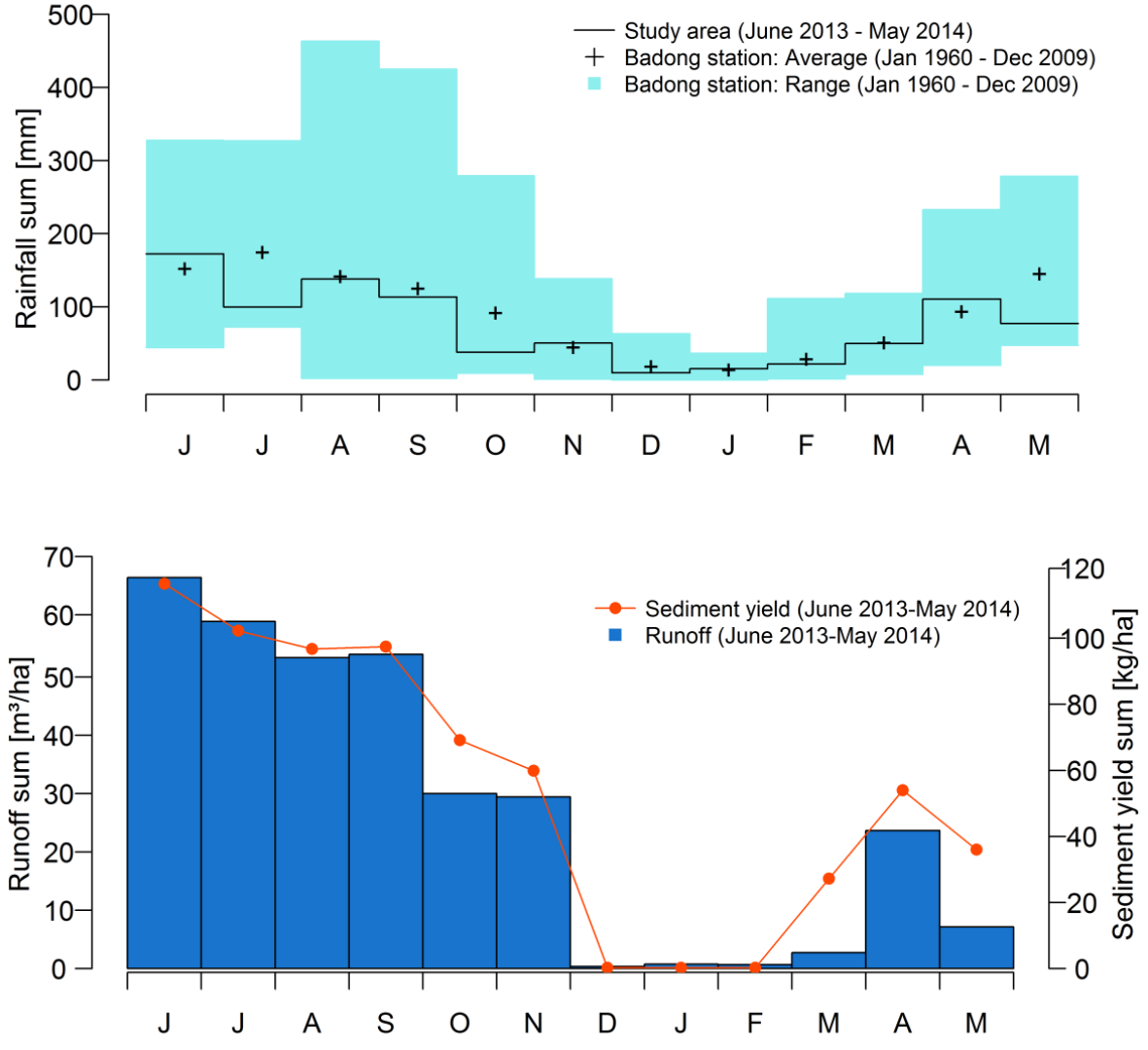

Figure 3: Regimes of monthly rainfall, runoff, and sediment yield data in the monitoring period. Rainfall records are compared to ranges and averages of long-term records from Badong station (above). Regimes of runoff and sediment yield are compared among each other (below).

6.3 Soil-landscape Model

In the present thesis, all DSM applications [Manuscript 2, 3, 4] are based on Random Forest (RF) regression. RF presents an ensemble classifier based on multiple randomized decision tree models [Breiman, 2001]. A decision tree applies a set of binary rules to compute a target variable [Manuscript 5; Quinlan, 1986]. Those binary rules are based on multiple environmental covariates and the soil property that should be mapped. The final soil property map in RF regression is computed by averaging the results over all individual trees for each pixel of the map. Since RF is robust to noise and multi-collinearity in the predictors, no pre-processing and pre-selection of covariates is required [Díaz-Uriate & De Andres, 2006; Behrens *et al.*, 2010].

Robustness of the RF model primarily depends on a large number of individual trees, which should be as diverse as possible [Prasad *et al.*, 2006; Peters *et al.*, 2007]. Optimized tree diversity ensures to derivate the entire scope of relevant information that is comprised in the model input data for the aggregated final prediction [Hansen & Salamon, 1990; Peters *et al.*, 2007]. RF increases the diversity of the trees by using randomized subsets of predictor covariates at each split of the trees and a randomized (by bootstrapping) soil sample set for each tree.

The subset of samples, which are not used to build a specific tree, are called out-of-bag (oob) data. Using this oob data for validating the respective trees, an error estimate (oob-error) can be derived by averaging the MSE (mean squared error) over all trees. The number of trees (k) and the size of the random feature subset at each node (m_{try}) are user-defined model parameters. Both can be determined by comparing the oob-errors of various RF realizations with different settings for k and m_{try} [Grimm *et al.*, 2008; Schmidt *et al.*, 2010]. For this study the soil property distributions with k = 1,500 and $m_{try} = 2\sqrt{p}$ was computed with p presenting the total number of covariates [Manuscript 2, 3, 4; Breiman, 2001]. For processing, the R-package ‘randomForest’ [Liaw & Wiener, 2002] was applied.

6.4 Soil Sampling Design

6.4.1 Latin Hypercube Sampling

Referring to *Manuscript 2*, a conditioned Latin Hypercube Sampling (cLHS) design was modified in order to cover the feature space of relevant DSM covariates, to compensate limited field accessibility, and to provide efficiency improvements in terms of integrating legacy samples and optimizing the sample set size. The target soil properties were topsoil fractions of coarse sand (CS: 2 - 0.63 mm), medium sand (MS: 0.63 - 0.2 mm), and fine sand (FS: 0.2 - 0.063 mm). Those 50 topsoil samples that were obtained during the reconnaissance survey in October 2012 (cf., Section 6.2.1) were designated as legacy samples.

The cLHS presents a stratified random method for sampling a multivariate distribution of environmental covariates. The idea is that the combined feature space of the covariates is fully covered by the sample set. Therefore, cLHS divides the range of each covariate into a number of equally probable strata (intervals), which corresponds to the sample set size. The sample set is derived by iteratively sampling from the entire feature space and by finally selecting target sites that in combination cover each stratum of each covariate once. This optimization procedure is accomplished by simulated annealing [Metropolis *et al.*, 1953] and ensures that each covariate is uniformly sampled in the final sample set [Minasny & McBratney, 2006]. Due to the purely statistical nature and the focus of the method on feature space, sampling locations might be selected that do not exist in the real world. Hence, the target site selection is conditioned by rejecting covariate combinations that do not exist in the real world. As proposed by Minasny & McBratney [2006], the final sampling set in cLHS is derived if the following criteria are fulfilled: (i) all strata of all selected covariates are occupied by one unique target site, (ii) the correlation between the covariates in the entire study area is preserved in the sampling set, and (iii) the combination of all samples fully covers the entire feature space of the covariates.

6.4.2 Covariate Selection and Sample Set Size

A feature subset of covariates from all covariates was selected (Table 1) to set up a cLHS design. This selection followed the criteria of a plausible correlation to the target variables

and a low correlation within the subset to avoid collinearity [Gessler *et al.*, 2000; Hengl *et al.*, 2003; Mulder *et al.*, 2013]. Using legacy soil samples, the correlations (r) of each covariate to the target variables were determined. Further, the results across all target variables for each covariate (r_1) were averaged. Subsequently, (i) the covariate with the highest r_1, and (ii) all other covariates with $r_1 > 0.4$ and a correlation < 0.4 among each other (r_2) defined the cLHS covariates.

The determination of the sample set size n is based on the comparison of the feature space of the cLHS covariates x_i ($i = 1, \ldots, k$) referring to the entire study area and 10 cLHS sample sets with a size n_j ($j = 10, 20, \ldots, 100$). The statistical variance (*var*) was used as an indicator to test the representativeness of the sample set sizes. The averaged variances of the covariates in the sample sets (sample set variance) were compared to the averaged variance of the covariates in the entire study area (global variance). The optimal sample set size n is defined by the minimum difference between the global variance and the sample set variance and by identifying the knee point of the curve, which takes the form:

$$n\,(j) = \left(\frac{\sum_{i=1}^{k} var(x_i)}{k}\right) - \left(\frac{\sum_{i=1}^{k} var(x_{ij})}{k}\right) \qquad \text{(Eq. 5)}$$

The knee point of the curve indicates the value of the minimum sample set size before the curve starts to level off disproportionally. The corresponding sample set size was assumed as the best tradeoff between sampling effort and representativeness to adequately reflect the feature space of the entire study area [Schmidt *et al.*, 2014; Ramirez-Lopez *et al.*, 2014].

6.4.3 Adapted Conditioned Latin Hypercube Sampling

Using the previously determined covariate selection and sample set size, cLHS was applied according to Schmidt *et al.* [2014] in order to facilitate to set the minimum and maximum value of each cLHS covariate as predefined. Thus, a full spread of the feature space in the hypercube is assured. From the derived strata with the original cLHS target sites ($cLHS_{orig}$), pixels with a slope angle higher than 35° and the land use classes ‘broadleaf’, ‘conifer’, ‘shrub’, ‘built’ as well as water bodies were defined as inaccessible, and subsequently excluded from sampling. The land use class ‘woods’ was also excluded unless the pixel was

in distance of less than 150 m from a path, and therefore accessible in reasonable temporal expense.

Inaccessible $cLHS_{orig}$ target sites were replaced by a potentially available legacy sample that occupied the respective stratum. For those strata with no accessible $cLHS_{orig}$ target sites, nor a matching legacy sample, a new target site was selected from all accessible pixels of the corresponding strata. Therefore, test sample sets of all possible combinations of accessible pixels over all remaining strata were generated, while taking the accessible and replaced $cLHS_{orig}$ target sites as predefined. The test sample sets were compared to the $cLHS_{orig}$ target sites using the cLHS search criteria of a preserved correlation between the covariates in the sample set and the coverage of the feature space in the entire study area (cf., Section 6.4.1). Primarily, those five test sample sets, which were most similar to $cLHS_{orig}$ referring to the correlations (r) between the covariates, were compared to $cLHS_{orig}$ according to their feature space coverage. Therefore, the frequency distribution of samples across the quartiles (Q) was used as simple measures. Ideally, 25% of the samples would fall in the first and third quartiles (Q1 and Q3) and 50% of the samples would fall in the second quartile (Q2). One final sample set ($cLHS_{adapt}$) was selected according to the smallest deviation from the ideal distribution.

For evaluating the presented cLHS design, two model calibration sets were compared. First, the sample set obtained according to the adapted cLHS design ($cLHS_{adapt}$), and second, $cLHS_{adapt}$ in combination with the legacy samples ($cLHS_{adapt+}$). Previously, the legacy sample set was randomly reduced by 20 samples to set up an independent validation data set. The accuracy of the RF regression models for all target variables and both calibration sets was evaluated by using independent and bootstrap validation (number of bootstrap samples: 20). For both accuracy estimations, the accuracy measures coefficient of determination (R^2) and root mean squared error (*RMSE*) were computed. Since the predicted target variables represent compositional data, the coherence of their predicted sum, which ideally amounts to 100%, was additionally assessed. For processing the R-package "base" (R Core Team, 2014) has been applied.

6.5 Spatial Uncertainty and Additive Sampling

Referring to *Manuscript 3*, a method for deriving spatial uncertainties of digital soil maps was developed. Furthermore, the uncertainty information was used to demarcate target sites relevant for additional soil sampling to improve initial RF mapping approaches for topsoil silt (2-63 µm) and clay (< 2 µm) fractions. The initial RF soil property maps were based on a model calibration set of 60 topsoil samples (LD), randomly derived from the pool of samples (n = 80) that originates from the previous sampling campaigns in October 2012 and April 2013. However, LD was not specifically obtained to cover the variability of silt and clay fractions in the study area, therefore attenuating the DSM performance. Thus, the uncertainty-guided sampling comprises the identification of relevant sampling areas based on the spatial uncertainty, and the application of the adapted cLHS design within this sampling area to obtain additional samples purposively.

The spatial uncertainty measure is based on the concept to generate a compilation of equiprobable realizations of spatial model predictions and analyzing the divergences among the simulated maps [Goovaerts, 2001]. In RF, this concept is already inherent since the RF predictions are aggregated from the results of multiple randomized decision tree models [Breiman, 2001]. Due to randomization, the results of the single tree predictions are spatially variable [Peters *et al.*, 2007; Grimm & Behrens, 2009]. Thus, a specific prediction interval at each location can be derived. The variability of an interval refers to the uniformity of the single decision tree results, and therefore, the local robustness of the RF model. Consequently, a prediction interval with a high statistical variance (s^2) indicates decreased robustness and vice versa [Sun *et al.*, 2013]. In this context, s^2 was applied as local error variance, thus generating a spatially distributed uncertainty measure ($errs^2$). For each location j, with k outlining the number of trees (i =1, 2,…, k) and x indicating the values of the prediction interval, $errs^2$ is defined as the following:

$$err^{s^2}(j) = \frac{1}{k} \sum_{i=1}^{k} (x_i - \bar{x})^2 \qquad \text{(Eq. 6)}$$

For processing, the R-package “base” [R Core Team, 2014] was applied.

To limit the sampling effort, one spatial uncertainty-guided sampling scheme for both target variables (silt, clay) was conducted to purposively obtain additional samples. Therefore, the

spatial uncertainty maps of both initial RF approaches (U_1, U_2) were merged into one single combined uncertainty map (U_{com}), which then underlied the sampling. The merging was conducted by retaining the maximum (*max*) uncertainty value (M_{errs^2}) of the standardized spatial uncertainties u_1 and u_2 for each location *j* according to

$$M_{errs^2}(j) = max(u_{1j}, u_{2j}) \quad \text{(Eq. 7)}$$

Subsequently, a new sampling area was identified based on areas with increased uncertainty values of $U_{com,}$ reflecting a decreased coverage of the soil variability by the legacy samples. Primarily, four potential sampling areas were derived, defined by the entire study area (Q1) and by the quartile-breaks > 25% (Q2), > 50% (Q3), and > 75% (Q4) of U_{com}. Since the predictor covariates serve as proxies for the soil variability, it was tested how precisely available legacy samples cover the variability of the covariates within each potential sampling area. This was achieved by computing the divergence between the distribution in the potential sampling area (P_1) and the distribution based on available legacy samples (P_2) referring to each covariate separately. For this, the Kullback-Leibler divergence (*KL*) [Kullback & Leibler, 1951] was applied to examine the divergence between two distributions.

$$KL\,(P_1 \| P_2) = \int p_1\,(x)\; log\, \frac{p_1(x)}{p_2(x)}\, dx \quad \text{(Eq. 8)}$$

with p_1 and p_2 indicate the densities of P_1 and P_2.

The sum of the divergences over all covariates (t = 1, 2,…, m) indicates a measure (KL_{sum}) on how precise the legacy samples cover the variability of silt and clay. While an increased divergence indicates less coverage and vice versa, KL_{sum} takes the form

$$KL_{sum} = \sum_{t=1}^{m} KL_t \quad \text{(Eq. 9)}$$

Since the potential sampling areas were defined by quartile-breaks of the combined uncertainty distribution, an increasing *KL* divergence from Q1 to Q4 was assumed. Comparing KL_{sum} of all potential sampling areas, the final sampling area was identified, where KL_{sum} starts to level up disproportionally. The R-packages "flexmix" [Grün & Leisch, 2008) and "base" [R Core Team, 2014] were used for processing. Within the final sampling area, the adapted cLHS design was applied to obtain additional topsoil samples (cf., Section 6.4).

According to the spatial uncertainty-guided sampling, LD was augmented by 30 additional samples to form a second calibration set (LD_{Unc}) with a sample set size of n = 90. For a comparative evaluation, a third calibration set (LD_{Random}) was generated by augmenting LD with 30 additional samples that were obtained according to simple random sampling within the entire study area (n = 90). The remaining 20 model-free samples from previous sampling campaigns were used to validate the predictions. Thus, three RF DSM approaches were set up, each estimating topsoil silt and clay contents and using the model calibration sets LD, LD_{Random}, and LD_{Unc}. To assess the quality of the approaches comparatively, the spatial uncertainty measure ($errs^2$), as well as accuracy estimates based on a 10-fold cross-validation (*cv*), bootstrap validation (*boot*; number of bootstrap samples: 10) and independent validation (*val*; number of samples: 20) were calculated. The coefficient of determination (R^2) and the root mean squared error (*RMSE*) were used as accuracy measures. Processing has be conducted using the R-package "caret" by Kuhn [2009].

6.6 Modelling Sediment Reallocations

6.6.1 Erosive Rainfall-runoff Events

Analyses on rainfall-runoff events and their associated erosive response are based on monitoring data on rainfall, runoff, and sediment yield. In a first step, rainfall records were disaggregated according to a minimum inter-event time of six hours using the R-package 'hydromad' [Andrews & Guillaume, 2015]. This threshold is commonly applied in event-based erosion studies [Wischmeier & Smith, 1981; Xie *et al.*, 2002; Bagarello *et al.*, 2008; Soulis *et al.*, 2009; Taguas *et al.*, 2011] to identify independent rainfall events with similar initial soil moisture conditions that control runoff generation [Bracken *et al.*, 2008; Todisco, 2014]. In a second step, the direct runoff associated to each rainfall event was determined. Direct runoff originates from rainfall that contributes immediately to the streamflow, while baseflow reaches the streamflow with a substantial delay [Merz *et al.*, 2006]. To separate baseflow from direct runoff, a recursive digital filter technique was applied to the runoff record according to Nathan & McMahon [1990] and Arnold *et al.* [1995]. Using the R-package 'Ecohydrology' [Fuka *et al.*, 2014], the following filter equation was applied:

$$q_t = \beta * q_{t-1} + \frac{1+\beta}{2} * (Q_t - Q_{t-1}) \qquad \text{(Eq. 10)}$$

where q_t [m^3s^{-1}] is the filtered direct runoff at the time step t [min], Q_t [m^3s^{-1}] is the original streamflow, and β [-] is the filter parameter.

While an initial rainfall impulse defined the start of a rainfall-runoff event, the end was indicated when no longer associated direct runoff occurred. Using this event distinction, the respective sediment yield was attributed to each rainfall-runoff event to identify its erosive response. The adequacy of this procedure depends on the strength of the cause-effect relationship between rainfall, runoff, and sediment yields within the specific catchment [Todisco, 2014]. This was evaluated by comparing the hydroregimes revealed from the monitoring data over the measuring period by using a correlation matrix.

For further analyses, those events were selected that exhibit direct runoff and an associated erosive response. In contrast, those events, for which a distinct attribution of direct runoff to a rainfall-runoff event was impossible due to inadequate separation between direct runoff and baseflow, were rejected [Blume *et al.*, 2007].

Each of the erosive rainfall-runoff events was characterized according to their event-triggering rainfall properties, such as total rainfall amount P [mm], the duration of occurring rainfall D [h], the maximum rainfall intensity in 30 minutes I_{30} [mm h^{-1}], the maximum rainfall intensity in 60 minutes I_{60} [mm h^{-1}], and the erosivity EI_{30} calculated as [Brown & Foster, 1987],

$$EI_{30} = \sum_{r=1}^{0} E * I_{30} \qquad \text{(Eq. 11)}$$

where E [MJ ha^{-1}] is the rainfall kinetic energy for a time interval [r] that can be estimated by

$$E = 0.29 * [1 - 0.72 * exp(-0.05 i_r)] * P_r \qquad \text{(Eq. 12)}$$

6.6.2 Erosion Model Description

For event-based soil erosion modeling EROSION 3D [Schmidt, 1991, 1992] was applied. EROSION 3D is a raster- and physically based model that calculates soil losses and deposition initiated by single rainfall events or event sequences in small watersheds. The model includes the erosional processes of direct runoff, detachment of soil particles by rainfall splash and runoff, transport of detached particles by runoff, routing of runoff and

sediment, and sediment deposition. The mathematical incorporation of these processes is based on two subroutines addressing runoff and, more explicitly, soil erosion.

The runoff subroutine calculates the rainfall excess according to a modified Green-Ampt infiltration equation [Green & Ampt, 1911; Weigert & Schmidt, 2005; Schindewolf & Schmidt, 2012]:

$$i = k_s * g + k_s * \frac{\Psi_{m0}}{\sqrt{\frac{2k_s * \Psi_{m0} * t}{P_f * (\Theta_s - \Theta_0)}}} \quad \text{(Eq. 13)}$$

where i is the infiltration rate [kg/(m²s)], k_s is the saturated hydraulic conductivity [(kg s) m^{-3}], g is the gravity [m s^{-2}], Ψ_{m0} is the matric potential [N m kg^{-1}] related to the initial water content Θ_0 [N m kg^{-1}], t is time [s], P_f is fluid density [kg m^{-3}], and Θ_s is the saturated water content [m^3 m^{-3}]. The saturated hydraulic conductivity [k_s] is estimated by using pedotransfer functions according to Campbell [1991]:

$$k_s = 4 * 10^{-3} * \left(1.3 * \frac{10^{-3}}{P_b}\right)^{1.3*b} * exp(-0.069 * T - 0.037 * U \quad \text{(Eq. 14)}$$

with

$$b = (10^{-3} * D)^{-0.5} + 0.2 * \delta_p \quad \text{(Eq. 15)}$$

where P_b is the bulk density [kg m^{-3}], T is the clay content [kg kg^{-1}], U is the silt content [kg kg^{-1}], b is parameter [-], D is the average diameter of soil particles [m], and δ_p is the standard deviation of the average diameter of soil particles [-].

Since the pedotransfer function assumes a rigid soil matrix, the temporal variability of the soil structure is disregarded. Therefore, k_s is corrected by a multiplication with an empirically derived, so-called skinfactor to adjust the infiltration rates [Schindewolf & Schmidt, 2012].

The soil erosion subroutine, thus the spatial quantification of particle detachment, transport and deposition, is based on the momentum-flux approach [Schmidt, 1991]. Basically, this approach follows the assumption that the erosive impact of direct runoff and rainfall splash is proportional to their exerted momentum fluxes [Schindewolf & Schmidt, 2012] where the momentum flux of the direct runoff flow [ϕ_q] is defined by:

$$\phi_q = \frac{W_q * V_q}{\Delta X} \quad \text{(Eq. 16)}$$

the momentum flux of the rainfall splash [$\varphi_{r,\alpha}$] follows the equation:

$$\varphi_{r,\alpha} = W_r * V_r * sin\,\alpha * (1 - CL) \quad \text{(Eq. 17)}$$

where W_q and W_r are the mass rates of direct runoff flow respectively rainfall splash, V_q and V_r are the average flow velocity respectively velocity of the rainfall droplets, Δx is the length of the slope segment, α is the slope angle, and CL the soil cover.

Since an observable rate of soil erosion requires a minimum rate of direct runoff [q_{crit}], the erosion resistance of the soil is defined as the critical momentum flux [ϕ_{crit}], following the equation [Schindewolf & Schmidt, 2012]:

$$\phi_{crit} = \frac{q_{crit} * P_q * V_q}{\Delta X} \quad \text{(Eq. 18)}$$

where q_{crit} is the volume rate of flow [$m^3\ (ms)^{-1}$] at initial erosion, P_q is the fluid density [$kg\ m^{-3}$], Δx is the slope segment width [m], and V_q is the flow velocity [$m\ s^{-1}$] that was derived according to equation (cf., Eq. 4).

6.6.3 Erosion Model Application

Besides the obtained rainfall records and the DEM, EROSION 3D requires a set of raster-based soil properties that represent the soil's spatial heterogeneity at the catchment scale as good as possible. The parameters of particle size distributions [%], bulk density [$kg\ m^{-3}$], and organic carbon content [%] were assumed to be steady over the period of interest. In contrast, the parameters soil cover [%], erosion resistance [$N\ m^{-2}$], hydraulic roughness according to Manning`s n [$N\ m^{-1/3}$], skinfactor [-], and initial soil moisture [vol.-%] were adjusted for each event [Schmidt *et al.*, 1999; Schindewolf & Schmidt, 2012].

DSM was applied to derive the steady soil parameters. RF regression models were set up to link the 145 available soil property samples (Figures 1 and 2; cf., Section 6.2.1) with terrain covariates (Table 1). The results were evaluated using the RF internal oob-error (cf., Section 6.3), and applying the coefficient of determination (R^2) and the root mean squared error

(*RMSE*) as accuracy measures (Table 2). For processing, the R-package 'randomForest' [Liaw & Wiener, 2002] was used.

Table 2: Summary statistics (sd: standard deviation) and accuracy (coefficient of determination:R^2; root mean squared error: RMSE) of steady soil parameters.

Parameter	Minimum	Maximum	Average	sd	RMSE	R^2
Clay content [%]	18.6	44.8	32.6	3.7	5.1	0.58
Silt content [%]	43.5	69.0	62.3	3.9	5.0	0.57
Sand content [%]	1.4	30.8	4.9	5.2	3.9	0.79
Bulk density [kg m^{-3}]	700	2,000	1,200	100	100	0.36
Organic carbon [%]	1.0	3.2	2.1	0.4	0.5	0.45

The soil cover was estimated by interpreting the refined land use map (cf., Section 6.2.1) with crop rotation patterns in combinations with the seasonally occurring grow stages. The input parameters erosion resistance, hydraulic roughness, and skinfactor were estimated using a parameter catalogue [Michael, 2000]. This catalogue contains a progressively updated compilation of empirically obtained parameter values for different soils and crops, considering seasonal variations and management practices [Schmidt *et al.*, 1999; Schindewolf & Schmidt, 2012]. The parameter soil moisture is most sensitive and highly variable in time and space [Schmidt, 1992; Starkloff & Stolte, 2014]. Thus, the average soil moisture values from the parameter catalogue were initially used. Following, the model was run iteratively with varying soil moisture values. The best fit between observed and predicted direct runoff was then selected [Jetten *et al.*, 1999; Schmidt *et al*., 1999].

For the EROSION 3D model runs, all input parameter were harmonized to a cell size of 25 m x 25 m. The model output of each event was validated individually by comparing the predicted sediment yield at the catchment outlet with the observed sediment yield. To express the discrepancy, the proportional deviation (*ERR*) of the prediction from the respective observation was assessed. Moreover, the average model performance for the sequence of erosive events was analyzed by using the averaged individual prediction error ($ERR_{average}$), the root mean square error (*RMSE*) and the Nash-Sutcliff coefficient (*NS*) [Nash & Sutcliff, 1970; Krause *et al.*, 2005]. The equations of the quality measures are defined as follows:

$$ERR = \frac{|SY_{obs} - SY_{pred}|}{SY_{obs}} \quad \text{(Eq. 19)}$$

$$RMSE = \sqrt{\frac{\sum_{i=1}^{n}(SY_{pred,i} - SY_{obs,i})^2}{n}} \quad \text{(Eq. 20)}$$

$$NS = 1 - \frac{\sum_{i=1}^{n}(SY_{obs,i} - SY_{pred,i})^2}{\sum_{i=1}^{n}(SY_{obs,i} - SY_{ave,obs,i})^2} \quad \text{(Eq. 21)}$$

where SY_{obs} [Mg] is the observed sediment yield of an event *i*, SY_{pred} [Mg] is the predicted sediment yield, and $SY_{ave,obs}$ [Mg] is the average observed sediment yield. For model validation, the R-package 'hydroGOF' by Zambrano-Bigiarini [2014] was applied.

Finally, the soil loss and deposition patterns were mapped as a budget over the erosive events to spatially identify sediment sources and deposits dependent on the land use and topography. The model results of each pixel were separated according to four classes (severe: > 50 Mg ha^{-1}; high: 20 - 50 Mg ha^{-1}; moderate: 10 - 20 Mg ha^{-1}; low: 0 - 10 Mg ha^{-1}) for soil loss and deposition, respectively. This classification is based on thresholds that are commonly applied in the TGRA with respect to soil erosion studies [Shi *et al.*, 2004; Shi *et al.*, 2012].

7 Results

7.1 Adapted Conditioned Latin Hypercube Sampling

7.1.1 Covariate Selection and Sample Set Size

According to the correlations of each covariate to the target variables (r_1), the covariate 'Altitude Above Channel' (AAC) shows the highest value (r_1 = 0.65) and was therefore selected as first cLHS covariate. The covariates 'Altitude' (r_1 = 0.65), 'Plane curvature' (r_1 = 0.63) and 'Wetness Index' (SWI; r_1 = 0.41) are plausibly correlated to the target variables with r_1 > 0.4. However, 'Altitude' and 'Plane curvature' show correlations of r_2 = 0.62 and r_2 = 0.55 to AAC, thus, indicating collinearity. Subsequently, both were rejected from further analysis. SWI shows a lower collinearity with an r_2 of 0.38 and was therefore retained (Table 3). Consequently, the two covariates AAC and SWI were used to build the feature space for the adapted cLHS.

Table 3: Covariates ranked according to their averaged correlations r_1 to the target variables. The correlation between the covariates and the top ranked covariate is indicated by r_2.

Covariate	r_1	Rank	r_2
AAC	**0.65**	**1**	**1**
Altitude	0.65	2	0.62
Plane curvature	0.63	3	0.55
SWI	**0.41**	**4**	**0.38**
Slope angle, maximum	0.38	5	0.44
Terrain ruggedness	0.31	6	0.01
Slope angle	0.29	7	0.03
Slope length	0.28	8	0.37
Convergence index	0.23	9	0.33
Land use	0.23	10	0.22
Mass balance index	0.2	11	0.22
Combined curvature	0.19	12	0.29
Northing	0.19	13	0.15
Easting	0.18	14	0.10
Horizontal flow distance	0.18	15	0.07
Protection index	0.17	16	0.08
Profile curvature	0.16	14	0.27
Vertical flow distance	0.12	18	0.12
Flow accumulation	0.09	19	0.35
Overland flow distance	0.08	20	0.10
Position index	0.08	21	0.29
Catchment area	0.07	22	0.41

For the determination of the final sample set size *n*, the selected cLHS covariates AAC and SWI were used to set up 10 cLHS designs, which exhibit test sample set sizes ranging from 10 to 100. The numerical distances of the sample set variances to the global variance spans from 0.01 to 0.06 (Figure 4), while decreasing values indicate an increase in representativeness of the respective cLHS set. When plotting the sample set size against the sample set variance, the knee point of the resulting function shows a numerical distance of 0.02 (Figure 4) suggesting a final sample size of $n = 30$ for cLHSadapt. This results in a ratio of 7.1 samples per km².

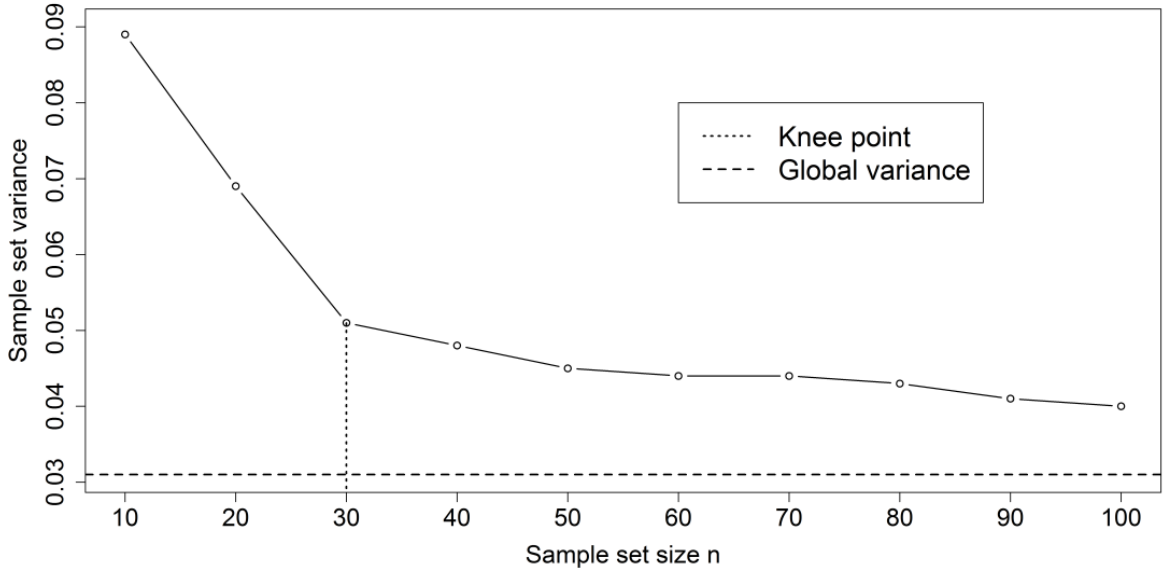

Figure 4: Determination of a sample set size by comparing the sample set variance to the global variance (dashed line), using the knee point (dotted line).

7.1.2 Target Site Selection

Corresponding to the previously determined sample set size n = 30, the final cLHS design ($cLHS_{adapt}$) results in 30 strata, each with a varying number of spatially scattered pixels ranging from 2 to 84. The variation and scattering is determined by the statistical properties of the cLHS covariates 'AAC' and 'SWI', which underlay the strata (Table 1). After excluding inaccessible areas, each stratum shows a number of 1 to 4 accessible pixels (Table 4).

Each stratum needs to be sampled at precisely one specific target site, while the combination of all sampled target sites results in an optimized coverage of the cLHS feature space formed by AAC and SWI. Seven strata are occupied by predefined target sites from $cLHS_{orig}$ or the legacy samples: Two sites refer to the $cLHS_{orig}$ design and match accessible pixels of a stratum. In the remaining five strata, legacy samples are available, which were used to cover the respective stratum. This results in 23 uncovered strata whether due to lacking accessibility at the $cLHS_{orig}$ target site or absent legacy samples (Table 4).

Since five legacy samples were integrated into the $cLHS_{adapt}$ design and 20 samples were extracted for validation, 30 legacy samples remained unused (cf. 6.2.1). Thus, they were combined with the $cLHS_{adapt}$ (n = 30) resulting in the further calibration set $cLHS_{adapt+}$ (n = 60), which was used for evaluating the approach comparatively.

Table 4: Number of accessible pixels and total number of pixels per stratum. The strata sampled by original cLHS sites and strata occupied by legacy samples are indicated (dots).

Strata	Number of accessible pixels	Total number of pixels	$cLHS_{orig}$ sample	Legacy sample
1	3	22	–	●
2	2	5	–	–
3	2	8	–	–
4	3	18	–	–
5	1	7	–	–
6	1	19	–	–
7	1	84	–	●
8	1	9	–	●
9	1	18	–	–
10	1	9	–	–
11	1	20	–	–
12	1	7	–	–
13	1	6	–	–
14	1	8	–	–
15	2	6	–	–
16	2	12	–	–
17	2	19	–	–
18	2	3	–	–
19	4	9	●	–
20	3	26	–	–
21	3	10	–	●
22	1	4	–	–
23	2	2	●	–
24	3	16	–	–
25	1	7	–	–
26	2	13	–	–
27	2	5	–	–
28	4	25	–	–
29	2	9	–	–
30	2	64	–	●

The target sites in the 23 uncovered strata were determined by analyzing all possible combinations of accessible pixels across those strata that were not sampled. For each combination, the 7 predefined target sites were added resulting in 10,592 test sample sets.

The test sample sets were examined according the cLHS criteria using $cLHS_{orig}$ as baseline to select the most adequate sample set for calibration ($cLHS_{adapt}$). Referring to the cLHS criterion of a preserved correlation between the covariates in the sample set, those five pre-selected sample sets that were most similar to $cLHS_{orig}$ show differences in correlation with $r < 0.01$. Contrary, the calibration set $cLHS_{adapt+}$ differs by $r > 0.05$. Referring to the criterion of optimized feature space coverage, the proportional frequency of samples across the quartiles of the cLHS covariates ($Q1\text{-}3_{AAC}$, $Q1\text{-}3_{SWI}$) was used. The deviations to $cLHS_{orig}$ over all quartiles and both covariates (dev.) were summed up. The deviations of the five pre-selected test sample sets range from 22 to 42 percent points (pp), while $cLHS_{adapt+}$ differs by 60 pp (Table 5). Thus, the calibration set $cLHS_{adapt+}$ ($n = 60$) shows less similarity to $cLHS_{orig.}$ than the five selected test sample set sizes with $n = 30$ (Table 5).

This test sample set, which is most similar to $cLHS_{orig}$ according to the cLHS criteria was selected as final calibration set ($cLHS_{adapt}$). For $cLHS_{adapt}$, the correlation r between the cLHS covariates in the entire study area and in the sample set differs by 0.0061. The summed up deviation of the proportional frequencies in the quartiles amounts to 22 pp (Table 5).

Table 5: Sample set comparison of the original cLHS set ($cLHS_{orig.}$), the test sets (test 1 to test 5), and the calibration sets $cLHS_{adapt}$ with a sample size n = 30, and $cLHS_{adapt+}$ with 30 additional legacy samples. The correlation (r) among the cLHS covariates in the sample sets, the proportional frequency across the quartiles of the cLHS covariates in the study area ($Q1\text{-}3_{AAC}$, $Q1\text{-}3_{SWI}$), and the summed up deviation (dev: deviation; pp: percent points) from $cLHS_{orig}$ are indicated.

Sample set	r	$Q1_{AAC}$ (%)	$Q2_{AAC}$ (%)	$Q3_{AAC}$ (%)	$Q1_{SWI}$ (%)	$Q2_{SWI}$ (%)	$Q3_{SWI}$ (%)	dev (pp)
$cLHS_{orig.}$	0.4003	23	50	27	23	50	27	-
test1/$cLHS_{adapt}$	0.3942	27	46	27	27	53	20	22
test 2	0.3923	27	43	30	17	57	26	28
test 3	0.4068	27	43	30	23	43	34	28
test 4	0.3905	27	43	30	20	60	20	34
test 5	0.4037	33	40	27	34	43	23	42
$cLHS_{adapt+}$	0.3365	45	38	17	17	58	25	60

7.1.3 Hypercube Sampling: Model Calibration and Prediction

According to the laboratory analysis of the two calibration sets $cLHS_{adapt}$ (n = 30) and $cLHS_{adapt+}$ (n = 60), the average topsoil sand content accounts to 6% in $cLHS_{adapt}$ and to 9.5% for $cLHS_{adapt+}$. Comparing the results referring to both calibration sets and all target sand fractions (CS, MS, FS), $cLHS_{adapt+}$ shows higher averages and variabilities for all sand fractions. These patterns are pronounced for CS, showing an average of 2.4% and an inter quartile range (*IQR*) of approximately 1.3 in $cLHS_{adapt}$ versus an average of 4.6% and an *IQR* of 8.9 in $cLHS_{adapt+}$. By contrast, the target variables MS and FS show increased similarity between the calibration sets. For MS, the average amounts to 2% with an *IQR* of approximately 0.9 in $cLHS_{adapt}$, while $cLHS_{adapt+}$ shows an average of almost 3% with an *IQR* of approximately 4. For FS, $cLHS_{adapt}$ shows an average of 1.6% with an *IQR* of 0.8 versus an average of 2.0 with an *IQR* of 2.2 in $cLHS_{adapt+}$ (Figure 5).

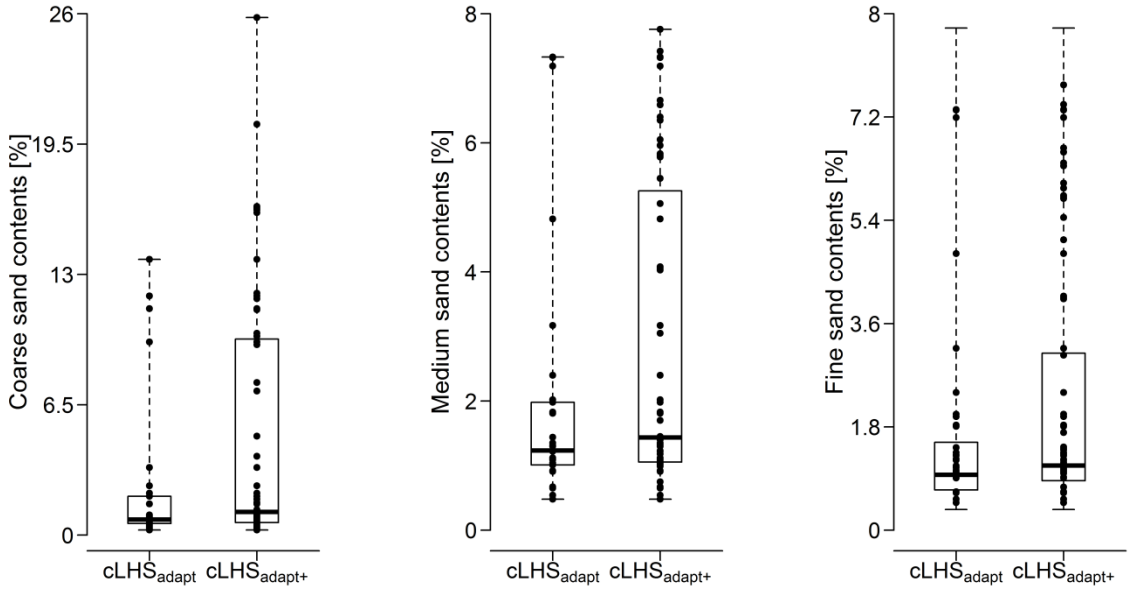

Figure 5: Topsoil sand fractions (CS: coarse sand, MS: medium sand, FS: fine sand) for both calibration sets ($cLHS_{adapt}$, $cLHS_{adapt+}$).

The RF prediction models couple the calibration sets $cLHS_{adapt}$ (n = 30) and $cLHS_{adapt+}$ (n = 60) with all available covariates to estimate all sand fractions (CS, MS, FS). The two-fold accuracy evaluation, which is based on independent and bootstrap validation, performs similar with deviations in R^2 ranging from 1% to 4% referring to each target variable and validation method. The accuracy estimation R^2 across all target variables, both calibration sets, and validation methods ranges between 0.57 and 0.80 (Table 6).

With respect to the independent validation and R^2, the FS-models ($cLHS_{adapt}$: R^2 = 0.59; $cLHS_{adapt+}$: R^2 = 0.61) are outperformed by the CS-models ($cLHS_{adapt}$: R^2 = 0.63; $cLHS_{adapt+}$: R^2 = 0.67), while the MS-models ($cLHS_{adapt}$: R^2 = 0.71; $cLHS_{adapt+}$: R^2 = 0.80) perform best. Moreover, for all target variables, the models calibrated by $cLHS_{adapt+}$ (n = 60) outperform the models using $cLHS_{adapt}$ (n = 30). The deviations amount to 2% for FS, 4% for CS and 9% for MS (Table 6).

Table 6: Random Forest model accuracies (R^2, RMSE) based on independent and bootstrap validation. The accuracy estimations refer to all calibration sets ($cLHS_{adapt}$, $cLHS_{adapt+}$) and target variables (CS: coarse sand, MS: medium sand, FS: fine sand).

Independent validation	$cLHS_{adapt}$		$cLHS_{adapt+}$	
	R^2	RMSE	R^2	RMSE
CS	0.63	4.03	0.67	3.75
MS	0.71	1.07	0.80	0.94
FS	0.59	0.34	0.61	0.38
Bootstrap validation	$cLHS_{adapt}$		$cLHS_{adapt+}$	
	R^2	RMSE	R^2	RMSE
CS	0.64	2.16	0.71	3.48
MS	0.69	0.91	0.78	1.01
FS	0.57	0.38	0.64	0.36

The sum of all predicted sand fractions ideally amounts to 100 %. The deviations from this ideal for the predictions of both calibration sets ($cLHS_{adapt}$, $cLHS_{adapt+}$) were mapped in percent points (Figure 6). Both model approaches show increased deviations in the northern Upper Badong catchment and in depression lines. For the $cLHS_{adapt}$-models, the deviations are more pronounced, while an additional hotspot of high deviations is located in the eastern study area (Figure 5). The summary statistics of the deviations show a maximum of 9.4 % and an average of 1.8% for the $cLHS_{adapt}$-models. The maximum of the $cLHS_{adapt+}$-models accounts for 7.6% with an average of 1.3%. Thus, the calibration set $cLHS_{adapt+}$ outperforms $cLHS_{adapt}$, which confirms the results of the accuracy estimations by independent and bootstrap validation (Table 6).

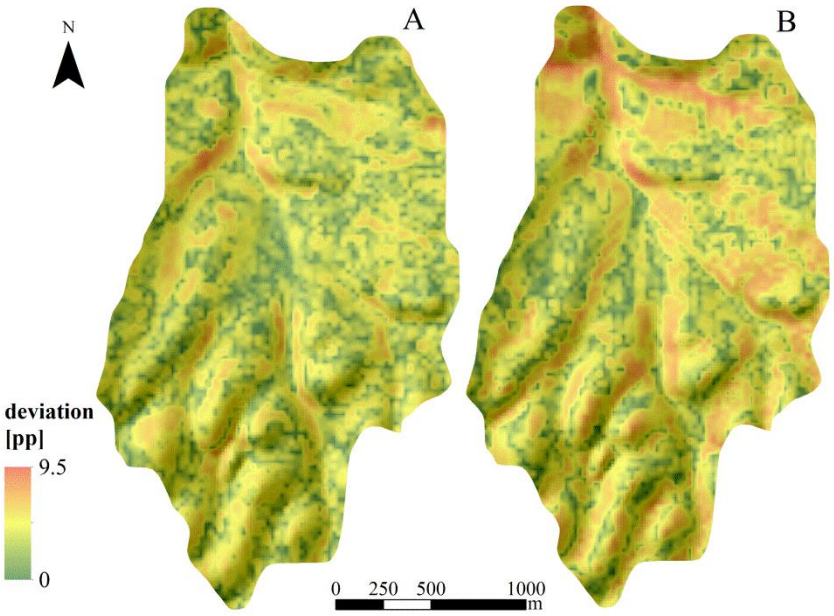

Figure 6: Coherence of the predicted sum referring to the compositional target variables (CS: coarse sand, MS: medium sand, FS: fine sand) and to the calibration sets (A) $cLHS_{adapt+}$ and (B) $cLHS_{adapt}$. Colors indicate the range of deviation in percent points (pp) from the ideal of 100%.

7.2 Spatial Uncertainty and map refinement

7.2.1 Uncertainty-guided Sampling

The average combined uncertainty (M_{errs^2}) in the entire study area, which corresponds to the potential sampling area Q1, accounts for 0.63 with a standard deviation (*sd*) of 0.12. Since the potential sampling areas Q2, Q3, and Q4 were defined according to the quartiles-breaks of the combined uncertainty (> 25%, > 50%, > 75%), successively increasing averaged M_{errs^2}-values can be expected. Thus, M_{errs^2} in Q2 amounts to 0.72 (sd = 0.1), and to 0.78 in Q3 (sd = 0.07), respectively to 0.86 in Q4 (sd = 0.04).

By comparing each distribution of area-covering covariates with the distributions of covariates from available legacy samples in Q1 to Q4, a successively increasing divergence of

the distributions in Q4 was revealed. The summarized Kullback-Leibler (*KL*) divergences in Q1 amounts to 16.4, to 24.5 in Q2, to 29.2 in Q3, and to 66.8 in Q4. However, the increase in Q4 amounts to 130% compared to 19% in Q3 and 49% in Q2. Subsequently, the available legacy samples in Q4 outline a disproportionally decreased coverage concerning the covariates (Figure 7). This results in Q4 as the final sampling area in order to obtain the additional samples of LD_{LHS} (Figure 8b).

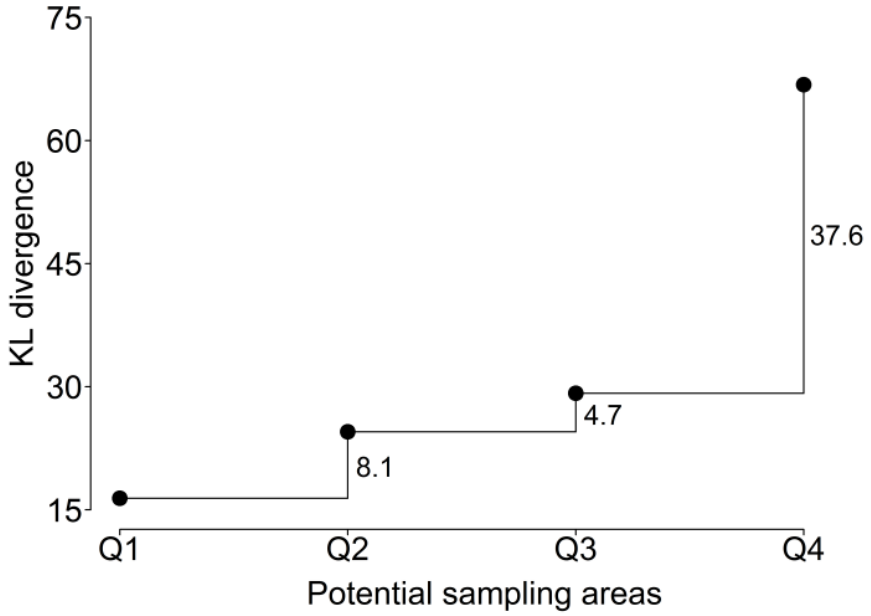

Figure 7: Determination of the sampling area by comparing the coverage of covariates using the legacy samples. The x-axis shows the potential sample areas Q1 to Q4. The y-axis shows the summarized Kullback-Leibler (KL) divergences between the distributions of covariates within the area and the distributions of covariates in the legacy samples.

The mapped combined uncertainty reveals increased values in the northern and southern study area, where the topography shows increased heterogeneity. Particularly, uncertainty hotspots with $M_{errs^2} > 0.8$ were predicted for areas along the topographic depression lines. In the

central western and eastern study area coherent patches of decreased uncertainties with M_{errs^2} < 0.5 occur (Figure 8a).

The LD_{Unc} samples were obtained according to an adapted cLHS design that optimally covers the variability of multiple covariates. Furthermore, the sample sites are spatially evenly distributed within the sampling area Q4 (Figure 7b). The calibration set LD shows a cluster in the north of the study area. The sample sites of the additional samples for LD_{Random} as well as the sites for the validation set are evenly distributed (Figure 8a).

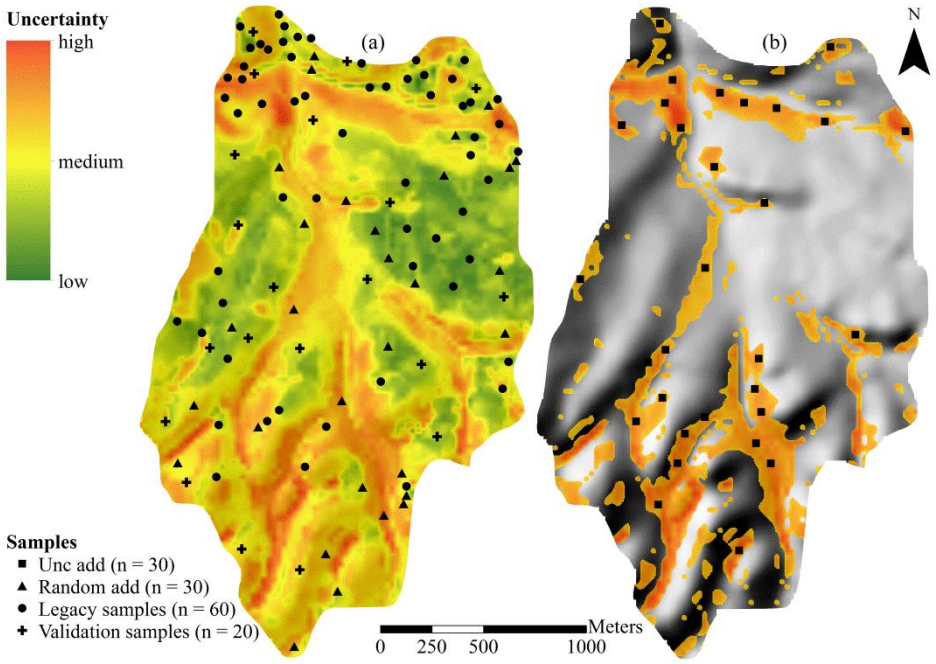

Figure 8: (a) Combined spatial uncertainty of initial silt and clay predictions with the legacy sample set (LD), the additive samples according to a simple random sampling (Random add) and the validation data. (b) Area for uncertainty-guided sampling with the additive samples (Unc add).

7.2.2 Map Refinement: Model Calibration and Prediction

According to the results from the laboratory analysis, the distributions of the model calibration sets LD (n = 60), LD_{Unc} (n = 90) and LD_{Random} (n = 90) show similar patterns in

central tendency and variability of both target soil properties (Figure 9). The average topsoil silt content amounts to 59.4% in LD (*sd* = 9.2), to 59.9% in LD_{Random} (*sd* = 9.0), and to 60.8% in LD_{Unc} (*sd* = 8.9). The average topsoil clay content varies from 28.5% in LD (*sd* = 6), to 29.6% in LD_{Random} (*sd* = 6), and to 28.9% in LD_{Unc} (*sd* = 5.9).

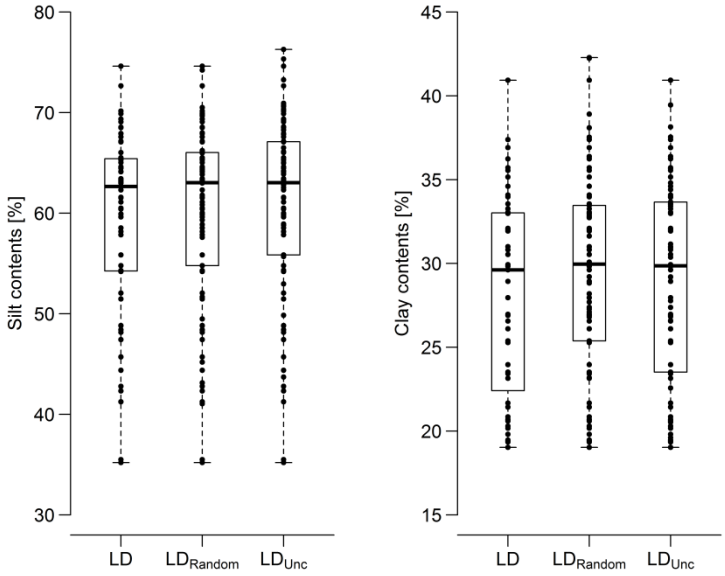

Figure 9: Observed topsoil silt and clay contents for all calibration sets (LD, LD_{Random}, LD_{Unc}). The notches indicate the median of the respective distribution.

All RF prediction approaches reveal increased averaged values of topsoil silt and clay contents compared to the averaged observed values resulting from the laboratory analysis. The increase varies from 2% to 2.5% for the silt contents and from 1% to 2.7% for the clay contents.

The predicted average silt content amounts to 61.6% (*sd* = 3.7) for the LD approach, to 61.9% (*sd* = 4.4) for the LD_{Random} approach, and to 63.3% (*sd* = 3.9) for the LD_{Unc} approach. All mapping approaches show a similar trend with increasing silt contents from the northern to the southern Upper Badong catchment. Generally, decreased silt contents occur in the topographic depression lines (Figure 10).

The RF predictions of topsoil clay show an average content of 29.9% for the LD approach (*sd* = 2.6). The average clay content revealed in the LD_{Random} approach amounts to 30.7% (*sd* = 2.8), while an average clay content of 31.6% was predicted in the LD_{Unc} approach (*sd* = 2.5). All mapping approaches show the lowest clay contents in the very north of the study area. In the central study area, increased clay contents are homogeneously distributed. In the south, clay contents are generally higher compared to the very north, but lower and less homogeneously distributed compared to the central study area (Figure 10).

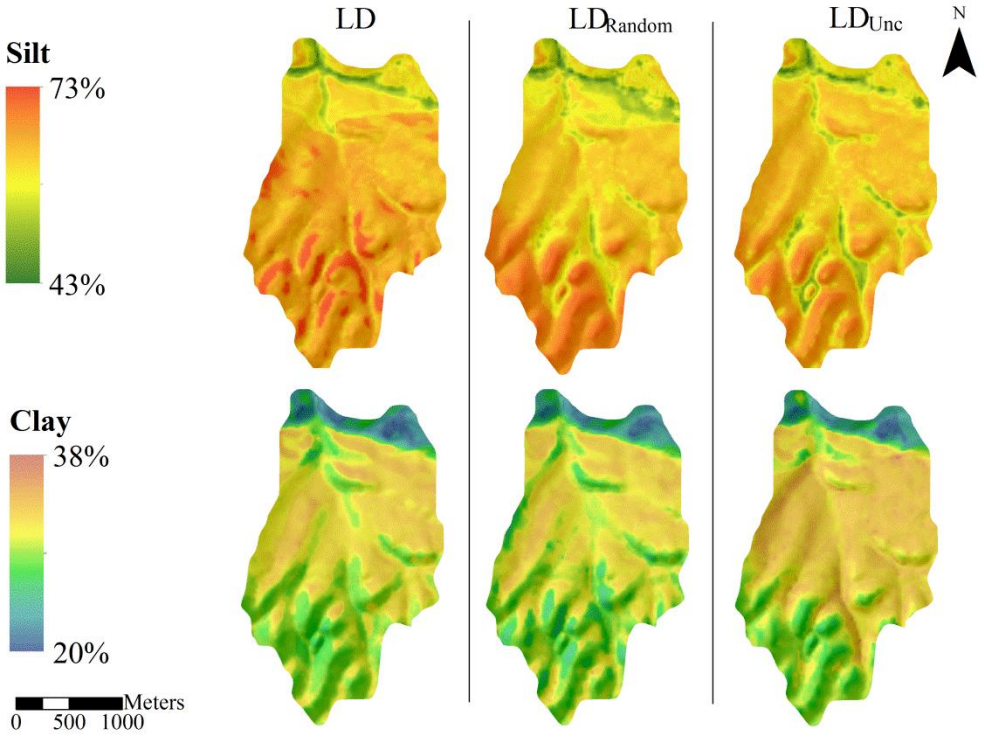

Figure 10: Mapping results for predicted topsoil silt and clay contents using the legacy sample set (LD), LD combined with additional samples according to simple random sampling (LD_{Random}), and LD combined with additional samples according to the uncertainty-guided sampling (LD_{Unc}).

For both target variables, the averaged spatial uncertainty gradually decreases from the LD approach (9.3 for silt; 7.7 for clay), followed by the LD_{Random} (6.7 for silt; 5.9 for clay) to the LD_{Unc} approach (6.4 for silt; 5.6 for clay). This trend of quality increase also applies for the

prediction accuracies derived from cross- (*cv*), bootstrap- (*boot*), and independent (*val*) validation (Table 7).

Referring to the silt prediction accuracy considering independent validation (*val*), the approaches show increasing explained variances with R^2 = 0.45 for LD, R^2 = 0.54 for LD_{Random} , and R^2 = 0.59 for LD_{Unc}. The clay predictions show *val*-accuracies of R^2 = 0.44 for the LD approach, R^2 = 0.47 for the LD_{Random} approach, and R^2 = 0.56 for the LD_{Unc} approach (Table 7; Figure 10).

Moreover, comparing the prediction approaches for the two different target variables shows a generally increased level of uncertainty and decreased level of *cv*- and *boot*-accuracy for the silt predictions. Across all approaches the increase in uncertainty ranges between 12% and 17%, while the decrease in accuracy ranges from 10% to 17% for *cv*, and from 17% to 22% for *boot*. Referring to *val*, the accuracies of silt and clay predictions are equal, while the divergences range between 2% and 13% across all approaches (Table 7; Figure 10).

Table 7: Spatial uncertainty and accuracies for the predictions of topsoil silt and clay contents, listed according to the prediction approaches. Averaged spatial uncertainty (unc), cross- (cv), bootstrap- (boot) and independent- (val) validation are used.

		unc	cv		boot		val	
Target variable	Prediction approach	$\sum err^{s^2}$ {1,…,n}/n	R^2	RMSE	R^2	RMSE	R^2	RMSE
Silt	**LD**	9.3	0.39	5.68	0.44	5.59	0.45	5.33
	LD_{Random}	6.7	0.44	6.13	0.46	5.72	0.54	4.86
	LD_{Unc}	6.4	0.47	4.64	0.54	4.58	0.59	4.27
Clay	**LD**	7.7	0.47	4.95	0.54	4.41	0.44	5.09
	LD_{Random}	5.9	0.49	4.78	0.59	3.82	0.47	4.63
	LD_{Unc}	5.6	0.55	4.52	0.65	3.59	0.56	4.49

Furthermore, the spatial uncertainty distributions of the silt and clay prediction approaches were compared. Referring to the silt predictions, the uncertainty values of the LD approach vary uniformly with *sd* = 1.1. Their uncertainty values range from 8.6 to 9.8. The very northern study area and a small area in the central catchment show low uncertainty values smaller than the 25%-quartile (≙ 9.1), while high values larger than the 75%-quartile (≙ 9.4)

are evenly distributed all over the study area. The LD_{Random} approach shows an increased variability with *sd* = 1.8 and a range from 5.5 to 8.1. Increased values larger than 75%-quartile (>7.3) were revealed for the northern study area, but are less pronounced in the south. The LD_{Unc} approach shows a similar distribution with *sd* = 1.7 and a range from 5.5 to 8.2, while an increased variability and high values larger than 75%-quartile (≙ 6.6) were revealed for the northern study area (Figure 11).

In terms of clay predictions, the LD approach also shows a comparatively low variability with *sd* = 1 and a range from 6.9 to 8.5. The variability of the LD_{Random} approach is increased with *sd* = 1.4 (range from 5 to 7.8), while the LD_{Unc} approach shows a decreased variability with *sd* = 0.7 (range from 5.3 to 6.4). The spatial distribution of all approaches shows increased values larger than 75%-quartile (LD approach: 8; LD_{Random} approach: 6; LD_{Unc} approach: 5.7) in the northern Upper Badong catchment (Figure 11).

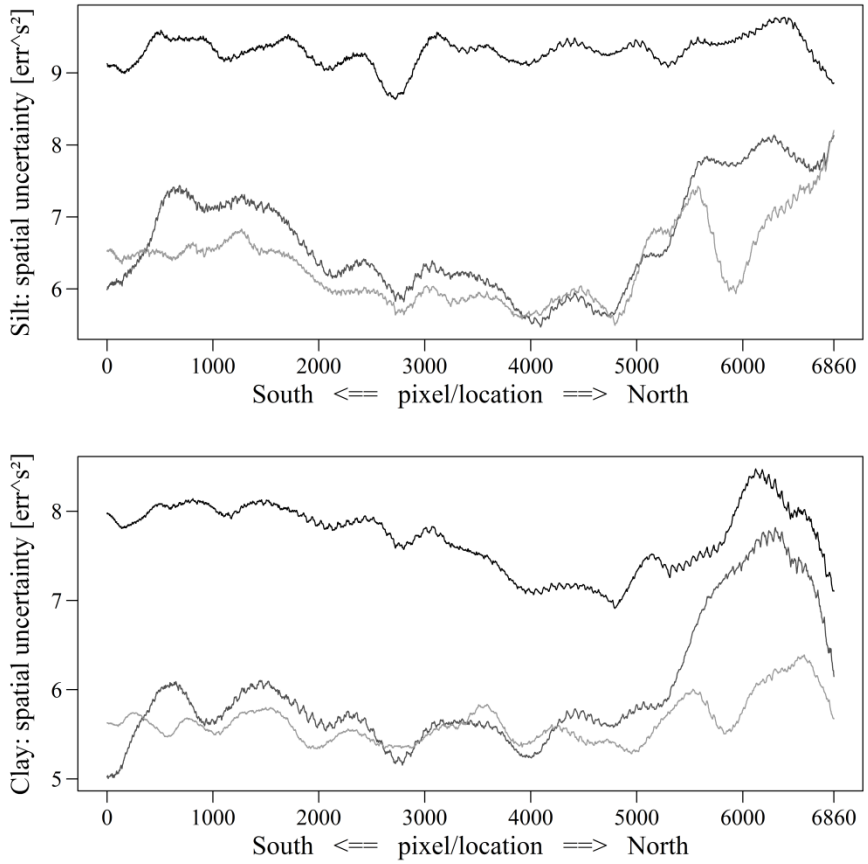

Figure 11: Comparison of spatial uncertainty for topsoil silt (above) and topsoil clay (below) predictions. The curves refer to prediction approaches using the calibration sets LD (black), LD_{Random} (dark gray) and LD_{Unc} (bright gray). The x-axis schematically indicates the localization of the values in the study area. The y-axis indicates the spatial uncertainty.

7.3 Erosive Rainfall and Sediment Reallocation

7.3.1 Erosive Rainfall Events

Monitored rainfall data (June 213 to May 2014) were compared to the long-term records from Badong climate station (January 1960 to December 2009; Figure 3). With 895 mm, the total rainfall amount of the short-term records is less compared to the long-term annual average of 1,082 mm, revealing relatively dry conditions during the monitoring period. This decline is

attributable to the months of May, July, and October with a reduced rainfall amount ranging between 54 mm and 68 mm. The deviations of the remaining months range between 1 mm in January and 20 mm in June with a positive budget of 11 mm. Furthermore, the short-term rainfall amounts per month were compared to the long-term average maxima and minima of rainfall per month. The results show that the monitored records were all within the range of the long-term records (Figure 3). Both, short- and long-term records exhibit an unimodal distribution with 67% and 68% of the annual rainfall occurring during the wet season from May to September. The analogy between the rainfall records reveals that the short-term record is representative for the area.

Moreover, the interrelation between the monitored rainfall, runoff, and sediment records within the study area (Figure 3) was evaluated. The annual distribution of the observed runoff sums and sediment yields per month corresponds to the recorded rainfall regime. With a total of 324 m^3 ha^{-1}, 80% of annual runoff occurs during wet season from May to September. The maximum runoff is in June with 66 m^3 ha^{-1}, while from December to January less than 1 m^3 ha^{-1} runoff was recorded. Similarly, the total annual sediment yield sums up to 666 kg ha^{-1}, of which 71% occur during wet season. With 116 kg ha^{-1}, June shows the maximum sediment yield, while minima less than 3 kg ha^{-1} occur from December to February (Figure 3). By using the correlation coefficient, the relation between rainfall, runoff, and sediment yield was calculated. With a temporal resolution of 10 minutes, rainfall data exhibit an r of 0.94 to runoff and 0.89 to sediment yield data, while the latter two are correlated with $r = 0.84$. The similar regimes of the recorded data and the associated r-values (>0.80) approve a strong cause-effect relationship between rainfall, runoff, and sediment yield.

During the monitoring period, 19 erosive events were identified, of which five events were excluded from further analyses (Table 8). Compared to the selected events and referring to the average event properties, the excluded events show an increase in rainfall duration [D] and total rainfall amount [P] of 1,140 min and 19.4 mm, respectively. The average peak intensities I_{60} and I_{30} are lower by 4.6 mm $60min^{-1}$ and 4.5 mm $30min^{-1}$, respectively. The average erosivity EI_{30} is lower by 273.9 MJ ha^{-1} mm h^{-1}. Moreover, the excluded events show intra-event periods of no rainfall close to the inter-event time of 6 h. They generally exhibit increased durations with decreased intensities of discontinuous rainfall. These patterns result

in temporally variable runoff generation, thus, impeding an adequate separation between direct runoff and baseflow.

The average properties of the 14 selected events show a duration *D* of 276 min, a total rainfall *P* of 19.4 mm, peak intensities I_{60} and I_{30} of 14.7 and 11.8, and an erosivity EI_{30} of 331.7 MJ ha^{-1} mm h^{-1}. These event properties result in sediment yields SY_{obs} ranging between 0.18 Mg and 7.03 Mg with an average SY_{obs} of 1.77 Mg and a total sediment yield of 24.8 Mg. Eight events show sediment yields less than 1 Mg with an average SY_{obs} of 0.61 Mg (small events). Six events show sediment yields above 1 Mg with an average SY_{obs} of 3.32 Mg (large events; Table 8). The large events account for 80.3% of the sediment yield and 61% of the total rainfall amounts over all events.

Table 8: Properties of selected and excluded rainfall-runoff events. The duration (D), the rainfall amount (P), the peak intensity of 60 and 30 minutes intervals (I_{60}, I_{30}), the erosivity (EI_{30}), and the observed sediment yield (SY_{obs}) are applied to characterize the events.

		Time	D [min]	P [mm]	I_{60} [mm/60min]	I_{30} [mm/30min]	EI_{30} [MJ ha^{-1}*I_{30}]	SY_{obs} [Mg]
Selected for further analysis	SY < 1 Mg	20.06.2013	100	13.2	12.6	11.6	88.1	0.43
		29.07.2013	220	17.2	9.2	7.8	52.2	0.92
		18.08.2013	100	6.8	6.4	6.4	23.4	0.34
		25.08.2013	340	11.2	7.4	6.8	19.9	0.88
		27.03.2014	50	9.8	9.8	8.0	26.4	0.18
		28.03.2014	200	19.8	13.0	7.6	53.8	0.79
		01.05.2014	530	14.6	7.8	5.2	8.8	0.73
		24.05.2014	310	11.8	7.0	4.4	5.9	0.62
	SY > 1 Mg	22.06.2013	170	28.6	22.2	16.4	501.7	4.21
		30.06.2013	100	14.2	13.6	13.6	154.5	1.03
		05.07.2013	530	39.4	26.0	17.6	516.5	3.88
		21.07.2013	270	19.8	14.2	12	116.9	2.58
		03.08.2013	400	22.0	21.6	15.2	286	1.19
		28.08.2013	720	42.6	34.8	32.4	2,789.9	7.03
Excluded		05.06.2013	1,158	49.2	13.6	9.6	120.2	-
		24.06.2013	1,458	36.4	7.0	4.6	22.5	-
		23.08.2013	2,368	25.0	8.0	5.6	17.0	-
		09.09.2013	1,692	41.2	9.0	7.4	48.4	-
		20.04.2014	1,422	42.0	13.8	9.4	81.1	-

7.3.2 Model Performance and Sediment Reallocation

To evaluate the model performance for each event, the individual model errors (*ERR*) were derived and compared to SY_{obs} (Figure 12). Generally, small events with SY_{obs} below 1 Mg exhibit increased model errors compared to events with SY_{obs} above 1 Mg. The average model error ($ERR_{average}$) of the eight small events amounts to 36.2%, ranging between 15.1% and 62%. Except for one event, the *ERR* refer to severe underprediction. In contrast, the six large events show an average model error of 7.5%, ranging from 0.1 to 14.7%. Those values mainly result from overprediction. The summed up $SY_{pred.}$ for all events amounts to 24.2 Mg and deviates by 2.3% from SY_{obs} that amounts to 24.8 Mg. The $ERR_{average}$ of all modeled events

results in 23.9%. Comparing the observed versus the modeled sediment yields across all events show a *NS*-value of 0.98 and a *RMSE* of 0.27 (Figure 12). Thus, the average model quality is considered to be high. However, the evaluation of the individual model errors reveals ambiguous patterns. While the model results for large events (>1 Mg) show low *ERR*s, the model runs for the small events (<1 Mg) result in increased *ERR*s.

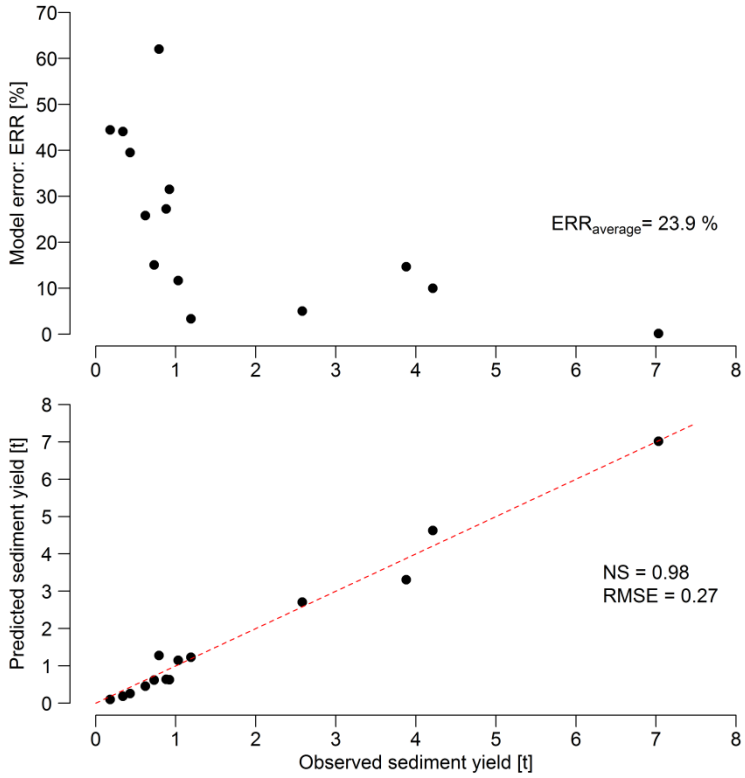

Figure 12: Individual and average model performance for all erosive events (black dots). Performance variability is expressed by comparing the individual prediction error (ERR) to the observed sediment yields (above). Average model performance is revealed by the averaged individual prediction error (ERR$_{average}$, above) and by comparing observed to predicted sediment yields, applying the Nash-Sutcliffe coefficient (NS) and the root mean square error (RMSE; below).

The model results were classified according to four soil erosion classes of 'severe' (> 50 Mg ha^{-1}), 'high' (20 - 50 Mg ha^{-1}), 'moderate' (10 - 20 Mg ha^{-1}), and 'low' (< 10 Mg ha^{-1}) soil

loss and deposition, respectively (Figure 13). Moreover, the spatial extents of soil loss and deposition zones (Table 9) were evaluated according to land use patterns (Table 10). Since the large events with SY_{obs} > 1 Mg account for the vast majority of all events (80.3%) and uncertainties of the small events (<1 Mg) are high ($ERR_{average}$ of 36.2%), the small events were excluded from further spatial analysis.

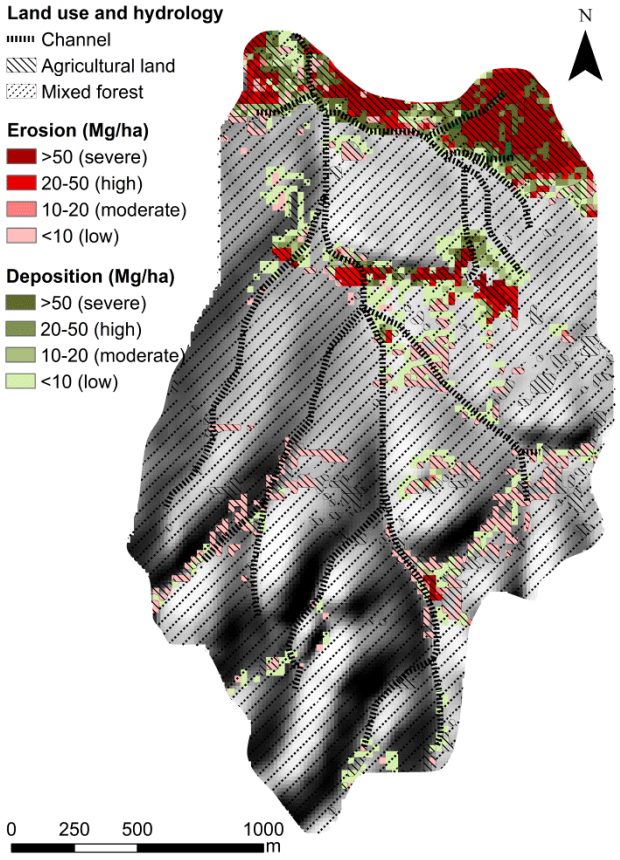

Figure 13: Sediment sources and deposits as budget across erosive events with sediment yields higher than 1 Mg. Depression channels and land use classes according to agricultural land (composed of the classes 'cropland' and 'grassland') and mixed forest (composed of 'broadleaf', 'conifer' , 'woods', and 'shrub') are indicated.

17% (73.2 ha) of the total study area (428.7 ha) is used as agricultural land (land use classes: 'corn-rapeseed', 'potato-cabbage', 'grassland'). Approximately 79% (340.4 ha) of the entire study area is characterized by 'mixed forest', composed of the land use classes 'broadleaf',

‘conifer’, ‘woods’, and ‘shrub’. Only a small proportion of approximately 4% (15.1 ha) is dedicated to small farm buildings.

Corresponding to the spatial pattern and distribution of agricultural area, ‘severe’ and ‘high’ soil losses are predominantly located in the lowlands of the northern study area where the elevation ranges between 500 m a.s.l. and 650 m a.s.l. A further band of ‘severe’ and ‘high’ soil losses extends south of the major agricultural area at elevations between 800 m a.s.l. and 900 m a.s.l. ‘Low’ soil losses mainly occur on agricultural land in the southern Upper Badong catchment at elevations between 900 m a.s.l. and 1,400 m a.s.l. Slope inclinations in the areas of soil loss range from 4.3° to 39.4° and amount to an average of 21.5°. The mapping results show a total area of 47.5 ha that is affected by soil loss. This accounts to approximately 11% of the entire study area (Figure 13). The modeled soil loss rates range between 0.01 and 527 Mg ha^{-1} with an average of 49.9 Mg ha^{-1}. 37.5% (17.8 ha) of this soil loss area are classified as ‘severe’ and 45.1% (21.4 ha) are classified as ‘low’ (Table 9) in terms of soil loss hazard. With regard to the land use, soil losses mainly occur on ‘corn-rapeseed’ and ‘potato-cabbage’ amounting to approximately 69% of the respective area (Table 10).

Table 9: Total area of soil loss and deposition (ha) in the Upper Badong catchment and percentage of areas affected by soil loss and deposition classified into 'severe' (> 50 Mg ha^{-1}), 'high' (20 - 50 Mg ha^{-1}), 'moderate' (10 -20 Mg ha^{-1}), and 'low' (< 10 Mg ha^{-1}).

Soil erosion process	Total area [ha]	Severe [%]	High [%]	Moderate [%]	Low [%]
Soil loss	47.5	37.5	13.8	3.6	45.1
Deposition	47.3	15.8	13.4	9.3	61.5

‘Severe’ and ‘high’ sediment depositions mainly occur in the two major erosive areas in the northern study area (Figure 12). Depositions are concentrated lateral of topographical depression channels, at field borders with high vegetation cover, and in infrastructural areas. In the southern study area at an elevation between 900 m a.s.l. and 1,400 m a.s.l., depositions are located adjacent to erosive areas and mainly classified as ‘low’. The total deposition area outlines an average slope inclination of 19.8°. Slope angles in the area that is affected by deposition range from 1.1° to 35.5°, therefore showing a marginal decline compared to the areas of soil loss. Deposition occurs on 47.3 ha, thus, 11% of the study area (Figure 13). The

deposition rate ranges between 0.01 and 499.5 Mg ha^{-1} with an average of 40.3 Mg ha^{-1}. A proportion of approximately 61.5% (29.1 ha) of the deposition area is classified as 'low', while the remaining classes occupy areal proportions between 9.3% (4.4 ha) and 15.8% (7.5 ha; Table 9). Referring to land use, deposition occurs on each class, while 'built' is occupied by 41.7% (6.3 ha) of the area. The proportional deposition area of the remaining land use classes range between 9.7% (33.0 ha) for 'mixed forest' and 18.4% (1.1 ha) for 'grassland' (Table 10).

Table 10: Rates of soil loss (loss) and deposition (dep.) according severity classes (severe: > 50 Mg ha^{-1}, high: 20-50 Mg ha^{-1}, moderate: 10-20 Mg ha^{-1}, low: <10 Mg ha^{-1}) and different land uses (ha).

Land use	Area [ha]	loss (dep.) [%]	loss (dep.) severe [%]	loss (dep.) high [%]	loss (dep.) moderate [%]	loss (dep.) low [%]
Corn-rapeseed	47.8	69.2 (13.6)	26.1 (1.3)	10.3 (3.6)	2.3 (3.2)	30.5 (5.5)
Potato-cabbage	19.4	69.1 (11.3)	29.9 (0.5)	8.8 (4.6)	3.1 (2.1)	27.3 (4.1)
Grassland	6.0	5.0 (18.4)	- (8.3)	- (1.7)	- (1.7)	5.0 (6.7)
Mixed forest	340.4	0.5 (9.7)	- (1.4)	- (0.8)	- (0.6)	0.5 (6.9)
Built	15.1	- (41.7)	- (10.6)	- (6.6)	- (4.0)	- (20.5)

8 Discussion

8.1 Hypercube Soil Sampling for Digital Soil Mapping

The cLHS method identifies samples, which are stratified in the multivariate feature space in a two-step approach. First, strata are generated in a hypercube, which spans the feature space. Second, one target site per stratum is selected according to an optimization procedure [Metropolis *et al.*, 1953] that covers the feature space by a combination of unique target sites. The latter target site selection process is conditioned by only selecting feature space locations that exist in the real world [Minasny & McBratney, 2006].

Roudier *et al.* [2012], Mulder *et al.* [2013], and Clifford *et al.* [2014] further constrained the target site selection by penalizing spatial locations with limited accessibility within each predefined stratum. This implies a potential bias in the final sample set size, since inaccessible areas might occupy segments of the feature space that were not sampled. Further, accessibility at the target sites is not guaranteed because the existence of accessible locations in the specific stratum cannot be ensured. Clifford *et al.* [2014] eludes the latter problem by additionally analyzing the relation of each location in a defined neighborhood to the initial target site, providing an ordered list of alternative target sites. While it is a combination of one unique sample per stratum covering the feature space initially, the generation of alternatives follows a biased assumption that all other target sites have been successfully sampled before. However, according to a simulation study, Clifford *et al.* [2014] showed that the feature space coverage remains preserved by replacing up to 50% of the initial target sites by alternatives sites.

In the present thesis, instead of penalizing locations in the stage of target site selection and generating alternatives for each initial target site individually, all possible combinations of accessible locations were analyzed according to their feature space coverage and with respect to the original cLHS design. This enables for quantifying the deviation to the original cLHS design and for providing alternative target sites, while avoiding assumptions about previously sampled target sites. Ensuring that at least one accessible location per stratum is available requires to increase the number of locations within each stratum. This is accomplished by

decreasing the number of covariates, which build the feature space and the sample set size [Minasny & McBratney, 2006].

The number of covariates was reduced to the two most adequate (i.e., ACC and SWI) according to a plausible correlation to the target variables [Gessler *et al.*, 2000], and avoidance of multicollinearity within the feature space [Hengl *et al.*, 2003; Mulder *et al.*, 2013; Schmidt *et al.*, 2014]. Other studies that applied cLHS used more covariates (approximately four to ten) to build the feature space, while the ratio of samples per km² varies between 0.005 and 0.465 in study areas with sizes ranging from 720 km² to 12,800 km² [Mulder *et al.*, 2013; Clifford *et al.*, 2014; Taghizadeh-Mehrjardi *et al.*, 2014; Kidd *et al.*, 2015]. Brungard & Boettinger [2010] suggested a minimum ratio of 0.7 to 1 samples per km² using cLHS in a study area of a size of 300 km². In this study, the sample set size was optimized to $n = 30$ for a study area of 4.2 km², thus, 7.1 samples per km², by analyzing ten simulated cLHS sets with different sample set sizes. Moreover, it was shown that the deviation of the feature space coverage from the original cLHS set is marginally (Table 5), while 93% of the original samples were replaced by alternatives (Table 4).

Referring to the incorporation of legacy samples to cover the feature space, Clifford *et al.* [2014] used 8,669 legacy samples as predefined basis to locate 300 additional target sites. Since the subset of legacy samples was not obtained purposively to cover the feature space, redundancies within the subset were not considered and potentially led to a bias in the combined sample set. In this context, Carré *et al.* [2007] proposed to analyze the distribution of legacy samples across the strata to evaluate the adequacy of legacy samples for the feature space coverage. Following the principles of this approach, only those five legacy samples were used, which are located within a stratum, thus, avoiding redundancies and reducing the sampling effort. Consequently, the increased number of locations per stratum also accommodates with the goal to integrate legacy samples, which are adequate to cover the feature space by a predefined sample size n. In the present study, only one legacy sample is available in the respective stratum, thus, no evaluation of preference is necessary. Apart from this situation, the results suggest to consider multiple legacy samples within a stratum simply as potential accessible target sites and to follow the methodological procedure as described in Section 6.4.

Any cLHS or stratified sampling design must be seen as a specific case study resulting in a partially limited generalizability. This is attributed to the assumptions that the feature space, determined by local framework conditions, sufficiently describes the targeted soil property in space and time [Clifford *et al.*, 2014]. Besides these limitations, this study's approach is transferable to any other study area, considering that an increasing number of samples and spatial resolution increases the computational load. Thus, the applied approach is suitable for small study areas with highly limited accessibility.

Soil texture estimations using DSM typically show accuracies less than 0.50, while studies with $R^2 > 0.70$ are rare [Malone *et al.*, 2009; Lacoste *et al.*, 2011; Wang *et al.*, 2012; de Carvalho Junior *et al.*, 2014; Mansuy *et al.*, 2014]. The results of the present study (Table 6) show accuracies with $R^2 > 0.50$ for all sand fractions and for both calibration sets ($cLHS_{adapt}$ with $n = 30$; $cLHS_{adapt+}$ with $n = 60$). Comparing the prediction accuracies for both calibration sets and referring to independent and bootstrap validation, the $cLHS_{adapt}$ approach results in slightly decreased accuracies by only 0.5 %. This is confirmed by referring to the coherence of the total sand fraction, ideally amounting to 100%. The similarity between the two DSM approaches confirms the robustness of the proposed sampling approach. Moreover, since the calibration sample set size of $n = 30$ is relatively small compared to other studies with n between 165 and 4,920 for Random Forest (RF) regression analysis [Grimm *et al.*, 2008; Lacoste *et al.*, 2011; Mansuy *et al.*, 2014], and considering the topographical heterogeneity of the study area, the accuracy of the proposed DSM approach is noticeable.

8.2 Spatial Uncertainty and Soil Map Refinement

The present thesis includes the development of a method to derive a practicable, spatial uncertainty measure in context of a DSM approach using RF. For geostatistical soil property mapping, the kriging variance presents a spatially distributed error estimate [Knotters *et al.*, 1995; Carré & Girard, 2002; Diodato & Ceccarelli, 2006; Bourennane *et al.*, 2007; Qu *et al.*, 2013; Sun *et al.*, 2013]. Generally in geostatistics, the spatial dependence of a target variable is modeled by the variogram function, whereby local predictions are derived from the weighted averages of neighboring observations [Goovaerts, 1999]. While the weights are determined by minimizing the variance of each local prediction, this quantity represents the kriging error [Burgess & Webster, 1980]. Besides, Malone *et al.* [2011] proposed a method to

quantify spatial uncertainties based on prediction intervals (PI-uncertainty). Primarily, the intervals are derived from the residuals between predicted and observed data. Subsequently, a covariate space is clustered according to similar residuals. Then, a prediction interval is generated for each cluster based on the empirical distribution of residual observations of each cluster. According to the grade of membership to each cluster, a prediction interval is ascribed for each prediction location in the covariate space.

The proposed spatial uncertainty method is based on multiple decision tree realizations within a RF regression approach (cf., Section 6.3). The uncertainty measure is also expressed by the variability of prediction intervals. However, the intervals are straightforwardly derived for each prediction location, based on the results of the multiple randomized RF decision tree models (cf., Section 6.3). Thus, compared to the PI-uncertainty, the applied spatial uncertainty does not require an additional regionalization of prediction errors, which limits practicability due to statistical complexity and usually scarce temporal resources. Nevertheless, the PI-uncertainty accounts for all sources of uncertainty, only depending on the residuals derived from the model output and the observed data. Contrary, the kriging error depends on the model assumption for the variogram, the observed soil data and their spatial configuration [Brus *et al.*, 2011; Lark & Lapworth, 2012]. Furthermore, the kriging error relies on the use and limitations of geostatistical methods, such as a relatively high sample density and the smoothing of local details in the predictions [Goovaerts, 1999]. The application of the spatial uncertainty measure also implies dependencies, such as the prerequisite to use a RF prediction model. Moreover, the RF model is often discussed to only allow limited interpretability, since the relation between predictor and prediction cannot be assessed for each tree. However, RF is increasingly applied in DSM [Grimm *et al.*, 2008; Wiesmeier *et al.*, 2011; Ließ *et al.*, 2012; Heung *et al.*, 2014; Schmidt *et al.*, 2014]. This can be ascribed to the combined merits of modeling non-linear relationships, handling categorical and continuous covariates, resistance to overfitting, robustness to noise in the feature space, an implemented unbiased measure of error and variable importance, only a few user-defined model parameters, and a reduced computational load [Svetnik *et al.*, 2003; Díaz-Uriate & de Andrés, 2006; Peters *et al.*, 2007].

While the kriging error presents a well-established spatial error estimate [Knotters *et al.*, 1995; Carré & Girard, 2002; Diodato & Ceccarelli, 2006; Bourennane *et al.*, 2007; Qu *et al.*, 2013; Sun *et al.*, 2013], the PI-uncertainty is less common. Malone *et al.* [2011] applied it

using a DSM case study predicting organic carbon and available water capacity. The proposed method was approved by comparing three RF prediction approaches referring to conventional accuracy measures and the proposed uncertainty measure (cf., Section 6.5). The calibration of the model approaches were based on legacy samples (LD), LD augmented by uncertainty-guided sampling (LD_{Unc}), and LD augmented by simple random sampling (LD_{Random}), respectively. For both target soil properties, topsoil silt and topsoil clay, all quality estimation methods show uniform results. Thus, the LD_{Unc} approach outperforms the approach using LD_{Random}, while both outperform the LD approach in terms of a decreased spatial uncertainty and increased prediction accuracies (Table 7; Figure 10). The uniform similarity between the results of all quality estimations approves the validity of (i) the conventional accuracy measures and (ii) the proposed spatial uncertainty measure.

A further aim of this thesis was to improve the initial DSM approaches of silt and clay predictions that were solely based on legacy samples. Thus, the initial legacy calibration set was augmented by an uncertainty guided sampling. Clifford *et al.* [2014] selected additional samples that, in combination with available legacy samples, cover the covariate space and approved the method by a simulation study. Carré *et al.* [2007] proposed a method to identify locations for additional samples by previously analyzing the distribution of legacy samples in the covariate space. Although the approach was approved by two different data sets, the method only refers to the covariate space, thus, disregarding geographical information. In this study, the study area was stratified according to the quartile distribution of the previously determined spatial uncertainty. Subsequently, additional samples were obtained in those strata with the lowest conformity between the covariate distributions in the strata and available legacy samples (Figure 7).

The spatial uncertainty values of both approaches were combined (cf., Section 6.5). This procedure implies a favored incorporation for the soil property, which generally shows increased prediction uncertainty. Furthermore, the procedure implies a harmonization in quality of both initial soil property predictions. The results confirmed these implications, while silt was favored with an uncertainty decrease of 31% compared to clay with a decrease of 27% in the LD_{Unc} approaches (Table 7; Figure 10). The similar proportions of decreasing uncertainty between both predictions approve the method of combining the uncertainty maps in our case study.

Collard *et al.* [2014] sampled a legacy soil map for calibrating a regression model and improved the class purity by 10%. Other studies showed an accuracy improvement of 6% to 19% using DSM approaches to upgrade legacy soil maps [Kempen *et al.*, 2009; Yang *et al.*, 2011; Rad *et al.*, 2014]. The results from this study show increases in accuracy of 12% and 14% for the predictions of clay and silt when comparing the LD approach with the LD_{Unc} approach. Generally in DSM, accuracies with $R^2 > 70\%$ are unusual, while $R^2 < 50\%$ are common [Malone et al., 2009]. The accuracy results of the best performing RF approach, which has been calibrated with LD_{Unc}, show explained variances of $R^2 = 0.59$ for silt and $R^2 = 0.56$ for clay. The successful application of the spatial uncertainty measure, thus, improving the quality of initial DSM products by an uncertainty guided sampling, approves the practicability and validity of this method.

8.3 Sediment Reallocation

8.3.1 Rainfall-runoff Events and Hydrological Data

Rainfall-runoff events were delimited by an initial rainfall impulse and the remission of the associated direct runoff. This procedure is in accordance with other studies on rainfall-runoff events [Baltas *et al.*, 2007; Blume *et al.*, 2007]. Subsequently, observed sediment yields were attributed to identify the respective erosive response. However, the event properties that determine the erosive response highly depend on methodological settings for data acquisition, event exclusion, event classification rules, and the inter-event time to disaggregate a rainfall record [Dunkerley, 2008]. Todisco *et al.* [2014] argued that the event properties change in time and space and can be referred to as arbitrary due to customized settings for individual applications and environments. This limits the comparability in terms of event-based soil erosion studies.

High quality monitoring data on soil erosion become increasingly important to enable an evaluation of the site-specific cause-effect relationship and to address the requirements of complex model structures [Aksoy & Kavvas, 2005; Fang *et al.*, 2013]. Commonly, continuous and high resolution data on rainfall and runoff are available. Contrary, continuous data on sediment loads are often difficult to obtain due to required maintenance and operating personnel [Rickemann & McArdell, 2007].

Within the TGRA, Fang *et al*. [2013] investigated erosive events in a small catchment of 1,670 ha. Rainfall and runoff data were continuously measured in a resolution of 15 min. Data on sediment loads were manually obtained only during rainfall events. From a total of 205 rainfall-runoff events between 1989 and 2004, 10 were classified as extreme according to a qualitative assessment of surface damage due to soil erosion. These events caused 83.3% of the sediment load. This is also supported by Cai *et al*. [2005], who stated that most soil erosion in the TGRA is associated with very few, but heavy rainfall events each year.

In this study, data on rainfall, runoff, and sediment yield were continuously monitored in a 10 min resolution and over a period of 12 months within a catchment of 429 ha (Figure 1). The rainfall data was approved to be representative for the region, since the total rainfall per months was within the range of averaged daily long-term records (Figure 3). Similar to Fang *et al*. [2013], a few large events caused the major proportion of the total sediment yield. In this study, 14 rainfall-runoff events were identified of which six showed sediment yields above 1 Mg. They account for 80.3% of the total sediment yield. Moreover, high correlations between the regimes of rainfall, runoff, and sediment yields with *r*-values above 0.8 were detected, while all regimes outline peak values during the wet season and minimum values in winter. Both, the high correlations and similar distributions indicate a strong cause-effect relationship between the monitoring data on rainfall, runoff, and sediment yield.

8.3.2 Soil Erosion Modelling in the Three Gorges Reservoir Area

The performance of physically-based soil erosion models depends on the model capability to deal with the natural complexity of the erosion process and the spatial heterogeneity of the study area [De Vente & Poesen, 2005]. Furthermore, the availability and quality of the input data needs to be in agreement with the complexity of the model routines [Van Rompaey & Govers, 2002; De Vente *et al.*, 2013]. Thus, the combined criteria of the model design, environmental conditions, and data infrastructure determine the adequacy of a model for a specific research question [Boardman, 2006]. In the TGRA, a few physically-based model attempts have been conducted to test model performances and to assess soil erosion control measures at the catchment scale [Shen *et al*., 2010; Shi *et al*., 2012].

Shi *et al*. [2012] applied WaTEM/SEDEM in catchment of 1,670 ha. This model uses the empirical RUSLE to calculate annual water erosion on hillslopes and a sediment routing along

the runoff channels by incorporating local sediment transport capacity [Van Rompaey *et al*., 2001]. Shen *et al*. [2010] applied the WEPP model in a catchment of 162 ha. WEPP uses the Green-Ampt infiltration approach to simulate runoff and a steady-state sub-routine to solve a sediment continuity equation at a peak runoff rate [Flanagan & Nearing, 2000]. In this study, EROSION 3D was applied in a catchment of 429 ha. This model also uses the Green-Ampt infiltration equation for the runoff routine. However, the soil erosion routine is based on the momentum flux approach that relates the erosive impact of runoff and rainfall to their exerted momentum flux [Schmidt *et al*., 1999; Schindewolf & Schmidt, 2012].

Both, WaTEM/SEDEM and WEPP present continuous model approaches producing average values for soil loss and deposition. In contrast, EROSION 3D is an event-based model, and therefore capable to assess the variability of erosive responses due to singular rainfall-runoff events. Event-based models require event-specific parameterization due to a high sensitivity to initial conditions. Thus, requirements for data quality in terms of accuracy and continuity are higher [Jetten *et al*. 2003; Aksoy & Kavvas 2005; Boardman, 2006]. This especially accounts for the parameters that control infiltration, such as soil moisture and hydraulic conductivity [Schmidt *et al*. 1999; Jetten *et al*., 2003; Shen *et al*., 2010]. Particularly in the TGRA, where major sediment reallocations are due to very few extreme events, the event-based assessment is of substantial interest in context of implementing soil erosion control measures to prevent hazardous impacts [Cai *et al*., 2005; Fang *et al*., 2013].

Continuous runoff data and discontinuous sediment yield data from the outlet were available for both model attempts by Shen *et al*. [2010] and Shi *et al*. [2012]. The data was used to calibrate the WEPP model, while WaTEM/SEDEM was parameterized by available RUSLE data. Both studies were validated by the outlet data. In the present study, continuous data on runoff and sediment yield were used, therefore providing an increased data consistency. Model calibration was enabled by using DSM techniques to calculate high resolution soil property information. Thus, DSM provided a solution to enable the parameterization of a physically- and event-based soil erosion model at the catchment scale in a generally data scarce environment [Manuscript 2, 3, 4]. Further model parameters are based on land use data derived from satellite images and an empirically compiled parameter catalogue [Michael, 2000]. Only the sensitive soil moisture parameter was adjusted using observed and predicted runoff data, a procedure that is commonly applied in event-based soil erosion modelling

[Schmidt *et al*., 1999; Jetten *et al*., 2003]. Similar to the WaTEM/SEDEM and WEPP approach in the TGRA [Shen *et al*., 2010; Shi *et al*., 2012], model performance of the presented approach was assessed using outlet data on sediment yield. However, due to the variability in the sediment delivery ratio with changing temporal and spatial scale, sediment yield data have been criticized for field soil erosion measurements [Boardman, 2006]. Nevertheless, the assumption of a stable and high sediment delivery ratio is reasonable, since the cause-effect relationship between the monitoring data (rainfall, runoff, sediment yield) is strong ($r > 0.8$), and erosive events are mainly due to high intensity rainfall events that are reported to cause high sediment connectivity [Lexartza-Artza & Wainwright, 2011; Baartman *et al.*, 2013; Todisco, 2014; Marchamalo *et al.*, 2015].

Both physically-based model attempts in the TGRA [Shen *et al*., 2010, Shi *et al*., 2012] showed acceptable average model accuracies with *NS*=0.65 for the WaTEM/SEDEM approach and *NS* = 0.84 (average deviation: 3.9%) for the WEPP modelling. Contrary, the present study using EROSION 3D, exhibits an increased average accuracy of *NS* = 0.98 and a decreased average deviation of 2.3 over all modelled events. Moreover, since EROSION 3D is event-based, event-specific accuracies were also be derived. Ambiguous model performances between small events (< 1 Mg; $ERR_{average}$ of 36.2%) and large events (> 1 Mg; $ERR_{average}$ of 7.5%) were detected. The increasing model performance for large events is in agreement with other event-based model attempts [Zhang *et al.*, 1996; Nearing *et al*., 1999; Nearing, 2000; Gumiere *et al.*, 2011; Lee *et al.*, 2013]. In this context, Jetten *et al.* [2003] argued that small-scale events are generally difficult to simulate, since the deterministic character of soil erosion models is incapable to deal with the random component of measured data. Boardman [2006] relates the low accuracy of small-scale events to oversimplified runoff routines, which solely simulate runoff by infiltration excess and thereby underrating the erosive power of low intensity rainfall on saturated soil. Moreover, the decreased sediment connectivity of low intensity rainfall could cause variability in the outlet data, therefore leading to biased estimation [Marchamalo *et al.*, 2015].

For the WaTEM/SEDEM approach ‘severe’ and ‘high’ soil losses occurred on 10.5% of the study area with an average soil loss rate of 13 Mg ha^{-1}. Deposition was detected on 20.5%, while no classification on magnitude was conducted [Shi *et al.*, 2012]. For the WEPP approach, the average soil loss rate was reported to range between 2 and 38 Mg ha^{-1}, while

quantitative information on proportional areas of soil loss and deposition was not provided. In this thesis, 'severe' and 'high' rates of soil loss were found on 5.7% of the study area, while 11% of the catchment area were affected by deposition. The average soil loss rate is 49.9 Mg ha^{-1}, calculated for the total area affected by soil loss and using the budget of the modelled events that account for 80.3% of the total sediment yield.

Other model-based erosion studies within the TGRA applied the empirical RUSLE, the semi-empirical SWAT model, or radionuclide inventories of (^{137}Cs) in various spatial scales as shown in Table 11 [Manuscript 1; Quine *et al.*, 1999; Lu & Higgit, 2000; Shi *et al.*, 2004; He *et al.*, 2007; Zhang, 2008]. The estimated soil loss rates by water erosion range between 26 Mg ha^{-1} a^{-1} and 76 Mg ha^{-1} a^{-1}. Since the average soil loss rate of the present study lies within the range of other soil erosion studies in this region, the applied approach can therefore be considered as reliable. However, the comparability of soil loss rates is limited due to scale-dependency in terms of space and time, a variety of measurement methods, and the complex relationship between environmental factors and soil erosion [Boardman, 2006; De Vente *et al.*, 2007; Cantón *et al.*, 2011; Vanmaercke *et al.*, 2011; García-Ruiz *et al.*, 2015]. In this context, García-Ruiz *et al.* [2015] compiled a data base of studies on soil loss rates from more than 4,000 sites worldwide, and analyzed the data for their relation to (non-) environmental factors. The meta-analysis revealed general trends of positive relations to factors, such as slope, annual precipitation, and land use. However, the results show high variability since the included studies comprised various spatial scales, durations of the experiments, and methods García-Ruiz *et al.* [2015]. Moreover, García-Ruiz *et al.* [2015] argued that insufficient descriptions of study areas, methods, and results, further exacerbate the comparability of erosion studies.

Table 11: Model-based soil erosion studies in the Three Gorges Reservoir Area based on physical (EROSION 3D, WaTEM/SEDEM, WEPP), semi-empirical (SWAT), empirical (USLE/RUSLE), and radionuclide inventory (^{137}Cs) methods.

Method	Area [ha]	Average soil loss rate [Mg ha^{-1}a^{-1}]	Reference
EROSION 3D	429	49.9	present study
WaTEM/SEDEM	1,670	13.2	Shi *et al.*[2012]
WEPP	162	2 - 38	Shen *et al.* [2010]
SWAT	162	27.0	Shen *et al.* [2009]
USLE	$2.3*10^6$	32.8	Zhang [2008]
RUSLE	$3.2*10^5$	52 - 76	Strehmel *et al.* [2015]
RUSLE	162	26 - 52	Shi *et al.* [2004]
^{137}Cs	70	45.0	Lu & Higgit [2000]
^{137}Cs	0.21	51.5	Quine *et al.* [1999]
^{137}Cs	$1.1*10^8$	24.2	He *et al.* [2007]

8.3.3 Sediment Reallocation and Land Use

This thesis investigates rainfall-triggered sediment reallocations to enable sustainable land management at the catchment scale. However, the sedimentological response of a landscape is complex, since it depends on a variety of interacting physical processes, which are related to topography, climate, soil, and vegetation among others [Martínez-Mena *et al.*, 1998; Cammeraat, 2004; Puigdefábregas, 2005; Bracken & Croke, 2007; Bautista *et al.*, 2007; Kröpfl *et al.*, 2013; Marchamalo *et al.*, 2015].

The quantification of the landscape response is increasingly achieved using the concept of landscape connectivity, which describes the water-mediated sediment fluxes within a catchment [Bracken & Croke, 2007; Lexartza-Artza & Wainwright, 2011; Fryirs, 2013]. Marchamalo *et al.* [2015] presented a method to identify hotspots of sediment sources, deposits, and their linkages by repeatedly mapping after rainfall events. Keesstra *et al.* [2009] combined field surveys, site-specific expert knowledge, and a sediment delivery model to establish a detailed sediment budget. However, the aforementioned approaches are accompanied by extensive field work, since detailed landscape features related to connectivity are difficult to derive from DEMs and remote sensing images [Lesschen *et al.*, 2009; Marchamalo *et al.*, 2015].

In contrast, the presented approach outlines a modelling framework of automated field monitoring and DSM techniques to calibrate a physically- and event based soil erosion model. The framework reduces efforts for field work and is applicable in data scarce and highly dynamic environments. However, the validation by outlet data only addresses overall model accuracy, while an uncertainty assessment of quantified sediment reallocations is limited [Jetten *et al.*, 1999; Boardman, 2006].

Nevertheless, the results of the spatial modelling approach are in agreement with average soil loss rates of main land use types in southern China [Hill & Peart, 1998; Huang *et al*., 1998; Xiang *et al*., 2001; Gao *et al*., 2004; Zheng & Zhang, 2006; Guo *et al.*, 2015]. The data is based on plot-scale studies, from which an average soil loss rate of 0.38 Mg ha^{-1} a^{-1} for the land use type 'forest', 5.5 Mg ha^{-1} a^{-1} for 'grassland', and 35.4 Mg ha^{-1} a^{-1} for 'cropland' were identified. According to a review by Hill & Peart [1998], average soil loss in southern China amounts to 0.1 Mg ha^{-1} a^{-1} for 'forest', 2.4 Mg ha^{-1} a^{-1} for 'grassland', and 62.4 Mg ha^{-1} a^{-1} for 'cropland'. In the present study, soil loss mainly occurs in the land use classes 'corn-rapeseed' and 'potato-cabbage'. Both land use classes were classified as 'severe'(> 50 Mg ha^{-1}) for approximately one third of the specific land use area (Table 10).

In addition, Takken *et al*. [1999] mapped soil erosion patterns and calculated the soil loss rates after an extreme rainfall event for different land use types in a small catchment in Belgium. The results confirm the aforementioned soil loss rates with no loss for 'forest', 0.2 Mg ha^{-1} for 'grassland', 53 Mg ha^{-1} for 'potato', and 76 Mg ha^{-1} for 'corn'. Moreover, Takken *et al.* [1999] found deposition on 3.5% of the study area, while major deposition zones were concentrated along the topographical depression lines, at field borders with high vegetation, and on roads. These results are generally confirmed by the present study, while deposition occurred on each land use class, but concentrated in topographic depression lines and in infrastructure areas (Figure 12; Table 10).

9 Conclusions

The present thesis addresses the development of a methodological framework that facilitates a detailed assessment of sediment reallocations in mountainous and data scarce catchments within the Three Gorges Reservoir Area in China [Manuscript 1]. The framework is based on an automated monitoring network to continuously obtain hydrological data in high temporal resolution [Manuscript 2, 3, 4] and optimized digital soil mapping techniques [Manuscript 2, 3, 5] to furnish a physically- and event-based soil erosion model [Manuscript 4]. The experiments were conducted in a small catchment of 429 ha, which is representative for the Three Gorges Reservoir Area in terms of land use, climate, and topography [Manuscript 1, 2, 3, 4].

The thesis presents a DSM soil sampling design, which is based on the principles of conditioned Latin Hypercube Sampling. The final sample set adequately reproduces the variation of selected terrain parameters, which serve as proxies for the target soil properties. The design compensates for limited field accessibility, integrates the use of legacy samples and uses an optimized sample set size. Consequently, the approach provides better operability in difficult terrain and improves efficiency in terms of temporal and monetary constraints compared to other cLHS approaches. Using a Random Forest regression model, topsoil sand fractions were estimated with convincing accuracies [Manuscript 2].

Within the framework of a DSM approach using the widely applied Random Forest regression model, this thesis further presents a method to straightforwardly derive reliable information on spatial uncertainties. In addition, the method supports the identification of relevant sampling areas to refine initial maps. The uncertainty measure represents pixel-wise prediction intervals that are based on the multiple randomized decision trees of the Random Forest model. The validity of the method was approved by a DSM case study for topsoil silt and clay fractions. Compared to initial soil maps that were based on legacy soil samples, the results show convincing quality improvements referring to the proposed spatial uncertainty and conventional accuracy measures [Manuscript 3].

Subsequently, sediment reallocations due to erosive rainfall events were analyzed. Thus, a methodological workflow for the parameterization of EROSION 3D was set up for testing the

model as a tool to spatially identify sediment sources and deposits. The complex model parameterization was accomplished by using the optimized Digital Soil Mapping techniques [Manuscript 2, 3], land use maps based on satellite data, and a parameter catalogue that contains empirically derived values for various conditions. Continuous model calibration data on rainfall, runoff, and sediment yields are representative for the region and show a strong cause-effect relationship that facilitates to derive erosive events. The majority of the total sediment yield (80.3%) was attributed to only six large erosive events. EROSION 3D performed well for large events, while small events showed high uncertainties. An average soil loss rate of 49.9 Mg ha^{-1} was detected. An area of approximately 11% of the entire study area is affected by soil loss. The major proportions of the soil loss area are classified as ‘severe’ (37.5%) and ‘low’ (45.1%). Primarily, soil loss occurs on cropland, concentrating on the land use classes ‘corn-rapeseed’ and ‘potato-cabbage’. Deposition occurs on 11% of the study area, mainly classified as ‘low’ deposition (61.5%). Contrary to the soil loss area, each land use class is affected by deposition, while the major areal proportions are attributed to the classes ‘built’ (47.1%) and ‘grassland’ (18.4%).

In summary, the thesis presents an efficient methodological outline to meet the complex data requirements of a physically- and event-based soil erosion model. Moreover, considering that the major sediment yields in the region are associated to a few large events, EROSION 3D can be recommended to identify sediment reallocations in small catchments in the Three Gorges Reservoir Area [Manuscript 4].

References

Adhikari K., Hartemink A.E., 2016. Linking soils to ecosystem services – a global review. *Geoderma* 262: 101–111.

Adhikari K., Minasny B., Greve M.B., Greve M.H., 2014. Constructing a soil class map of Denmark based on the FAO legend using digital techniques. *Geoderma* 214: 101–113.

Aksoy H., Kavvas M.L., 2005. A review of hillslope and watershed scale erosion and sediment transport models. *Catena* 64: 247–271.

Alewell C., Meusburger K., Juretzko G., Mabit L., Ketterer M.E., 2014. Suitability of $^{239+240}$Pu and ^{137}Cs as tracers for soil erosion assessment in mountain grasslands. *Chemosphere* 103: 274–280.

Anderson C.W., 2005. Turbidity: U.S. Geological Survey (USGS) Techniques of Water-Resources Investigations. [http://pubs.water.usgs.gov/twri9A; accessed: September 2014]

Andrews F, Guillaume J., 2015. 'hydromad': Hydrological Model Assessment and Development. R package version 0.9-22. [http://hydromad.catchment.org/; accessed May 2014]

Arnold J.G., Allen P.M., Muttiah R., Bernhardt G., 1995. Automated Base Flow Separation and Recession Analysis Techniques. *Ground Water* 33: 1010–1018.

Baartman J.E.M., Jetten V.G., Ritsema C.J., De Vente J., 2011. Exploring effects of rainfall intensity and duration on soil erosion at the catchment scale using openLISEM – Prado catchment, SE Spain. Hydrological Processes 26: 1034–1049.

Bagarello V., Di Piazza G.V., Ferro V., Giordano G., 2008. Predicting unit plot soil loss in Sicily, south Italy. *Hydrological Processes* 22: 586–595.

Bakr N., Weindorf D.C., Zhu Y., Arceneaux A.E., Selim H.M., 2012. Evaluation of compost/mulch as highway embankment erosion control in Louisiana at the plot-scale. *Journal of Hydrology* 468: 257–267.

Baltas E.A., Dervos N.A., Mimikou M.A., 2007. Technical Note: Determination of the SCS initial abstraction ratio in an experimental watershed in Greece. *Hydrological Earth System Sciences* 11: 1825–1829.

Bautista S., Mayor A.G., Bourakhouadar J., Bellot J., 2007. Plant spatial pattern predicts hillslope runoff and erosion in a semiarid Mediterranean landscape. *Ecosystem* 10: 987–998.

Behrens T., Schmidt K., Ramirez-Lopez L., Gallant J., Zhu A.X., Scholten T., 2014. Hyper-scale digital soil mapping and soil formation analysis. *Geoderma* 213: 578–588.

Behrens T., Schmidt K., Zhu A.X., Scholten T., 2010. The ConMap approach for terrain-based digital soil mapping. *European Journal of Soil Science* 61: 133–143.

Behrens T., Scholten T., 2006. Digital soil mapping in Germany – a review. *Journal of Plant Nutrition and Soil Science* 169: 434–443.

Behrens T., Förster H., Scholten T., Steinrücken U., Spies E.-D., Goldschmitt M., 2005. Digital Soil Mapping using Artificial Neural Networks. Journal of Plant Nutrition and Soil Science 168, 1–13.

Breiman, L. (2001): Random Forests. Mach. Learn. 45, 5-32.

Betts H.D., Trustrum N.A., de Rose R.C., 2003. Geomorphic changes in a complex gully system measured from sequential digital elevation models, and implications for management. *Earth Surface Processes and Landforms* 28: 1043–1058.

Bishop T.F.A., Horta A., Karunaratne S.B., 2015. Validation of digital soil maps at different spatial support. *Geoderma* 241: 238–249.

Bishop T.F.A., Minasny B., McBratney A.B., 2006. Uncertainty analysis for soil-terrain models. *International Journal of Geographic Information Science* 20: 117–134.

Bishop T.F.A., Minasny B., 2005. Digital soil-terrain modelling: the predictive potential and uncertainty. In: Grunwald S. (ed.). Environmental soil-landscape modeling: Geographic information technologies and pedometrics. CRC Press, USA, pp. 183–213.

Bishop T.F.A., McBratney A.B., Whelan B.M., 2001. Measuring the quality of digital soil maps using information criteria. *Geoderma* 103: 95–111.

Blum W.E.H., 2005. Functions of soil for society and the environment. *Reviews in Environmental Science and Bio/Technology* 4: 75–79.

Blume T., Zehe E., Bronstert A., 2007. Rainfall-runoff response, event-based runoff coefficients and hydrograph separation. *Hydrological Sciences Journal* 52: 843–862.

Boardman J., 2006. Soil erosion science: Reflections on the limitations of current approaches. *Catena* 68: 73–86.

Boix-Fayos C., Martínez-Mena M., Arnau-Rosalén E., Calvo-Cases A., Castillo V., Albaladejo J., 2006. Measuring soil erosion by field plots: Understanding the sources of variation. *Earth-Science Reviews* 78: 267–285.

Bossa A.Y., Diekkrüger B., Igué A.M., Gaiser T., 2012. Analyzing the effects of different soil databases on modeling of hydrological processes and sediment yield in Benin (West Africa). *Geoderma* 173: 61–74.

Bourennane H., King D., Couturier A., Nicoullaud B., Mary B., Richard G., 2007. Uncertainty assessment of soil water content spatial patterns using geostatistical

simulations: an empirical comparison of simulation accounting for single attribute and a simulation for secondary information. *Ecological Modelling* 205: 323–335.

Bracken L.J., Croke J., 2007. The concept of hydrological connectivity and its contribution for understanding sediment transfer at multiple scales. *Earth Surface Processes and Landforms* 21: 1749–1763.

Brantley S.L., 2008. Understanding soil time. *Science* 321: 1454–1455.

Bracken L.J., Cox N.J., Shannon J., 2008. The relationship between rainfall inputs and flood generation in south–east Spain. *Hydrological Processes* 22: 683–696.

Brazier, R., 2004. Quantifying soil erosion by water in the UK: a review of monitoring and modelling approaches. Progress in Physical Geography 28: 340–365.

Breiman L., 2001. Random Forests. *Machine Learning* 45: 5–32.

Brevik E.C., Cerdà A., Mataix-Solera J., Pereg L., Quinton J.N., Six J., Van Oost K., 2015. The interdisciplinary nature of soil. *Soil* 1: 117–129.

Brown L., Foster G., 1987. Storm erosivity using idealized intensity distribution. *American Society of Agricultural Engineers* 30: 379–386.

Brus D.J., Kempen B., Heuvelink G.B.M., 2011. Sampling for validation. *European Journal of Soil Science* 62: 394–407.

Brungard C.W., Boettinger J.L., 2010. Conditioned Latin Hypercube Sampling: Optimal sample size for Digital Soil Mapping of Arid Rangelands in Utah, USA. In: Boettinger J.L., Howell D.W., Moore A.C., Hartemink A.E., Kienast-Brown S. (eds.). Digital Soil Mapping. Bridging Research, Environmental Application, and Operation, Progress in Soil Science, Vol. 2. Springer, pp. 67–75.

Brus D., De Gruijter J., Van Groeningen J., 2006. Designing spatial coverage samples using k-means clustering algorithm. In: Lagacherie P., McBratney A.B., Voltz M. (eds.). Digital Soil Mapping, an introductory perspective. Developments in Soil Science, Vol. 31. Elsevier, Netherlands, pp. 183–192.

Bui E.N., 2004. Soil survey as a knowledge system. *Geoderma* 120: 17–26.

Burgess T.M., Webster R., 1980. Optimal interpolation and isarithmic mapping of soil properties. The semi-variogram and punctual kriging. *Journal of Soil Science* 31: 315–331.

Cai Q.G., Wang H., Curtin D., Zhu Y., 2005. Evaluation of the EUROSEM model with single event data on steeplands in the Three Gorges Reservoir Areas, China. *Catena* 59: 19–23.

Cambule A., Rossiter D., Stoorvogel J., 2013. A methodology for digital soil mapping in poorly-accessible areas. *Geoderma* 192: 341–353.

Cammeraat L.H., 2004. Scale dependent thresholds in hydrological erosion response of a semi-arid catchment in southeast Spain. *Agricultural Ecosystems and Environment* 104: 317–332.

Campbell G.B., 1991. Soil Physics with Basic Transport Models for Soil–Plant Systems, 1st edition. Elsevier, Netherlands, pp. 150–152.

Cantón Y., Solé-Benet A., De Vente J., Boix-Fayos C., Calvo-Cases A., Asensio C., Puigdefábregas J., 2011. A review of soil erosion across scales in semi-arid south-eastern Spain. *Journal of Arid Environments* 75: 1254–1261.

Capolongo D., Pennetta L., Piccarreta M., Fallacara G., Boenzi F., 2008. Spatial and temporal variations in soil erosion and deposition due to land-levelling in a semi-arid area of Basilicata (Southern Italy). *Earth Surface Processes and Landforms* 33: 364–379.

Carré F., McBratney A. B., Minasny B., 2007. Estimation and potential improvement of the quality of legacy soil samples for digital soil mapping. *Geoderma* 141: 1–14.

Carré F., Girard M., 2002. Quantitative mapping of soil types based on regression kriging of taxonomic distances with landform and land cover attributes. *Geoderma* 110: 241–263.

Castillo V.M., Gomez-Plaza A., Martinez-Mena M., 2003. The role of antecedent soil water content in the runoff response of semiarid catchments: a simulation approach. *Journal of Hydrology* 284: 114–130.

Chaubey I., Haan C.T., Grunwald S., Salisbury J.M., 1999. Uncertainty in the model parameters due to spatial variability of rainfall. *Journal of Hydrology* 220: 48–61.

Clifford D., Payne J., Pringle M., Searle R., Butler N., 2014. Pragmatic soil survey design using flexible Latin hypercube sampling. *Computer & Geosciences* 67: 62–68.

CMA, 2012. Chinese Meteorological Administration, Beijing: Climate Data. [http://2011.cma.gov.cn/en/; accessed February 2014]

Collard F., Kempen B., Heuvelink G.B.M., Saby N.P.A., Richer de Forges A.C., Lehmann S., Nehlig P., Arrouays D., 2014. Refining a reconnaissance soil map by calibrating regression models with data from the same map (Normandy, France). *Geoderma Regional* 1: 21–30.

Cook S.E., Corner R.J., Grealish G., Gessler P.E., Chartres C.J., 1996. A rule-based system to map soil properties. *Soil Science Society of America Journal* 60: 1893–1900.

Costanza R., d`Arge R., de Groot R., Farber S., Grasso M., Hannon B., Limburg K., Naeem S., O`Neill R.V., Paruelo J., Raskin R.G., Sutton P., van den Belt M., 1997. The value of the world`s ecosystem services and natural capital. *Nature* 387: 253–260.

Daily G.C., 1997. Nature`s services – societal dependence on natural ecosystems. Island Press, USA, pp. 113–132.

De Carvalho Junior W., Lagacherie P., Silva Chagas C., Filho B., Bhering S., 2014. A regional-scale assessment of digital soil attributes in a tropical hillslope environment. *Geoderma* 234: 479–486.

De Vente J., Poesen J., Verstraeten G., Govers G., Vanmaercke M., Van Rompaey A., Arabkhedri M., Boix-Fayos C., 2013. Predicting soil erosion and sediment yield at regional scales: Where do we stand? Earth-Science Reviews 127: 16–29.

De Vente J., Poesen J., Arabkhedri M., Verstraeten G., 2007. The sediment yield problem revisited. *Progress in Physical Geography* 31: 155–178.

De Vente J., Poesen J., 2005. Predicting soil erosion and sediment yield at the basin scale: scale issues and semi-quantitative models. *Earth-Science Reviews* 71: 95–125.

De Vries F.T., Thébault E., Liiri M., Birkhofer K., Tsiafouli M.A., Bjørnlund L., Jørgensen H.B., Brady M.V., Christensen S., de Ruiter P.C., d`Hertefeldt T., Frouz J., Hedlund K., Hemerik L., Hol W.H.G., Hotes S., Mortimer S.R., Setälä H., Sgardelis S.P., Uteseny K., van der Putten W.H., Wolters V., Bargett R.D., 2013. Soil food web properties explain ecosystem services across European land use systems. *PNAS* 110: 14296–14301.

Díaz-Uriarte R., De Andrés S., 2006. Gene selection and classification of microarray data using random forest. *BMC Bioinformatics* 7: 3–4.

Diodato N., Ceccarelli M., 2006. Computational uncertainty analysis of groundwater recharge in catchment. *Ecological Informatics* 1: 377–389.

Dobermann A., Simbahan G.C., 2007. Methodology for using secondary information in sampling optimization for making fine-resolution maps of soil organic carbon. In: Lagacherie P., McBratney A.B., Voltz M. (eds.). Digital Soil Mapping, an introductory perspective. Developments in Soil Science, Vol. 31. Elsevier, Netherlands, pp. 167–182.

Dorji T., Odeh I.O.A., Field D.J., Baillie I.C., 2014. Digital soil mapping of soil organic carbon stocks under different land use and land cover types in montane ecosystems, Eastern Himalayas. *Forest Ecology and Management* 318: 91–102.

Duck R.W., McManus J., 1994. A long-term estimate of bedload and suspended sediment yield derived from reservoir deposits. *Journal of Hydrology* 159: 365–373.

Dunkerley D., 2008. Rain event properties in nature and in rainfall simulation experiments: a comparative review with recommendations for increasingly systematic study and reporting. *Hydrological Processes* 22: 4415–4435.

Everitt B., 2002. The Cambridge dictionary of statistics. Cambridge University Press, UK, p. 3.

Fang N.F., Shi Z.H., Yue B.J., Wang L., 2013. The Characteristics of Extreme Erosion Events in a Small Mountainous Watershed. *PLoS One* 8: 1–10.

FAO, 2015. Food and Agricultural Organization of the United Nations. [http://www.fao.org/soils-2015/en/; accessed October 2015].

Ferreira V., Panagopoulos T., Andrade R., Guerrero C., Loures L., 2015. Spatial variability of soil properties and soil erodibility in the Alqueva reservoir watershed. *Solid Earth* 6: 383–392.

Finke P.A., 2007. Quality assessment of digital soil maps: Producers and users perspectives. In: Lagacherie P., McBratney A.B., Voltz M. (eds.), Chapter 39. Digital Soil Mapping, an introductory perspective. Developments in Soil Science, Vol. 31. Elsevier, Netherlands, pp. 523–541.

Fisher P.F., 1999. Models of uncertainty in spatial data. In: Longley P., Goodchild M., Maguire D., Rhind D. (eds.). Geographical information systems: Principles, techniques, management and application. Wiley & Sons, UK, pp. 191–205.

Flanagan D.C., Nearing M.A., 2000. Sediment particle sorting on hillslope profiles in the WEPP model. *American Society of Agricultural Engineers* 43: 576–583.

Fryirs K., 2013. (Dis) Connectivity in catchment sediment cascades: a fresh look at the sediment delivery problem. *Earth Surface Processes and Landforms* 38: 30–46.

Fuka D.R., Walter M.T., Archibald J.A., Steenhuis T.S., Easton Z.M., 2014. 'EcoHydRology': community modeling foundation for Eco-Hydrology. R package version 04-12. [http://cran.r-project.org/package=EcoHydRology; accessed April 2014]

Gao Z.Q., Zhang H.J., Shi Y.H., 2004. Study on soil erosion rate in different land use types in the granite area of Three Gorges. *Journal of Soil Water Conservation* 2: 26–29.

García-Ruiz J.M., Beguería S., Nadal-Romero E., Gonzáles-Hidalgo J.C., Lana-Renault N., Sanjuán Y., 2015. A meta-analysis of soil erosion rates across the world. *Geomorphology* 239: 160–173.

Gessler P., Chadwick O., Chamran F., Althouse L., Holmes K., 2000. Modeling soil-landscape and ecosystem properties using terrain attributes. *Soil Science Society of America Journal* 64: 2046–2056.

Gessler P.E., Moore I.D., McKenzie N.J., Ryan P.J., 1995. Soil-landscape modelling and spatial prediction of soil attributes. *International Journal of Geographical Information Systems* 9: 421–432.

Godfray H.C.J., Beddington J.R., Crute I.R., Haddad L., Lawrence D., Muir J.F., Pretty J., Robinson S., Thomas S.M., Toulmin C., 2010. Food security: the challenge of feeding 9 billion people. *Science* 327: 812–818.

Goovaerts P., 2001. Geostatistical modelling of uncertainty in soil science. *Geoderma* 103: 3–26.

Goovaerts P., 1999. Geostatistics in soil science: state-of-the-art and perspectives. *Geoderma* 89: 1–45.

Green W.H., Ampt G.A., 1911. Studies on soil physics: I. The flow of air and water through soils. *Journal of Agricultural Sciences* 4: 1–24.

Grimm R., Behrens T., 2009. Uncertainty analysis of sample locations within digital soil mapping approaches. *Geoderma* 155: 154–163.

Grimm R., Behrens T., Märker M., Elsenbeer H., 2008. Soil organic carbon concentrations and stocks on Barro Colorado Island - Digital Soil Mapping using Random Forests analysis. *Geoderma* 146: 102–113.

Grønsten H.A., Lundekvam H., 2006. Prediction of surface runoff and soil loss in southeastern Norway using the WEPP Hillslope model. *Soil &Tillage Research* 85: 186–199.

Grunwald S., 2009. Multi-criteria characterization of recent digital soil mapping and modelling approaches. *Geoderma* 152: 195–207.

Grunwald S., 2005. What do we really know about the space-time continuum of soil-landscapes? In: Grunwald S. (ed.). Environmental soil-landscape modeling: Geographic information technologies and pedometrics. CRC Press, USA, pp. 3–36.

Grün B., Leisch F., 2008. Felxmix Version 2: Finite mixtures with concomitant variables and varying and constant parameters. *Journal of Statistical Software* 28: 1–35.

Gumiere S.J., Raclot D., Cheviron B., Davy G., Louchart X., Fabre J., Moussa R., Le Bissonais Y., 2011. MHYDAS-Erosion: a distributed single-storm water erosion model for agricultural catchments. *Hydrological Processes* 25: 1717–1728.

Guo Q., Hao Y., Liu B., 2015. Catena Rates of soil erosion in China : A study based on runoff plot data. *Catena* 124: 68–76.

Ha H.A.P., Huon S., des Tureaux T.H., Orange D., Jouquet P., Valentin C., de Rouw A., Duc T.T., 2012. Impact of fodder cover on runoff and soil erosion at plot scale in a cultivated catchment of North Vietnam. *Geoderma* 177: 8–17.

Hansen L.K., Salamon P., 1990. Neural network ensembles. *IEEE Transactions on Pattern Analysis and Machine Intelligence* 12: 993–1001.

He X., Xu Y., Zhang X., 2007. Traditional farming system for soil conservation on slope farmland in southwestern China. *Soil & Tillage Research* 94: 193–200.

Hengl T., Husnjak S., 2006. Evaluating adequacy and usability of soil maps in Croatia. *Soil Science Society of America Journal* 70: 920–929.

Hengl T., Heuvelink G., Stein A., 2004. A generic framework for spatial prediction of soil variables based on regression-kriging. *Geoderma* 120: 75–93.

Hengl T., Rossiter D., Stein A., 2003. Soil sampling strategies for spatial prediction by correlation with auxiliary maps. *Soil Research* 41: 1403–1422.

Heung B., Bulmer C.E., Schmidt M.G., 2014. Predictive soil parent material mapping at a regional-scale: A Random Forest approach. *Geoderma* 214: 141–154.

Heuvelink G.B., Brus D.J., de Gruijter J.J., 2007. Optimization of sample configurations for digital soil mapping of soil properties with universal Kriging In: Lagacherie P., McBratney A.B., Voltz M. (eds.). Digital Soil Mapping, an introductory perspective. Developments in Soil Science. Vol. 31. Elsevier, Netherlands, pp.137–152.

Hewawasam T., Von Blanckenburg F., Schaller M., Kubik P., 2015. Increase of human over natural erosion rates in tropical highlands constrained by cosmogenic nuclides. Geology 31: 597–600.

Hill R.D., Peart M.R., 1998. Land use, runoff, erosion and their control: a review for southern China. *Hydrological Processes* 12: 2029–2042.

Huang L., Ding S.W., Zhang G., Peng Y.X., 1998. Preliminary estimation of soil and water conservation under different tillages on purple soil slope land in the Three Gorges Reservoir area. *Journal of Huazhong Agricultural University* 17: 45–49. [in Chinese]

Hudson B.D., 1992. The soil survey as a paradigm-based science. *Soil Science Society of America Journal* 56: 836–841.

Immerzeel W.W., Rutten M.M., Droogers P., 2009. Spatial downscaling of TRMM precipitation using vegetative response in the Iberian Peninsula. *Remote Sensing Environment* 113: 362–370.

Jenny H., 1941. Factors of soil formation. McGraw-Hill, USA, pp. 281–295.

Jetten V., Govers G., Hessel R., 2003. Erosion models: Quality of spatial predictions. *Hydrological Processes* 17: 887–900.

Jetten V.G., de Roo A.P.J., Favis-Mortlock D., 1999. Evaluation of field - scale and catchment - scale soil erosion models. *Catena* 3: 521–541.

Jordan G., Van Rompaey A., Szilassi P., Csillag G., Mannaerts C., Woldai T., 2005. Historical land use changes and their impact on sediment fluxes in the Balaton basin (Hungary). *Agriculture, Ecosystems & Environment* 108: 119–133.

Oldeman L.R., 1994. An international methodology for an assessment of soil degradation, land georeferenced soils and terrain data base. FAO-RAPA Publications, Thailand, pp. 35–60.

Onyando J.O., Kisoyan P., Chemelil M.C., 2005. Estimation of potential soil erosion for river Perkerra catchment in Kenya. *Water Resources Management* 19: 133–143.

Kaihura F.B.S., Kullaya I.K., Kilasara M., Aune J.B., Singh B.R., Lal R., 1999. Soil quality effects of accelerated erosion and management systems in the three eco-regions of Tanzania. *Soil & Tillage Research* 53: 59–70.

Kateb H.E., Zhang H., Zhang P., Mosandl R., 2013. Soil erosion and surface runoff on different vegetation covers and slope gradients: a field experiment in Southern Shaanxi Province, China. *Catena* 105: 1–10.

Keesstra S.D., Bruijnzeel L.A., Van Huissteden J., 2009. Meso-scale catchment sediment budgets: combining field surveys and modeling in the Dragonja catchment, southwest Slovenia. *Earth Surface Processes and Landforms* 34: 1547–1561.

Kempen B., Brus D.J., Heuvelink G.B.M., Stoorvogel J.J., 2009. Updating the 1:50,000 Dutch soil map using legacy soil data: a multinominal logistic regression approach. *Geoderma* 151: 311–326.

Kepa Brian Morgan T.K., Sardelic D.N., Waretini A.F., 2012. The Three Gorges Project: How sustainable? *Journal of Hydrology* 460: 1–12.

Kidd D., Malone B., McBratney A.B., Minasny B., Webb M., 2015. Operational sampling challenges to Digital Soil Mapping in Tasmania, Australia. *Geoderma Regional* 4: 1–10.

Kirkby M.J., 1978. Hillslope hydrology. Wiley & Sons, UK, pp 145–170.

Knotters M., Brus D.J., Oude Voshaar J.H., 1995. A comparison of kriging, co-kriging and kriging combined with regression for spatial interpolation of horizon depth with censored observations. *Geoderma* 67: 227–246.

Krause P., Boyle D.P., Bäse F., 2005. Comparison of different efficiency criteria for hydrological model assessment. *Advances in Geosciences* 5: 89–97.

Krol, B., 2008. Towards a data quality management framework for digital soil mapping with limited data. In: Hartemink A.E., McBratney A.B., Mendonça-Santos M.L. (eds.). Digital Soil Mapping with Limited Data. Springer, pp. 136–149.

Kröpfl A.I., Cecchi G.A., Villasuso N.M., Distel R.A., 2013. Degradation and recovery processes in semi-arid patchy rangelands of northern Patagonia, Argentinia. *Land Degradation & Development* 24: 393–399.

Kuhn, M., 2009. The caret package. [http://cran.r-project.org/web/packages/caret/index.html; accessed October 2014]

Kullback S., Leibler R.A., 1951. On information and sufficiency. *Annals of Mathematical Statistics* 22: 79–86.

Lacoste M., Lemercier B., Walter C., 2011. Regional mapping of soil parent material by machine learning based on point data. *Geomorphology* 133: 90–99.

Lagacherie P., 2008. Digital Soil Mapping: A State of the Art. In: Hartemink A.E., McBratney A.B., Mendonça-Santos M.L. (eds.). Digital Soil Mapping with Limited Data. Springer, pp. 3–14.

Lal R., Griffin M., Apt J., Lave L., Morgan M.G., 2004. Managing soil carbon. Science 304: 393–394.

Lal R., 2003. Soil erosion and the global carbon budget. *Environment International* 29: 437–450.

Lal R., 2001. Soil degradation by erosion. *Land Degradation & Development* 12: 519–539.

Lark R.M., Lapworth D.J., 2012. Quality measures for soil surveys by lognormal kriging. *Geoderma* 173: 231–241.

Lee G., Yu W., Jung K., 2013. Catchment-scale soil erosion and sediment yield simulation using a spatially distributed erosion model. *Environmental Earth Sciences* 70: 33–47.

Lesschen J.P., Schoorl J.M., Cammeraat L.H., 2009. Modelling runoff and erosion for semi-arid catchment using a multi-scale approach based on hydrological connectivity. *Geomorphology* 109: 174–183.

Lexartza-Artza I., Wainwright J., 2011. Making connections: changing sediment sources and sinks in an upland catchment. *Earth Surface Processes and Landforms* 36: 1090–1104.

Li J., Heap A.D., 2011. A review of comparative studies of spatial interpolation methods in environmental sciences: performance and impact factors. *Ecological Informatics* 6: 228–241.

Liaw A., Wiener M., 2002. Classification and Regression by Random Forest. *R News* 2: 18–22.

Ließ M., Glaser B., Huwe B., 2012. Uncertainty in the spatial prediction of soil texture. Comparison of regression tree and Random Forest models. *Geoderma* 170: 70–79.

Liu C., Wang Q.X., Watanabe M., 2006. Nitrogen transported to the Three Gorges Dam from agro-ecosystems. *Biogeochemistry* 81: 291–312.

Liu J, Liu M, Tian H, Zhuang D, Zhang Z, Zhang W, Tang X, Deng X., 2005. Spatial and temporal patterns of China's cropland during 1990-2000: An analysis based on Landsat TM data. *Remote Sensing Environment* 98: 442–456.

Loughran R.L., 1989. The measurement of soil erosion. *Progress in Physical Geography* 13: 216–233.

Lu X.X., Higgitt D.L., 2000. Estimating erosion rates on sloping agricultural land in the Yangtze Three Gorges, China, from caesium-137 measurements. *Catena* 39: 33–51.

Mabit L., Meusburger K., Fulajtar E., Alewell C., 2013. The usefulness of ^{137}Cs as a tracer for soil erosion assessment: a critical reply to Parsons and Foster (2011). *Earth-Science Reviews* 127: 300–307.

Maetens W., Vanmaercke M., Poesen J., Jankauskas B., Jankauskiene G., Ionita I., 2012. Effects of land use on annual runoff and soil loss in Europe and the Mediterranean: a meta-analysis of plot data. *Progress in Physical Geography* 36: 599–653.

Malone B.P., McBratney A.B., Minasny B., 2011. Empirical estimates of uncertainty for mapping continuous depth functions of soil attributes. *Geoderma* 160: 614–626.

Malone B., McBratney A., Minasny B., Laslett G., 2009. Mapping continuous depth functions of soil carbon storage and available water capacity. *Geoderma* 154: 138–152.

Mansuy N., Thiffault E., Paré D., Bernier P., Guindon L., Villemaire P., Poirier V., Beaudoin, A., 2014. Digital mapping of soil properties in Canadian managed forests at 250 m of resolution using k-nearest neighbor method. *Geoderma* 236: 59–73.

Marchamalo M., Hooke J.M., Sandercock P.J., 2015. Flow and sediment connectivity in semi-arid landscapes in SE Spain: Patterns and control. *Land Degradation & Development*. [Early View: DOI: 10.1002/ldr.2352]

Martínez-Mena M., Albaladejo J., Castillo V.M., 1998. Factors influencing surface runoff generation in a Mediterranean semi-arid environment. *Hydrological Processes* 12: 74 –754.

Matisoff G., Whiting P.J., 2011. Measuring soil erosion rates using natural (^{7}Be, ^{210}Pb) and anthropogenic (^{137}Cs, ^{239}Pu, ^{240}Pu). In: Baskaran M. (eds.). Handbook of environmental isotope geochemistry, vol.1. Advances in Isotope Geochemistry, pp. 487–519.

McBratney A.B., Minasny B., Viscarra Rossel R., 2006. Spectral soil analysis and inference systems: a powerful combination for solving the soil data crisis. *Geoderma* 136: 272–278.

McBratney A.B., Mendonça Santos M.L., Minasny B., 2003. On digital soil mapping. *Geoderma* 117: 3–52.

McBratney A.B., Odeh I.O.A., Bishop T.F.A., Dunbar M.S., Shatar T.M., 2000. An overview of pedometric techniques for use in soil survey. *Geoderma* 97: 293–327.

McKensie N.J., Gessler P.E., Ryan P.J., O´Connel D., 2000. The role of terrain analysis in soil mapping. In: Wilson J., Gallant J. (eds.). Terrain Analysis: principals and applications. Wiley & Sons, USA, pp. 245–265.

McKenzie, N., Ryan, P., 1999. Spatial prediction of soil properties using environmental correlation. *Geoderma* 89: 67–94.

McMillan R.A., 2008. Experiences with applied DSM: protocol, availability, quality and capacity building. In: Hartemink A.E., McBratney A.B., Mendonça-Santos M.L. (eds.). Digital Soil Mapping with Limited Data. Springer, pp. 113–135.

McSweeney K.M., Gessler P.E., Slater B., Hammer R.D., Bell J., 1994. Towards a new framework for modelling the soil-landscape continuum. *Soil Science Society of America Journal, Special Publication* 33: 127–145.

Merritt W.S., Letcher R.A., Jakeman A.J., 2003. A review of erosion and sediment transport models. *Environmental Modelling & Software* 18: 761–799.

Merz J., Dangol P.M., Dhakal M.P., Dongol B.S., Nakarmi G., Weingartner R., 2006. Rainfall-runoff events in a middle mountain catchment of Nepal. *Journal of Hydrology* 331: 446–458.

Metropolis N., Rosenbluth A, Rosenbluth M., Teller A., Teller E., 1953. Equation of state calculations by fast computing machines. *Journal of Chemical Physics* 21: 1087–1092.

Michael A. 2000. Anwendung des physikalisch begründeten Erosionsprognosemodells EROSION 2D/3D - Empirische Ansätze zur Ableitung der Modellparameter. Technical University Freiberg, Germany. [Dissertation]

Middleton N., Thomas D., 1997. World atlas of desertification, 2nd edition. Arnold Publications, UK, pp. 182–183.

Minasny B., Bishop T.F.A., 2008. Analyzing uncertainty. In: McKenzie N., Grundy M., Webster R., Ringrose-Voase A. (eds.). Guidelines for surveying soil and land resources. CSRO Publishing, Australia, pp. 383–393.

Minasny B., McBratney A.B., 2006. A conditioned Latin hypercube method for sampling in presence of ancillary data. *Computer & Geosciences* 32: 1378–1288.

Mitasova H., Hofierka J., Zlocha M., Iverson L.R., 1996. Modeling topographic potential for erosion and deposition using GIS. *International Journal of Geographic Information Systems* 10: 629–641.

Molina A., Govers G., Vanacker V., Poesen J., Zeelmaeker E., Cisneros F., 2007. Runoff generation in a degraded Andean ecosystem: interaction of vegetation cover and landuse. *Catena* 71: 357–370.

Moore I.D., Gessler P.E., Nielsen G.A., Petersen G.A., 1993. Soil attribute prediction using terrain analysis. *Soil Science Society of America Journal* 57: 443–452.

Morgan R.P.C., Nearing M.A., 2011. Handbook of Erosion Modelling. Blackwell Publishing, UK, pp. 401–408.

Morgan R.P.C., 2005. Soil erosion and conservation, 3rd edition. Blackwell Publishing, Australia, pp. 1–67.

Mulder V.L., De Bruin S., Schaepman M., 2013. Representing major soil variability at regional scale by constrained Latin hypercube sampling of remote sensing data. *International Journal of Applied Earth Observation and Geoinformation* 21: 301–310.

Naumann T.W., Thompson J.A., 2014. Semi-automated disaggregation of conventional soil maps using knowledge driven data mining and classification trees. *Geoderma* 213: 385–399.

Nash J.E., Sutcliff J.V., 1970. River flow forecasting through conceptual model. Part 1: A discussion of principles. *Journal of Hydrology* 10: 282–290.

Nathan R.J., McMahon T.A., 1990. Evaluation of automated techniques for base flow and recession analysis. *Water Resources Research* 26: 1465–1473.

Nearing M.A., Jetten V., Baffaut C., Cerdan O., Couturier A., Hernandez M., Le Bissonnais Y., Nichols M.H., Nunes J.P., Renschler C.S., Souchère V., Van Oost K., 2005. Modeling response of soil erosion and runoff to changes in precipitation and cover. *Catena* 61: 131–154.

Nearing M.A., 2000. Evaluating soil erosion models using measured plot data: accounting for variability in the data. *Earth Surface Processes and Landforms* 25: 1035–1043.

Nearing M.A., Govers G., Darrell N.L., 1999. Variability in soil erosion data from replicated plots. *Soil Science Society of America Journal* 63: 1829–1835.

Nelson M.A., Bishop T.F.A., Triantafilis J., Odeh I.O.A., 2011. An error budget for different sources of error in digital soil mapping. *European Journal of Soil Science* 62: 417–430.

Oberthur T., Goovaerts P., Dobermann A., 1999. Mapping soil texture classes using field texturing, particle size distribution and local knowledge by both conventional and geostatistical methods. *European Journal of Soil Science* 50: 457–479.

Padarian J., Minasny B., McBratney A.B., 2015. Using Google`s cloud-based platform for digital soil mapping. *Computers & Geosciences* 83: 80–88.

Palazón L., Gaspar L., Latorre B., Blake W.H., Navas A., 2014. Evaluating the importance of surface soil contributions to reservoir sediment in alpine environments: a combined modelling and fingerprinting approach in the Posets-Maladeta Natural Park. *Solid Earth* 5: 963–978.

Park S., Oh C., Jeon S., Jung H., Choi C., 2011. Soil erosion risk in Korean watersheds, assessed using the revised universal soil loss equation. *Journal of Hydrology* 399: 263–273.

Parson A.J., Foster I.D.L., 2011. What can we learn about soil erosion from the use of ^{137}Cs? *Earth-Science Reviews* 108; 101–113.

Peng C.U.I., Yonggang G.E., Yongming L.I.N., 2011. Soil Erosion and Sediment Control Effects in the Three Gorges Reservoir Region, China. *Journal of Resources and Ecology* 2: 289–297.

Penneck D.J., Corre M.D., 2001. Development and application of landform segmentation procedures. *Soil and Tillage Research* 58: 151–161.

Peters J., De Baets B., Verhoest N.E.C., Samson R., Degroeve S., De Becker P., Huybrechts W., 2007. Random Forests as a tool for ecohydrological distribution modelling. *Ecological Modelling* 207: 304–318.

Pimentel D., 2006. Soil Erosion: a food and environmental threat. *Environment, Development and Sustainability* 8: 119–137.

Pimentel D., Kounang N., 1998. Ecology of soil erosion in ecosystems. *Ecosystems* 1: 416–426.

Pimentel D., Harvey C., Resosudarmo P., Sinclair K., Kurz D., McNair M., Crist S., Shpritz L., Fitton L., Saffouri R., Blair R., 1995. Environmental and economic costs of soil erosion and conservation benefits. *Science* 267: 1117–1123.

Prasad A.M., Iverson L.R., Liaw A., 2006. Newer classification and regression tree techniques: Bagging and random forests for ecological prediction. *Ecosystems* 9: 181–199.

Prosser I.P., Dietrich W.E., 1995. Field experiments on erosion by overland flow and their implication for a digital terrain model of channel initiation. Water Resources Research 31: 2867–2876.

Puigdefábregas J., 2005. The role of vegetation patterns in structuring runoff and sediment fluxes in drylands. *Earth Surface Processes and Landforms* 30: 133–148.

Qu M., Li W., Zhang C., 2013. Assessing the spatial uncertainty in soil nitrogen mapping through stochastic simulations with categorial land use information. *Ecological Informatics* 16: 1–9.

Quine T.A., Walling D.E., Chakela Q.K., Mandiringana O.T., Zhang X., 1999. Rates and patterns of tillage and water erosion on terraces and contour strips: evidence from caesium-137 measurements. *Catena* 36: 115–142.

Quinlan J.R., 1986. Induction of decision trees. *Machine Learning* 1: 81–106.

Rad M.R.P., Toomanian N., Khormali F., Brungard C.W., Komaki C.B., Bogaert P., 2014. Updating soil survey maps by using random forest and conditioned Latin hypercube sampling in the loess derived soils of northern Iran. *Geoderma* 232: 97–106.

R Core Team, 2014. R: A language and environment for statistical computing. R Foundation for Statistical Computing, Vienna, Austria. [http://www.R-project.org; accessed May 2014]

Ramirez-Lopez L., Schmidt K., Behrens T., Van Wesemael B., Dematte J., Scholten T., 2014. Sampling optimal calibration sets in soil infrared spectroscopy. *Geoderma* 226: 140–150.

RapidEye. 2012. Satellite Imagery Product Specifications.-.version 4.1. [http://www.rapideye.com/upload; accessed February 2013]

Renard K., Foster G., Weesies G., McCool D., Yoder D., 1997. Predicting soil erosion by water: a guide to conservation planning with the Revised Universal Soil Loss Equation (RUSLE). USDA Agricultural Handbook No. 703. [http://www.osmre.gov/resources/library/ghm/USDA_AH703.pdf; accessed May 2014]

Rickemann D., McArdell B.W., 2007. Continuous measurement of sediment transport in the Erlenbach stream using piezoelectric bedload impact sensors. *Earth Surface Processes and Landforms* 32: 1362–1378.

Roudier P., Hewitt A.E., Beaudette D.E., 2012. A conditioned Latin Hypercube Sampling algorithm incorporating operational constraints. In: Minasny B., Malone B.P., McBratney A.B. (eds.). Soil Assessment and Beyond. CRC Press, Australia, pp. 227–231.

SAGA GIS, 2012. System for Automated Geoscientific Analyses -Version 2.0.6. [http//:www.saga-gis.org; accessed January 2013]

Satterland D.R., Adams P.W., 1992. Wildland watershed management. Wiley & Sons, USA, pp. 24–36.

Schindewolf M., Schmidt J., 2012. Parameterization of the EROSION 2D/3D soil erosion model using a small-scale rainfall simulator and upstream runoff simulation. *Catena* 91: 47–55.

Schönbrodt-Stitt S., Behrens T., Schmidt K., Shi X., Scholten T., 2013. Degradation of cultivated bench terraces in the Three Gorges Area: Field mapping and data mining. *Ecological Indicators* 34: 478–493.

Schmidt J., Werner M.V., Michael A., 1999. Application of the EROSION 3D model to the CATSOP watershed, the Netherlands. *Catena* 37: 449–456.

Schmidt J., 1992. Modeling long term soil loss and landform change. In: Parson A.J., Abrahams A.D. (eds.). Overland Flow - Hydraulics and Erosion Mechanics. UCL Press, UK, pp. 389–415.

Schmidt J., 1991. A mathematical model to simulate rainfall erosion. *Catena Supplememt* 19: 101–109.

Schmidt K., Behrens T., Daumann J., Ramirez-Lopez L., Werban U., Dietrich P., Scholten T., 2014. A comparison of calibration sampling schemes at the field scale. *Geoderma* 232: 243–256.

Schmidt K., Behrens T., Friedrich K., Scholten T., 2010. A method to generate soilscapes from soil maps. *Journal of Plant Nutrition and Soil Science* 173: 163–172.

Schönbrodt S., Saumer P., Behrens T., Seeber C., Scholten T., 2010. Assessing the USLE Crop and Management Factor C for Soil Erosion Modelling in a Large Mountainous Watershed in Central China. *Journal of Earth Science* 21: 835–845.

Scull P., Franklin J., Chadwick O.A., McArthur D., 2003. Predictive soil mapping: a review. *Progress in Physical Geography* 27: 171–197.

Shen Z.Y., Gong Y.W., Li Y.H., Liu R.M., 2010. Analysis and modeling of soil conservation measures in the Three Gorges Reservoir Area in China. *Catena* 81: 104–112.

Shen Z.Y., Gong Y.W., Li Y.H., Hong Q., Xu L., Liu R.M., 2009. A comparison of WEPP and SWAT for modeling soil erosion of the Zhangjiachong Watershed in the Three Gorges Reservoir Area. *Agricultural Water Management* 96: 1435–1442.

Shi Z.H., Ai L., Fang N.F., Zhu H.D., 2012. Modeling the impacts of integrated small watershed management on soil erosion and sediment delivery: A case study in the Three Gorges Area, China. *Journal of Hydrology* 438: 156–167.

Shi Z.H., Cai C.F., Ding S.W., Wang T.W., Chow T.L., 2004. Soil conservation planning at the small watershed level using RUSLE with GIS: A case study in the Three Gorge Area of China. *Catena* 55: 33–48.

Shrestha D.L., Solomatine D.P., 2006. Machine learning approaches for estimation of prediction interval for model output. *Neural Networks* 19: 225–235.

Soulis K.X., Valiantzas J.D., Dercas N., Londra P.A., 2009. Analysis of the runoff generation mechanism for the investigation of the SCS-CN method applicability to a partial area experimental watershed. *Hydrological Earth System Sciences* 6: 373–400.

Starkloff T., Stolte J., 2014. Applied comparison of the erosion risk models EROSION 3D and LISEM for a small catchment in Norway. *Catena* 118: 154–167.

Sulaeman Y., Minasny B., McBratney A.B., Sarwani M., Sutandi A., 2013. Harmonizing legacy soil data for digital soil mapping in Indonesia. *Geoderma* 192: 77–85.

Sun W., Shao Q., Liu J., 2013. Soil erosion and its response to the changes of precipitation and vegetation cover on the Loess Plateau. *Journal of Geographical Sciences* 23: 1091–1106.

Svetnik V., Liaw A., Tong C., Culberson C.J., Sheridan R.P., Feuston B.P., 2003. Random forest: a classification and regression tool for compound classification and QSAR modeling. Journal of Chemical Information and Computer Sciences 43: 1947–1958.

Taghizadeh-Mehrjardi R., Minasny B., Sarmadian F., Malone B., 2014. Digital soil mapping of soil salinity in Ardakan region, central Iran. *Geoderma* 213: 15–28.

Taguas E.V., Moral C., Ayuso J.L., Pérez R., Gómez J.A., 2011. Modeling the spatial distribution of water erosion within a Spanish olive orchard microcatchment using the SEDD model. *Geomorphology* 133: 47–56.

Takken I., Beuselinck L., Nachtergaele J., Govers G., Poesen J., Degraer G., 1999. Spatial evaluation of a physically-based distributed erosion model (LISEM). *Catena* 37: 431–447.

Tan Y., Yao F., 2006. Three Gorges Project: Effects of resettlement on the Environment in the reservoir area and countermeasures. *Population and Environment* 27: 351–371.

Tarboton D.G., 1997. A new method for the determination of flow directions and upslope areas in grid digital elevation models. *Water Resources Research* 33: 309–319.

Terranova O., Antronico L., Coscarelli R., Iaquinta P., 2009. Soil erosion risk scenarios in the Mediterranean environment using RUSLE and GIS: An application model for Calabria (southern Italy). *Geomorphology* 112: 228–245.

Todisco F., 2014. The internal structure of erosive and non-erosive storm events for interpretation of erosive processes and rainfall simulation. *Journal of Hydrology* 519: 3651–3663.

Tutmez B., Hatipoglu Z., 2010. Comparing two data driven interpolation methods for modeling nitrate distribution in aquifer. *Ecological Informatics* 5: 311–315.

Vanmaercke M., Poesen J., Verstraeten G., De Vente J., Ocakoglu F., 2011. Sediment yield in Europe: spatial patterns and scale dependency. *Geomorphology* 130: 142–161.

Van Rompaey A., Govers G., 2002. Data quality and model complexity for continental scale soil erosion modelling. *International Journal of Geographical Information Science* 16: 663–680.

Van Rompaey A., Verstraeten G., Van Oost K., Govers G., Poesen J., 2001. Modelling mean annual sediment yield using a distributed approach. *Earth Surface Processes and Landforms* 26: 1221–1236.

Van Rompaey A., Govers G., Baudet M., 1999. A strategy for controlling error of distributed environmental models by aggregation. *International Journal of Geographical Information Science* 16: 577–590.

Verheijen F.G.A., Jones R.J.A., Rickson R.J., Smith C.J., 2009. Tolerable versus actual soil erosion rates in Europe. *Earth-Science Reviews* 94: 23–38.

Viscarra Rossel R.A., McBratney A.B., 1998. Soil chemical analytical accuracy and costs: implications from precision agriculture. *Australian Journal of Experimental Agriculture* 38: 765–775.

Wainwright J., Parsons A.J., Abrahams A.D., 2000. Plot-scale studies of vegetation, overland flow and erosion interactions: case studies from Arizona and New Mexico. *Hydrological Processes* 14: 2921–2943.

Wall D.H., Bardgett R.D., Behan-Pelletier V., Herrick J.E., Jones T.H., Ritz K., Six J., Strong D.R., van der Putten W.H., 2012. Soil ecology and ecosystem services. Oxford University Press, UK, pp. 5–7.

Wang D.C., Zhang G.L., Pan X.Z., Zhao Y.G., Zhao M.S., Wang G.F., 2012. Mapping soil texture of a plain area using Fuzzy-C-Means Clustering method on land surface diurnal temperature difference. *Pedosphere* 22: 394–403.

Webster R., Oliver M.A., 2005. Modeling spatial variation of soil as random functions. In: Grunwald S. (ed.). Environmental soil-landscape modeling: Geographic information technologies and Pedometrics. CRC Press, USA, pp. 241–287.

Webster R., 1977. Quantitative and numerical methods in soil classification and survey. Oxford University Press, UK, pp. 120–163.

Weigert A., Schmidt J., 2005. Water transport under winter conditions. *Catena* 64: 193–208.

Wellmann F.J., 2013. Information theory for correlation analysis and estimation of uncertainty reduction in maps and models. *Entropy* 15: 1464–1485.

White R.E., 2006. Principles and practice of soil Science – the soil as a natural resource, 4th edition. Blackwell Publishing, UK, pp. 3–10.

Wiesmeier M., Barthold F., Blank B., Kögel-Knabner I., 2011. Digital mapping of soil organic matter stocks using random forest modeling in semi-arid steppe ecosystems. *Plant & Soil* 340: 7–24.

Wischmeier W.H., Smith D.D., 1981. Predicting rainfall erosion losses – a guide to conservation planning. U.S. Department of Agriculture, Handbook 537. [http://naldc.nal.usda.gov/download/CAT79706928/PDF; accessed April 2014]

Wilding L.P., 1985. Spatial variability: its documentation, accommodation and implication to soil surveys. In: Nielsen D.R., Bouma J. (eds.). Soil spatial variability. Proceedings of a workshop of ISSS and the SSSA, USA, Nov. 30 – Dec. 1, 1984.

WRB, 2014. World Reference Base for Soil Resources. [http://www.fao.org/soils-portal/soil-survey/soil-classification/world-reference-base/en/; accessed March 2015]

Wu D.M., Yu Y.C., Xia L.Z., Yin S.X., Yang L.Z., 2011. Soil fertility indices of citrus orchard land along topographic gradients in the three gorges area of China. *Pedosphere* 21: 782–792.

Wysocki D.A., Schoeneberger P.J., LaGarry H.E., 2000. Geomorphology of soil landscapes. In: Sumner M.E. (ed.). Handbook of soil science. CRC Press, USA, pp. 5–40.

Xiang W.S., Liang C.F., Li W.H., 2001. Soil and water loss from cultivated slope land derived from granite under different cropping systems in the Three Gorges Reservoir area. *Chinese Journal of Applied Ecology* 12: 47–50. [in Chinese]

Xie Y., Liu B., Nearing M.A., 2002. Practical thresholds for separating erosive and non-erosive events. *American Society of Agricultural Engineers* 45: 1843–1847.

Xu X., Tan Y., Yang G., 2013. Environmental impact assessments of the Three Gorges Project in China: issues and interventions. *Earth-Science Reviews* 124: 115–125.

Xu X., Tan Y., Yang G., Li H., Su W., 2011. Impacts of China's Three Gorges Dam Project on net primary productivity in the reservoir area. *Science of the Total Environment* 409: 4656–4662.

Yin S., Xie Y., Nearing M.A., Wang C., 2007. Estimation of rainfall erosivity using 5- to 60-minute fixed-interval rainfall data from China. *Catena* 70: 306–312.

Yang L., Jiao Y., Fahmy S., Zhu A.X., Hann S., Burt J.E., Qi F., 2011. Updating conventional soil maps through digital soil mapping. Soil *Science Society of America Journal* 75: 1044–1053.

Young I.M., Crawford J.W., 2004. Interactions and self-organization in the soil-microbe complex. *Science* 304: 1634–1637.

Zambrano-Bigiarini M., 2014. 'hydroGOF': Goodness-of-fit functions for comparison of simulated and observed hydrological time series. R package version 0.3-8. [https://cran.r-project.org/web/packages/hydroGOF/index.html; accessed July 2015]

Zhang B., 2008. Impact on mountainous agricultural development in the Three Gorges Reservoir Area forced by migrants of the Three Gorges Project. *Chinese Journal of Population Resources and Environment* 6: 83–89.

Zhang Q., Lou Z., 2011. The environmental changes and mitigation actions in the Three Gorges Reservoir region, China. *Environmental Science & Policy* 14: 1132–1138.

Zhang H., Nearing M.A., Liu B.Y., Van Pelt R.S., Stone J.J., Wei H., Scott R.L., 2011. Comparative rates of wind versus water erosion from a small semiarid watershed in southern Arizona, USA. *Aeolian Research* 3: 197–204.

Zhang J., Zhengjun L., Xiaoxia S., 2009. Changing landscape in the Three Gorges Reservoir Area of Yangtze River from 1977 to 2005: land use/land cover, vegetation cover changes estimated using multi-source satellite data. *International Journal of Applied Earth Observation and Geoinformation* 11: 403–412.

Zhang L., O'Neill A.L., Lacey S., 1996. Modelling approaches to the prediction of soil erosion in catchments. *Environmental Software* 11: 123–133.

Zhao G., Mu X., Wen Z., Wang F., Gao P., 2013. Soil erosion, conservation, and eco-environment changes in the Loess Plateau of China. *Land Degradation & Development* 24: 499–510.

Zheng D., Hunt E.R., Running S.W., 1996. Comparison of available soil water capacity estimated from topography and soil series information. *Landscape Ecology* 11: 3–14.

Zheng W.W., Zhang C.L., 2006. Soil conservation benefit analysis for citrus orchard in the reservoir basin of Three Gorges. *Subtropical Soil Water Conservation* 18: 15–18.

Zhou P., Luukkanen O., Tokola T., Nieminen J., 2008. Effect of vegetation cover on soil erosion in a mountainous watershed. *Catena* 75: 319–325.

Zhu A.X., Liu J., Du F., Zhang S.J., Qin C.Z., Burt J., Behrens T., Scholten T., 2015. Predictive soil mapping with limited sample data. *European Journal of Soil Science* 66: 535–547.

Appendix

Personal Contribution

Erklärung nach § 5 Abs. 2 Nr. 7 der Promotionsordnung der Math.-Nat. Fakultät

-Anteil an gemeinschaftlichen Veröffentlichungen-

Declaration according to § 5 Abs. 2 No. 7 of the PromO of the Faculty of Science

-Share in publications done in team work-

Name: Felix Stumpf

List of Publications

1. Assessment of Geo-Hazards in a Rapidly Changing Landscape: The Three Gorges Reservoir Region in China
2. Incorporating Limited Field Operability and legacy Samples in a Hypercube Sampling Design for Digital Soil Mapping
3. Spatial Uncertainty-Guided Sampling to Improve Digital Soil Maps
4. Sediment reallocation due to erosive rainfall events in the Three Gorges Reservoir Area, Central China
5. Rule-based analysis of throughfall kinetic energy to evaluate leaf and tree architectural trait thresholds to mitigate erosive power

Nr.	Accepted for publication	Number of all authors	Position of the candidate in list of authors	Scientific ideas of candidate (%)	Data generation by candidate (%)	Analysis and Interpretation by candidate (%)	Paper writing by candidate (%)
1	YES	19	5	20	30	40	15
2	NO	9	1	70	90	90	80
3	NO	8	1	70	90	90	80
4	YES	8	1	80	90	90	80
5	YES	7	5	15	15	40	40

I certify that the above statement is correct.

Date, Signature of the candidate

I/We certify that the above statement is correct.

Date, Signature of the doctoral committee or at least of one of the supervisors

Manuscript 1

Assessment of Geo-Hazards in a Rapidly Changing Landscape: The Three Gorges Reservoir Region in China

Environmental Earth Sciences, published 74 (2015) 4939 – 4960

Alexander Strehmel[1)]*, Sarah Schönbrodt-Stitt[2)], Giovanni Buzzo[3)], Christian Dumperth[4)], Felix Stumpf[2)], Karsten Zimmermann[5)], Katrin Bieger[6)], Thorsten Behrens[2)], Karsten Schmidt[2)], Renneng Bi[4)], Joachim Rohn[4)], Joachim Hill[3)], Thomas Udelhoven[3)], Xiang Wei[7)], Xuezheng Shi[8)], Qinghua Cai[9)], Tong Jiang[10)], Nicola Fohrer[1)], Thomas Scholten[2)]

[1)]University of Kiel, Institute of Natural Resource Conservation, Department of Hydrology and Water Resources Management, Kiel, Germany,
[2)]University of Tübingen, Department of Geosciences, Chair of Soil Science and Geomorphology, Tübingen, Germany,
[3)]University of Trier, Department of Environmental Remote Sensing and Geo-informatics, Trier, Germany,
[4)]University Erlangen-Nuremberg, Geo-Center of Northern Bavaria, Chair of Applied Geology, Erlangen, Germany,
[5)]DMT GmbH & Co. KG, Exploration and Geosurvey, Essen, Germany,
[6)]Texas A&M AgriLife, Blackland Research and Extension Center, Temple, TX, USA,
[7)]China University of Geosciences, Department of Geotechnical Engineering and Engineering Geology, Wuhan, P. R. China,
[8)]Institute of Soil Science, Department for Soil Resources and Remote Sensing Application, Chinese Academy of Sciences, Nanjing, P. R. China,
[9)]Institute of Hydrobiology, Chinese Academy of Sciences, Wuhan, P.R. China, [10)]China Meteorological Administration, National Climate Center, Beijing, P.R. China

*Corresponding author. University of Kiel, Institute of Natural Resource Conservation, Department of Hydrology and Water Resources Management, Kiel, Germany, Olshausenstraße 75, Kiel, Germany Tel.: +49 431 880-1238, E-mail address: astrehmel@hydrology.uni-kiel.de (Alexander Strehmel).

Abstract

Large dam projects attract worldwide scientific attention due to their environmental impacts and socioeconomic consequences. One prominent example is the Three Gorges Dam (TGD) at the Yangtze River in China. Due to considerable resettlements, large-scale expansion of infrastructure and shifts in land use and management, the TGD project has irreversible impacts on the Upper Yangtze River Basin and strongly challenges the environmental conditions of this fast-developing region. Soil erosion and landslides are major geo-hazards. Knowing the extent and consequences of those geo-hazards for the landscape is essential to predict and evaluate their risk potential and allows for the development of strategies for a sustainable future land use in the Three Gorges Region (TGR). In this context, our research objectives are (i) to better understand the mechanisms of soil erosion, landslides, and diffuse matter fluxes in the TGR and their anthropogenic and environmental control factors, (ii) to predict their hazard potential by combining spatial and temporal, scenario-driven high-resolution modeling in combination with multi-scale earth observation data, and (iii) to develop a multi-component approach for the assessment and monitoring of geogene structures and processes. The paper describes the workflow of the project and introduces case studies, representing the current state of our research. It is shown, that land use changes as well as the water level fluctuations of the reservoir are the crucial drivers for the soil erosion and landslide hazard. Furthermore, we present a framework aiming at the establishment of a monitoring and measuring network as well as an early-warning system.

Keywords

Three Gorges Reservoir Region; land use change; soil erosion; landslides; diffuse matter inputs; integrated modeling

1 Introduction

1.1 Background

Large dam projects and hydropower engineering schemes are important for the industrial development of many national economies and are amongst the most extensive human impacts into landscapes. They exhibit significant and irreversible environmental and social impacts at different scales (Wang et al. 2014a). In China alone, approximately 45% of the world's large dams have been constructed (Ponseti and Lopéz-Pujol 2006; Lehner et al. 2011). The Three Gorges Dam (TGD) in central China is one of the most prominent dam sites worldwide and makes the Three Gorges Reservoir Region (TGR) one of the most dynamic large-scale anthropogenic influenced region in the world (Yang et al. 2005). The short period of dam construction and the huge dimensions of the reservoir with a length of 660 km and a surface area of 1,084 km² have left the region with long-term environmental consequences that are difficult to predict and appear in an unforeseeable magnitude (e.g., Ponseti and López-Pujol 2006; Stone 2008). These consequences are closely linked to large scale changes in land use and socioeconomic structures. The realization of this megaproject has required massive resettlements of more than 1.3 million people (McDonald et al. 2008). Approximately 632 km² of land has been flooded alongside the Yangtze River and its tributaries. Estimated 29,500 to 40,000 ha of this submerged land was classified as agricultural land on fertile valley soils (Ponseti and Lopéz-Pujol 2006; Gleick 2009). Associated land use changes mainly account for large-scale shifts in agriculture, a loss of natural forest and shrubland, and new land reclamation for agriculture and infrastructure construction to compensate the inundation of valuable land (Zhang et al. 2009). Arable land used for subsistence farming was largely converted to orange orchards as cash crops. They are intended to boost the farmer’s income after the resettlements and to reduce soil and nutrient losses to favor a suitable use of slopes (Meng et al. 2001; Shi et al. 2012). At the same time afforestation projects, such as the 'Grain for Green Program' have been started in the steepest-sloping regions of the TGR, where arable land is most erosion-prone (Liu and Wu 2010), leading to an increase in forested areas (Zhang et al. 2012; Bieger et al. 2015). From 2005 to 2008, more than 778 km of rural roads were constructed (SEPA 2006; MEP 2008; 2009). From 2007 to 2008, more than 2.75 million m² of new rural and urban houses were constructed for the resettled population (MEP 2008;

2009). In 2009, the area of arable land in the TGR was 209,647 ha which is about 7% higher than in 2008 and almost 9% higher than in 2007 (MEP 2009; 2010).

1.2 Soil Erosion, landslides, and matter transport as geo-hazards in the TGR

Soil erosion and landslides are geomorphic hazards that constitute powerful natural forces in landscape evolution, e.g., by redistributing sediments and associated essential plant nutrients (e.g., Densmore et al. 1998; Figueiredo et al. 1999). However, different studies consider the landscape's susceptibility to geo-hazards to be even higher when intense human changes meet unfavorable physio-geographic prerequisites (e.g., Stanley et al. 2006; Bai et al. 2013).

'Soil erosion' denotes the interactive process involving the detachment of individual soil particles from the soil mass, their breakdown, transport, and their redistribution and deposition with declining energy of the transport agents (e.g., Morgan 2005). Splash detachment and the transport downslope by overland flow constitute the main driving processes of water erosion (e.g., Morgan 2005; Ghahramani et al. 2011).

The term 'landslide' indicates the mass movement of soil, rock, and debris downslope, mainly aided by gravitational forces responding to the soils' shear stress exceeding its shear strength (Cruden and Varnes 1996; Dale et al. 2011). The global economic costs due to the occurrence of landslides are estimated to range between annually US$ 1.6 to 3.2 billion (Petley et al. 2005). With this, landslides belong to the most devastating natural disasters worldwide and constitute an enormous risk for life and property (e.g., Petley 2013).

With the start of the Yangtze River impoundment in 2003, land reclamation began to affect the steep sloping up-hill sites adjacent to the new river line. Even though farming has predominantly moved to terraces as important soil conservation measure (Schönbrodt-Stitt et al. 2013a), agricultural cultivation on steep slopes is still the most significant cause of water erosion (Lu and Higgitt 2000; Cui et al. 2011). Before dam construction and resettlements started, the total annual soil loss in the TGR was estimated to be 157 million tons (Shi et al. 1992). For post-construction times, estimations revealed an increase of total annual eroded soil of about 20%, accounting for 189 million tons in total (Wu et al. 2011).

The destabilization of slopes during the seasonal artificial water level fluctuation of 30 m at the dam, high cutting slopes, which have been formed during the infrastructure construction,

and the increasing number of landslides (e.g., Wu and Luo 2006; Ehret et al. 2010) still might accelerate the potential of hillslope erosion by dislodging soil and moving it downhill, followed by an enhanced use of alternative land that in turn can influence the occurrence of rainfall-triggered landslides (e.g., Glade 2003; Pimentel 2006). Landslides are a major problem in the TGR endangering ship traffic by water waves, but also infrastructure, new settlements, industrial zones, and agricultural areas (e.g., Kallen et al. 2006; Fourniadis et al. 2007). In 2002, a geological survey prior to the river impoundment based on ASTER imagery revealed the existence of about 2,500 large-scale landslides along the Yangtze River and its tributaries (Liu et al. 2004). Huang and Chen (2007), and Xiang et al. (2009) expect numerous newly triggered landslides and the reactivation of formerly inactive landslides due to the changing soil pore water pressure induced by the water level fluctuations. In 2012, Chinese media reported that the number of landslides is 70% higher than predicted (CRI 2012).

Landslides and soil erosion induce essential sediment and nutrient losses on steep slopes with subsequent matter inputs into the reservoir, encompassing sediment and sediment-bound fertilizers and pesticides (e.g., Luo et al. 2010; Tian et al. 2010). From 2005 to 2009, the use of chemical fertilizers and pesticides in the TGR ranged from 88,400 to 160,000 tons and from about 541 to 699 tons respectively (SEPA 2006; MEP 2010). Especially phosphorous is a limiting factor for algal growth in the Yangtze River and its tributaries (Liu et al. 2003). It usually attaches to the transported sediment and leads to eutrophication due to its accumulation in the reservoir triggered by low flow velocities (e.g., Ye et al. 2009; Bieger et al. 2015). The observed increase of algal blooms in the backwater areas of the tributaries clearly illustrates the seriousness of this geo-hazard and its consequences for the water quality (e.g., Wang et al. 2010; Holbach et al. 2012).

2 Research objectives and study workflow

Based on these considerations, a framework for the integrated analysis and assessment of the ecological and geological hazard of soil erosion, landslides, and diffuse matter inputs into the reservoir due to the Yangtze River impoundment and the associated land use changes was designed within the interdisciplinary Sino-German project 'YANGTZE-GEO' (Subklew et al. 2010). The research objectives of this project are:

(i) Improvement of the understanding of relevant factors and trigger mechanisms of soil erosion, landslides, and diffuse matter inputs in a heterogeneous and highly-dynamic region and their spatially explicit analysis and prediction by modeling,

(ii) Simulation of scenarios by integrating spatial and temporal information on geo-hazards and the land use to quantify the impacts of future land use changes for the development of suitable land use and land management strategies which can support the adjustment of the local agriculture to the new environmental conditions created by the construction of the TGD and

(iii) Development of a multi-component approach for the qualitative and quantitative assessment and monitoring of geogene structures and processes by geophysical and geodetic methods and creation of a data basis for an integrative early warning system (EWS) for landslides that will allow for a realistic estimation of the risk potential of landslides in settlement area in the TGR.

To investigate these research objectives we set up an integrated approach that combines multi-scale earth observation data with state-of-the-art techniques from soil science, geology, hydrology, geophysics, geodesy, and remote sensing (Figure 1).

Detailed process studies, data surveys, field experiments, and dynamic modeling will be conducted on three investigation scales from the plot to the landscape level. On the micro-scale, we aim at detailed, process-oriented soil erosion and landslide analysis and modeling as well as monitoring of landslide activity. On the meso-scale, the land use changes will be mapped based on remote sensing data. Moreover, eco-hydrological modeling of the pathways and quantities of diffuse inputs of sediment and phosphorous will be performed on this scale represented by hydrological catchments of tributaries to the Three Gorges Reservoir.

As the precise assessment of the geo-processes is time-consuming and access to terrain in the mountainous TGR is limited, remote sensing of data serves as a fast and available supplier of spatially explicit data as input into the integrated, scenario-driven modeling on the micro- and meso-scale. The results extracted from these analyses will constitute the prerequisite for the assessment of the extent of ecological and geological hazards of landslides, soil erosion, and diffuse matter inputs on the macro-scale (Figure 1).

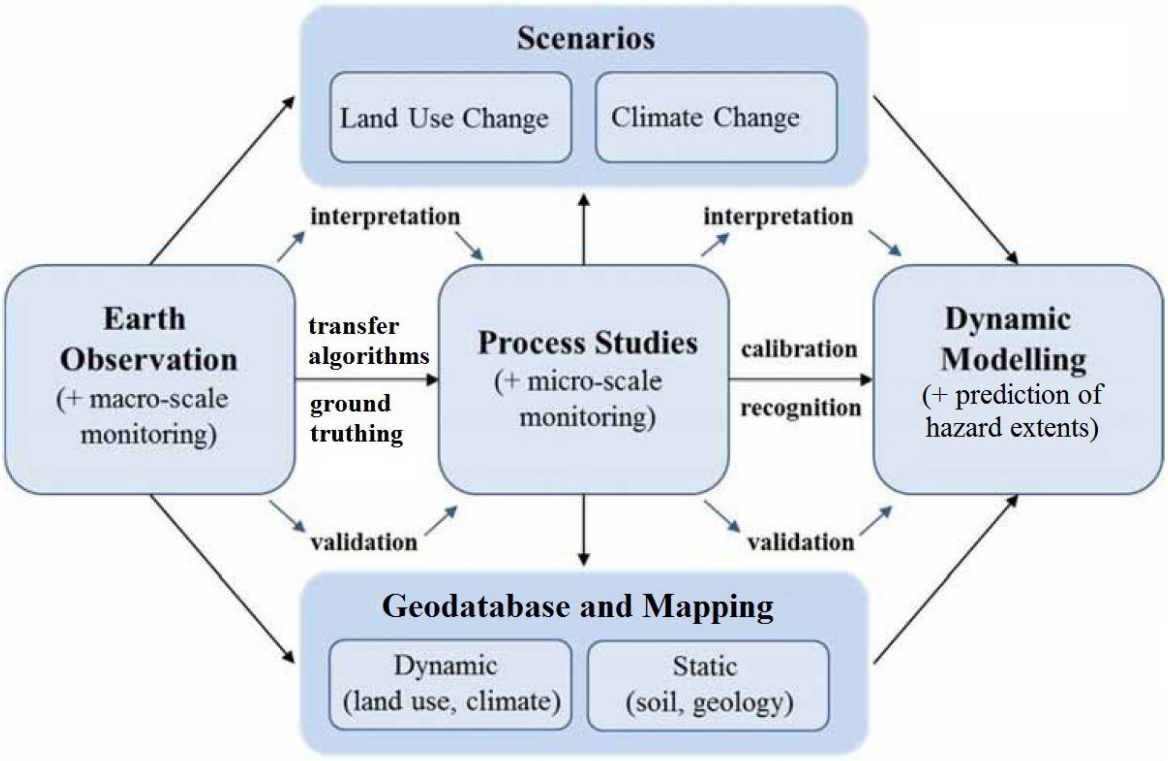

Figure 1: Workflow of the YANGTZE-GEO project.

From these research objectives, a plethora of specific research questions can be derived. In the present study we address three of them as they represent the current state of our research activities and refer to major geo-hazards in the TGR. These are:

(i) Which landscape features are drivers for soil erosion, and where are source areas of sediment and nutrient inputs in rivers located?

(ii) How can the temporal dynamics of soil loss be described, and what are the annual amounts of sediment entering the rivers and streams?

(iii) How do the water level fluctuations of the reservoir affect the stability of mass movements on its sloping banks?

We hypothesize that the land use pattern is the crucial driver for soil erosion, with highest soil loss rates in areas characterized by a high share of agricultural fields and lowest rates in

forested areas. Furthermore, the topography distinctly controls the spatial distribution for soil erosion. Additionally, it is expected, that highest sediment yields occur during the time of strong rainfall events, mainly in the summer months. We also hypothesize that the potential for the occurrence of landslides at the banks of the reservoir is highest during periods of decreasing and low reservoir water level.

3 Study sites

The study area on the macro-scale, respectively the landscape level is represented by the central TGR. It is defined by the area draining into the Three Gorges Reservoir, excluding the inflow of the Yangtze River itself (Figure 2). It has a total area of 35,080 km² and stretches westwards over about 330 km from the TGD near the city of Yichang in the east towards Chongqing in the west, where its terrain is characterized by plains and gently undulating hills. In the east, it exhibits steeper slopes and higher elevations, reaching a maximum of 3,106 m a.s.l. at Mount Shennongjia in the Xiangxi basin (Figure 2). The area is characterized by an anticline structure with a pre-Sinian crystalline basement complex cropping out sporadically from the Sinian-Jurassic and Triassic sedimentary cover (Wu et al. 2001; Ehret et al., 2010). The major soil groups are Cambisols, Alisols, and Luvisols (FAO/IIASA/ISRIC/ISSCAS/JRC 2012). The climate is humid subtropical with dry winters. The unimodal rainfall regime is governed by the East Asian Monsoon (Fu et al. 2008) with an average annual precipitation of 1,146 mm and an average annual temperature of 17.2 °C (CMA 2012). Land use is strongly linked to the terrain and characterized by rainfed cropland (30%) in its western, more gentle part and by forests and shrubland in the steep eastern part of the TGR (Bontemps et al. 2011).

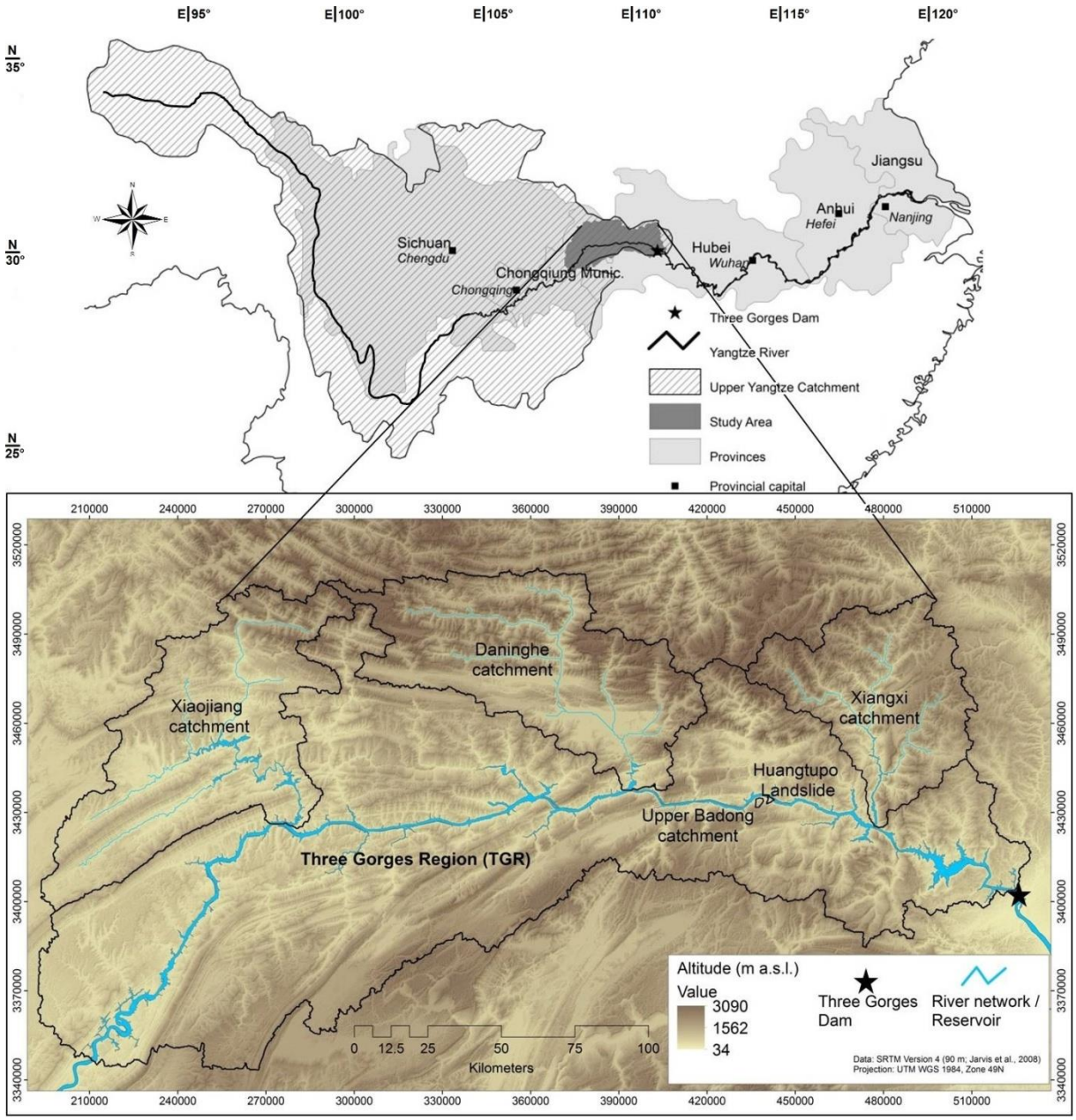

Figure 2: Geographical position of the study area in the Upper Yangtze River catchment in Central China in the provinces of Hubei and Chongqing, and range of altitude. The projection is UTM WGS 1984, Zone 49N. The DEM is derived from SRTM data (Jarvis et al., 2008).

Within the central TGR, further smaller study sites on the meso- and micro-scale are located (Figure 2). They are represented by the catchments of the rivers Xiangxi, Daninghe, and Xiaojiang (Table 1), which constitute first class tributaries to the Yangtze River. These

mountainous and steep sloping catchments with sizes ranging from approximately 3,200 to 5,300 km² exhibit average altitudes of about 700 to almost 1,240 m a.s.l. (Table 1).

The Xiangxi catchment constitutes the most closely studied area and main site of research. It is located in western Hubei Province. After a passage of approximately 100 km from the Shennongjia Mountains, the Xiangxi River joins the Yangtze River almost 40 km westward of the TGD. The backwater area of the Three Gorges Reservoir stretches approximately 35 km towards the central Xiangxi catchment and forms the Xiangxi Bay. The headwater zone of the Xiangxi catchment is strongly characterized by dense woodland with deciduous trees and conifers, shrubland, and grassland (Guo et al. 2000; Seeber et al. 2010). Scattered plots of arable land with dry land crop cultivation and rarely paddy rice exclusively occur alongside the river network with less steep sloping topography. Tea plantations are typical for the Northern temperate zone above 1,200 m a.s.l. (Wu et al. 2006; Seeber et al. 2010; Figure 3a). In the southern catchment, land use is strongly linked to the terrain with the Xiangxi Bay acting as a dividing line between predominantly agricultural cultivation on the western riverside and mainly forests and shrubs with scattered plots of cultivation on the eastern riverside (Seeber et al. 2010). Cash crop farming mixed with subsistence farming of lower productivity located on higher altitudes strongly characterizes the agriculture in the west (Schönbrodt-Stitt et al. 2013a). Typical agricultural use in the area of the Xiangxi Bay is orange cultivation as cash crop (Figure 3b), and arable land with rapeseed, wheat, soybean, and maize as main crops.

The Daninghe catchment is located in Chongqing municipality. Its topography is comparable to the one of the Xiangxi catchment (Table 1). However, it exhibits higher area percentages of rainfed cropland. The largest study area on the meso-scale is the Xiaojiang catchment that is also located in Chongqing municipality (Figure 2). Its land use is predominantly characterized by rainfed farmland, and hence, among the three catchments most strongly influenced by agricultural use (Table 1).

Table 1 Characterization of the project's study areas based on the geo-factors terrain, climate, geology, soil, and land use.

Geo-factor	TGD reservoir	Xiaojiang catchment	Daninghe catchment	Xiangxi catchment	Upper Badong catchment
Area (km²)	35,080	5,330	4,875	3,208.8	4.3
Average altitude (m. a.s.l.)	920	706	1,239	1,230	1,053
Average slope angle (°)	19	17	25	24	26
Average annual temperature (°C)	17.2	17	16.1	16.5	17.4
Average annual precipitation (mm)	1,146	1,218	1,163	1,004	1,089
Stratigraphy (GK 200)	Pre-cambrium - Jurassic	--	--	Pre-cambrium - Jurassic	Triassic - Jurassic
Soil types (WRB)	Cambisols - Alisols	Cambisols - Alisols	Cambisols - Alisols	Cambisols - Alisols	Cambisols - Alisols
Land Use (ESA, 2009)					
Rainfed cropland	29.8	33.4	23.1	14.9	--
Mosaic cropland (50-70%) / vegetation (grassland/shrubland/ forest) (20-50%)	6	10.5	3.8	2.4	--
Mosaic vegetation (grassland/ shrubland/forest) (50-70%) / crop-land (20-50%)	16.5	21.4	8.6	6.8	--
Closed to open (>15%) (broad-leaved or needleleaved, evergreen or deciduous) shrubland (<5m)	11.5	8.4	9.6	15.4	--
Closed (>40%) needleleaved ever-green forest (>5m)	10.4	4.4	11	24.6	--
Closed to open (>15%) mixed broadleaved and needleleaved forest (>5m)	15.8	12.2	10.8	31.5	--
Closed to open (>15%) broad-leaved evergreen or semi-deciduous forest (>5m)	8	8.4	8.6	3.1	--

The Upper Badong catchment (4.3 km²) close to Badong city on the southern bank of the Yangtze River constitutes a detailed study site on the micro-scale (Figure 3c). It is

characterized by scattered plots of agricultural land and resettlements in a largely wooded, steep sloping, and mountainous area (Table 1).

The Huangtupo landslide constitutes the smallest investigation unit and is located about 5 km east of the city center of Badong (Figures 3d and 4). It is exposed towards the riverside and has a length of 3,500 m and a width of 2,000 m. Its area is largely covered by buildings and densely populated. With a total volume of 69 million m^3, it is one of the four largest landslides in the TGR (Hu et al. 2012; Jian and Yang 2013). It was partially reactivated after the river impoundment and the deformation still continues (Hu et al. 2012; Jiang et al. 2012). Its sliding surface is located in a depth of 80 to 100 meters. Within the active sliding landslide body a rock laboratory was constructed by the Chinese government. This laboratory comprises a main tunnel of 900 meter length with smaller test tunnels and recesses in the tunnel walls going off on both sides, which allow for continuous monitoring of the movement activity and for sampling of the deep sliding soil (Jian and Yang 2013).

4 Material and methods

4.1 Geodatabase

The most suitable database to assess environmental variables covering the large mountainous areas is provided by space-borne remote sensing data. Hence, our basic data sources for the topography of the research area include the SRTM-DEM from the Shuttle Radar Topographic Mission in a spatial resolution of 90 m × 90 m (Jarvis et al. 2008).

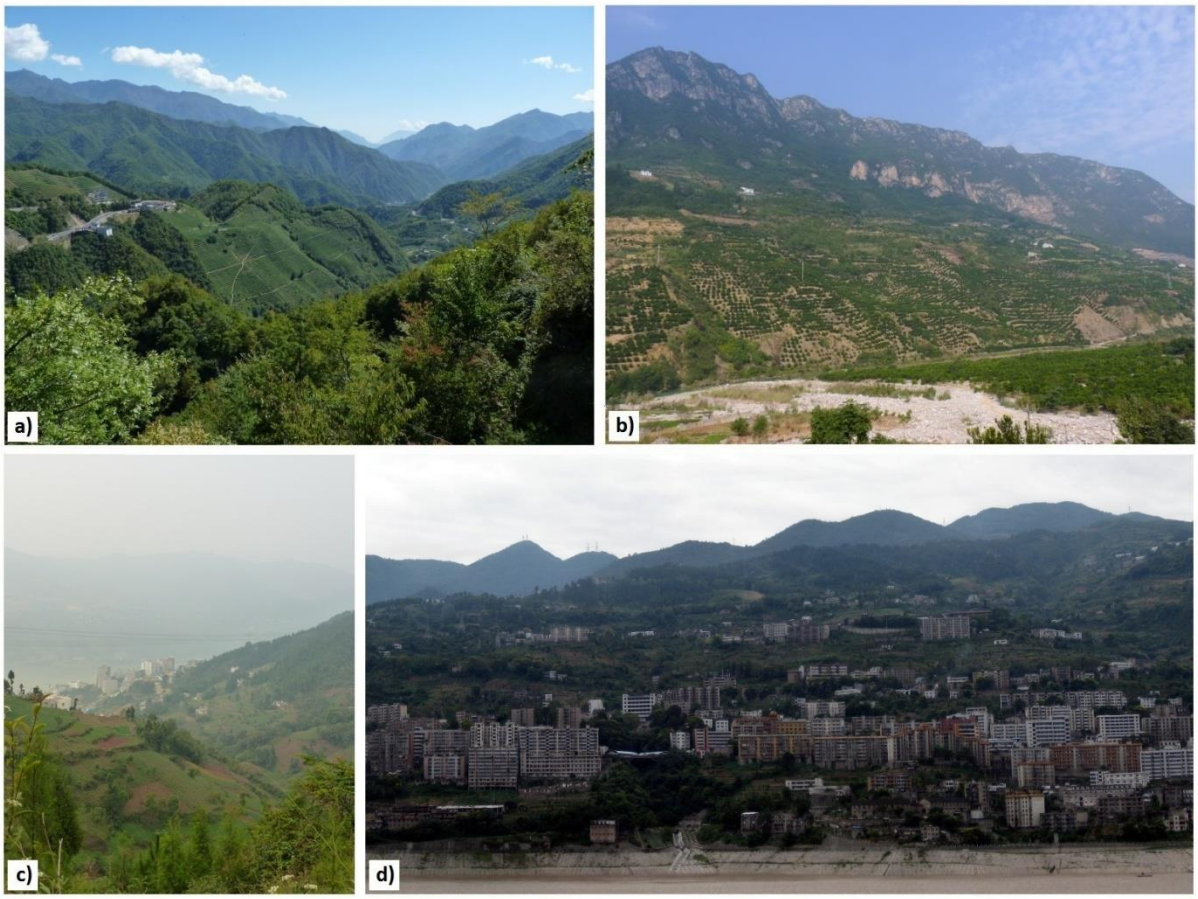

Figure 3: Scenes from the different investigation units; (a) orange orchards as a cash crop adjacent to the lower Xiangxi River (Photo: A. Strehmel), (b) tea plantation in the headwater zone of the Xiangxi catchment (Photo: A. Strehmel), (c) small-scale subsistence farming in the Upper Badong catchment (Photo: F. Stumpf), and (d) view on the Huangtupo landslide from the opposite bank of the Yangtze River. The buildings were left by their inhabitants due to the landslide hazard (Photo: C. Dumperth).

Land use information originate from a land use classification based on a Landsat-TM image from 2007 conducted for the Xiangxi catchment by Seeber et al. (2010). Thus, the land use classification refers to the time after the establishment of resettlement schemes and the completion of the dam construction.

Data on soil distribution and soil properties are based on available legacy data. Soil data originate from available soil maps and profile descriptions based on the Second National Soil

Survey in China (Shi et al. 2010). In the Xiangxi catchment, the soils were surveyed at a scale of 1:160,000 to 1:180,000.

Climate data with daily records are available from three stations within and around the Xiangxi catchment for the period from 1960 to 2009 and originate from the China Meteorological Administration (CMA 2012). Time series of discharge and sediment at a daily resolution from the gauging station Xingshan (31.25° N; 110.73° E) are available for the period from 2001 to 2008 (Changjiang Water Resources Commission 2014).

The occurrence of landslides and their properties in the area around Badong were surveyed in field campaigns. Soft rock samples were taken from the Huangtupo landslide body to adequately parameterize the landslide model.

4.2 Soil erosion modeling

In our study we focus on the application of the empirical Revised Universal Soil Loss Equation (RUSLE; e.g., Renard et al. 1997). The RUSLE can be applied to a high variety of field settings including disturbed and undisturbed lands (e.g., agricultural sites, forests, and constructions sites), and newly or established reclaimed land (Toy and Renard 1998). It involves six major factors that affect upland soil erosion in terms of sheet erosion by raindrop impact and overland flow as well as rill erosion (Toy and Renard 1998). Using a set of mathematical equations in a multiplicatory approach, the RUSLE is written as:

$$A = LS * R * K * C * P \qquad \text{(Eq. 1)}$$

where A is the potential long-term, average annual soil loss (t ha^{-1} a^{-1}), R is the rainfall erosivity (MJ mm ha^{-1} h^{-1} a^{-1}), LS is the combined factor from the terrain based factors slope length L (-) and slope steepness S (-), K is the soil erodibility (t ha h ha^{-1} MJ^{-1} mm^{-1}), C is the crop and management factor (-), and P is the support practice factor (-). A detailed description on the derivation of factors is provided by Wischmeier and Smith (1978) and Renard et al. (1997).

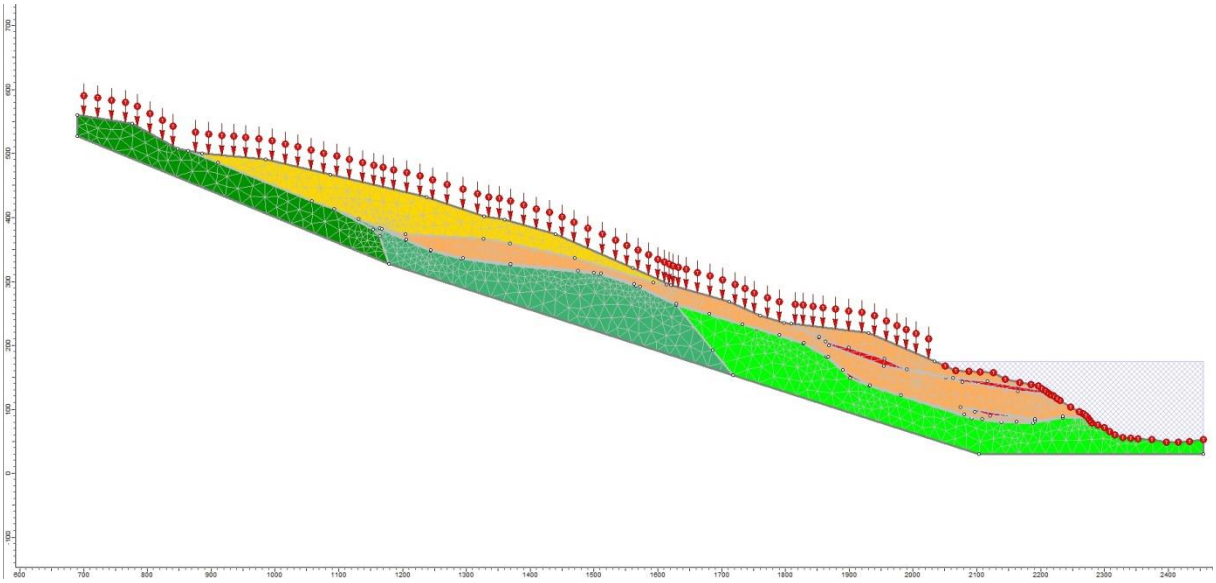

Figure 4: 2D finite element model created with 'Rocscience Slide'. Different rock/soil types are marked with different colors. Red arrows illustrate the boundary conditions of changing infiltration rates applied to each grid point.

The combined *LS* factor was derived from pre-processed separate DEM-based grids using the RUSLE approach according to Renard et al. (1997) that was also applied by Konz et al. (2009) for complex steep sloping areas using Eq. 2 and Eq. 3a-b:

$$L\,factor = \left(\frac{\lambda}{22.13}\right) * m \qquad \text{(Eq. 2)}$$

with

$$m = \frac{\beta}{1+\beta} \text{ and } \beta = \frac{\frac{\sin(\theta)}{0.0896}}{3*[\sin(\theta)]*0.8+0.56}$$

and

$$S\,factor = 0.063 + 10.461 * \sin(\theta) \qquad \text{(Eq. 3a)}$$

for slopes < 5.14,

$$S\,factor = 16.8 * \sin(\theta) - 0.5 \qquad \text{(Eq. 3b)}$$

for slopes ≥ 5.14.

where λ is the real slope length referring to the upstream flow length (m) based on the Monte-Carlo aggregation calculated separately for each land use class to simulate flow divergence reflecting a more natural spatial flow pattern in complex landscapes (e.g., Behrens et al. 2008), m is the slope length exponent (-), β is the susceptibility to rill erosion (-), and θ is the slope gradient (°) computed from a slope grid based on the steepest slope algorithm introduced by Tarboton (1997).

The rainfall erosivity factor *R* is a key factor in soil erosion modeling and crucially depends on rainfall characteristics (i.e., amount, intensity, duration). In the present study, *R* factor values are based on the long-term, average annual rainfall erosivity (1971-2000) that was approximated and spatially regionalized using elevation bands and considering the orographic precipitation pattern in the Xiangxi catchment (Schönbrodt-Stitt et al. 2013b). The *R* factor amounts to an average of 5,222 MJ mm ha^{-1} h^{-1} a^{-1}, generally showing enormous rainfall erosivity, and ranges from 1,986 MJ mm ha^{-1} h^{-1} a^{-1} at the outlet of the catchment to 7,547 MJ mm ha^{-1} h^{-1} a^{-1}at the highest altitude Mt. Shennongjia (Schönbrodt-Stitt et al. 2013b).

The *K* factor values were calculated for each soil mapping unit based on available profile descriptions according to Shirazi and Boersma (1984) using Eq. 4:

$$K = 7.594\,\{0.0017 + 0.044\exp\left[-\frac{1}{2}\left(\frac{\log(D_g)+1.675}{0.6987}\right)^2\right]\} \qquad \text{(Eq. 4)}$$

where *Dg* is the geometric average particle size (mm). This equation is based on the symmetric Gaussian distribution of geometrically average particle sizes (Song et al. 2005). Since the data on soil texture refer to the Russian classification system according to Kachinsky (1965) based on the ratio of particle sizes smaller than 0.01 mm, and further erosion-relevant sub-factors, such as organic matter content, soil structure class, and soil permeability class (Shi et al. 2012) were not provided, the function by Song et al. (2005) adequately approximates the *K* factor that was originally introduced by Wischmeier and Smith (1978). Generally, the soils show a moderate to low resistance to particle detachment and transport by water ranging from 0.30 to 0.44 t ha h ha^{-1} MJ^{-1} mm^{-1}. With 0.39 t ha h ha^{-1} MJ^{-1} mm^{-1}, the average soil erodibility *K* in the Xiangxi catchment is classified as high (Wischmeier and Smith 1978). The standard deviation is 0.05 t ha h ha^{-1} MJ^{-1} mm^{-1}.

The *C* factor was taken from literature, as no previous adequate data were available and monitoring on specific vegetation and crop parameters in the Xiangxi catchment was considered not practical and unfeasible (Schönbrodt et al. 2010). Those *C* factor values refer to the land use classes depicted for the study area by Seeber et al. (2010) and have been assigned to the respective land use pixel for the entire catchment area. These *C* factors are 0.46 for arable land according to Liu and Luo (2005) and 0.13 for orange orchard according to Shi et al. (2004). Both represent common seasonal crop rotations within one year for subtropical agriculture in the Wangjiaqiao and Taipingxi watersheds in the TGR close to the Xiangxi catchment. Thus, they are supposed to adequately represent the condition in the study area. The land use class 'woodland' is presented by a *C* factor value of 0.005 according to Liu and Luo (2005), grassland is presented by a *C* factor value of 0.2 according to Erencin (2000), and built-up land is presented by a *C* factor value of 0.08 according to Liu and Luo (2005). For the latter it is assumed that the settlements are associated with small-scale home gardening. Generally, the higher the *C* factor values, the lower the effect of the respective crop management systems and vegetation cover to protect the surface against soil erosion by water (Renard et al. 1997).

Since dry-stone walling bench terraces are common features in the TGR (Shi et al. 2004), farming terraces were considered in the modeling with the *P* factor assigned to all pixels presenting agricultural land (i.e., arable land and orange orchard) assuming it to be completely terraced. As no data on the spatial distribution and design of farming terraces were available, the *P* factor was set to a default of 0.55, a value which was suggested by Shi et al. (2004) and Liu and Luo (2005) for dry-stone walling bench terraces on agricultural land sloping between 20° and 25°.

The RUSLE was implemented into GIS-based modeling by integrating and manipulating available spatial grids on the above factors in a spatial resolution of 45 m × 45 m (Schönbrodt-Stitt et al. 2013a).

To assess the soil erosion hazard potential for the Xiangxi catchment, the grid-based estimates on the potential long-term average soil losses were further classified according to the Chinese Soil Erosion Rate Standard (Technological Standard of Soil and Water Conservation SD238-87) issued by the Ministry of Water Resources (e.g., Xu et al. 2009).

4.3 Modeling of diffuse sediment inputs to streams

The assessment of the spatial and temporal patterns of sediment inputs form diffuse landscape sources into the major tributaries of the Three Gorges Reservoir is an important prerequisite for the quantification of its non-point source pollution. This assessment is based on a modeling approach with the semi-distributed eco-hydrological Soil and Water Assessment Tool (SWAT; Arnold et al. 1998) for the Xiangxi catchment (c.f., Section 3).

The concept of the SWAT model consists of the division of a catchment in several sub-watersheds (subbasins), which contain a number of Hydrological Response Units (HRUs). The HRUs are generated by aggregating all areas with a distinct land use, soil type and slope class within a subbasin. Thus, every HRU is defined by a unique parameter set which drives its hydrological behavior. The water balance equation is employed for every HRU at every time step using Eq. 5 according to Neitsch et al. (2011):

$$SW_t = SW_0 + \sum_{i=1}^{t}(R_{day} - Q_{surf} - E_a - W_{seep} - Q_{gw}) \quad \text{(Eq. 5)}$$

where SW_t is the soil water content on day t (mm), SW_0 is the initial soil water content (mm), R_{day} is the precipitation amount on day i (mm), Q_{surf} is the amount of surface runoff on day i (mm), E_a is the amount of actual evapotranspiration on day i (mm), w_{seep} is the amount of percolation on day i (mm) and Q_{gw} is the amount of return flow on day i (mm). The components of the water balance equation are calculated on the base of different well-established hydrological concepts: For the surface runoff calculation the 'SCS' curve number approach (SCS 1972; Rallison and Miller 1981) is employed. The calculation of evapotranspiration is based on the Penman-Monteith equation (Penman 1948; Monteith 1965). The different hydrological components contribute to stream flow with different delay factors, and are forming stream flow after being summed up for every subbasin at every time step. From the outlet of every subbasin, the generated stream flow is then routed through the river network to the basin outlet.

The amount of sediment, which is generated in every HRU at every time step and that enters the stream is calculated by the Modified Universal Soil Loss Equation (MUSLE; Williams 1975), which was adapted for SWAT as follows:

$$sed = 11.8 * (Q_{surf} * Q_{peak} * area_{hru})^{0.56} * K * C * P * LS * CFRG \quad \text{(Eq. 6)}$$

where *sed* is the sediment amount in the HRU (t), Q_{surf} is the amount of surface runoff (mm), Q_{peak} is the peak runoff rate ($m^3 s^{-1}$), $area_{hru}$ is the HRU area (km^2), *K* is the USLE *K* factor (-), *C* is the USLE *C* factor (-), *P* is the USLE *P* factor (-), *LS* is the USLE *LS* factor (-) and CFRG is a coarse fragment factor (-). Contrary to the RUSLE, the MUSLE relies on a runoff-erosivity factor instead of the rainfall erosivity. The other factors correspond to the respective RUSLE factors (c.f., Section 4.2).

For the SWAT model setup, the SRTM-DEM, the available soil data set, and the land use map of 2007 by Seeber et al. (2010) were used to define the HRUs. As climate input, data from the three available stations were used. Since such a low density of stations is insufficient for a reliable reproduction of the spatial variability of climate characteristics in a mountainous catchment, elevation bands for precipitation and temperature were implemented into the model. This enables for an adjustment of low annual precipitation amounts and volume of discharge as recommended by Bieger et al. (2014) and Schönbrodt-Stitt et al. (2013b).

Table 2: Model evaluation statistics for the calibration and validation of the SWAT model for the Xiangxi catchment.

Evaluation parameter	Calibration	Validation
	Discharge (daily)	
Nash-Sutcliffe-Efficiency	0.65	0.75
PBIAS	23.14	19.16
	Sediment amount (monthly)	
Nash-Sutcliffe-Efficiency	0.65	0.24
PBIAS	39.26	-7.04

The SWAT model was calibrated for stream flow for the period from 2003 to 2005 with available discharge data of Xiangxi River, following the calibration parameter set as used in Bieger et al. (2014). Afterwards, the sediment calibration was conducted, addressing uncertainties in the estimation of the *K* factor values of the MUSLE, and the adjustment of two parameters affecting sediment transport in the river. Subsequently, the model was validated using observed stream flow and sediment time series data for the period from 2007

to 2008. The efficiency measures for calibration and validation can be seen in Table 2. Based on the quality criteria established by Moriasi et al. (2007) for SWAT model performance, the prediction accuracy of the SWAT model can be seen as sufficient, and the SWAT model setup can be used for further analyses. The output of the calibrated SWAT model was then extracted for the period from 1993 to 2002 to allow for a sufficient variability of inter-annual precipitation amounts and distributions.

4.4 Assessment of mass movement stability affected by water level fluctuations

Changing water levels due to river impoundments are a well-known problem concerning slope stability. According to a simplification of slope equilibrium (e.g., Ehret et al. 2009), the mechanical situation of slopes near reservoirs can be divided into four different states, which are characterized by different fluid flow conditions within the rock material, and associated changes in pore water pressure. Especially during the rapid drawdown of the reservoir water level, the stability of a slope can be changed significantly by increasing the downhill force (Ehret et al. 2009). To evaluate the extent of the changes in the slope equilibrium during different stages of water level, a modeling approach can be feasible using geological cross-sections obtained from intensive ground truth investigations. For this study, a two-dimensional model was set up for one cross-section of the Huangtupo landslide (Figure 4) for the identification of potential slip surfaces, and their corresponding factors of safety (FOS). The FOS is a measure for the stability of a hillslope and is frequently used in landslide and mass movement calculation. It is the ratio between the strength (resisting force) of a structure and its stress (disturbing forces). A FOS lower than 1 indicates a slope failure. Higher values can directly be related to the stability of the slope. In this study, two FOS calculation methods according to Bishop (1955) and Janbu (1973) were applied. To calculate the FOS values in the two-dimensional model, the mechanical characteristics of the different rock materials were parameterized based on the Mohr-Couloumb theory, which describes responses of rock materials to normal stress and shear stress (e.g., Prinz and Strauss 2006). The boundary conditions of the model were then adjusted to simulate changing reservoir water levels and changes in vertical infiltration rates (Figures 5 and 6).

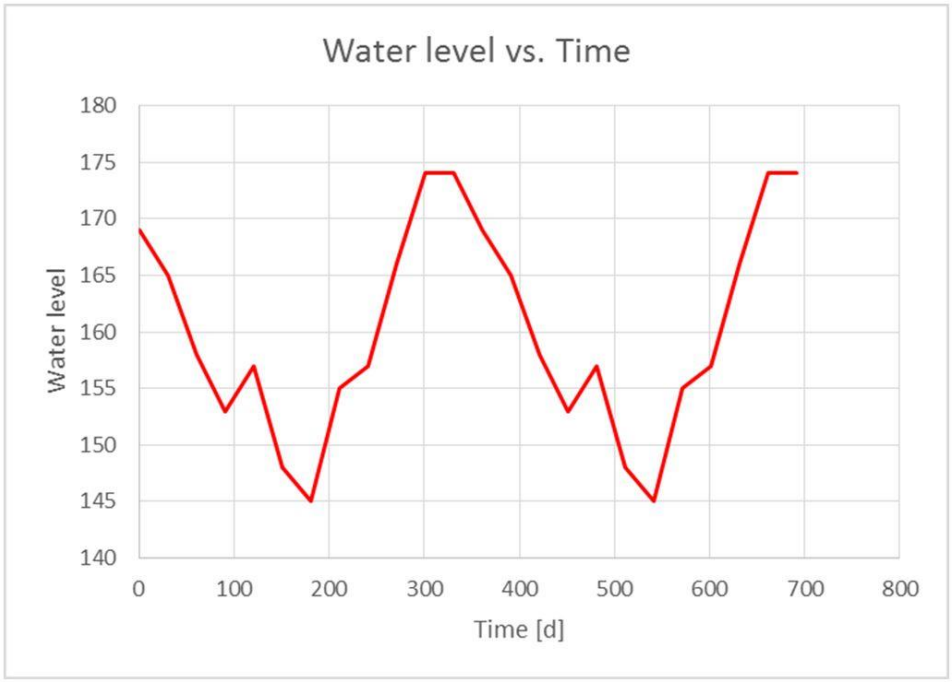

Figure 5: Impoundment levels of the Three Gorges Reservoir over two years.

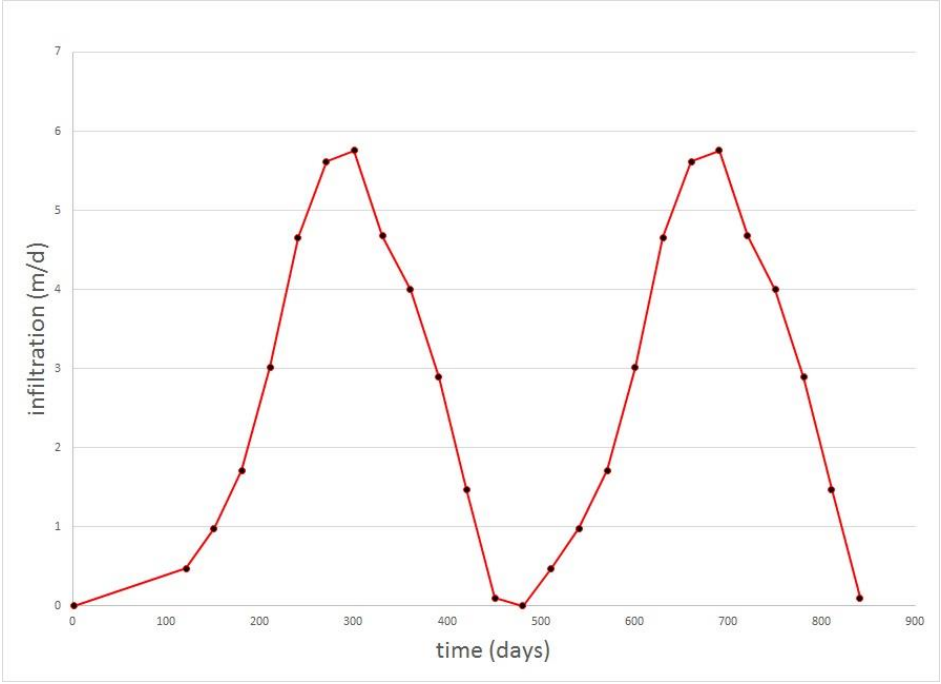

Figure 6: Course of vertical infiltration over two years.

5 Results and discussion

5.1 Potential long-term annual soil losses

Soil erosion modeling revealed an average annual soil loss potential of 52.3 t ha^{-1} a^{-1} for the entire Xiangxi catchment. Thus, the predicted soil loss is relatively consistent to analyses by Lu and Higgitt (2000) who measured an average long-term soil loss of 45 t ha^{-1} a^{-1} in Yiwanshui catchment in the western TGR. Based on findings by Lu and Higgitt (2000), Zhang (2008), and Wu et al. (2011) this soil loss amount is in range with other sites in China but slightly higher compared to average soil loss rates ranging from annually 30 to 40 t ha^{-1} for Asian countries as stated by Taddese (2001; quoted in Pimentel 2006).

Based on the Caesium-137 (^{137}Cs) technique, Quine et al. (1999) reported rates of actual soil loss by water erosion under comparable subtropical conditions for Yanting in Sichuan province in the Upper Yangtze River Basin of 51.5 t $ha^{-1}a^{-1}$ for farmland sloping with 6.2°. For the Xiangxi catchment, average soil loss on agriculturally used land (arable land and orange orchard) on slopes inclining between 1° and 7° is 52.8 t ha^{-1} a^{-1}. For farmland inclining with 6°, potential annual soil loss was estimated comparably higher with on average 75.5 t ha^{-1} a^{-1}. This slight offset is assumed to result from the fact that the study by Quine et al. (1999) was conducted for one single plot whilst our result comprises an area of approximately 11.2 km^2 of farmland inclining by 6°. Findings by Cui et al. (2011) according to which regional average soil loss rates on sloping farmland in the TGR range from approximately 45 to 67 t ha^{-1} a^{-1}, that are likely to exceed 10×10^3 t km^2 a^{-1} in places, further corroborate the reliability of our predictions, even though Cui et al. (2011) do not provide information on the physical settings of the studied slopes.

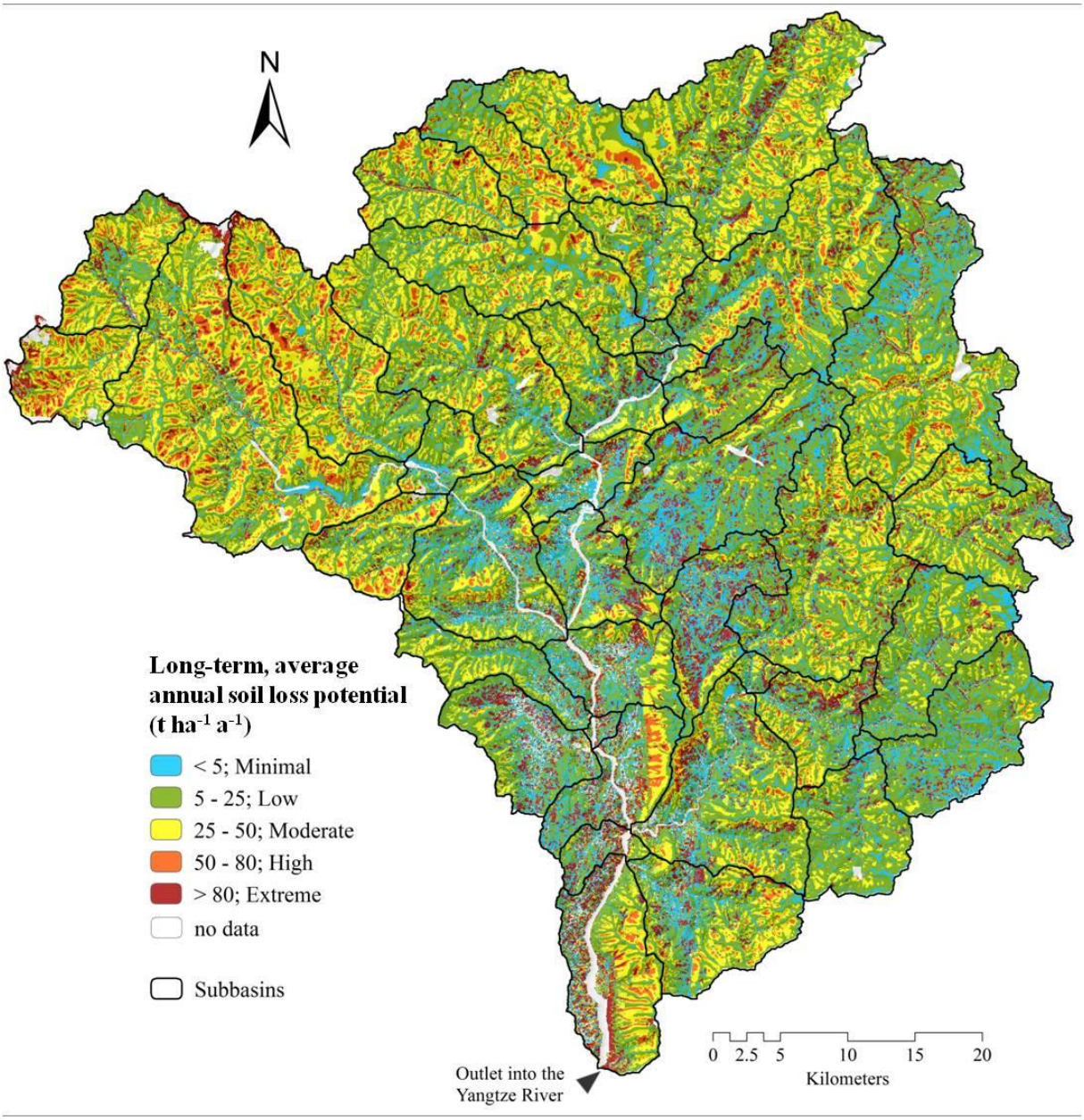

Figure 7: Estimations on the long-term, average annual soil loss potential (t ha^{-1}a^{-1}) by water erosion in the Xiangxi catchment classified according to the Technological Standard of Soil and Water Conservation SD238-87 . No data refers to pixel presenting bare rock and inland water that were not parameterized in soil erosion modeling.

By separating our results from the gridded soil loss prediction into the five classes formulated by the Chinese Soil Erosion Rate Standard (c.f., Section 4.2), we are able to show the spatial distribution of the soil erosion hazard potential: 15.9% (509.8 km²) and 43.6% (1,399.1 km²)

of the Xiangxi catchment exhibit minimal, respectively, low soil erosion potential (Figure 7). This is assumed to be an effect of the largely wooded headwater zone and hinterland with only scattered plots of land use as detected by Seeber et al. (2010). Approximately 38% of the total area of the Xiangxi catchment, accounting for an area size of 1,211.2 km², is affected by moderate to extreme soil erosion potential (Figure 7). We assume this to distinctly result from the agricultural use of steep sloping land mainly in the immediate surroundings of the Xiangxi Bay in the southern catchment and alongside the river network in the northern catchment (Figure 7). A statistical evaluation of the effect of the shares of different land use, slope and rainfall erosivity classes (Table 3) shows that the land use pattern mostly correlates with the soil losses within one subbasin. At the same time, slope steepness and rainfall erosivity are considered to contribute to the long-term annual soil loss potential to a relatively low to mainly moderate extent (Table 3). With this, the hypothesis that land use and slope patterns affect the soil losses strongly, can be confirmed for the land use pattern, but should be rejected for the influence of the slope class distribution.

Considering an average annual value of 10 t ha^{-1} as tolerable soil loss in the TGR (RWCSCB 1998; Shi et al. 2004) our results clearly underpin the seriousness of soil erosion in the Xiangxi catchment with approximately 68% (2,186 km²) of the total area above that boundary measure of soil loss. This is particularly relevant, as most of the sloped farmland is directly adjacent to the river network which implies a transport of eroded soil enriched with agro-chemicals from the fields into the streams.

5.2 Diffuse inputs of sediment in streams

The application of SWAT with the MUSLE approach for the calculation of sediment yield revealed an average annual sediment yield of 2.75 t ha^{-1} a^{-1}. This is considerably lower than the predicted soil loss estimates by the RUSLE. Field observations show that a large portion of eroded soil in the catchment is re-deposited on site and caught by flood channels across the slopes. The observed sediment amounts between 2001 and 2008 at the gauge of the Xiangxi catchment sum up to annually 26×10^4 tons, which translates into a sediment yield of about 1.2 t ha^{-1} a^{-1} for the catchment area of 1,850 km² upstream of the gauge. With this, the SWAT model overestimates average sediment loads in the rivers considerably. This is assumed to be

mainly caused by small reservoirs, which are present in the Xiangxi catchment, but were not implemented in the SWAT model.

*Table 3: Spearman's rank correlation coefficient (Spearman's R) and associated significance values (P uncorr) for the share of land use, slope, and rainfall erosivity classes in all subbasins with the long-term annual soil loss potential as calculated with the RUSLE. Land use classes originate from the land use classification for the Xiangxi catchment by Seeber et al. (2010). The slope classes are defined as used in the SWAT model of the Xiangxi catchment. The classes on rainfall erosivity R refer to Schönbrodt-Stitt (2013b). *= significance level of 10%; ** = significance level of 5%; ****= significance level of 1%*

Geo-factor	Spearman's	P uncorr
Land use class		
Forest	-0.573	0.00***
Built-Up	0.392	0.01***
Orange Orchard	0.324	0.04**
Grassland	-0.146	0.36
Arable Land	0.555	0.00***
Slope class		
0° - 15°	-0.135	0.4
15° - 25°	-0.143	0.37
25° - 35°	0.019	0.9
35° - 45°	0.193	0.23
> 45°	0.334	0.03**
Rainfall erosivity factor *R* (MJ mm ha-1 h-1 a-1)		
1986 - 2780	0.322	0.04**
2780 - 4369	0.218	0.17
4369 - 5958	-0.012	0.94
5958 - 7547	-0.276	0.08*

One reason for the distinct mismatch between soil loss potential estimated with the RUSLE and the SWAT results lies in the conceptual intention of the SWAT model's MUSLE to solely calculate the sediment yield contributing to stream flow. This will automatically reduce sediment amounts drastically during the calibration process to adjust them to the observed amounts in the river. The ratio between the sediment yield at the outlet and the gross soil loss of a catchment can be expressed with the sediment delivery ratio (SDR). Combining the

results of the RUSLE with the SWAT sediment calculations, a SDR of 0.05 can be determined for the Xiangxi catchment. According to Lenhart et al. (2005), the SDR value is governed by the geomorphology of the catchment, which determines whether concave or convex topographical features prevail, but also by the transport capacity of the streams. The SDR tends to decrease with an increase in catchment area (Ferro and Minacapilli 1995; Hua et al. 2006). A study by Shi et al. (2012) in a small catchment (17 km²) in the TGR found SDR values to vary between 0.29 and 0.48. The observed sediment yield at the gauge and the yield modeled with SWAT in the stream flow of the much larger Xiangxi catchment indicate a very low SDR value, but confirm that the SWAT model results after calibration are reliable. With this, and considering the validation results of SWAT (c.f., Section 4.3), it can be shown that SWAT is able to depict the sediment yields into the streams sufficiently well, and hence, can be used for an assessment of diffuse matter inputs in the TGR.

The comparison of long-term soil loss potential per subbasin as evaluated by the RUSLE (Figure 7) with the SWAT sediment yields per subbasin (Figures 7 and 8) shows that not only the annual amounts differ strongly, but also the spatial distribution of soil losses among subbasins. This behavior can again be explained with the conceptual differences between the MUSLE and the RUSLE. While the RUSLE results represent long-term annual rainfall erosivity (Schönbrodt-Stitt et al. 2013b), the MUSLE in SWAT is applied at every time step, and relies on surface runoff as driver (Williams 1975). The surface runoff calculation is based on the SCS curve number, which is a function of the land use and the antecedent moisture condition of the soil (SCS 1972). With this, the soil loss in SWAT is also a function of the temporal pattern of rainfall, and due to the connection with the antecedent moisture condition of the soil, especially linked to rainfall amounts of preceding time steps, soil evaporation rates, the lateral flow amount and the percolation rate to the groundwater (c.f., Section 4.3). The sediment yields in SWAT are also a result of stream flow and sediment calibrations towards observed time series values. While for the sediment calibration only the *K* factor of the MUSLE was slightly adjusted, the preceding calibration for stream flow can significantly alter sensitive hydrological parameters, and hence also distinctly affect the soil loss amounts. The comparison shows, that a careful parametrization of the RUSLE and the MUSLE are crucial in order to obtain reliable modeling results based on the intention and purpose of a study.

The season-wise comparison of sediment yield shows that highest sediment inputs to streams are observed in the summer months. Lowest amounts are observed in the winter months (Figure 8). In spring, the percentages of annual sediment yield are lower, than in autumn. This pattern is also reflected by the temporal distribution of precipitation amounts among seasons, which are also highest in summer, and lowest in winter. In spring and autumn, the percentages of annual precipitation are on average similar (Figure 8). While the sediment yields are closely linked to the inter-seasonal precipitation pattern, confirming the hypothesis that seasonal rainfall amounts strongly correlate with the sediment input to streams, the spatial distribution of sediment yields within one season, however, does not reflect the distribution of rainfall amounts. This corroborates the other hypothesis, that the land use distribution within one subbasin is the crucial driver for sediment yields into the streams (c.f., Section 5.1, Table 3) also for the use of the MUSLE.

5.3 Impact of water level changes on the stability of mass movements

While the upper parts of the Huangtupo landslide can be seen as relatively stable, the lower portion close to the banks of the Yangtze River is still moving. Therefore, the two-dimensional model calculations are focusing on this lower part. The model setup is based on the one introduced by Wang et al. (2014b). This approach has already been validated by comparing its results to long term GPS measurements. All relevant parameters can be seen from Table 4. Subsequently, the model was used to calculate the lowest rated potential slip surface during the rapid drawdown process. Its FOS according to Janbu (1973) is 1.216, which can be been seen as stable. Referring to Ehret et al. (2009) this corresponds with the third and fourth of the simplified mechanical conditions during water level changes of the reservoir. Before the drawdown, a high reservoir and steady groundwater level result in weaker flow forces in the slope, resulting in a high stability of the landslide mass (Ehret et al. 2009). During and after the drawdown, the downward flow within the landslide leads to a higher downhill force, and hence to an unstable slope condition (Ehret et al. 2009). All stability factors over one year (Figure 9) were calculated for a comparison to different impoundment levels. It can be seen that the course of the values of the FOS for the two different calculation methods over time is similar, which is an indication for reliable calculation results. The comparison with the course of the water level over time clearly shows, that the landslide mass is in its most unstable state during the drawdown phase,

confirming the hypothesis, that instabilities of banks are closely related to the drawdown of water levels. In this phase, a minor intervention into the force equilibrium of the landslide mass can change its mechanical situation and subsequently trigger a rapid movement. This finding is crucial for the development of an integrated EWS. With a more intensive focus on these periods in modeling, the effectiveness of an EWS can be substantially improved. At the same time the obtained results describe the overall situation for a simplified cross section of the mass movement. The use of a three-dimensional model applied to the whole landslide can improve the spatial resolution and extent of FOS predictions and can lead to higher prediction accuracy.

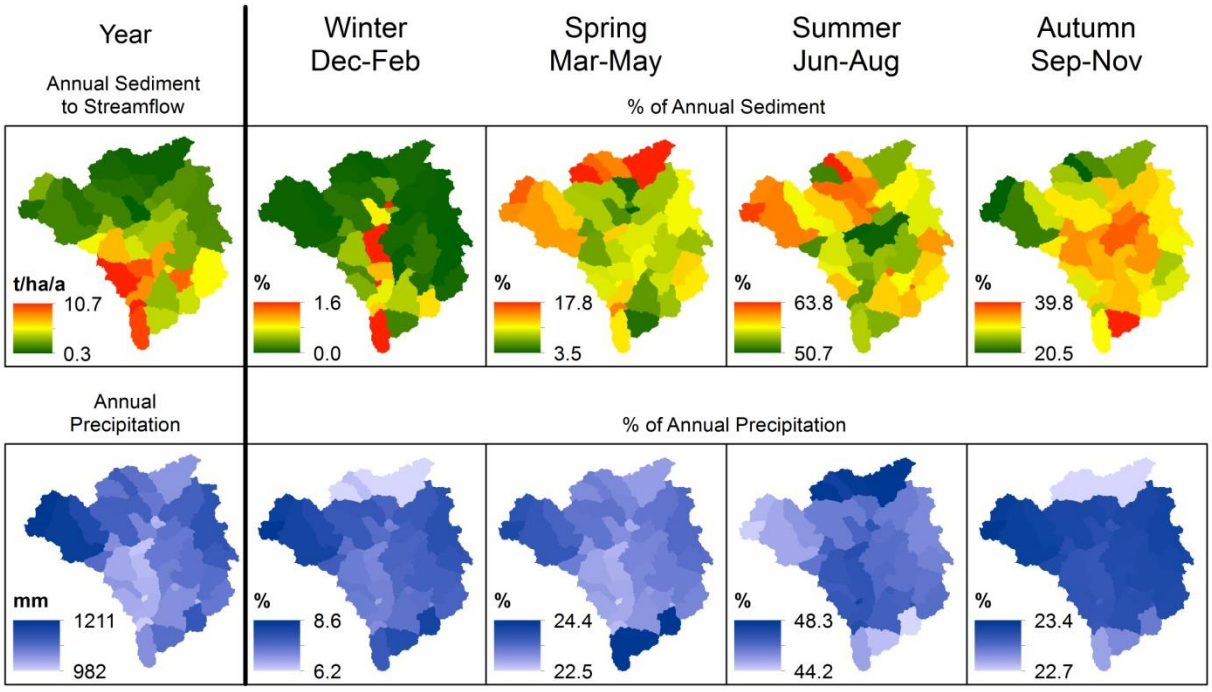

Figure 8: Spatial and temporal distribution of sediment yield and precipitation in the Xiangxi catchment, as estimated by the SWAT model.

6 Current research and perspectives on model improvements

Based on the results and experiences gained for the Xiangxi catchment and the Huangtupo landslide, we aim at the improvement of modeling accuracies to enhance the spatial and temporal resolution of erosion, landslide and eco-hydrological modeling and to improve the understanding of the impact of the TGD project on the environmental processes in the TGR. This inter alia includes the (i) improvement of model parameterization based on further specification and provision of reliable input data of higher spatial and temporal resolution and (ii) transfer of modeling frameworks onto the further study sites of Daninghe and Xiaojiang catchments that are also affected by the TGD project (Li et al 2009; Holbach et al 2012), and (iii) the development of an integrated EWS for a realistic estimation of the risk potential of landslides in settlement areas in the TGR.

Table 4: Hydrologic and mechanical parameters of the Huangtupo landslide based Wang et al. (2014) completed with own measurements. γ is the unity weight, c is the cohesion, ϕ is the friction angle, WC sat/res is the water content saturated/residual, KS is the hydraulic conductivity, E is the Young's modulus, and μ is the Poisson ratio.

Material	γ (kN/m³)	c (kPa)	ϕ (°)	WC sat (%)	WC res (%)	K_S (m/s)	E (MPa)	μ
Bed rock	26.3	420.8	48.5	0.2	0.1	1.16E-04	52,730	0.23
Dense soil and rock debris	21.5	31.4	23.3	0.26	0.1	8.10E-06	2,560	0.28
Loose soil and rock debris	20.2	29.4	20.8	0.26	0.1	2.20E-05	1,210	0.31

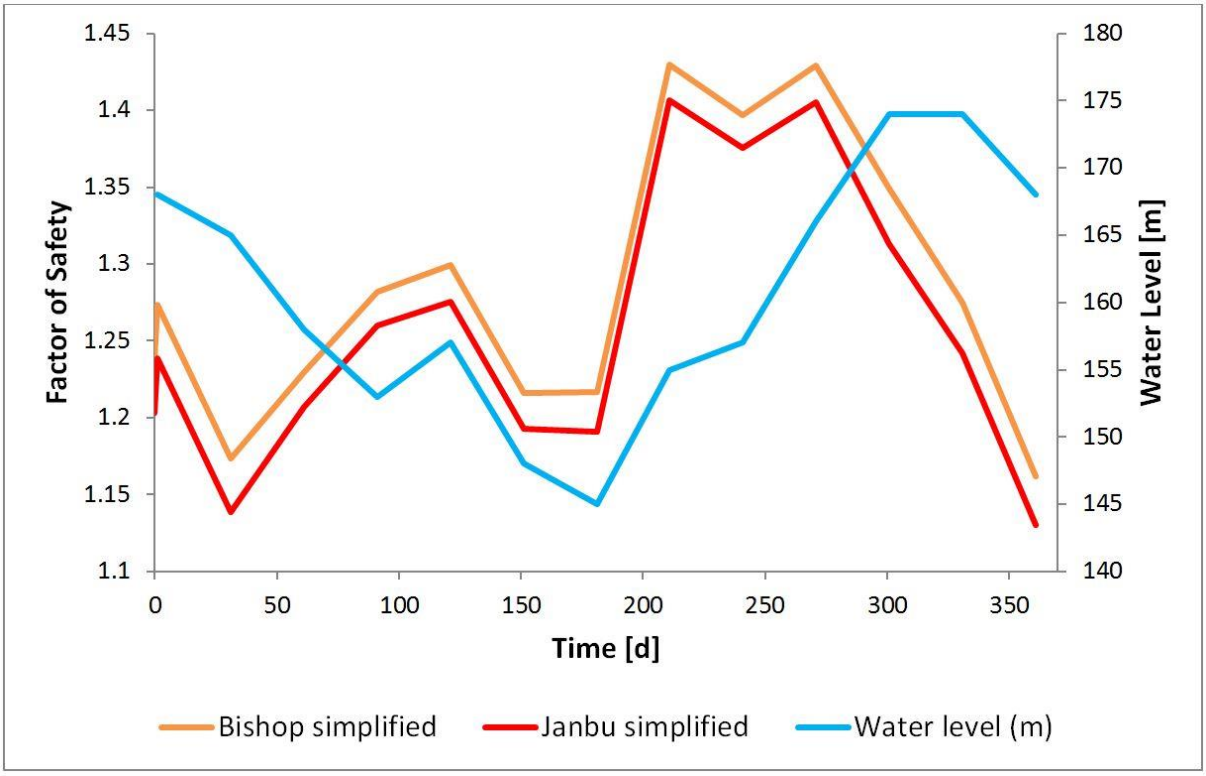

Figure 9: Factor of safety over time compared to the corresponding water level.

6.1. Improvement of the land use classification and analysis of land use change

The results of the soil loss estimation and the sediment yield results by SWAT show, that the land use is the crucial driver of soil loss and diffuse matter inputs into water bodies. Therefore, an accurate representation of current land use and land use changes as input for further analyses is of major importance. Thus, land use was mapped in the Upper Badong and Xiangxi catchments and in the headwater zones of the Daninghe and Xiaojiang catchments. A detailed classification of recent RapidEye imagery (RapidEye 2012) towards the representation of land use in the Xiangxi and Upper Badong catchments is ongoing. For the assessment of the regional-scale dam-induced land use change in the Xiangxi catchment, Landsat scenes were acquired from the USGS repository taking into account the period from 1985 onwards to cover also the phase before the start of the construction of the TGD. The collection is kept updated adding the new acquisitions from the current Landsat-8 mission. The present activities comprise the identification of the standard spectral features of land use types in annual time-series. This annual spectral variability is expected to provide a criterion

to separate land use types. Since the spatial coverage is often limited, a composition of scenes in a three to five years window is necessary.

Table 5: Average values of the User's accuracy (UA), producer's accuracy (PA), overall accuracy (OA), and Kappa (K). The values are derived from the classifications of the five RapidEye datasets covering the Xiangxi and Upper Badong catchments. σ is the respective standard deviation. Dry land includes spectral sub-classes of pixels covered by crops, bare soil or plastic mulch. Unused land identifies exposed rocks, quarries, and river beds.

Class (1st level)		PA	σ	UA	σ
1	Cropland	0.77	0.1	0.76	0.11
2	Woodland	0.91	0.09	0.9	0.07
3	Grassland	0.88	0.06	0.92	0.08
4	Built-up	0.64	0.17	0.59	0.13
5	Unused land	0.28	0.01	0.6	0.14
	OA	0.81	0.07		
	K	0.69	0.11		

Class (2nd level)		PA	σ	UA	σ
1.1	Dry land	0.77	0.09	0.74	0.12
1.2	Paddy land	0.5	0.06	0.63	0.01
2.1.1	Forest-broadleaf	0.72	0.2	0.64	0.07
2.1.2	Forest-conifer	0.72	0.16	0.76	0.1
2.2.1	Shrub	0.33	0.22	0.45	0.23
2.2.2	Woods	0.52		0.38	
2.2.3	Orange	0.7	0.11	0.61	0.04
2.2.4	Tea	0.34	0.24	0.55	0.21
3	Grassland	0.88	0.06	0.92	0.08
4	Built-up	0.64	0.17	0.59	0.13
5	Unused land	0.28	0.01	0.6	0.14
	OA	0.68	0.05		
	K	0.59	0.05		

The results of the RapidEye classifications are summarized in Table 5. Figure 10 displays the resulting land use maps for the Upper Badong catchment. For the land use classification, two classification levels were applied, a coarser level 1 and a finer level 2. These classification levels vary in terms of differentiation of land use classes and are subject to the spatial and

spectral resolutions of the sensors used. The first level classes retrieved higher classification accuracy (81%) than the second level classes (68%). The attempt to distinguish the ‘Cropland’ and ‘Woodland’ classes in greater detail based on the sole pixel reflectance was not completely satisfying. Nevertheless, misclassifications mostly occur among second level classes belonging to the same first level class. Broadleaf and conifer forest are generally not confused. 'Unused Land' retrieves low accuracies due to its confusion with 'Built-Up Land'. The separation between 'Dry Land' and 'Built-Up Land' is sometimes undermined by the widespread use of transparent plastic mulch for dry land agriculture.

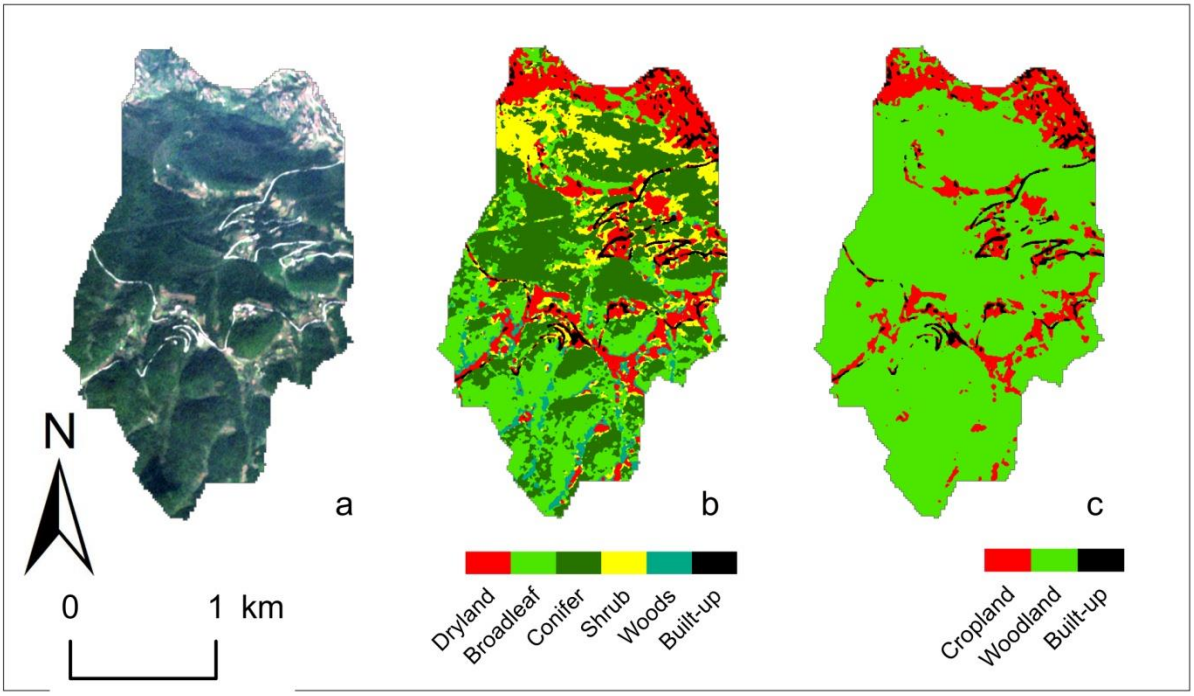

Figure 10: Land use classification in the Upper Badong catchment based on RapidEye data of 2012-09-28 (a). Second level (b) and first level classification (c).

These land use maps provide input data to related studies and establish a benchmark for the assessment of the land use in a diachronic perspective. The work achieved the definition of a methodology and got to emerge useful critical points which will be focused in the follow-up of the project. Critical points related to the use of RapidEye data will be overcome by adopting data of the Landsat missions. At the price of a lower spatial resolution, Landsat data

ensure the synchronous coverage of larger areas and the free access to a historical archive. The use of multi-temporal data is expected to improve the land use classification. By composing images selected in different periods of the year it is possible to take advantage of the seasonal variability of the land-cover for the correct discrimination of a richer set of land use classes.

6.2 Improvement of the accuracy of the soil erosion modeling

One major constraint originates from the assumption of equal soil conservation practice for the entire Xiangxi catchment (c.f., Section 4.2) that is likely to either overestimate or underestimate soil erosion locally. This is particularly important in areas with steep-sloping terrain where agriculture commonly takes place on terraced slopes inclining between 20° and 25°. However, taking into account a *P* factor of 0.55 for level bed terraces is likely to estimate soil erosion in an adequate range. This is true for 31% of the slopes in the Xiangxi catchment ranging from 20° to 25°, but needs to be improved for slopes with higher and lower inclinations. Since information on the spatial distribution and design of terraces is rare, Schönbrodt-Stitt et al. (2013a) developed the model framework of *TerraCE* for an analysis of the status of bench terraces and spatial analysis of the strength and direction of the effect of TGD on the terraced landscape in the Xiangxi catchment. The basic idea is that the occurrence of soil erosion strongly depends on the condition of the bench terraces, which is crucially influenced by the land use pattern and land accessibility (Figure 11). Hence, the *TerraCE* modeling approach will be further refined and linked to the RUSLE to avoid over- or underestimations of soil losses by adequately modifying the *P* factor according to the local-specific variability of the condition of bench terraces.

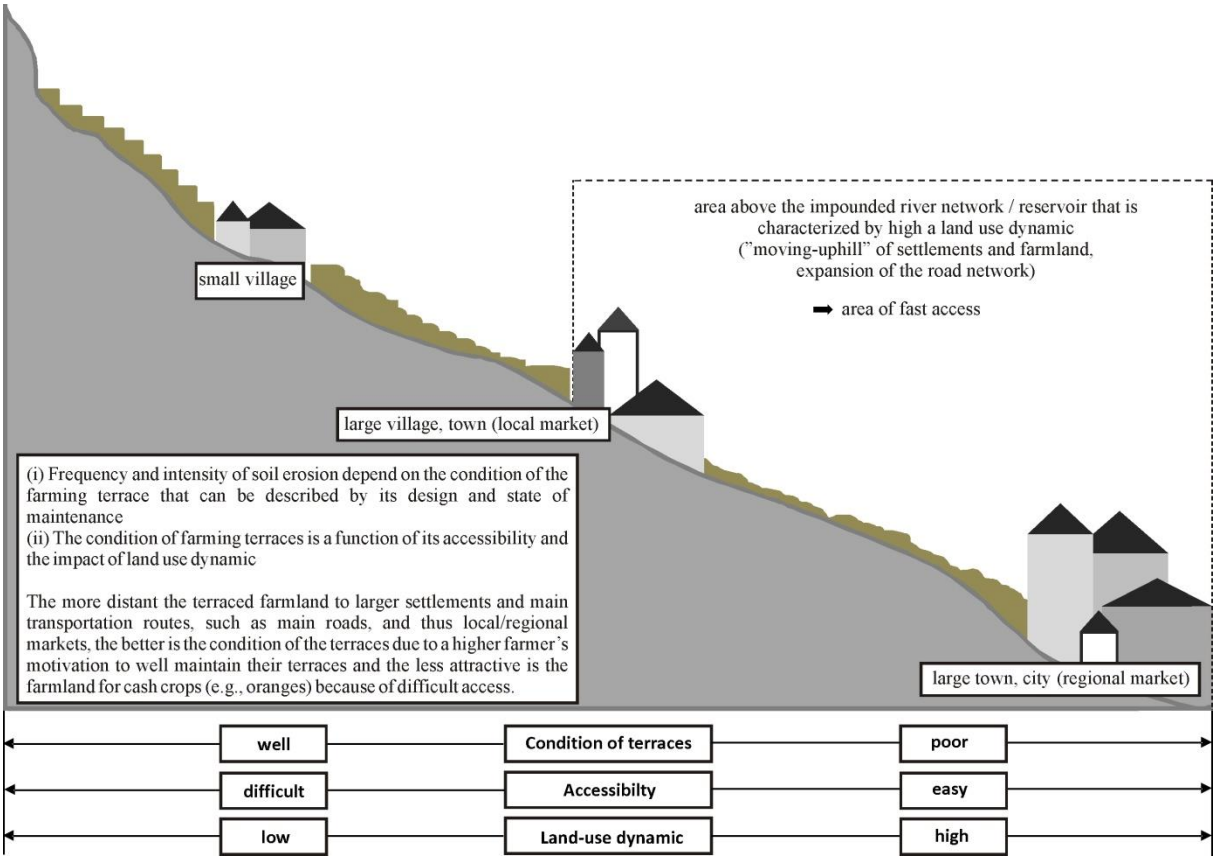

Figure 11: Schematic presentation of the conceptual TerraCE approach.

To improve the knowledge on the uncertainties of empirical soil erosion modeling and to validate our results, a further focus lies on the process-oriented soil erosion modeling in the Upper Badong catchment (c.f., Section 3). Due to a general mismatch between existing legacy data and data required for modeling and predicting soil erosion in the TGR (Zhu et al. 2013), further research will deal with the spatial regionalization of soil erosion factors to parameterize the detailed process-based soil erosion models, such as EROSION 3D (Schmidt et al. 1999) that is considered to adequately reveal the relevant erosion processes. Comprehensive field surveys were already conducted. Information on soil properties, such as soil texture, bulk density, soil organic sediment content, and carbonate, were collected based on appropriate state-of-the-art sampling designs and digital soil mapping approaches (McBratney et al. 2003; Scull et al. 2003), e.g., decision trees (Schmidt et al. 2008), neural networks (Behrens et al. 2005), and new hyperscale contextual terrain analysis approaches

(Behrens et al. 2014). Additional information on land use and vegetation properties will be gained from remote sensing (c.f., Section 6.1).

6.3 Improvement of the accuracy of modeling the sediment and nutrient inputs

The improvement of the existing SWAT model by implementing of spatially distributed land management patterns, the effect of bench terraces, and a dynamic representation of land use changes to account for the rapidly changing conditions in the catchment is in progress. During a recent mapping campaign, areas with different land use and land management patterns, and different conditions of bench terraces were identified in the Xiangxi catchment. A methodology is developed to include this information into SWAT. Thus, an improved SWAT model based on the RapidEye level 2 land use classification for the year 2012 will be set up for the Xiangxi catchment. In a final step, land use maps, which are generated for different years during the course of the construction phase of the TGD and the impoundment phase, will be utilized to move away from a purely static land use input into the SWAT model, but to depict the land use changes in the model framework dynamically. A previous land use change assessment (Bieger et al. 2015), including the development of land use change scenarios for the Xiangxi catchment, will be refined and extended by means of including improved model algorithms and a combination of geostatistical methods for the development of management strategies of soil and water resources in the TGR. The model framework will then be transferred onto the catchments of Daninghe and Xiaojiang Rivers.

6.4. Development of an early-warning system for landslides

The design of an EWS focuses on the assessment of boundary conditions under which the landslide exhibits a low stability and includes two components: (i) the geotechnical monitoring of the landslide at risk to assess its current and previous states and (ii) a model of the landslide body which is able to predict its future development and state. To address the latter, a three-dimensional model of the Huangtupo landslide will be set up using the numerical modeling software Flac3D (Itasca Consulting Group 2002). First model runs for changing input values were already tested to estimate the model's reliability and to enhance the prediction accuracy. Laboratory tests are in progress to obtain more accurate soil parameters aiming at an improvement of the model efficiency.

Figure 12: Analyzing the microseismic activity and slope movements; (a) geophones and (b) seismic recording hardware inside the rock laboratory at the Huangtupo landslide, (c) terrestrial radar interferometer installed at the Yangtze River, and (d) schematic presentation on the radar observation area of the Huangtupo landslide.

For the geotechnical monitoring of the Huangtupo landslide, dynamic seismic processes are recorded, which are caused by the rock mass in response to variable environmental condition

changes, e.g., changes in the reservoir water level or in infiltration rates. Additionally, several other dynamic influences are determined such as tele-seismic earthquakes or anthropogenic seismic noise in the study area around Badong and inside the rock laboratory at the Huangtupo landslide (Figures 12a-b; c.f., Section 3). Micro-seismic events can be triggered when instantaneous rupture occurs along geological boundaries (Amitrano et al. 2010). The continuous data recording of time series, such as rainfall and temperature, allows for a correlation of the observed seismic events and conditioning factors, and thus, for a direct mapping of subsurface changes to possible trigger mechanisms. For the micro-seismic monitoring of the landslide, a highly sensitive measurement network with borehole sensors was installed at the end of 2012 inside the rock laboratory (Figures 12a-b). It is currently operating and will run for two further years. These investigations will enable for a description of landslides by measuring micro-seismic events within the nanometer range, the localization of events, and the correlation of frequency and amplitude of landslides to indicate the changes of stress state in the rock mass. Recent developments in terrestrial radar interferometry show that this method is promising for monitoring of slope stability. State-of-the-art radar interferometers generally allow a contactless, continuous, and spatially dense measurement of movements, independent of the time of day and weather conditions (Strozzi et al. 2000; Werner et al. 2003; Farina 2010). Selected slope areas above the observation tunnel will be monitored to detect changes in the slope geometry in the millimeter range (Figures 12c-d). The measured changes are expected to give insights into the effects of water level changes in the geological structure of the slope and the possible hazard.

7 Conclusions

Our results show that the human influence in the TGR is able to foster the susceptibility of landscapes towards soil erosion and mass movements to considerably higher levels. Land use change is the decisive factor for an increase in soil erosion and diffuse matter inputs into streams and water bodies. Moreover, the annual water level fluctuations of the Three Gorges Reservoir threaten the stability of its sloping banks. Hence, the water level fluctuations and the land use change are concluded to act as the key drivers for the geo-hazards examined in this research framework.

At the same time, the intensity of land use change in the TGR and the management of land themselves are strongly linked to the landscape characteristics. Subsequently, the dam-induced impoundment of the Yangtze River and its main tributaries and the associated human interventions (e.g., resettlement, road construction, and conversion of land) are concluded to result in a complex system of natural and anthropogenic processes interacting with both soil erosion and mass movements, and thus, diffuse matter inputs into the reservoir. Moreover, under the massive human influence the effects of the controlling factors are supposed to subsume.

Our results from the Xiangxi catchment, therefore, are appropriate to describe and explain the situation in the TGR and, thus, improve the understanding of influencing factors and drivers for soil erosion and diffuse matter inputs. They furthermore show that our modeling approaches are suitable for the explicit analysis of the spatial and temporal dimension of these environmental processes, while the successful validation of the models is a step towards reliable predictions for future development paths of the landscape under land use change.

The implementation of an EWS for landslides in our project is based on the combination of a modeling and a monitoring approach. While the modeling approach is able to generate relevant information on the mechanical conditions within the landslide under changing boundary conditions, the monitoring can provide relevant input data for the modeling, as well as validation data. With the evaluation of monitoring data, the process understanding of landslide dynamics for the specific conditions of the TGR can be enhanced. With this, differences in monitoring and modeling results can be identified towards a better representation of processes in the model and an improved model parameterization. Therefore, the combination of monitoring and modeling is able to enhance the reliability of an EWS for landslides considerably.

Based on the consideration of complex interactions of effects of large hydrological projects on the large scale rather than addressing individual environmental consequences, our approach can serve as a basis for political decisions at a higher level, as the multitude of applied methods on different scales is able to approach system relations in an integrative way. Our results show that our methodological approach generates relevant information on the causes and trigger mechanisms for geo-hazards such as landslides, soil erosion, and matter fluxes for

both the small scale and the landscape scale for the whole TGR. Based on land use scenarios, long-term strategies for a reduction of the geo-hazard potential in the area can be developed.

Hence, this collaborative study can contribute to the understanding of large-scale anthropogenic impacts and thus, rapidly changing conditions in landscapes and their impact on geo-hazards. Such profound knowledge is urgently required to increase and maintain the environmental quality of soil and water resources and thus, sustainability of the densely populated TGR with a low environmental carrying capacity. Against this background and with a view on further large dam projects planned at the Yangtze River and worldwide, the project not only enables an enhanced understanding of the trigger mechanisms of geo-hazards and large-scale human impacts on landscapes, but also provides an important interface between research, national policy and planning as well as useful tools and approaches for projected environmental impact assessments.

8 Acknowledgements

The authors gratefully acknowledge funding from the German Ministry of Education and Research (BMBF, grant no. 03G0669 and 03G0827A) for the German-Sino research collaboration YANGTZE-GEO. We especially thank Dr. Xiang Wei and the students of the Department of Geotechnical Engineering and Engineering Geology of the China University of Geosciences in Wuhan for collaborating and supporting in the field campaigns. We further highly appreciate assistance in laboratory analyses that have been carried out at the Institute of Hydrobiology and the Changjiang River Scientific Research Institute in Wuhan.

9 References

Amitrano D, Arattano M, Chiarle M, Mortara G, Occiena C, Pirulli M, Scavia C (2010) Microseismic activity analysis for the study of rupture mechanisms in unstable rock masses. Nat Hazards Earth Syst 10:831-841.

Arnold JG, Srinivasan R, Muttiah RS, Williams JR (1998) Large-area hydrologic modeling and assessment: Part I. model development. J Am Water Res Ass JAWRA 34(1):73-89.

Bai S, Xu Q, Wang J, Zhou P (2013) Pre-conditioning factors and susceptibility assessments of Wenchuan Earthquake Landslide at the Zhouqu Segment of Bailongjiang Basin, China. Journal Geological Society of India 82:575-582.

Behrens T, Schmidt K, Ramirez-Lopez L, Gallant J, Zhu AX, Scholten T (2014) Hyper-scale digital soil mapping and soil formation analysis. Geoderma 213:578-588.

Behrens T, Schmidt K, Scholten T (2008) An approach to remove uncertainties in nominal environmental covariates and soil class maps. In: Hartmenink AE, McBratney A, Mendoca-Santos ML (eds) Digital soil mapping for regions and countries with sparse soil data infrastructure. Springer, New York, pp 213-224.

Behrens T, Förster H, Scholten T, Steinrücken U, Spies ED, Goldschmitt M (2005) Digital Soil mapping using artificial neural networks. J Plant Nutr Soil Sci 168:21-33.

Bieger K, Hörmann G, Fohrer N (2014) Simulation of streamflow and sediment with the SWAT model in a data scarce catchment in the Three Gorges Region, China. J Environ Qual 43:37-45.

Bieger K, Hörmann G, Fohrer N (2015) The impact of land use change in the Three Gorges Region (China) on water balance and sediment transport. Reg Environ Change 15(3):485-498.

Bishop AW (1955) The Use of the Slip Circle in the Stability Analysis of Slopes. Geotechnique 5:7-17

Bontemps S, Defourny P, van Bogaert E, Arino O, Kalogirou V, Perez JR (2011) GlobCover 2009 - products description and validation report. UCLouvain & ESA.

Changjiang Water Resources Commission (2014) Discharge Data. Gauge Xingshan, China.

CMA (2012) Climate data 1961-2009. Chinese Meteorological Administration, Beijing, China.

CRI (2012) Three Gorges Dam Set to Displace 100,000. China Radio International, China. Online at: http://english.cri.cn/6909/2012/04/18/2021s694058.htm (accessed 10-12-2013).

Cruden DM, Varnes DJ (1996) Landslide types and processes. In: Turner AK, Shuster RL (eds) Landslides: Investigation and Mitigation. Transp Res Board, Spec Rep 247:36-75.

Cui P, Ge Y, Lin Y (2011) Soil erosion and sediment control effects in the Three Gorges Reservoir Region, China. Journal of Resources and Ecology 2(4):289-297.

Dale F, Ritter DF, Kochel RC, Miller JR (2011) Process Geomorphology, 5th edn. Waveland Press, Long Grove, IL.

Densmore AL, Ellis MA, Anderson RS (1998) Landsliding and the evolution of normal-fault-bounded mountains. Journal of Geophysical Research 103(B7):15203-15219.

Ehret D, Rohn J, Dumperth C, Eckstein S, Ernstberger S, Otte K, Rudolph R, Wiedenmann J, Xiang W, Bi R (2010) Frequency ratio analysis of mass movements in the Xiangxi catchment, Three Gorges Reservoir area, China. J Earth Sci 21(6):824-834.

Ehret D, Rohn J, Xiang W (2009) Large water level changes and their influence on slope stability and reactivation of landslides in the Three Gorges Reservoir, P. R. China. In: Bayerisches Landesamt für Umwelt (eds.), 6th EUREGEO - European Congress on Regional Geoscientific Cartography and Information Systems 1:355-358.

Erencin Z (2000) C-factor mapping using remote sensing and GIS - a case study of Lom Sak/Lom Kao, Thailand. Dissertation, Institute of Geography of the University of Giessen and Soil Science Devision, International Institute for Aerospace Survey and Earth Sciences (ITC). Giessen, Germany.

FAO/IIASA/ISRIC/ISSCAS/JRC (2012) Harmonized World Soil Database (version 1.2). FAO, Rome, Italy and IIASA, Laxenburg, Austria.

Farina P (2010) IBIS-M: An innovative solution for slope monitoring within open-pit mines, IDS company and product presentation.

Ferro V, Minacapilli M (1995) Sediment delivery processes at basin scale. Hydrological Sciences Journal 40(6):703-717.

Figueiredo M, Augustin, CHRR, Fabris JD (1999) Mineralogy, size, morphology and porosity of aggregates and their relationship with soil susceptibility to water erosion. Hyperfine Interactions 122(1-2):177-184.

Fourniadis IG, Liu JG, Mason PJ, 2007. Landslide hazard assessment in the Three Gorges area, China, using ASTER imagery: Wushan-Badong. Geomorphology 84:126-144.

Fu C, Jiang Z, Guan Z, He J, Xu Z (2008) Regional Climate Studies of China, 1st edn. Springer, Berlin.

Ghahramani A, Yoshiharu I, Mudd SM (2011) Field experiments constraining the probability distribution of particle travel distance during natural rainstorms on different slope gradients. Earth Surf Proc Land 37:473-485.

Glade T (2003) Landslide occurrence as a response to land use change: a review of evidence from New Zealand. Catena 51:297-314.

Gleick PH (2009) Three Gorges Dam Project, Yangtze River, China, In: Gleick PH (ed) The world's water 2008 - 2009: the biennial report on freshwater resources. Island Press, Washington DC, pp 139-150.

Guo Z, Xiao X, Li D (2000) An assessment of ecosystem services: Water flow regulation and hydroelectric power production. Ecological Applications 10:925-936.

Holbach A, Wang L, Chen H, Hu W, Schleicher N, Zheng B, Norra S (2012) Water mass interaction in the confluence zone of the Daning River and the Yangtze River - a driving force for algal growth in the Three Gorges Reservoir. ESPR 10:7027-7037.

Hu X, Tang H, Li C, Sun R (2012) Stability of Huangtupo riverside slumping mass #II under water level fluctuation of Three Gorges Reservoir. J Earth Sci 23(3):326-334.

Hua L, Moran CJ, Prosser IP (2006) Modelling sediment delivery ratio over the Murray Darling Basin. Env Mod & Softw 21(9):1297-1308.

Huang BL, Chen XT (2007) Deformation failure mechanism of Baijiabao Landslide in Xiangxi River Valley. Chinese Journal of Geotechnical Engineering, 29(6):938-942. In Chinese.

Itasca Consulting Group (2002) FLAC3D - Fast Lagrangian Analysis of Continua in 3 Dimensions. Version 2.1 (computer program). Itasca Consulting Group, Minneapolis.

Janbu N (1973) Slope stability computations. In: Hischfied RC, Poulos SJ (eds) Embankment dam engineering. Wiley & Sons, New York, pp 49-86.

Jarvis A, Reuter HI, Nelson A, Guevara E (2008) Hole-filled seamless SRTM data V4, International Centre for Tropical Agriculture (CIAT), Palmira, Colombia.

Jian WX, Yang J (2013) Formation mechanism of no. 1 part slide of Huangtupo landslide in the Three Gorges Reservoir Area. J China Univ Geosci 38(3):625-631. In Chinese.

Jiang J, Xiang W, Rohn J, Schleier M (2012) Research on the water-rock (soil) interaction mechanism with a dynamic tracing method taking Huangtupo Riverside landslide in the Three Gorges Reservoir. Chinese Journal of Geotechnical Engineering 34(7):1209-1216.

Kachinsky NA (1965) Soil Physics, Part I. Kolos Publishers, Moscow, pp 132-139. In Russian.

Kallen D, Xiang W, Ehret D, Rohn J (2006) Landslides at Qingjiang river in the downstream area of Shuibuya dam site, China. J China Univ Geosci 17(2):158-162.

Konz N, Schaub M, Prasuhn V, Baenninger D, Alewell C (2009) Caesium-137-based erosion-rate determination of a steep mountainous region. Journal of Plant Nutrition and Soil Science 172:615-622.

Lehner B, Reidy-Liermann C, Revenga C, Vörösmarty C, Fekete B, Crouzet P, Döll P, Endejan M, Frenken K, Magome J, Nilsson C, Robertson JC, Rödel R, Sindorf N, Wisser D (2011) High resolution mapping of the world's reservoirs and dams for sustainable river flow management. Front Ecol Environ 9(9):494-502.

Lenhart T, Van Rompaey A, Steegen A, Fohrer N, Frede HG, Govers G (2005) Considering spatial distribution and deposition of sediment in lumped and semi-distributed models. Hydrological Processes 19(3):785-794.

Li Z, Guo J, Long M, Fang F, Sheng J, Zhou H (2009) Seasonal variation of nitrogen and phosphorus in Xiaojiang River - A tributary of the Three Gorges Reservoir. Frontiers of Environmental Science & Engineering in China 3:334-340.

Liu Y, Luo Z (2005) A study on estimation of the amount of soil erosion in small watershed based on GIS: a case study in the Three Gorge Area of China. Geoscience and Remote Sensing (IGARSS), IEEE International Geoscience and Remote Sensing Symposium 3:1859-1863.

Liu C, Wu B (2010) 'Grain for Green Programme' in China: policy making and implementation? Briefing Series - Issue 60, China Policy Institute, University of Nottingham, Nottingham, UK.

Liu JG, Mason PJ, Clerici N, Chen S, Davis A, Miao F, Deng H, Liang L (2004) Landslide hazard assessment in the Three Gorges Area of the Yangtze River using ASTER imagery: Zigui-Badong. Geomorphology 61:171-187.

Liu SM, Zhang J, Chen HT, Wu Y, Xiong H, Zhang ZF (2003) Nutrients in the Changjiang and its tributaries. Biogeochemistry 62:1-18.

Lu XX, Higgitt DL (2000) Estimating erosion rates on sloping agricultural land in the Yangtze Three Gorges, China, from caesium-137 measurements. Catena 39:33-51.

Luo G, Bu F, Xu X, Cao J, Shu W (2010) Seasonal variations of dissolved inorganic nutrients transported to the Linjiang Bay of the Three Gorges Reservoir, China. Environ Monit Assess 173:55-64.

McBratney AB, Mendoca-Santos ML, Minasny B (2003) On digital soil mapping. Geoderma 117:3-53.

McDonald B, Webber M, Duan Y (2008) Involuntary resettlement as an opportunity for development: the case of urban resettlers of the Three Gorges Project, China. J Refug Stud 21(1):82-102.

Meng QH, Fu BJ, Yang LZ (2001) Effects of land use on soil erosion and nutrient loss in the Three Gorges Reservoir Area, China. Soil Use Manage 17:288-291.

MEP (2010) Bulletin on the ecological and environmental monitoring results of the Three Gorges Project 2010. Ministry of Environmental Protection of the People's Republic of China. http://english.mep.gov.cn/down_load/Documents/201104/P020110407569629279171.pdf (accessed 05-28-2013).

MEP (2009) Bulletin on the ecological and environmental monitoring results of the Three Gorges Project 2009. Ministry of Environmental Protection of the People's Republic of China. http://english.mep.gov.cn/down_load/Documents/201002/P020100225376514651439.pdf (accessed 05-28-2013).

MEP (2008) Bulletin on the ecological and environmental monitoring results of the Three Gorges Project 2008. Ministry of Environmental Protection of the People's Republic of China. http://english.mep.gov.cn/down_load/Documents/200906/P020090629499562609329.pdf (accessed 05-28-2013).

Monteith L (1965) Evaporation and environment. Symposia of the Society for Experimental Biology 19:205-224.

Morgan RPC (2005) Soil erosion and conservation. 3rd edn. Blackwell Publishing, Oxford.

Moriasi DN, Arnold JG, Van Liew MW, Bingner RL, Harmel RD, Veith TL (2007) Model evaluation guidelines for systematic quantification of accuracy in watershed simulations. Trans. ASABE 50(3):885-900.

Neitsch SL, Arnold JG, Kiniry JR, Williams JR (2011) Soil and Water Assessment Tool Theoretical Documentation Version 2009, Texas Water Resources Institute Technical Report No. 406. Texas A&M University System, College Station, Texas, USA.

Penman HL (1948) Natural evaporation from open water, bare soil and grass. Proc Roy Soc London 194:120-145.

Petley DN (2013) Global losses from landslides associated with dams and reservoirs. Italian Journal of Engineering Geology and Environment 6:63-72.

Petley DN, Dunning SA, Rosser NJ (2005) The analysis of global landslide risk through the creation of a database of worldwide landslide fatalities. In: Hungr O, Fell R, Couture R, Eberhardt E (eds) Landslide risk management. Taylor & Francis, London, pp 367-374.

Pimentel D (2006) Soil erosion: a food and environmental threat. Environment Development and Sustainability 8:119-137.

Ponseti M, López-Pujol J (2006) The Three Gorges Dam project in China: history and consequences. ORIENTATS-2006, Revista HMiC No. IV, pp. 151-188.

Prinz H, Strauß R (2006) Abriss der Ingenieurgeologie. Spektrum Akademischer Verlag, Heidelberg. In German.

Quine TA, Walling DE, Chakela QK, Mandiringana OT, Zhang X (1999) Rates and patterns of tillage and water erosion on terraces and contour strips: evidence from caesium-137 measurements. Catena 36:115-142.

Rallison RE, Miller N (1981) Past, present and future SCS runoff procedure. In: Singh VP (ed) Rainfall runoff relationship. Water Resources Publication, Littleton, CO, pp. 353-364.

RapidEye (2012) Satellite Imagery Product Specifications - Version 4.1, http://www.rapideye.com/upload/RE_Product_Specifications_ENG.pdf (accessed: 07-31-2013)

Renard KG, Foster GR, Weesies GA, McCool DK, Yoder DC (1997) Predicting Soil Erosion by Water: A Guide to Conservation Planning with the Revised Universal Soil Loss Equation (RUSLE). U. S. Department of Agriculture, Agriculture Handbook No.703, United States Department of Agriculture, United States Government Printing Office, Washington, DC.

RWCSCB (1998) Technologic manual of soil and water conservation of Changjiang basin. Rural Water Conservancy and Soil Conservation Bureau, Changjiang River Water Resources Commission. Standards Press of China, Beijing. In Chinese.

Schmidt K, Behrens T, Scholten T (2008) Instance selection and classification tree analysis for large spatial datasets in digital soil mapping. Geoderma 146:138-146.

Schmidt J, Werner MV, Michael A (1999) Application of the EROSION3D model to the Catsop watershed, The Netherlands. Catena 37(3-4):449-456.

Schönbrodt-Stitt S, Behrens T, Schmidt K, Shi X, Scholten T (2013a) Degradation of cultivated bench terraces in the Three Gorges Area - field mapping and data mining. Ecol Indic 34:478-493.

Schönbrodt-Stitt S, Bosch A, Behrens T, Hartmann H, Shi X, Scholten T (2013b) Approximation and spatial regionalization of rainfall erosivity based on sparse data in a mountainous catchment at the Yangtze River in Central China. ESPR 10:6917-6933.

Schönbrodt S, Saumer P, Behrens T, Imbery S, Scholten T (2010) Assessing the USLE crop and management factor C for soil erosion modeling in a large mountainous watershed in Central China. J Earth Sci 21(6):835-845.

SCS (1972) Section 4: Hydrology. In: National Engineering Handbook. USDA Soil Conservation Service, Washington, DC.

Scull P, Franklin J, Chadwick OA, McArthur D (2003) Predictive soil mapping: a review. Prog Phys Geog 27:171-197.

Seeber C, Hartmann H, Xiang W, King L (2010) Land Use Change and Causes in the Xiangxi Catchment, Three Gorges Area, derived from Multispectral Data. J Earth Sci 21(6):846-855.

SEPA (2006) Bulletin on the ecological and environmental monitoring results of the Three Gorges Project 2006. State Environmental Protection Administration. http://english.mep.gov.cn/down_load/Documents/200712/P020071226462929438115.pdf (accessed 05-28-2013).

Shi ZH, Ai L, Fang NF, Zhu HD (2012) Modeling the impacts of integrated small watershed management on soil erosion and sediment delivery: a case study in the Three Gorges Area, China. J Hydrol 438-439:156-167.

Shi XZ, Yu DS, Xu SX, Warner ED, Wang HJ, Sun WX, Zhao YC, Gong ZT (2010) Cross-reference for relating Genetic Soil Classification of China with WRB at different scales. Geoderma 155:344-350.

Shi ZH, Cai CF, Ding SW, Wang TW, Chow TL (2004) Soil conservation planning at the small watershed level using RUSLE with GIS - A case study in the Three Gorges Area of China. Catena 55:33-48.

Shi DM, Yang YS, Lu XX (1992) Analysis of soil erosion characteristics and sediment sources for the Yangtze Three Gorges region. Int J Sediment Res 7(2):1-22.

Shirazi MA, Boersma L (1984) A unifying quantitative analysis of soil texture. Soil Science Society of America Journal 48:142-147.

Song Y, Liu L, Yan P, Cao T (2005) A review of soil erodibility in water and wind erosion research. Journal of Geographical Sciences 15(2):167-176.

Stanley JD, Jorstad TF, Goddio F (2006) Human impact on sediment mass movement and submergence of ancient sites in the two harbours of Alexandria, Egypt. Norwegian Journal of Geology 86:337-350

Stone R (2008) Three Gorges Dam: Into the Unknown. Science 321:628-321.

Strozzi T, Wegmüller U, Werner C, Wiesmann A (2000) Measurement of slow uniform surface displacement with mm/year accuracy. Proc. Geoscience and Remote Sensing Symposium 5:2239-2241.

Subklew G, Ulrich J, Fürst L, Höltkemeier A (2010) Environmental impacts of the Yangtze Three Gorges Project - an overview of the Chinese-German research cooperation. Journal of Earth Science 21(6):817-823.

Taddese G (2001) Land degradation: A challenge to Ethiopia. Environmental Management 27(6):815-824.

Tian Y, Huang Z, Xiao W (2010) Reductions in non-point pollution through different management practices for an agricultural watershed in the Three Gorges Reservoir Area. J Environ Sci 22:184-191.

Tarboton DG (1997) A new method for the determination of flow directions and upslope areas in grid digital elevation models. Water Resources Research 33:309-319.

Toy TJ, Renard KG (1998) Chapter 1 - Introduction. In: Toy TJ, Foster GR (eds) Guidelines for the use of the Revised Universal Soil Loss Equation (RUSLE) version 1.06 on mined land, construction sites, reclaimed land. Office of Surface Mining, Reclamation, and Enforcement, Denver, CO.

Wang P, Dong S, Lassoie JP (2014a) The large dam dilemma - an exploration of the impacts of hydro projects on people and the environment in China. Springer Science+Business Media, Dordrecht.

Wang J, Xiang W, Ning L (2014b) Landsliding triggered by reservoir operation: a general conceptual model with a case study at Three Gorges Reservoir. Acta Geotech. doi:10.1007/s11440-014-0315-2

Wang L, Cai Q, Zhang M, Tan L, Kong L (2010) Longitudinal patterns of phytoplankton distribution in a tributary bay under reservoir operation. Quatern Int 244:280-288.

Werner C, Wegmüller U, Strozzi T, Wiesmann A (2003) Interferometric point target analysis for deformation mapping. Proc. IGARSS 7:4362-4364.

Williams JR (1975) Sediment-yield prediction with universal equation using runoff energy factor. In: Present and prospective technology for predicting sediment yield and sources: Proceedings of the sediment yield workshop, USDA Sedimentation Lab, Oxford, MS, 28.-30.11.1972.

Wischmeier WH, Smith DD (1978) Predicting rainfall erosion losses - a guide to conservation planning. Agriculture Handbook No. 537, USDA, Washington, DC.

Wu C, Zhou Z, Xiao W, Wang P, Teng M, Huang Z (2011) Estimation of soil erosion in the Three Gorges Reservoir Area of China using RUSLE, remote sensing and GIS. J Food Agric Environ 9:728-734.

Wu YJ, King L, Jiang T (2006) Climatic vertical graduation and its use in the Xiangxi River catchment. In: Cai Q, Fohrer N (eds) Sino-German Workshop on Environmental Impacts of Large-scale Hydraulic Engineering - Programme and Abstracts, March 2006, Xingshan, China.

Wu SR, Shi L, Wang RJ, Tan CX, Hu DG, Mei YT, Xu RC (2001) Zonation of the landslide hazards in the forereservoir region of the Three Gorges Project on the Yangtze River. Eng Geol 59:51-58.

Wu F, Luo Y (2006) Cutting slope reinforcement in reconstructed migrants cities in the Three Gorges area of China. The Geological Society of London, IAEG2006 Paper No 714:1-5.

Xiang W, Jiang J, Cui D, Huang L (2009) Deformation mechanism of Dagouwan Landslide in Dongping Reservoir. J Earth Sci 34:855-860.

Xu Y, Peng J, Shao X (2009) Assessment of soil erosion using RUSLE and GIS: a case study of the Maotiao River watershed, Guizhou Province, China. Environmental Geology 56:1643-1652.

Yang SL, Zhang J, Zhu J, Smith JP, Dai SB, Gao A, Li P (2005) Impact of dams on Yangtze River sediment supply to the sea and delta intertidal wetland response. Journal of Geophysical Research 10(F03006). doi:10.1029/2004JF000271

Ye L, Cai Q, Liu R, Cao M (2009) The influence of topography and land use on water quality of Xiangxi River in Three Gorges Reservoir Region. Environ Geol 58:937-942.

Zhang L, Wu B, Zhu L, Wang P (2012) Patterns and driving forces of cropland changes in the Three Gorges Area, China. Reg Environ Change 12:765-776.

Zhang J, Liu Z, Sun X (2009) Changing landscape in the Three Gorges Reservoir Area of Yangtze River from 1977 to 2005: Land use/land cover, vegetation cover changes estimated using multi-source satellite data. Int J Appl Earth Obs 11:1403-1412.

Zhang B (2008) Impact on mountainous agricultural development in the Three Gorges Reservoir Area forced by migrants of the Three Gorges Project. Chinese Journal of Population, Resources and Environment 6:83-89.

Zhu AX, Wang P, Zhu T, Chen L, Cai Q, Liu H (2013) Modeling runoff and soil erosion in the Three-Gorge Reservoir drainage area of China using limited plot data. J Hydrol 492:163-175.

Manuscript 2

Incorporating Limited Field Operability and Legacy Soil Samples in a Hypercube Sampling Design for Digital Soil Mapping

Journal of Plant Nutrition and Soil Science, accepted with major revisions (2015)

Felix Stumpf*[1]), Karsten Schmidt[1]), Thorsten Behrens[1]), Sarah Schönbrodt-Stitt[1]), Giovanni Buzzo[2]), Christian Dumperth[3]), Alexandre Wadoux[1]), Wei Xiang[4]), Thomas Scholten[1])

[1]) University of Tübingen, Department of Geosciences, Chair of Soil Science and Geomorphology, Germany,
[2]) University of Trier, Department of Environmental Remote Sensing and Geoinformatics, Chair of Spatial and Environmental Planning, Germany,
[3]) University of Erlangen-Nuremberg, Department of Geology and Mineralogy, Chair of Applied Geology, Germany
[4]) China University of Geosciences Wuhan, Department of Geotechnical Engineering and Engineering Technology, China
*Corresponding author: University of Tübingen, Department of Geoscience, Chair of Soil Science and Geomorphology, Rümelinstraße 19-23, Tübingen, Germany, Phone: +49 7071 29 73942, e-mail: felix.stumpf@uni-tuebingen.de

Abstract

Calibration sampling designs play a key role for the accuracy of Digital Soil Mapping results. Most calibration sampling designs return spatially predefined sampling locations. Major challenges in practical applications are often limited field accessibility and the question on how to integrate legacy soil samples. Furthermore, temporal and monetary resources required for field sampling and laboratory analysis are often scarce. The focus of this study is therefore to develop and test a sampling approach that (i) compensates for limited field accessibility by providing alternative sampling locations and (ii) incorporates efficiency improvements by

integrating legacy samples and by deriving an optimized sample set size to spatially predict topsoil sand fractions. We used conditioned Latin Hypercube Sampling (cLHS) as sampling scheme that optimally covers the feature space of relevant covariates. We applied Random Forest regression to spatially predict topsoil sand fractions. Unlike other studies, we provided alternative target sites, while avoiding assumptions about previously sampled sites. Furthermore, our study site is small (4.2 km²), located in the Three Gorges Reservoir area in Central China. We evaluated the approach by comparing the proposed sampling design to the original cLHS design. We determined the optimal sample set size with n = 30. Same as for cLHS, the proposed design preserves the correlation between the covariates in the sample set compared to the entire covariates (r = 0.40 vs. r = 0.39) and shows a similar feature space coverage. Prediction accuracy for the target variables coarse sand (CS), medium sand (MS), and fine sand (FS) are high and only marginally decreased compared to an approach using all available samples (n = 60). Using an independent validation, CS exhibits R^2 = 0.63 (vs. R^2 = 0.67), MS shows R^2 = 0.71 (vs. R^2 = 0.80), and FS shows R^2 = 0.59 (vs. R^2 = 0.61) providing the validity of the proposed sampling approach.

Keywords

Digital Soil Mapping, field accessibility, legacy soil samples, sample set size, conditioned Latin Hypercube Sampling, Random Forest, Three Gorges Reservoir Area

1 Introduction

Digital Soil Mapping (DSM) couples soil information obtained at distinct spatial locations with statistically related, co-located, and area-covering predictor covariates. The coupling is accomplished by regression and classification approaches resulting in continuous or discrete maps of soil properties (*McBratney* et al., 2003; *Scull* et al., 2003; *McMillan*, 2008). DSM presents an established framework for soil mapping and has been successfully applied in numerous studies, addressing various soil properties, landscapes, and scales (*Florinsky* et al., 2002; *Behrens* et al., 2005; *Mora-Vallejo* et al., 2008; *Lacoste* et al., 2011; *Wang* et al., 2012;

Behrens et al., 2014; *de Carvalho Junior* et al., 2014; *Mansuy* et al., 2014; *Taghizadeh-Mehrjardi* et al., 2014; *Thomas* et al., 2015).

DSM predictor covariates can be derived inexpensively from existing data sets, such as digital elevation models (DEM) and remote sensing data (*McKenzie* and *Ryan*, 1999; *Gessler* et al., 2000; *Behrens* et al., 2010). By contrast, the field sampling of soil data remains a limiting factor in the DSM procedure. This is attributed to the requirements of statistical sampling designs, which need to be suited to local environmental conditions and pursue the incorporation of real field costs and budgetary constraints at the same time (*Lagacherie*, 2008; *Kidd* et al., 2015).

Primarily, the sampling design should reflect the variation of the target soil property in the study area (*Heuvelink* et al., 2007; *Brungard and Boettinger*, 2010). Suggested strategies infer sampling in the geographical space (*Brus* et al., 2006), in the feature space of soil covariates (*Minasny* and *McBratney*, 2006), or in a combination of both (*Dobermann* and *Simbahan*, 2007). Secondly, the sampling design should support field operability in terms of constrained accessibility, e.g., due to difficult terrain and restricted areas (*Kidd* et al., 2015). Few studies addressed this issue by excluding inaccessible areas in the process of sample site selection (e.g., *Roudier* et al., 2012; *Mulder* et al., 2013; *Clifford* et al., 2014) or by applying models from accessible areas to inaccessible areas based on similar environmental conditions (*Cambule* et al., 2013). Third, the sampling design should incorporate available legacy soil information to accommodate the demand on reducing high labor and monetary costs for sampling and laboratory analysis (*Lagacherie*, 2008). Existing soil maps served as covariates (*Mayr* and *Palmer*, 2007) and in disaggregated form as a source to calibrate prediction models (*Naumann* and *Thompson*, 2014). Legacy soil profiles provide local information on soil properties and served as input for statistical model procedures (*Carré* and *Girard*, 2002; *Hengl* et al., 2004). Yet, a spatial mismatch of statistically predefined target sites, a lack in harmonization with the target soil property, and different spatial resolutions, formats and objectives remain problems when incorporating legacy data into sampling designs (*Carré* et al., 2007; *Krol*, 2008; *Sulaeman* et al., 2013). A further possibility to increase the efficiency in soil data acquisition comprises an optimized sample set size. Few studies addressed this issue by comparing model results based on different calibration set sizes (*Brungard* and *Boettinger*, 2010; *Ramirez-Lopez* et al., 2014; *Schmidt* et al., 2014).

As a consequence of the described restriction and limitations, most sampling designs solely focus on reflecting the variation of the target soil property. They often do not consider operability and efficiency improvements in terms of accessibility, the integrative use of legacy samples and optimization of the sample set size (*Lagacherie*, 2008; *Cambule* et al., 2013). Thus, advances in surveying soil data for DSM depend on comprehensively addressing the statistical, operational, and efficiency potentials of sampling designs. Such comprehensive DSM sampling designs have been addressed by few studies (e.g., *Roudier* et al., 2012; *Mulder* et al., 2013; *Clifford* et al., 2014) that used conditioned Latin Hypercube Sampling (cLHS). Generally, the cLHS method presents a stratified random sampling design that provides maximal feature space stratification with a reduced number of samples (*Minasny* and *McBratney*, 2006). *Roudier* et al. (2012) and *Mulder* et al. (2013) implemented data on travelling costs, which were derived from terrain and land use parameters, into the cLHS algorithm to account for limited field accessibility. Similar to these approaches, thus, aiming to preserve a maximal stratification of the samples in the feature space while compensating limited field accessibility, *Clifford* et al. (2014) proposed 'flexible LHS'. The method additionally produces an ordered list of alternative target sites by analyzing the relation of each location in a defined neighborhood to the initial target site, in case the latter turns out to be inaccessible during field sampling.

The above approaches outline improvements concerning the applicability of hypercube sampling designs, mainly by addressing limited field accessibility. However, further improvements should combine these advances with the integrative use of legacy samples and an optimized sample set size. Thus, the objective of our study is to develop a comprehensive DSM sampling design. We aim to generate a sample set, which (i) covers the feature space of relevant covariates, (ii) compensates limited field accessibility, and (iii) provides efficiency improvements in terms of integrating adequate legacy samples and optimizing the sample set size. Within the framework of the joint Sino-German project 'YANGTZE GEO - Land use change, soil erosion, mass movements and matter fluxes along the Yangtze river, Three Gorges Reservoir area' (*Schönbrodt-Stitt* et al., 2013; *Strehmel* et al., 2015), we tested the sampling approach in a small hydrological catchment in the Three Gorges Reservoir area (TGRA) at the Yangtze River in China. Random Forest regression (*Breiman*, 2001) was applied to predict topsoil sand fractions to be used as sensitive input data in process-based erosion modeling.

2 Material and Methods

2.1 Study site and geodatabase

Our study site is a drainage basin of a size of 4.2 km², referred to as Upper Badong catchment (31°1′24″N, 110°20′35″E). It is located at the middle reaches of the Yangtze River approximately 74 km upstream the Three Gorges Dam (TGD) in the western Hubei province in Central China (*Strehmel* et al., 2015). With 72% the vast majority of the Upper Badong catchment is exposed to the north. The altitude ranges from 469 m to 1,483 m a.s.l. with an average altitude of 1,053 m a.s.l. Slope angles range from 0 to 53° with an average slope angle of 26°. The land use in the study area is dominated by woodland (81%) with scattered plots of cropland (15%) and small farm buildings (4%). The cropland area with mainly soybean, corn, and cabbage as agricultural products is located in the northern, lower part of the Upper Badong catchment. Woodland is predominant in the steep sloping southern catchment area.

A pool of environmental covariates served as geodatabase from which covariates were selected for the sampling design and for Random Forest regression analysis. Continuous covariates were derived by terrain analysis based on a DEM with cell sizes of 25 m x 25 m (Table 1) using *SAGA GIS* (2011). Land use was mapped and classified into six classes referring to ‘Cropland’, ‘Broadleaf’, ‘Conifer’, ‘Shrub’, ‘Woodland’ and ‘Built-up’ and included as categorial covariate.

Table 1: Environmental covariates with summary statistics.

Covariate	Unit	Minimum	Maximum	Average	Standard deviation
Altitude	m a.s.l.	469	1483	1054	255
Northing	-	1.42E-02	1.75E-02	1.62E-02	1.10E-03
Easting	-	0	1.30E-02	4.98E-03	3.74E-03
Wetness Index (SWI)	-	0	14.8	5.9	1.8
Slope angle	degree	0	53.2	26.4	6.9
Slope angle, maximum	degree	0	0.72	0.42	0.13
Slope length	m	0	2854	184	293
Catchment area	m^2 (log)	6.43	15.17	8.66	1.4
Plane curvature	m^{-1}	-1.03E-02	1.09E-02	-4.28E-05	2.82E-03
Profile curvature	m^{-1}	-1.09E-02	1.04E-02	-1.90E-04	2.30E-03
Combined curvature	m^{-1}	-8.80E-01	8.10E-01	-4.90E-03	1.54E-01
Flow accumulation	pixels (log)	2.8	6.1	3.9	0.56
Overland flow distance	m	0	377	91.9	75.1
Vertical flow distance	m	0	135	29.8	26.1
Horizontal flow distance	m (log)	0	2.6	1.5	0.88
Altitude above channel (AAC)	m	0	307	92	62
Terrain ruggedness	-	0.18	17.2	8.4	2.4
Mass balance index	-	-0.79	2.04	0.13	0.52
Convergence index	-	0	28.8	8.7	3.8
Position index	m	-26.9	35.7	0.25	7.2
Protection index	-	0	0.14	0.07	0.02

In October 2012, 55 topsoil samples (0 to 25 cm depth) were obtained in a preliminary reconnaissance survey according to land use pattern of our study site. These samples are considered as legacy data of which 24 samples were collected in the land use class ‘Cropland’, 12 in the class ‘Woodland’, nine in the class ‘Conifer’, six in the class ‘Broadleaf’, and four in the class ‘Shrub’. At each sampling point, five subsamples were pooled, one from the center point and four from the corner points of a surrounding 40 cm x 40 cm square. We choose sand fractions as target soil property to test our approach since texture is a very important predictor for soil erosion and the amount of fine sand is closely related to soil erodibility (*Salako* et al., 2006). Further, sand was defined as priority subject by the *Soil Conservation Law of the People`s Republic of China* (*Peng* et al., 2014). In total, three sand

fractions were separated by wet sieving. These are coarse sand (CS: 2 - 0.63 mm), medium sand (MS: 0.63 - 0.2 mm), and fine sand (FS: 0.2 - 0.063 mm). Each fraction was oven-dried (105 °C) and weighed.

2.2 Sampling design

2.2.1 Conditioned Latin Hypercube Sampling

The conditioned Latin Hypercube Sampling (cLHS) presents a stratified random method for sampling a multivariate distribution of environmental covariates. The idea is that the combined feature space of the covariates is fully covered by the sample set. Therefore, cLHS divides the range of each covariate into a number of equally probable strata (intervals), which corresponds to the sample set size. The sample set is derived by iteratively sampling from the entire feature space and finally selecting target sites that in combination cover each stratum of each covariate once. This optimization procedure is accomplished by simulated annealing (*Metropolis* et al., 1953; *Press* et al., 1992) and ensures that each covariate is uniformly sampled in the final sample set (*Minasny* and *McBratney*, 2006). Due to the purely statistical nature and the focus of the method on feature space, sampling locations might be selected that do not exist in the real world. Hence, the target site selection is conditioned by rejecting covariate combinations that do not exist in the real world. As proposed by *Minasny* and *McBratney* (2006), the final sampling set in cLHS is derived if following three criteria are fulfilled: (i) all strata of all selected covariates are occupied by one unique target site, (ii) the correlation between the covariates is preserved in the sampling set, and (iii) the combination of all samples fully covers the entire feature space.

2.2.2 Covariate selection and sample size

We selected a feature subset of covariates from all covariates referring to the terrain and land use (c.f., Section 2.1) to set up a cLHS design for all target sand fractions. This selection followed the criteria of a plausible correlation to the target variables and a low correlation within the subset to avoid collinearity (*Gessler* et al., 2000; *Hengl* et al., 2003; *Mulder* et al., 2012). Using the legacy soil samples, the correlations (r) of each covariate to all target sand fractions was determined and averaged for each covariate (r_1). We selected (i) the covariate

with the highest r_1, and (ii) all other covariates with $r_1 > 0.4$ and a correlation < 0.4 among each other (r_2).

To determine the sample set size *n*, we compared the feature space of the covariates x_i (i = 1, …,k) referring to the entire study area and 10 cLHS sample sets with a size n_j (j = 10, 20,…,100). We used the statistical variance (*var*) as an indicator to test the representativeness of the sample set sizes. The averaged variances of the covariates in the sample sets (sample set variance) were compared to the averaged variance of the covariates in the entire study area (global variance). The optimal sample set size *n* is defined by the minimum difference between the global variance and the sample set variance and by identifying the kneepoint of the curve, which takes the form,

$$n\,(j) = \left(\frac{\sum_{i=1}^{k} var(x_i)}{k}\right) - \left(\frac{\sum_{i=1}^{k} var(x_{ij})}{k}\right)$$

The kneepoint of the curve indicates the value of the minimum sample set size before the curve starts to level off disproportionally. We assumed the corresponding sample set size as the best tradeoff between sampling effort and representativeness to adequately reflect the feature space of the entire study area (*Schmidt* et al., 2014; *Ramirez-Lopez* et al., 2014).

2.2.3 Adapted conditioned Latin Hypercube Sampling

Using the covariates and the determined sample set size as described in the previous section, we applied cLHS according to *Schmidt* et al. (2014), which facilitates to set the minimum and maximum value of each cLHS covariate as predefined. Thus a full spread of the feature space in the hypercube is assured. From the derived strata with the original cLHS target sites ($cLHS_{orig}$), pixels with a slope angle higher than 35° and the land use classes ‘Broadleaf’, ‘Conifer’, ‘Shrub’, ‘Built-up’ as well as 'Water bodies' were defined as inaccessible and subsequently excluded from sampling. The land use class ‘Woodland’ was also excluded, unless the pixel was in distance of less than 150 m from a path and therefore accessible in reasonable temporal expense.

Inaccessible $cLHS_{orig}$ target sites were replaced by a potentially available legacy sample that occupies the respective stratum. For those strata with no accessible $cLHS_{orig}$ target sites, nor a matching legacy sample, a new target site was selected from all accessible pixels of the

corresponding strata. Taking the accessible and replaced $cLHS_{orig}$ target sites as predefined, we analyzed all possible combinations of accessible pixels over all remaining strata according to the cLHS search criteria (c.f., Section 2.2.1). For these test sample sets, the correlation (r) between the cLHS covariates were compared to the correlation of $cLHS_{orig}$. We selected those five sample sets that were most similar to $cLHS_{orig}$ and analyzed their coverage with the feature space of the cLHS covariates in the entire study area. Therefore, we used the frequency distribution of samples across the quartiles (Q) as simple measures. Ideally, 25% of the samples would fall in the first and third quartiles (Q1 and Q3) and 50% of the samples would fall in the second quartile (Q2). We selected one final sample set ($cLHS_{adapt}$) referring to the smallest deviation from the ideal distribution. The additional samples were obtained in April 2013. Survey of soil data and laboratory analysis was done the same way as for the legacy samples (c.f., Section 2.1).

2.3 Spatial predictions

We used Random Forest (RF) to build a regression model. RF is an ensemble classifier based on multiple randomized decision trees (*Breiman*, 2001). A decision tree presents a model that utilizes a set of binary rules to compute a target variable (*Quinlan*, 1986). In context of DSM, the binary rules are based on multiple environmental covariates and the target response variable (i.e., soil property) that should be mapped. The final prediction is computed by averaging the results over all individual trees for each pixel of the map. The single trees of a RF model should be as diverse as possible (*Grimm* et al., 2008). This is accomplished by (i) setting up each tree based on a bootstrap sample of the respective soil sample dataset, and by (ii) identifying the best split predictor covariate of each tree node from a random feature subset (*Peters* et al., 2007).

We applied RF using the R-package 'randomForest' by *Liaw* and *Wiener* (2002). The number of trees (k) and the size of the random feature subset at each node (m_{try}) are user-defined model parameters. We applied RF with k = 1,500 and $m_{try} = 2\sqrt{p}$, with p representing the total number of predictor variables (*Breiman*, 2001). Since RF is resistant to multi-collinearity, we used all available covariates (c.f., Section 2.1) for building the RF regression models. The sample set $cLHS_{adapt}$ was used for model calibration. From the legacy samples that were not included into $cLHS_{adapt}$, we randomly derived an independent validation set of 20 samples.

The remaining legacy samples were combined with $cLHS_{adapt}$ to generate a second RF calibration set ($cLHS_{adapt+}$) for a comparative analysis with the RF $cLHS_{adapt}$ approach.

We evaluated the accuracy of the RF regression models for all target variables and both calibration sets, using independent and bootstrap validation. For both accuracy estimations, the indicators coefficient of determination (R^2) and root mean squared error (RMSE) were derived. Since the predicted target variables represent compositional data, we additionally assessed the coherence of their predicted sum, which ideally amounts to 100%.

3. Results

3.1 Covariate selection and sample set size

According to the correlations of each covariate to the target variables (r_1), the covariate 'Altitude Above Channel' (AAC) shows the highest value (r_1 = 0.65) and was therefore selected as first cLHS covariate. The covariates 'Altitude' (r_1 = 0.65), 'Plane curvature' (r_1 = 0.63) and 'Wetness Index' (SWI; r_1 = 0.41) are plausibly correlated to the target variables with $r_1 > 0.4$. However, 'Altitude' and 'Plane curvature' show correlations of r_2 = 0.62 and r_2 = 0.55 to AAC, thus, indicating collinearity and were rejected. SWI shows a lower collinearity with an r_2 of 0.38 and was retained (Table 2). This results in the two covariates AAC and SWI, building the feature space for cLHS.

Table 2: The covariates ranked according to their averaged correlations r_1 to the target variables. The correlation between the covariates and the top ranked covariate is indicated by r_2.

Covariate	r_1	Rank	r_2
AAC	**0.65**	**1**	**1**
Altitude	0.65	2	0.62
Plane curvature	0.63	3	0.55
SWI	**0.41**	**4**	**0.38**
Slope angle, maximum	0.38	5	0.44
Terrain ruggedness	0.31	6	0.01
Slope angle	0.29	7	0.03
Slope length	0.28	8	0.37
Convergence index	0.23	9	0.33
Land use	0.23	10	0.22
Mass balance index	0.2	11	0.22
Combined curvature	0.19	12	0.29
Northing	0.19	13	0.15
Easting	0.18	14	0.1
Horizontal flow distance	0.18	15	0.07
Protection index	0.17	16	0.08
Profile curvature	0.16	14	0.27
Vertical flow distance	0.12	18	0.12
Flow accumulation	0.09	19	0.35
Overland flow distance	0.08	20	0.1
Position index	0.08	21	0.29
Catchment area	0.07	22	0.41

For the determination of the final sample set size *n*, the selected cLHS covariates AAC and SWI were used to set up 10 cLHS designs, which exhibit test sample set sizes ranging from 10 to 100. The numerical distances of the sample set variances to the global variance spans from 0.01 to 0.06 (Fig. 1), while decreasing values indicate an increase in representativeness of the respective cLHS set. When plotting the sample set size against the sample set variance, the kneepoint of the resulting function shows a numerical distance of 0.02 (Fig. 1), suggesting a final sample size of $n = 30$ for $cLHS_{adapt}$. This results in a ratio of 7.1 samples per km².

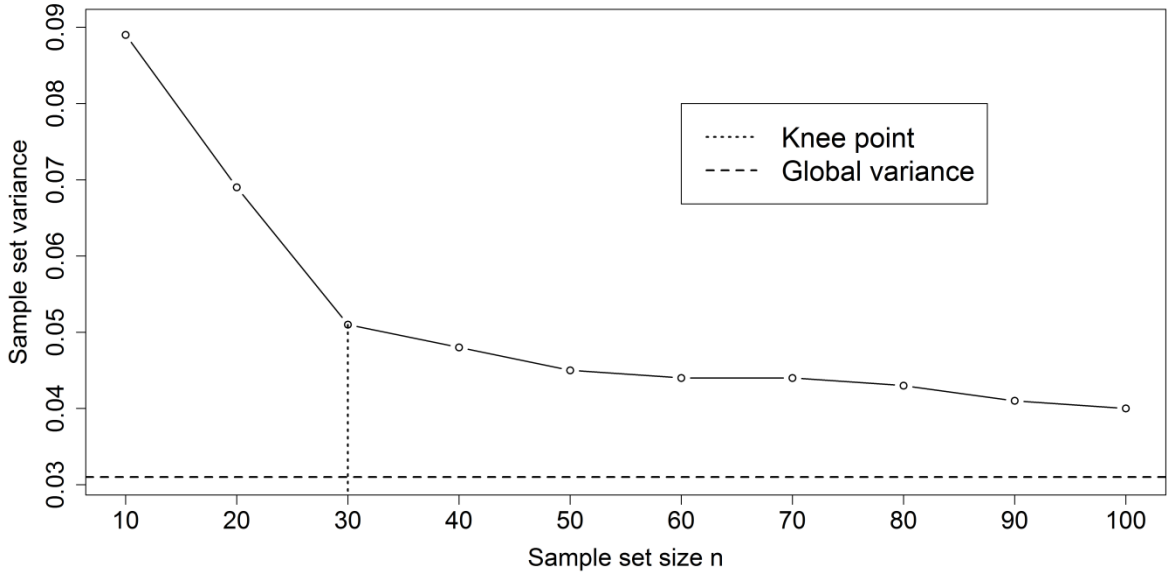

Figure 1: Determination of a sample set size by comparing the sample set variance to the global variance (dashed line), using the kneepoint (dotted line).

3.2 Sampling design

Corresponding to the previously determined sample set size n = 30, the final cLHS design ($cLHS_{adapt}$) results in 30 strata, each with a varying number of spatially scattered pixels ranging from 2 to 82. The variation and scattering is determined by the statistical properties of the cLHS covariates 'AAC' and 'SWI', which underlay the strata (c.f., Section 2.2.1). After we excluded inaccessible areas, each stratum shows a number of 1 to 4 accessible pixels (Table 3).

Each stratum needs to be sampled at precisely one specific target site, while the combination of all sampled target sites results in an optimized coverage of the cLHS feature space, formed by AAC and SWI. Seven strata are occupied by predefined target sites from $cLHS_{orig}$ or the legacy samples: Two sites refer to the $cLHS_{orig}$ design and match accessible pixels of a stratum. In the remaining five strata, legacy samples are available, which were used to cover the respective stratum. This results in 23 uncovered strata whether due to lacking accessibility at the $cLHS_{orig}$ target site or absent legacy samples (Table 3).

Since we integrated five legacy samples into the $cLHS_{adapt}$ design and extracted 20 samples for validation, 30 legacy samples remained unused. We combined these legacy samples with the $cLHS_{adapt}$ (n = 30), resulting in the further calibration set $cLHS_{adapt+}$ (n = 60), which we used to evaluate our approach.

Table 3: Number of accessible pixels and total number of pixels per stratum. The strata sampled by original cLHS sites and strata occupied by legacy samples are indicated (dots).

Strata	Number of accessible pixels	Total number of pixels	$cLHS_{orig}$ sample	legacy sample
1	3	22	–	●
2	2	5	–	–
3	2	8	–	–
4	3	18	–	–
5	1	7	–	–
6	1	19	–	–
7	1	84	–	●
8	1	9	–	●
9	1	18	–	–
10	1	9	–	–
11	1	20	–	–
12	1	7	–	–
13	1	6	–	–
14	1	8	–	–
15	2	6	–	–
16	2	12	–	–
17	2	19	–	–
18	2	3	–	–
19	4	9	●	–
20	3	26	–	–
21	3	10	–	●
22	1	4	–	–
23	2	2	●	–
24	3	16	–	–
25	1	7	–	–
26	2	13	–	–
27	2	5	–	–
28	4	25	–	–
29	2	9	–	–
30	2	64	–	●

The target sites in the 23 uncovered strata were determined by analyzing all possible combinations of accessible pixels across those strata that were not sampled. For each combination the 7 predefined target sites were added, resulting in 10,592 test sample sets.

The test sample sets were examined according the cLHS criteria (c.f., Section 2.2.1) using $cLHS_{orig}$ as baseline to select the most adequate sample set for calibration ($cLHS_{adapt}$). Referring to the cLHS criterion of a preserved correlation between the covariates in the sample set, those five pre-selected sample sets that were most similar to $cLHS_{orig}$ show differences in $r < 0.01$. Contrary, the calibration set $cLHS_{adapt+}$ differs by $r > 0.05$. Referring to the criterion of optimized feature space coverage, we used the proportional frequency of samples across the quartiles of the cLHS covariates ($Q1\text{-}3_{AAC}$, $Q1\text{-}3_{SWI}$) and summed up the deviations to $cLHS_{orig}$ over all quartiles and both covariates (dev.). The deviations of the five pre-selected test sample sets range from 22 to 42 percent points (pp), while $cLHS_{adapt+}$ differs by 60 pp (Table 4). Thus, the calibration set $cLHS_{adapt+}$ ($n = 60$) shows less similarity to $cLHS_{orig.}$ than the five selected test sample set sizes with $n = 30$ (Table 4).

We selected this test sample set as final calibration set ($cLHS_{adapt}$), which is most similar to $cLHS_{orig}$ according the cLHS criteria. For $cLHS_{adapt}$, the correlation r between the cLHS covariates in the entire study area and in the sample set differs by 0.0061. The summed up deviation of the proportional frequencies in the quartiles amounts to 22 percent points (Table 4).

Table 4: Sample set comparison of the original cLHS set ($cLHS_{orig.}$), the test sets (test 1 to test 5) and the calibration sets $cLHS_{adapt}$ with a sample size n = 30, and $cLHS_{adapt+}$ with 30 additional legacy samples. The correlation (r) among the cLHS covariates in the sample sets, the proportional frequency across the quartiles of the cLHS covariates in the study area ($Q1\text{-}3_{AAC}$, $Q1\text{-}3_{SWI}$) and the summed up deviation (dev.; pp: percent points) from $cLHS_{orig}$, are indicated.

Sample set	r	$Q1_{AAC}$ (%)	$Q2_{AAC}$ (%)	$Q3_{AAC}$ (%)	$Q1_{SWI}$ (%)	$Q2_{SWI}$ (%)	$Q3_{SWI}$ (%)	dev. (pp)
$cLHS_{orig.}$	0.4003	23	50	27	23	50	27	-
test1/ $cLHS_{adapt}$	0.3942	27	46	27	27	53	20	22
test 2	0.3923	27	43	30	17	57	26	28
test 3	0.4068	27	43	30	23	43	34	28
test 4	0.3905	27	43	30	20	60	20	34
test 5	0.4037	33	40	27	34	43	23	42
$cLHS_{adapt+}$	0.3365	45	38	17	17	58	25	60

3.3 Spatial predictions

According to the laboratory analysis of the two calibration sets $cLHS_{adapt}$ (n = 30) and $cLHS_{adapt+}$ (n = 60), the average topsoil sand content accounts to 6% in $cLHS_{adapt}$ and to 9.5% for $cLHS_{adapt+}$. Comparing the results referring to both calibration sets and all target sand fractions (CS, MS, FS), $cLHS_{adapt+}$ shows higher averages and variability for all sand fractions. These patterns are pronounced for CS, showing an average of 2.4% and an inter quartile range (IQR) of approximately 1.3 in $cLHS_{adapt}$ versus an average of 4.6% and an IQR of 8.9 in $cLHS_{adapt+}$. By contrast, the target variables MS and FS show increased similarity between the calibration sets. For MS, the average amounts to 2% with an IQR of approximately 0.9 in $cLHS_{adapt}$, while $cLHS_{adapt+}$ shows an average of almost 3% with an IQR of approximately 4. For FS, $cLHS_{adapt}$ shows an average of 1.6% with an IQR of 0.8 versus an average of 2.0 with an IQR of 2.2 in $cLHS_{adapt+}$ (Fig. 2).

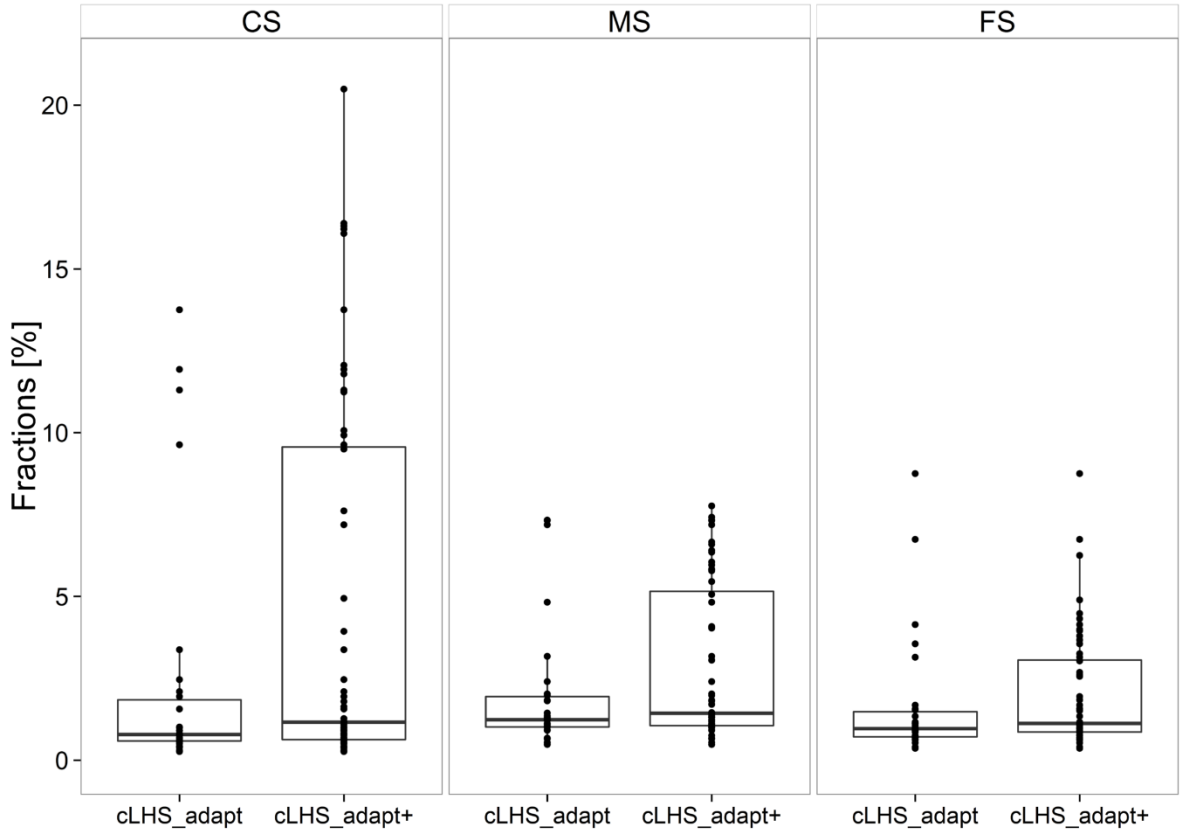

Figure 2: Topsoil sand fractions (CS: coarse sand, MS: medium sand, FS: fine sand) for both calibration sets ($cLHS_{adapt}$, $cLHS_{adapt+}$).

The RF prediction models couple the calibration sets $cLHS_{adapt}$ (n = 30) and $cLHS_{adapt+}$ (n = 60) with all available covariates (c.f., Section 2.1) and estimate all sand fractions (CS, MS, FS). The two-fold accuracy evaluation, which is based on independent and bootstrap validation, performs similar with deviations in R^2 ranging from 1% to 4% referring to each target variable and validation method. The accuracy estimation R^2 across all target variables, both calibration sets, and validation methods range between 0.57 and 0.80 (Table 5).

With respect to the independent validation and R^2, the FS-models ($cLHS_{adapt}$: R^2 = 0.59; $cLHS_{adapt+}$: R^2 = 0.61) are outperformed by the CS-models ($cLHS_{adapt}$: R^2 = 0.63; $cLHS_{adapt+}$: R^2 = 0.67), while the MS-models ($cLHS_{adapt}$: R^2 = 0.71; $cLHS_{adapt+}$: R^2 = 0.80) perform best. Moreover, for all target variables the models calibrated by $cLHS_{adapt+}$ (n = 60) outperform the

models using $cLHS_{adapt}$ (n = 30). The deviations amount to 2% for FS, 4% for CS and 9% for MS (Table 5).

Table 5: Random Forest model accuracies (R^2, RMSE) based on independent and bootstrap validation. The accuracy estimations refer to all calibration sets ($cLHS_{adapt}$, $cLHS_{adapt+}$) and target variables (CS: coarse sand, MS: medium sand, FS: fine sand).

Independent validation	$cLHS_{adapt}$		$cLHS_{adapt+}$	
	R^2	RMSE	R^2	RMSE
CS	0.63	4.03	0.67	3.75
MS	0.71	1.07	0.8	0.94
FS	0.59	0.34	0.61	0.38
Bootstrap validation	$cLHS_{adapt}$		$cLHS_{adapt+}$	
	R^2	RMSE	R^2	RMSE
CS	0.64	2.16	0.71	3.48
MS	0.69	0.91	0.78	1.01
FS	0.57	0.38	0.64	0.36

The sum of all predicted sand fractions ideally amounts to 100 %. We mapped the deviations from this ideal for the predictions of both calibration sets ($cLHS_{adapt}$, $cLHS_{adapt+}$) in percent points (Fig. 3). Both model approaches show increased deviations in the northern Upper Badong catchment and in depression lines. (Fig. 3). For the $cLHS_{adapt}$-models, the deviations are more pronounced, while an additional hotspot of high deviations is located in the eastern study area (Fig. 3). The summary statistics of the deviations show a maximum of 9.4 % and an average of 1.8% for the $cLHS_{adapt}$-models. The maximum of the $cLHS_{adapt+}$-models accounts for 7.6% with an average of 1.3%. Thus, the calibration set $cLHS_{adapt+}$ outperforms $cLHS_{adapt}$, confirming the results of the accuracy estimations by independent and bootstrap validation (Table 5).

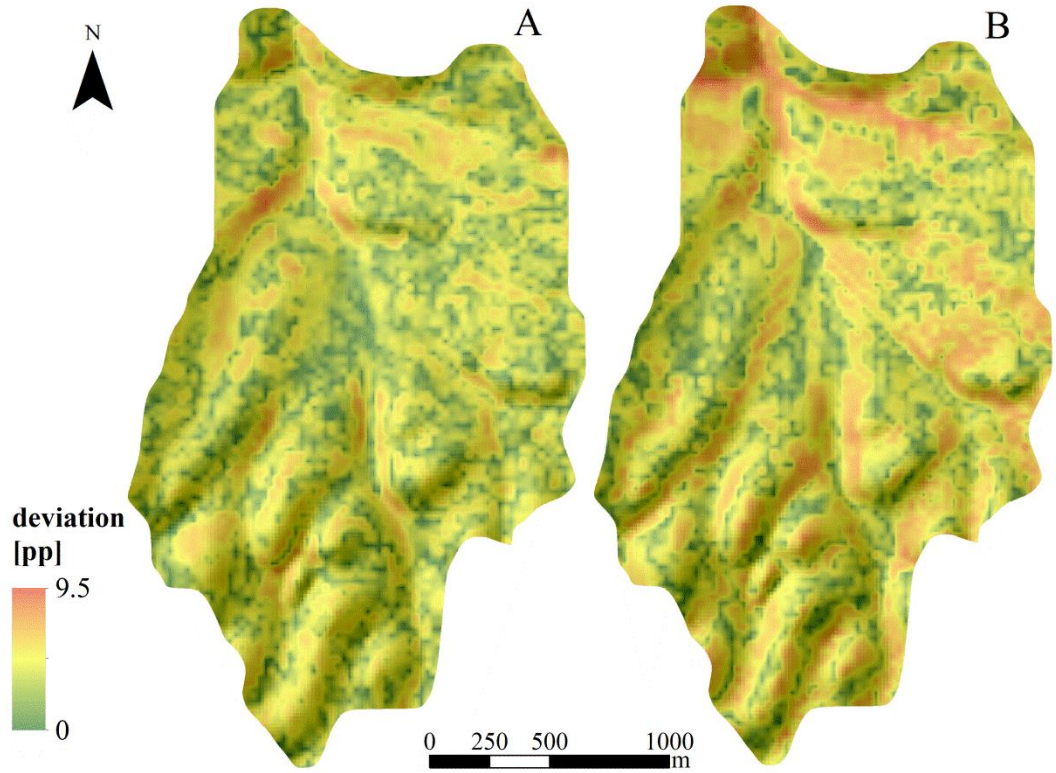

Figure 3: Coherence of the predicted sum referring to the compositional target variables (CS: coarse sand, MS: medium sand, FS: fine sand) and to the calibration sets (A) $cLHS_{adapt+}$ and (B) $cLHS_{adapt}$. Colors indicate the range of deviation in percent points (pp) from the ideal of 100%.

4 Discussion

4.1 Hypercube sampling

The cLHS method identifies samples, which are stratified in the multivariate feature space in a two-step approach. First, strata are generated in a hypercube, which spans the feature space. Second, one target site per stratum is selected according to an optimization procedure (*Metropolis* et al., 1953) that covers the feature space by a combination of unique target sites. The latter target site selection process is conditioned by only selecting feature space locations that exist in the real world (*Minasny* and *McBratney*, 2006).

Roudier et al. (2012), *Mulder* et al. (2013), and *Clifford* et al. (2014) further constrained the target site selection by penalizing spatial locations with limited accessibility within each predefined stratum. This implies a potential bias in the final sample set size, since inaccessible areas might occupy segments of the feature space that were not sampled. Further, accessibility at the target sites is not guaranteed because the existence of accessible locations in the specific stratum cannot be ensured. *Clifford* et al. (2014) eludes the latter problem by additionally analyzing the relation of each location in a defined neighborhood to the initial target site, providing an ordered list of alternative target sites. While it is a combination of one unique sample per stratum covering the feature space initially, the generation of alternatives follows a biased assumption that all other target sites have been successfully sampled before. However, according to a simulation study, *Clifford* et al. (2014) showed that the feature space coverage remains preserved by replacing up to 50% of the initial target sites by alternatives sites.

In our approach, instead of penalizing locations in the stage of target site selection and generating alternatives for each initial target site individually, we analyzed all possible combinations of accessible locations according to their feature space coverage and with respect to the original cLHS design. This enables for quantifying the deviation to the original cLHS design and for providing alternative target sites, while avoiding assumptions about previously sampled target sites. Ensuring that at least one accessible location per stratum is available, requires to increase the number of locations within each stratum. This is accomplished by decreasing the number of covariates, which build the feature space, and the sample set size (*Minasny* and *McBratney*, 2006).

We reduced the number of covariates to the two most adequate (i.e., ACC and SWI), according to a plausible correlation to the target variables (*Gessler* et al., 2000) and avoidance of multicollinearity within the feature space (*Hengl* et al., 2003; *Mulder* et al., 2013; *Schmidt* et al., 2014). Other studies that applied cLHS used more covariates (approximately four to ten) to build the feature space, while the ratio of samples per km² varies between 0.005 and 0.465 in study areas with size ranging from 720 km² to 12,8000 km² (*Mulder* et al., 2013; *Clifford* et al., 2014; *Taghizadeh-Mehrjardi* et al., 2014; *Kidd* et al., 2015). *Brungard* and *Boettinger* (2010) suggested a minimum ratio of 0.7 to 1 samples per km² using cLHS in a study area of a size of 300 km². We optimized the sample set size to $n = 30$ in a study area of 4.2 km², thus, 7.1 samples per km², by analyzing ten simulated cLHS sets with different

sample set sizes. Moreover, we showed that the deviation of the feature space coverage from the original cLHS set is marginally (Table 4), while 93% of the original samples were replaced by alternatives (Table 3).

Referring to the incorporation of legacy samples to cover the feature space, *Clifford* et al. (2014) used 8,669 legacy samples as predefined basis to locate 300 additional target sites. Since the subset of legacy samples was not obtained purposively to cover the feature space, redundancies within the subset were not considered and potentially led to a bias in the combined sample set. In this context, *Carré* et al. (2007) proposed to analyze the distribution of legacy samples across the strata to evaluate the adequacy of legacy samples for the feature space coverage. Following the principles of this approach, we only used those five legacy samples which are located within a stratum, thus, avoiding redundancies and reducing the sampling effort. Consequently, the increased number of locations per stratum also accommodates with the goal to integrate legacy samples, which are adequate to cover the feature space by a predefined sample size *n*. In our study, only one legacy sample is available in the respective stratum, thus, no evaluation of preference is necessary. Apart from this situation, we suggest to consider multiple legacy samples within a stratum simply as potential accessible target sites and follow the methodological procedure as described in section 2.2.

Any cLHS or stratified sampling design must be seen as a specific case study, resulting in a partially limited generalizability. This is attributed to the assumptions that the feature space, determined by local framework conditions, sufficiently describes the targeted soil property in space and time (*Clifford* et al., 2014). Besides these limitations, our approach is transferable to any other study area, considering that an increasing number of samples and resolution increases the computational load. Thus, our approach is suitable for small study areas with highly limited accessibility.

4.2 Spatial prediction

Soil texture estimation using DSM typically shows accuracies less than 0.50 while studies with $R^2 > 0.70$ are rare (*Malone* et al., 2009; *Lacoste* et al., 2011; *Wang* et al., 2012; *de Carvalho Junior* et al., 2014; *Mansuy* et al., 2014). Our results (Table 5) showed accuracies with $R^2 > 0.50$ for all sand fractions for both calibration sets ($cLHS_{adapt}$ with $n = 30$; $cLHS_{adapt+}$ with $n = 60$). Comparing the prediction accuracies for both calibration sets and

referring to independent and bootstrap validation, the $cLHS_{adapt}$ approach results in slightly decreased accuracies by only 0.5 %. This is confirmed by referring to the coherence of the total sand fraction, ideally amounting to 100%. The similarity between the two DSM approaches confirms the robustness of the proposed sampling approach. Moreover, since our calibration sample set size n = 30 is relatively small compared to other studies using n between 165 and 4,920 for RF regression analysis (*Grimm* et al., 2008; *Lacoste* et al., 2011; *Mansuy* et al., 2014), and considers the topographical heterogeneity of the study area, the accuracy of the proposed DSM approach is noticeable.

5 Conclusion

We present a DSM sampling design, which is based on the principles of conditioned Latin Hypercube Sampling (cLHS). The final sample set adequately reproduces the variation of selected terrain parameters, which serve as proxies for the target soil properties. The design compensates for limited field accessibility, integrates the use of legacy samples and uses an optimized sample set size. Consequently, our approach provides better operability in difficult terrain and improves efficiency in terms of temporal and monetary constraints compared to other cLHS approaches. We applied the approach in a small catchment in the Three Gorges Reservoir area at the Yangtze River in Hubei, Central China. Using a Random Forest regression model we estimated the topsoil sand fractions with convincing accuracies.

Acknowledgements

We thankfully acknowledge funding from the German Ministry of Education and Research (BMBF, grant No. 03 G 0827A) for the German-Sino research collaboration YANGTZE GEO. We thank Bi Renneng from the University of Erlangen-Nuremberg and Alexander Strehmel from the Christian-Albrechts-University of Kiel for data sharing. We thank all students from the China University of Geosciences (CUG) in Wuhan that were involved in field campaigns and laboratory analyzes. We are also very grateful for the general support of the whole YANGTZE GEO research group.

References

Behrens, T., Schmidt, K., Ramirez-Lopez, L., Gallant, J., Zhu, A., Scholten, T. (2014): Hyper-scale digital soil mapping and soil formation analysis. Geoderma 213, 578-588.

Behrens, T., Schmidt, K., Zhu, A., Scholten, T. (2010): The ConMap approach for terrain-based digital soil mapping. Eur. J. Soil Sci. 61, 133-143.

Behrens, T., Förster, H., Scholten, T., Steinrücken, U., Spies, E.-D., Goldschmitt, M. (2005): Digital Soil Mapping using Artificial Neural Networks. J. Plant Nutr. Soil Sci. 168, 1-13.

Breiman, L. (2001): Random Forests. Mach. Learn. 45, 5-32.

Brungard, C.W., Boettinger, J.L. (2010): Conditioned Latin Hypercube Sampling: Optimal sample size for Digital Soil Mapping of Arid Rangelands in Utah, USA, in: Boettinger, J.L., Howell, D.W., Moore, A.C., Hartemink, A.E., Kienast-Brown, S. (eds.): Digital Soil Mapping. Bridging Research, Environmental Application, and Operation. Progress in Soil Science. Vol. 2. Springer, Netherlands, pp. 67-75.

Brus, D., De Gruijter, J., Van Groeningen, J. (2006): Designing spatial coverage samples using k-means clustering algorithm, in: Lagacherie, P., McBratney, A.B., Voltz, M. (eds.): Digital Soil Mapping, an introductory perspective. Developments in Soil Science. Vol. 31. Elsevier, Amsterdam, pp. 183-192.

Cambule, A., Rossiter, D., Stoorvogel, J. (2013): A methodology for digital soil mapping in poorly-accessible areas. Geoderma 192, 341-353.

Carré, F., Girard, M. (2002): Quantitative mapping of soil types based on regression kriging of taxonomic distances with landform and land cover attributes. Geoderma 110, 241-263.

Carré, F., McBratney, A. B., Minasny, B. (2007): Estimation and potential improvement of the quality of legacy soil samples for digital soil mapping. Geoderma 141, 1-14.

Carvalho Junior, de W., Lagacherie, P., Silva Chagas, C., Filho, B., Bhering, S. (2014): A regional-scale assessment of digital soil attributes in a tropical hillslope environment. Geoderma 232/234, 479-486.

Clifford, D., Payne, J., Pringle, M., Searle, R., Butler, N. (2014): Pragmatic soil survey design using flexible Latin hypercube sampling. Comput. Geosci. 67, 62-68.

Dobermann, A., Simbahan, G.C. (2007): Methodology for using secondary information in sampling optimization for making fine-resolution maps of soil organic carbon, in: Lagacherie, P., McBratney, A.B., Voltz, M. (eds.): Digital Soil Mapping, an introductory perspective. Developments in Soil Science. Vol. 31. Elsevier, Amsterdam, pp. 167-182.

Gessler, P., Chadwick, O., Chamran, F., Althouse, L., Holmes, K. (2000): Modeling soil-landscape and ecosystem properties using terrain attributes. Soil Sci. Soc. Am. J. 64, 2046-2056.

Grimm, R., Behrens, T., Märker, M., Elsenbeer, H. (2008): Soil organic carbon concentrations and stocks on Barro Colorado Island – Digital Soil Mapping using Random Forests analysis. Geoderma 146, 102-113.

Hengl, T., Rossiter, D., Stein, A. (2003): Soil sampling strategies for spatial prediction by correlation with auxiliary maps. Soil Res. 41, 1403-1422.

Hengl, T., Heuvelink, G., Stein, A. (2004): A generic framework for spatial prediction of soil variables based on regression-kriging. Geoderma 120, 75-93.

Heuvelink, G.B., Brus, D.J., de Gruijter, J.J. (2007): Optimization of sample configurations for digital soil mapping of soil properties with universal Kriging, in: Lagacherie, P., McBratney, A.B., Voltz, M. (eds.): Digital Soil Mapping, an introductory perspective. Developments in Soil Science. Vol. 31. Elsevier, Amsterdam, pp. 137-152.

Kidd, D., Malone, B., McBratney, A.B., Minasny, B., Webb, M. (2015): Operational sampling challenges to Digital Soil Mapping in Tasmania, Australia. Geoderma Regional 4, 1-10.

Krol, B. (2008): Towards a data quality management framework for digital soil mapping with limited data, in: Hartemink, A.E., McBratney, A.B., Mendonça-Santos, M.L. (eds.): Digital Soil Mapping with Limited Data. Springer, pp. 136-149.

Lacoste, M., Lemercier, B., Walter, C. (2011): Regional mapping of soil parent material by machine learning based on point data. Geomorphology 133, 90-99.

Lagacherie, P. (2008): Digital Soil Mapping: A State of the Art, in: Hartemink, A.E., McBratney, A.B., Mendonça-Santos, M.L. (eds.): Digital Soil Mapping with Limited Data. Springer, pp. 3-14.

Liaw, A., Wiener, M. (2002): Classification and Regression by Random Forest. R News 2, 18-22.

Florinsky, I.V., Eilers, R.G., Manning, G.R., Fuller, L.G. (2002): Prediction of soil properties by digital terrain modelling. Environ. Modell Softw. 17, 295-311.

Malone, B., McBratney, A., Minasny, B., Laslett, G. (2009): Mapping continuous depth functions of soil carbon storage and available water capacity. Geoderma 154, 138-152.

Mansuy, N., Thiffault, E., Paré, D., Bernier, P., Guindon, L., Villemaire, P., Poirier, V., Beaudoin, A. (2014): Digital mapping of soil properties in Canadian managed forests at 250 m of resolution using k-nearest neighbor method. Geoderma 235/236, 59-73.

Mayr, T., Palmer, R. (2007): Digital Soil Mapping: An England and Wales perspective, in: Lagacherie, P., McBratney, A.B., Voltz, M. (eds.): Digital Soil Mapping, an introductory perspective. Developments in Soil Science. Vol. 31. Elsevier, Amsterdam, pp. 365-376.

McBratney, A.B., Mendonça-Santos, M.L., Minasny, B. (2003): On digital soil mapping. Geoderma 117, 3-52.

McKay, M., Beckman, R., Conover, W. (1979): A comparison of three methods for selecting values of input variables in the analysis of output from a computer code. Technometrics 21, 239–245.

McKenzie, N., Ryan, P. (1999): Spatial prediction of soil properties using environmental correlation. Geoderma 89, 67–94.

McMillan, R.A. (2008): Experiences with Applied DSM: Protocol, Availability, Quality and Capacity Building, in: Hartemink, A.E., McBratney, A.B., Mendonça-Santos, M.L. (eds.): Digital Soil Mapping with Limited Data. Springer, pp. 113-135.

Metropolis, N., Rosenbluth, A, Rosenbluth, M., Teller, A., Teller, E. (1953): Equation of state calculations by fast computing machines. J. Chem. Phys 21, 1087-1092.

Minasny, B., McBratney, A.B. (2006): A conditioned Latin hypercube method for sampling in presence of ancillary data. Comput. Geosci. 32, 1378-1288.

Mora-Vallejo, A., Claessens, L., Stoorvogel, J., Heuvelink, G. (2008): Small scale digital soil mapping in Southeastern Kenya. Catena 76, 44-53.

Mulder, V.L., De Bruin, S., Schaepman, M. (2013) Representing major soil variability at regional scale by constrained Latin hypercube sampling of remote sensing data. Int. J. Appl. Earth Obs. Geoinf. 21, 301-310.

Naumann, T.W., Thompson, J.A. (2014): Semi-automated disaggregation of conventional soil maps using knowledge driven data mining and classification trees. Geoderma 213, 385-399.

Peng, X., Shi, D., Jiang, D., Wang, S., Li, Y. (2014): Runoff erosion processes on different underlying surfaces from disturbed soils in the Three Gorges Reservoir Area, China. Catena 123, 215-224.

Peters, J., De Baets, B, Verhoest, N., Samson, R., Degroeve, S., De Becker, P., Huybrechts, W. (2007): Random Forests as a tool for ecohydrological distribution modelling. Ecol. Model. 207, 304-318.

Press, W.H., Flannery, B.P., Teukolsky, S.A., Vetterling, W. T. (1992): Numerical recipes in FORTRAN: The art of scientific computing. Cambridge University Press. New York.

Quinlan, J.R. (1986): Induction of decision trees. Mach. Learn. 1, 81-106.

Ramirez-Lopez, L., Schmidt, K., Behrens, T., Van Wesemael, B., Dematte, J., Scholten, T. (2014): Sampling optimal calibration sets in soil infrared spectroscopy. Geoderma 226, 140-150.

Roudier, P., Hewitt, A.E., Beaudette, D.E. (2012): A conditioned Latin Hypercube Sampling algorithm incorporating operational constraints, in: Minasny, B., Malone, B.P., McBratney, A.B. (eds.): Soil Assessment and Beyond. CRC Press, Sydney, pp. 227-231.

SAGA GIS (2011): System for Automated Geoscientific Analyses (Version 2.0.6.). Available at www.saga-gis.org (accessed 11 August 2013; verified 14 September 2013). SAGA User Group Association, Hamburg.

Salako, F.K., Tian, G., Kirchhof, G., Akinbola, G.E. (2006): Soil particles in agricultural landscapes of a derived savanna in southwestern Nigeria and implications for selected soil properties. Geoderma 137, 90-99.

Schmidt, K., Behrens, T., Daumann, J., Ramirez-Lopez, L., Werban, U., Dietrich, P., Scholten, T. (2014): A comparison of calibration sampling schemes at the field scale. Geoderma 232, 243-256.

Schönbrodt-Stitt, S., Bosch, A., Behrens, T., Hartmann, H., Shi, X., Scholten, T. (2013): Approximation and spatial regionalization of rainfall erosivity based on sparse data in a mountainous catchment of the Yangtze River in Central China. Environ. Sci. Pollut. Res. 20, 6917-6933.

Scull, P., Franklin, J., Chadwick, O.A., McArthur, D. (2003): Predictive soil mapping: a review. Prog. Phys. Geog. 27, 171-197.

Strehmel, A., Schönbrodt-Stitt, S., Buzzo, G., Dumperth, C., Stumpf, F., Zimmermann, K., Bieger, K., Behrens, T., Schmidt, K., Bi, R., Rohn, J., Hill, J., Udelhoven, T., Xiang, W., Shi, X., Cai, Q., Jiang, T., Fohrer, N., Scholten, T. (2015): Assessment of Geo-Hazards in a rapidly changing landscape: The Three Gorges Reservoir region in China. Environmental Earth Sciences. doi: 10.1007/s12665-015-4503-7.

Sulaeman, Y., Minasny, B., McBratney, A.B., Sarwani, M., Sutandi, A. (2013): Harmonizing legacy soil data for digital soil mapping in Indonesia. Geoderma 192, 77-85.

Taghizadeh-Mehrjardi, R., Minasny, B., Sarmadian, F., Malone, B. (2014): Digital soil mapping of soil salinity in Ardakan region, central Iran. Geoderma 213, 15-28.

Thomas, M., Clifford, D., Bartley, R., Philip, S., Brough, D., Gregory, L., Willis, R, Glover, M. (2015): Putting regional digital soil mapping into practice in Tropical Northern Australia. Geoderma 241, 145-157.

Wang, D.C., Zhang, G.L., Pan, X.Z., Zhao, Y.G., Zhao, M.S., Wang, G.F. (2012): Mapping soil texture of a plain area using Fuzzy-C-Means Clustering method on land surface diurnal temperature difference. Pedosphere 22, 394-403.

Manuscript 3

Spatial Uncertainty-Guided Sampling to Improve Digital Soil Maps

CATENA, under review (2015)

Felix Stumpf*[1]), Karsten Schmidt[1]), Philipp Goebes[1]), Thorsten Behrens[1]), Sarah Schönbrodt-Stitt[1]), Alexandre Wadoux[1]), Wei Xiang[2]), Thomas Scholten[1])

[1])Department of Geoscience, Chair of Soil Science and Geomorphology, University of Tübingen, Rümelinstraße 19-23, 72070 Tübingen, Germany
[2]) Department of Geotechnical Engineering and Engineering Geology, China University of Geosciences, Lumo Road 388, 430074 Wuhan, P.R. China
*Corresponding author: University of Tübingen, Department of Geoscience, Chair of Soil Science and Geomorphology, Rümelinstraße 19-23, 72070 Tübingen, Germany, Phone: +49 7071 29 73942, E-mail: felix.stumpf@uni-tuebingen.de

Abstract

Digital soil mapping (DSM) products represent estimates of spatially distributed soil properties. These estimations comprise an element of uncertainty that is not evenly distributed over the area covered by DSM. If we quantify the uncertainty spatially, this information can be used to improve the quality of DSM by optimizing the sampling design. This study follows a DSM approach using a Random Forest regression model, legacy soil samples and terrain covariates to estimate topsoil silt and clay contents in a small catchment of 4.2 km² in the Three Gorges reservoir area, Central China. We aim (i) to introduce a method to derive spatial uncertainty, and (ii) to improve the initial DSM approaches by additional sampling, guided by the spatial uncertainty. The proposed uncertainty measure is based on local prediction intervals, derived from multiple decision tree models that form the Random Forest. We used the spatial uncertainty of the initial DSM approaches to stratify the study area and thereby demarcate potential sampling areas of high uncertainties. Further, we tested how precisely

available legacy samples cover the variability of the covariates within each potential sampling area to define the final sampling area and apply a purposive sampling design. For the final Random Forest model calibration, we combined the legacy sample set with the additional samples. This uncertainty-driven DSM refinement was evaluated by a comparison to a second approach, where the additional samples were replaced by a random sample set of the same size, obtained from the entire study area. For the comparative analysis, the quality of the approaches was assessed by independent, bootstrap-, and cross-validation. The DSM approach using the uncertainty-driven refinement performed best and reduced the averaged spatial uncertainty by 31% for silt and 27% for clay compared to the initial DSM approach. Using independent validation, the accuracy increased by the same proportions, while showing an overall accuracy of $R^2 = 0.59$ for silt and $R^2 = 0.56$ for clay. The results confirm the proposed method to be a reliable tool in DSM to support decision-making in context of soil management.

Keywords

Digital Soil Mapping, Spatial uncertainty, Sampling, Map quality improvement, Random Forest, Three Gorges Reservoir area

1. Introduction

Information on soil properties and their spatial distribution is essential for environmental protection and management. Because classical soil mapping is expensive and time consuming, cost-efficient methods are required (Behrens and Scholten, 2006; Behrens et al., 2010a; Bishop et al., 2001; Parr et al., 1992; Scull et al., 2003). Digital Soil Mapping (DSM) gives response to this demand in a quantitative manner by linking soil samples at points with correlated and colocated environmental predictor covariates using regression or classification rules (Lagacherie and McBratney, 2007; McBratney et al., 2000; McBratney et al., 2003; McMillan, 2008). Efficiency benefits of the DSM procedure largely depend on the availability and distribution of soil samples, and on the availability and quality of predictor covariates (Krol, 2008). While the covariates can be derived inexpensively from remote sensing data

(McBratney et al., 2003; Mendonça-Santos et al., 2008), the use of legacy soil data becomes increasingly interesting to avoid cost-intensive sampling campaigns (Krol, 2008; Lagacherie, 2008, Stumpf et al. 2015). Additionally, legacy data potentially serve as a knowledge base for understanding the local soil-landscape relationships, and thus for planning new sampling campaigns (Bui and Moran, 2003; Lagacherie et al., 1995).

DSM products present an approximated description of spatially distributed soil properties that comprise an element of uncertainty (Minasny and Bishop, 2008; Webster and Oliver, 2006). According to Nelson et al. (2011), the uncertainty in DSM originates from four error sources, which are (i) covariate error, (ii) model error, (iii) positional error, and (iv) analytical error. The covariate error refers to the error in the predictor covariates. As data are usually derived from remote sensing devices, the error is sourced in the measurement or in an additional interpolation error if the data requires geostatistical pre-processing (c.f., Bishop et al., 2006). The model error refers to an insufficient understanding and therefore to an oversimplification of real processes (Minasny and Bishop, 2008). Depending on the type of model the error can be ascribed to model specifications, estimations of model parameters or interpolations. McBratney et al. (2006) quantified the model error by applying bootstrapping that fits a model to different realizations of a data set to obtain an error variance. The positional error refers to the imprecise localization of spatial data, which is sourced in measurement errors of the GPS technology (c.f., Grimm and Behrens, 2009). The analytical error refers to measurement errors of soil properties occurring during the laboratory analysis. According to Viscarra Rossel and McBratney (1998), the analytical errors are low compared to other DSM error sources and in most cases well documented.

The use of legacy data as DSM input data prevents monetary and temporal expenditures, such as field sampling and laboratory analyses (Cambule et al., 2013). However, the increase in practicability is accompanied by additional error sources since including legacy data from multiple sources into DSM poses the question of reliability (Carré et al., 2007; Krol, 2008).

The various error sources in the DSM procedure as well as the use of legacy data combined with secondary information, such as terrain derivatives, opens the question of quality assessment. In DSM, this is still limited and primarily related to prediction accuracy (Finke, 2007; Grunwald, 2009; Hengl and Husnjak, 2006; Krol, 2008). The term ‘accuracy’ comprises measures of how close a prediction is to the true value (Everitt, 2002) and is

conventionally based on the variance between observed and predicted values at validation sites (Bishop et al., 2001). Brus et al. (2011) reviewed methodologies for validating soil maps, stating the importance of quantifying the accuracy by independent validation, using model-free samples.

However, disregarding the relevance of a comprehensive uncertainty assessment weakens the confidence of soil scientists and decision makers in the final DSM product (Fischer, 1999). According to Minasny and Bishop (2008) as well as Wellmann (2013), an uncertainty analysis should give response to three questions that may arise from a user`s perspective: (i) How good is the prediction, (ii) where are the areas of significant uncertainties and (iii) where to spend available resources to reduce uncertainties? In this context, Wellmann (2013) postulates that mapped information necessarily require analysis and visualization of compound errors if it is used for further decision making. Furthermore, Sun et al. (2013) emphasized the spatial aspect of uncertainty analyses, stating that mapped uncertainty is inevitable for DSM products and its further applications.

Few studies in the field of DSM addressed the issue of a comprehensive, spatially distributed and therefore practicable uncertainty analyses (Grunwald, 2009). However, if geostatistical methods are applied to map soil properties (Li and Heap, 2011; Tutmez and Hatipoglu, 2010), a spatially distributed error estimate, called kriging variance, is reported along with the predictions (Bourennane et al., 2007; Carré and Girard, 2002; Diodato and Ceccarelli, 2006; Knotters et al., 1995; Qu et al., 2013; Sun et al., 2013). These quality maps are restricted to the use of geostatistical interpolation methods and depend on the model-assupmtions used for the predictions (Brus et al., 2011). Besides geostatistical methods, Bishop et al. (2015) proclaimed to focus on uncertainty, which is represented by a prediction interval at each location. In this context, Malone et al. (2011) adapted a method by Shrestha and Solomatine (2006) for DSM, which spatially quantifies uncertainty by regionalizing prediction intervals (PIs) based on the residuals between predicted and observed data. However, this method was discussed as statistically complex and thus exhibiting limited practicability.

The present study builds on two initial DSM campaigns using Random Forest regressions and legacy samples for estimating topsoil silt (2 – 63 µm) and clay (< 2 µm) contents in a small catchment in the Three Gorges reservoir area, Central China. The objectives of the study are,

(i) to develop a method to derive spatially distributed uncertainties, and

(ii) to improve the initial DSM products based on additional sampling, guided by the spatial uncertainty.

Our case study is evaluated by a comparative analysis using (i) the initial sample set, (ii) the initial sample set augmented by uncertainty-guided sampling, and (iii) an approach where the initial sample set was augmented by random sampling. For the comparative analysis, the map quality is assessed by accuracy estimates of independent, bootstrap-, and cross-validation, as well as by the presented spatial uncertainty measure.

2. Material and Methods

2.1 Study site and geodatabase

The study area is a drainage basin of 4.2 km². As a part of the Three Gorges Reservoir area, it is located at the middle reaches of the Yangtze River in Hubei, Central China (31°1′24″N, 110°20′35″E). The elevation ranges from 469 m to 1,483 m a.s.l. with an average of 1,053 m. Slope inclinations range from 0° to 53° with an average of 26°. With 72%, the majority of slopes is exposed to the north (Schönbrodt-Stitt et al., 2013; Strehmel et al., 2015). According to FAO (2006) silty clay (SiC) is predominant. A large area of woodland (81%) alternates with scattered plots of cropland (15%) and sparsely distributed farm buildings (4%).

The predictor covariates (Table 1) for the DSM approach present proxies to describe geomorphological repositioning processes of silt and clay contents locally and regionally within the study area. We derived 21 continuous terrain attributes from a digital elevation model (cell size 25 m x 25 m) as continuous predictor covariates, using SAGA GIS (SAGA GIS, 2011).

Table 1: Environmental covariates with summary statistics.

Covariate	Unit	Minimum	Maximum	Average	Standard deviation
Altitude	m a.s.l.	469	1483	1054	255
Northing	-	1.42E-02	1.75E-02	1.62E-02	1.10E-03
Easting	-	0	1.30E-02	4.98E-03	3.74E-03
Wetness Index (SWI)	-	0	14.8	5.9	1.8
Slope angle	degree	0	53.2	26.4	6.9
Slope angle, maximum	degree	0	0.72	0.42	0.13
Slope length	m	0	2854	184	293
Catchment area	m^2 (log)	6.43	15.17	8.66	1.4
Plane curvature	m^{-1}	-1.03E-02	1.09E-02	-4.28E-05	2.82E-03
Profile curvature	m^{-1}	-1.09E-02	1.04E-02	-1.90E-04	2.30E-03
Combined curvature	m^{-1}	-8.80E-01	8.10E-01	-4.90E-03	1.54E-01
Flow accumulation	pixels (log)	2.8	6.1	3.9	0.56
Overland flow distance	m	0	377	91.9	75.1
Vertical flow distance	m	0	135	29.8	26.1
Horizontal flow distance	m (log)	0	2.6	1.5	0.88
Altitude above channel (AAC)	m	0	307	92	62
Terrain ruggedness	-	0.18	17.2	8.4	2.4
Mass balance index	-	-0.79	2.04	0.13	0.52
Convergence index	-	0	28.8	8.7	3.8
Position index	m	-26.9	35.7	0.25	7.2
Protection index	-	0	0.14	0.07	0.02

In context of a reconnaissance survey, 80 topsoil samples were obtained. We randomly selected 60 samples to form the calibration set (LD) for the initial DSM approaches, estimating topsoil silt and clay contents. We augmented LD by 30 additional samples according to the proposed spatial uncertainty-guided sampling to form a second calibration set (LD_{Unc}) with a sample set size n = 90. For a comparative evaluation, we generated a third calibration set (LD_{Random}) by augmenting LD with 30 additional samples, obtained according to a simple random sampling within the entire study area (n = 90). The remaining 20 model-free samples from the reconnaissance survey were used to validate the predictions independently.

All soil samples used in this study were obtained and analyzed identically. At each sampling site five topsoil (0-25 cm depth) sub samples were pooled, four from the corner points of a surrounding 40 cm x 40 cm square and one from the center point of the square. For particle size analysis, the samples were dried (40°C) and sieved (< 0.63 mm). Subsequently, silt and clay contents were separated using the Sedigraph III 5120 by micromeritics GmbH.

2.2 Spatial uncertainty

Spatial uncertainty was derived from the initial DSM approaches for silt and clay contents using Random Forest (RF) regression and thereby linking the soil observations with the spatial predictor covariates. RF presents an ensemble classifier based on multiple randomized decision tree models (Breiman, 2001). A decision tree applies a set of binary rules to compute a target variable (Quinlan, 1986). In RF regression, the final result is the average of all predictions of the tree models. Since RF is robust to noise and multi-collinearity in the predictors (Behrens et al., 2010b; Díaz-Uriate and de Andres, 2006), no pre-processing and pre-selection of covariates is required.

Robustness of the RF model primarily depends on a large number of individual trees, which should be as diverse as possible (Prasad et al., 2006). An optimized tree diversity ensures to derivate the entire scope of relevant information, comprised in the model input data, for the aggregated final prediction (Hansen and Salamon, 1990; Peters et al., 2007). RF increases the diversity of the trees by using randomized subsets of predictor covariates at each split of the trees and a randomized (by bootstrapping) soil sample set for each tree.

The subset of samples, which are not used to build a specific tree, are called out-of-bag (oob) data. Using this oob data for validating the respective trees, an error estimate (oob-error) can be derived by averaging the MSE (mean squared error) over all trees. The number of trees (k) and the size of the random feature subset at each node (m_{try}) are user-defined model parameters. Both can be determined by using a grid-learning approach comparing the oob-errors of various RF realizations with different settings for k and m_{try} (Grimm et al., 2008; Schmidt et al. 2010). We computed the initial maps of topsoil silt and clay contents with k = 1,500 and $m_{try} = 2\sqrt{p}$, with p presenting the total number of covariates (Breiman, 2001). We

used all available covariates and the legacy sample set (LD) as input data. For processing, we used the R-package 'randomForest' (Liaw and Wiener, 2002).

The uncertainty mapping is based on the concept to generate a compilation of equiprobable realizations of spatial model predictions and analyzing the divergences among the simulated maps (Goovaerts, 2001). In RF, this concept is already inherent since the RF predictions are aggregated from the results of multiple randomized decision tree models (Breiman, 2001). Due to randomization, the results of the single tree predictions are spatially variable (Grimm and Behrens, 2010; Peters et al., 2007). Thus, a specific prediction interval at each location can be derived. The variability of an interval refers to the uniformity of the single decision tree results, and therefore, the local robustness of the RF model. Consequently, a prediction interval with a high statistical variance s^2 indicates decreased robustness and vice versa (Sun et al., 2013). In this context, we applied s^2 as local error variance, thus generating a spatially distributed uncertainty measure err^{s^2}. For each location j, with k outlining the number of trees (i =1, 2,…, k) and x indicating the values of the prediction interval, err^{s^2} is defined as the following,

$$err^{s^2}(j) = \frac{1}{k} \sum_{i=1}^{k} (x_i - \bar{x})^2. \qquad \text{(Eq.1)}$$

Accordingly, we computed uncertainty maps for both DSM approaches, estimating silt and clay contents. For processing, we used the R-package "base" (R Core Team, 2014).

2.3 Uncertainty-guided sampling

The initial soil property maps were based on legacy samples, which were not specifically obtained to cover the variability of the target soil properties in the study area. Hence, we refined the mapping approaches by augmenting the initial legacy sample set. To limit the sampling effort, we applied one spatial uncertainty-guided sampling scheme for both target variables silt and clay to purposively obtain additional samples. Therefore, we merged the spatial uncertainty maps of both RF approaches (U_1, U_2) to a single combined uncertainty map (U_{com}), which then underlies the sampling. The merging was conducted by retaining the maximum (*max*) uncertainty value (M_{errs^2}) of the standardized spatial uncertainties u_1 and u_2 for each location j according to,

$$M_{errs^2}(j) = max(u_{1j}, u_{2j}). \quad \text{(Eq. 2)}$$

Subsequently, we determined a new sampling area based on areas with increased uncertainty values of U_{com}, reflecting a decreased coverage of the soil variability by the legacy samples. Primarily, four potential sampling areas were derived, defined by the entire study area (Q1) and by the quartile-breaks > 25% (Q2), > 50% (Q3), and > 75% (Q4) of U_{com}. Since the predictor covariates serve as proxies for the soil variability, we tested how precisely available legacy samples cover the variability of the covariates within each potential sampling area. This was achieved by computing the divergence between the distribution in the potential sampling area (P_1) and the distribution based on available legacy samples (P_2) referring to each covariate separately. We used the Kullback-Leibler divergence (KL; Kullback and Leibler, 1951) to examine the divergence between two distributions.

$$KL\,(P_1 \| P_2) = \int p_1\,(x)\; log\, \frac{p_1(x)}{p_2(x)}\, dx. \quad \text{(Eq. 3)}$$

with p_1 and p_2 indicate the densities of P_1 and P_2.

The sum of the divergences over all covariates (t =1, 2,…, m) indicates a measure (KL_{sum}) on how precise the legacy samples cover the variability of silt and clay. While an increased divergence indicates less coverage and vice versa, KL_{sum} takes the form

$$KL_{sum} = \sum_{t=1}^{m} KL_t. \quad \text{(Eq. 4)}$$

Since the potential sampling areas were defined by quartile-breaks of the combined uncertainty distribution, we assumed an increasing KL divergence from Q1 to Q4. Comparing KL_{sum} of all potential sampling areas, we finally selected this area for sampling, where KL_{sum} starts to level up disproportionally. For processing we used the R-packages “flexmix” (Grün and Leisch, 2008) and “base” (R Core Team, 2014).

Within the final sampling area we applied an adapted hypercube sampling design according to Stumpf et al. (2015) to obtain 30 additional topsoil. This design follows conditioned Latin Hypercube Sampling (cLHS), which optimally covers the variability of multiple covariates by the sample set with a limited sample set size (Brungard and Boettinger, 2010; Minasny and McBratney, 2006). The adaption additionally compensates for limited field accessibility,

prevents redundancies in the covariate space referring to legacy samples, and enables for sampling several soil properties by one design. We used the R-packages "clhs" (Roudier, 2011) and "base" (R Core Team, 2014) for processing.

2.4 Prediction and evaluation

We set up three DSM approaches, each estimating topsoil silt and clay contents and using all predictor covariates (Table 1). For calibration we used the sample sets LD, LD_{Random}, and LD_{Unc} for the respective approach. Further, we applied the spatial uncertainty measure (err^{s^2}), as well as accuracy estimates based on cross-validation (*cv*), bootstrap validation (*boot*) and independent validation (*val*) to assess the quality of the approaches comparatively.

Both, *cv* and *boot* are based on statistical resampling of the calibration set. Therefore, the methods provide a generalization error of a calibration model and do not require a model-free validation data set (Good, 2006). While *cv* provides a nearly unbiased but highly variable accuracy estimate (Kim, 2009), *boot* is biased upwards but less variable, and thus appropriate for smaller sample sets (Molinaro et al., 2005).

For *cv*, the calibration set was randomly split into q subsets (u = 1, 2,…, q) of equal size. Leaving out subset q and fitting the model to the other q-1 subsets, the prediction error was computed using the left-out qth subset. Applying this repeatedly for each subset q and averaging the predictions errors, the *cv* error measure err^{cv} was obtained (Borra and Di Ciaccio, 2010). Thus, the equation for *cv* takes the form,

$$err^{cv}(q) = \frac{1}{q} \sum_{u=1}^{q} err_u^{cv}. \qquad \text{(Eq. 5)}$$

For *boot*, bootstrap sample sets were used instead of applying subsets of the initial calibration set to repeatedly fitting the model. A bootstrap sample set was generated by sampling random observations from the initial calibration set (n) with replacement. Applying a bootstrap sample set for model fitting, the prediction error was derived using the distinct observations from the initial calibration set for validation. The number of distinct observations appearing in the validation set is 0.368n (Efron and Tibshirani, 1993). The bootstrap validation error err^{boot} was obtained by averaging the model prediction errors of b bootstrap sample sets (z = 1, 2,…, b). Thus, the equation for bootstrap validation takes the form,

$$err^{boot}(b) = \frac{1}{b} \sum_{z=1}^{b} err_z^{boot}. \quad \text{(Eq. 6)}$$

The coefficient of determination (R^2) and root mean squared error (*RMSE*) were used as prediction error measures for the accuracy estimates err^{cv} and err^{boot}. R^2 represents a measure that gives the proportion how well the variance of observed values is explained by predicted values. While R^2 ranges between 0 and 1, an increased R^2-value indicates increased certainty of making predictions from the model. The *RMSE* outlines a measure of the differences between predicted and observed values. These residuals, respective predictions errors are aggregated into a single *RMSE* error, giving a scale-dependent measure of the predictive capability of the model. For v instances in a data set (l= 1, 2,…, v), with y^{pre} presenting the predicted values and y^{ob} the observed values the R^2, respectively *RMSE* takes the form,

$$R^2 = 1 - \frac{\sum_{l=1}^{v}(y_l^{ob} - y_l^{pre})^2}{\sum_{l=1}^{v}(y_l^{ob} - \overline{y^{ob}})^2} \quad \text{(Eq. 7)}$$

and

$$RMSE = \sqrt{\frac{\sum_{l=1}^{v}(y_l^{pre} - y_l^{ob})^2}{v}} \quad \text{(Eq. 8)}$$

For *cv* and *boot*, we determined the number of subsets q, respectively number of bootstrap sample sets b, as 10. For processing, we used the R-package "caret" by Kuhn (2009).

3. Results

3.1 Spatial uncertainty-guided sampling

The average combined uncertainty (M_{errs^2}) in the entire study area, which corresponds to the potential sampling area Q1, accounts for 0.63 with a standard deviation (sd) of 0.12. Since the potential sampling areas Q2, Q3, and Q4 were defined according to the quartiles-breaks of the combined uncertainty (> 25%, > 50%, > 75%), we expected successively increasing averaged M_{errs^2}-values. We found M_{errs^2} = 0.72 in Q2 (sd = 0.1), M_{errs^2} = 0.78 in Q3 (sd = 0.07), and M_{errs^2} = 0.86 in Q4 (sd = 0.04).

Similarly, comparing each distribution of area-covering covariates with the distributions of covariates from available legacy samples in Q1 to Q4, a successively increasing divergence of the distributions in Q4 was revealed. The summarized Kullback-Leibler (KL) divergences in Q1 amounts to 16.4, in Q2 to 24.5, in Q3 to 29.2, and in Q4 to 66.8. However, the increase in Q4 amounts to 130% compared to 19% in Q3 and 49% in Q2. Subsequently, the available legacy samples in Q4 outlined a disproportionally decreased coverage concerning the covariates (Figure 1). This results in Q4 as the final sampling area to obtain the additional samples of LD_{LHS} (Figure 2b).

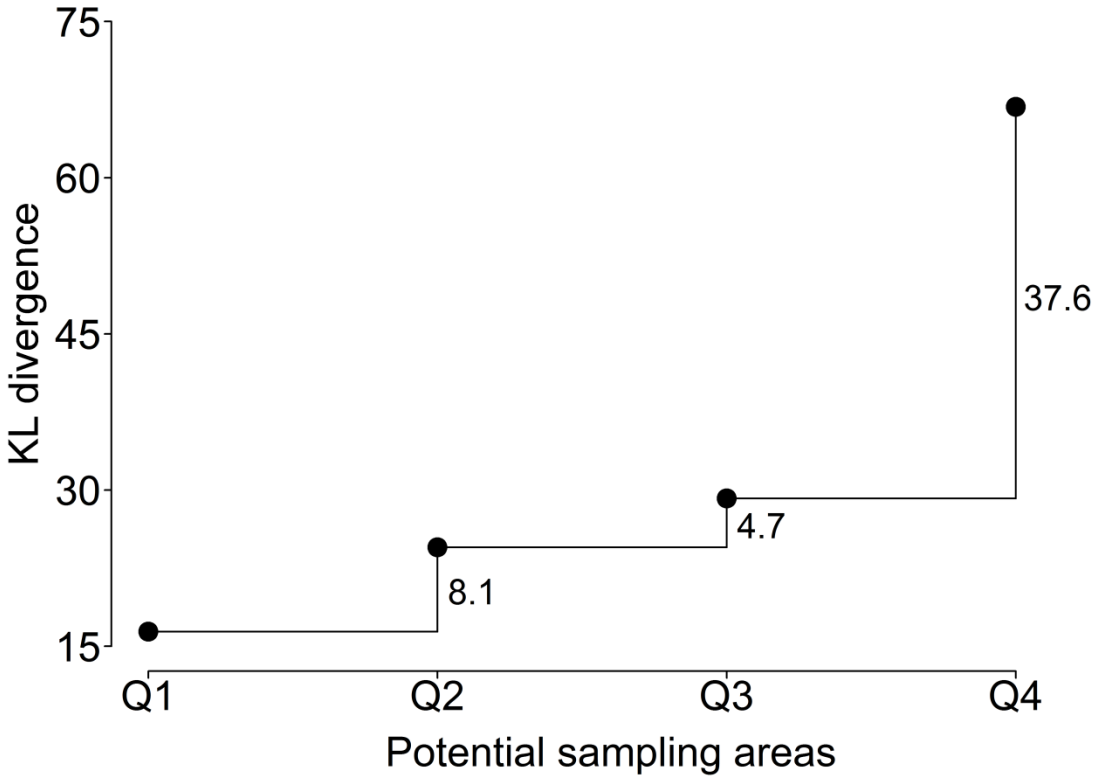

Figure 1: Determination of the sampling area. Comparing the coverage of covariates by the legacy samples. The x-axis shows the potential sample areas Q1 to Q4. The y-axis shows the summarized Kullback-Leibler (KL) divergences between the distributions of covariates within the area and the distributions of covariates in the legacy samples.

Mapping the combined uncertainty reveals increased values in the north and south of the study area, where the topography shows increased heterogeneity. Particularly, uncertainty hotspots with $M_{errs^2} > 0.8$ were predicted for areas along the topographic depression lines. In the middle-west and –east of the study area coherent areas of decreased uncertainties with $M_{errs^2} < 0.5$ occur (Figure 2a).

The LD_{Unc} samples were obtained according to an adapted cLHS design that optimally covers the variability of multiple covariates. Furthermore, the sample sites are spatially evenly distributed within the sampling area Q4 (Figure 2b). The calibration set LD shows a cluster in the north of study area. The sample sites of the additional samples for LD_{Random} as well as the sites for the validation set were evenly distributed (Figure 2a).

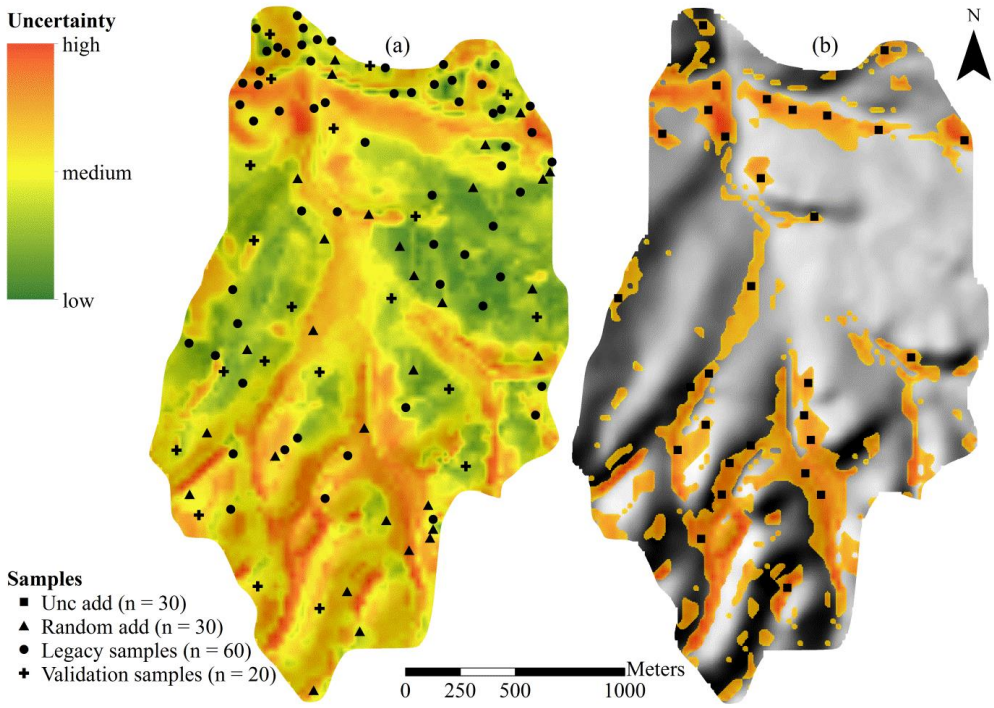

Figure 2: (a) Combined spatial uncertainty of initial silt and clay predictions with the legacy sample set (LD), the additive samples according to a simple random sampling (Random add) and the validation data. (b) Area for uncertainty-guided sampling with the additive samples (Unc add).

3.2 Predictions and evaluation

3.2.1 Calibration sets and predictions

According to the laboratory analysis, the distributions of the model calibration sets LD (*n* = 60), LD_{Unc} (*n* = 90) and LD_{Random} (*n* = 90) show similar patterns in central tendency and variability referring to both target soil properties (Figure 3). The average topsoil silt content amounts to 59.4% in LD (sd = 9.2), to 59.9% in LD_{Random} (sd = 9.0), and to 60.8% in LD_{Unc} (sd = 8.9). The average topsoil clay content varies from 28.5% in LD (sd = 6), to 29.6% in LD_{Random} (sd = 6), and to 28.9% in LD_{Unc} (sd = 5.9).

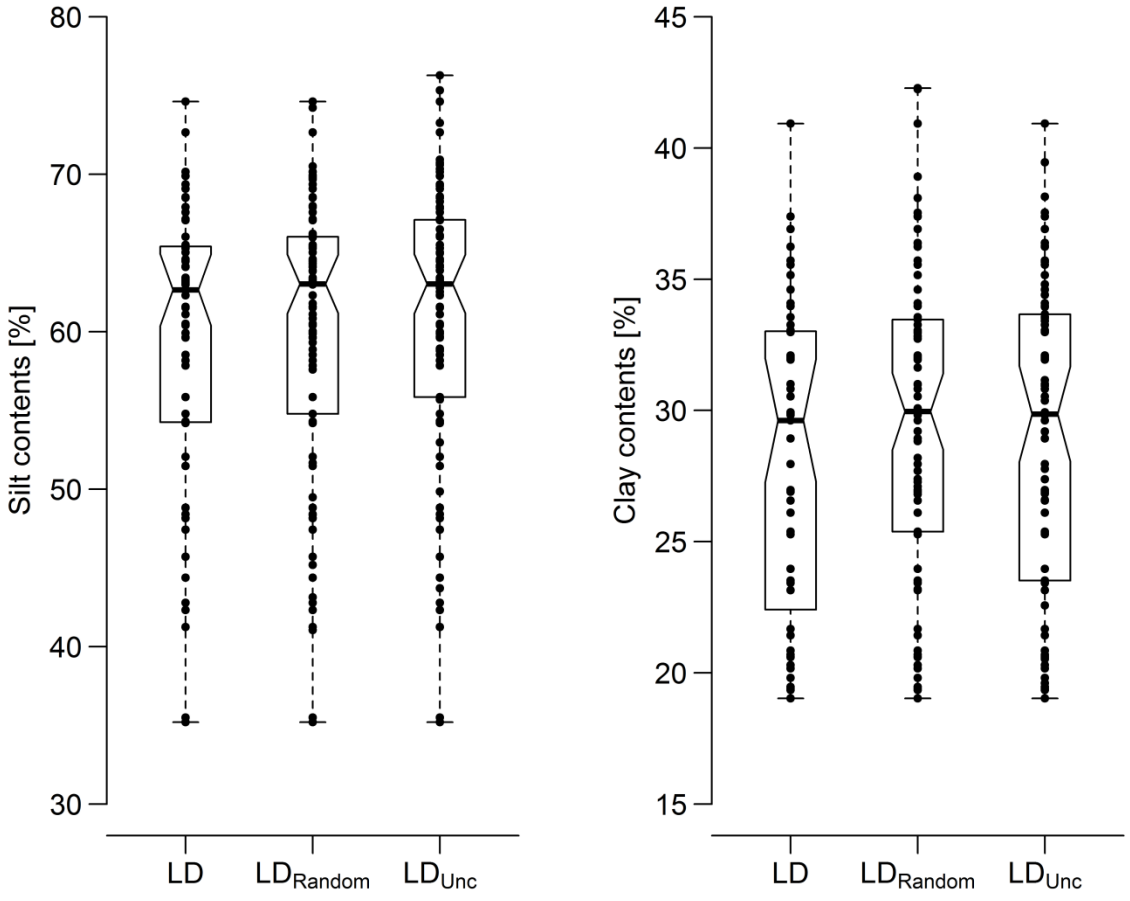

Figure 3: Observed topsoil silt and clay contents for all calibration sets (LD, LD_{Random}, LD_{Unc}). The notches indicate the median of the respective distribution.

All RF prediction approaches of silt and clay contents show increased averaged values compared to the averaged observed values of the laboratory analysis. The increase varies from 2% to 2.5% for the silt contents and from 1% to 2.7% for the clay contents.

The predicted average silt content amounts to 61.6% (sd = 3.7) for the LD approach, to 61.9% (sd = 4.4) for the LD_{Random} approach, and to 63.3% (sd = 3.9) for the LD_{Unc} approach. All mapping approaches show a similar trend with increasing silt contents from the north to the south. Generally, decreased silt contents occur in the topographic depression lines (Figure 4).

The RF predictions of clay contents show an average of 29.9% for the LD approach (sd = 2.6). The average of the LD_{Random} approach amounts to 30.7% (sd = 2.8), while an average of 31.6% was found for the LD_{Unc} approach (sd = 2.5). All mapping approaches show the lowest clay contents in the very north of the study area. In the middle part, increased clay contents are homogeneously distributed. In the south, clay contents are generally increased compared to the very north but decreased and less homogeneously distributed compared to the middle part (Figure 4).

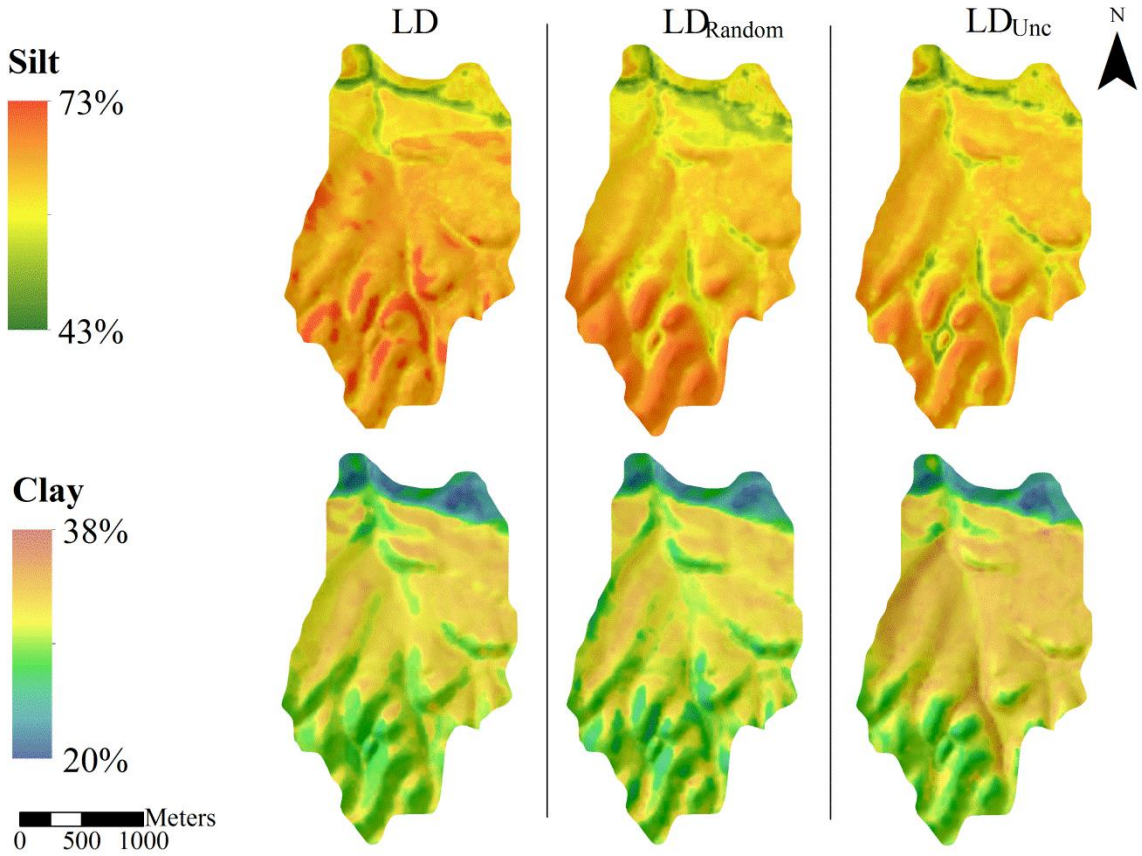

Figure 4: Mapping results for predicted silt and clay contents using the legacy sample set (LD), LD combined with additional samples according to simple random sampling (LD_{Random}), and LD combined with additional samples according to the uncertainty-guided sampling (LD_{Unc}).

3.2.2 Model comparison

For both target variables, the averaged spatial uncertainty of the prediction approaches gradually decreases from the LD approach (silt: 9.3; clay: 7.7), followed by the LD_{Random} (silt: 6.7; clay: 5.9) to the LD_{Unc} approach (silt: 6.4; clay: 5.6). This trend of a quality increase also applies for the prediction accuracies, derived by cross- (*cv*), bootstrap- (*boot*), and independent (*val*) validation (Table 2).

Referring to the silt prediction accuracy and according to the independent validation (*val*), the LD approach shows an explained variance of $R^2 = 0.45$, $R^2 = 0.54$ for the LD_{Random} approach, and $R^2 = 0.59$ for the LD_{Unc} approach. The clay predictions show *val*-accuracies of $R^2 = 0.44$

(LD approach), R^2 = 0.47 (LD_{Random} approach), and R^2 = 0.56 (LD_{Unc} approach; Table 2; Figure 5).

Moreover, comparing the prediction approaches according to the target variables shows a generally increased level of uncertainty and decreased level of *cv*- and *boot*-accuracy for the silt predictions. Across all approaches the uncertainty increase ranges between 12% and 17%, while the accuracy decrease ranges from 10% to 17% for *cv*, and from 17% to 22% for *boot*. Referring to *val*, the accuracies of silt and clay predictions are equal, , while the divergences range between 2% and 13% across all approaches (Table 2; Figure 5).

Table 2: Spatial uncertainty and accuracies for the predictions of silt and clay contents, listed according to the prediction approaches. Averaged spatial uncertainty (unc), cross- (cv), bootstrap- (boot) and independent- (val) validation are used.

		unc	cv		boot		val	
Target variable	Prediction approach	$\sum err^{s^2}$ {1,…,n}/n	R^2	RMSE	R^2	RMSE	R^2	RMSE
Silt	**LD**	9.3	0.39	5.68	0.44	5.59	0.45	5.33
	LD_{Random}	6.7	0.44	6.13	0.46	5.72	0.54	4.86
	LD_{Unc}	6.4	0.47	4.64	0.54	4.58	0.59	4.27
Clay	**LD**	7.7	0.47	4.95	0.54	4.41	0.44	5.09
	LD_{Random}	5.9	0.49	4.78	0.59	3.82	0.47	4.63
	LD_{Unc}	5.6	0.55	4.52	0.65	3.59	0.56	4.49

Furthermore, we compared the spatial uncertainty distributions of the silt and clay prediction approaches. Referring to the silt predictions, the uncertainty values of the LD approach vary uniformly with sd = 1.1 and a range from 8.6 to 9.8. The very north and a single area in the middle part shows low uncertainty values smaller than the 25%-quartile (9.1), while high values larger than the 75%-quartile (9.4) are distributed evenly over the study area. The LD_{Random} approach shows an increased variability with sd = 1.8 and a range from 5.5 to 8.1. Increased values larger than 75%-quartile (>7.3) were found in the north and are less pronounced in the south of the study area. The LD_{Unc} approach shows a similar distribution with sd = 1.7 and a range from 5.5 to 8.2, while increased variability and high values larger than 75%-quartile (6.6) were found in the north (Figure 5).

Referring to the clay predictions, the LD approach also shows a comparatively low variability with sd = 1 and a range from 6.9 to 8.5. The variability of the LD_{Random} approach is increased with sd = 1.4 (range: 5-7.8), while LD_{Unc} approach shows a decreased variability with sd = 0.7 (range: 5.3-6.4). The spatial distribution of all approaches show increased values larger than 75%-quartile (LD approach: 8; LD_{Random} approach: 6; LD_{Unc} approach: 5.7) in the north of the study area (Figure 5).

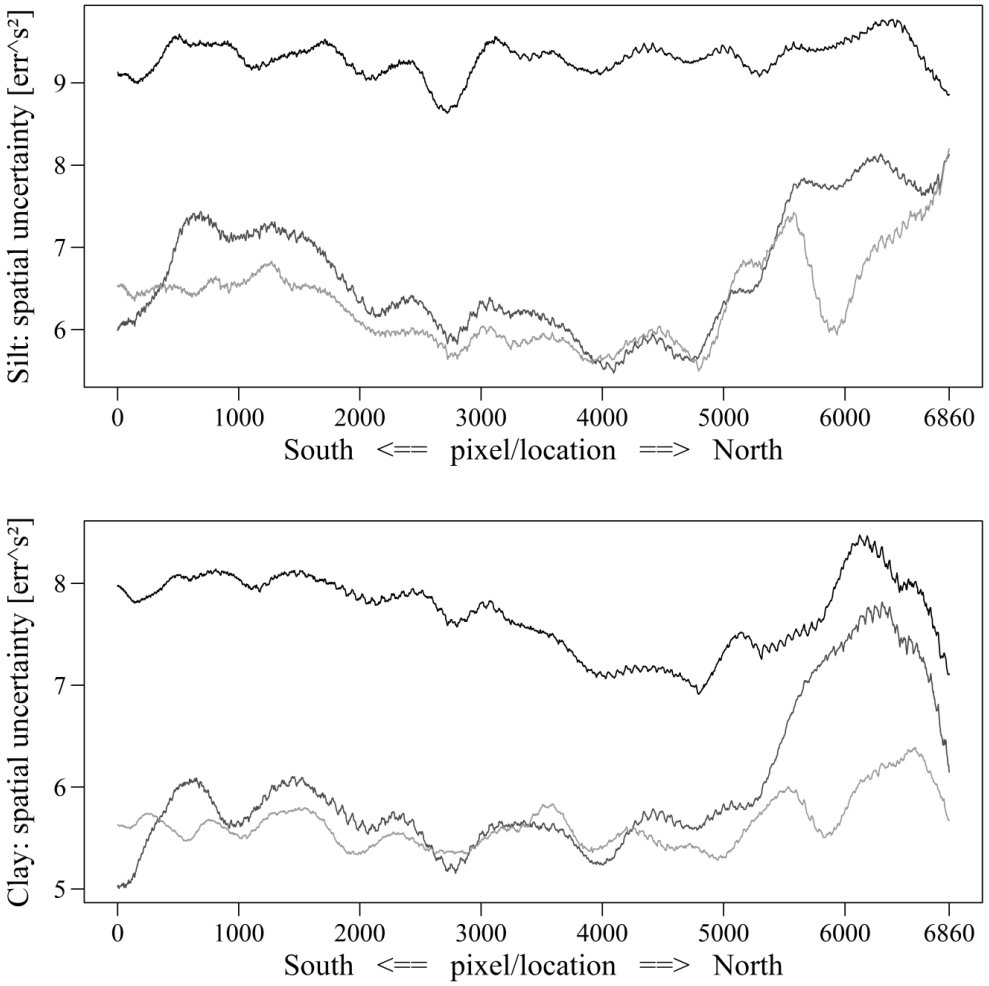

Figure 5: Comparison of spatial uncertainty for silt (above) and clay (below) predictions. The curves refer to prediction approaches using the calibration sets LD (black), LD_{Random} (dark gray) and LD_{Unc} (bright gray). The x-axis schematically indicates the localization of the values in the study area. The y-axis indicates the spatial uncertainty.

4. Discussion

4.1 Spatial uncertainty – methodological comparison

The aim of our study was to derive a practicable spatial uncertainty measure in context of a DSM approach using Random Forest. For geostatistical soil property mapping, the kriging variance represents a spatially distributed error estimate (Bourennane et al., 2007; Carré and Girard, 2002; Diodato and Ceccarelli, 2006; Knotters et al., 1995; Qu et al., 2013; Sun et al., 2013). Generally in geostatistics, the spatial dependence of a target variable is modeled by the variogram function, whereby local predictions are derived from the weighted averages of neighboring observations (Goovaerts, 1999). While the weights are determined by minimizing the variance of each local prediction, this quantity represents the kriging error (Burgess and Webster, 1980). Besides, Malone et al. (2011) proposed a method to quantify spatial uncertainties based on prediction intervals (PI-uncertainty). Primarily, the intervals are derived from the residuals between predicted and observed data. Subsequently, a covariate space is clustered according to similar residuals. Then, a prediction interval is generated for each cluster based on the empirical distribution of residual observations of each cluster. According to the grade of membership to each cluster, a prediction interval is ascribed for each prediction location in the covariate space.

Our spatial uncertainty method is based on multiple decision tree realizations within a Random Forest (RF) regression approach (c.f. 2.2). The uncertainty measure is also expressed by the variability of prediction intervals. However, the intervals are straightforwardly derived for each prediction location, based on the results of the multiple randomized RF decision tree models (c.f. 2.2). Thus, compared to the PI-uncertainty, our spatial uncertainty does not require an additional regionalization of prediction errors, which limits practicability due to statistical complexity and usually scarce temporal resources. Nevertheless, the PI-uncertainty accounts for all sources of uncertainty, only depending on the residuals derived from the model output and the observed data. Contrary, the kriging error depends on the model-assumption for the variogram, the observed soil data and their spatial configuration (Brus et al., 2011; Lark and Lapworth, 2012). Furthermore, the kriging error relies on the use and limitations of geostatistical methods, such as a relatively high sample density and the smoothing of local details in the predictions (Goovaerts, 1999). The application of our spatial

uncertainty measure also implies dependencies, such as the prerequisite to use a RF prediction model. Moreover, the RF model is often discussed to only allow limited interpretability, since the relation between predictor and prediction cannot be assessed for each tree. However, RF is increasingly applied in DSM (Grimm et al., 2008; Heung et al., 2014; Ließ et al., 2012; Schmidt et al., 2014; Wiesmeier et al., 2011). This can be ascribed to the combined merits of modeling non-linear relationships, handling categorial and continuous covariates, resistance to overfitting, robustness to noise in the feature space, an implemented unbiased measure of error and variable importance, only a few user-defined model parameters and a reduced computational load (Díaz-Uriate and de Andrés, 2006; Peters et al., 2007; Svetnik et al., 2003).

While the kriging error presents a well-established spatial error estimate (Bourennane et al., 2007; Carré and Girard, 2002; Diodato and Ceccarelli, 2006; Knotters et al., 1995; Qu et al., 2013; Sun et al., 2013), the PI-uncertainty is less common. Malone et al. (2011) applied it using a DSM case study predicting organic carbon and available water capacity. Our method was approved by comparing three RF prediction approaches referring to conventional accuracy measures (c.f. 2.4) and the proposed uncertainty measure (c.f. 2.2). The calibration of the model approaches were based on legacy samples (LD), LD augmented by uncertainty-guided sampling (LD_{Unc}), and LD augmented by simple random sampling (LD_{Random}, c.f. 2.1, 2.4), respectively. For both target soil properties, silt and clay, all quality estimation methods show uniform results. Thus, the LD_{Unc} approach outperforms the approach using LD_{Random}, while both outperform the LD approach in terms of a decreased spatial uncertainty (Table 2; Figure 5) and increased prediction accuracies (Table 2). The uniform similarity between the results of all quality estimations approves the validity of (i) the conventional accuracy measures and (ii) the proposed spatial uncertainty measure.

4.2 Soil map refinement – the case study

A further aim of our study was to improve the initial DSM approaches of silt and clay predictions that were solely based on legacy samples. Thus, we augmented the initial legacy calibration set by an uncertainty guided sampling. Clifford et al. (2014) selected additional samples that in combination with available legacy samples cover the covariate space and approved the method by a simulation study. Carré et al. (2007) proposed a method to identify

locations for additional samples by previously analyzing the distribution of legacy samples in the covariate space. Although the approach was approved by two different data sets, the method only refers to the covariate space, thus, disregarding geographical information. In our study, we stratified the study area according to the quartile distribution of the previously determined spatial uncertainty. Subsequently, we obtained additional samples in this strata with the lowest conformity between the covariate distributions in the strata and available legacy samples (Figure 1).

We pursued to improve both initial DSM approaches of silt and clay predictions with one augmented sample set. Therefore, we combined the spatial uncertainty values of both approaches (c.f. 2.3). Our procedure implies a favored incorporation for the soil property, which generally shows increased prediction uncertainty. Furthermore, the procedure implies a harmonization in quality of both initial soil property predictions. The results confirmed these implications, while silt was favored with an uncertainty decrease of 31% compared to clay with a decrease of 27% in the LD_{Unc} approaches (Table 2; Figure 5). The similar proportions of decreasing uncertainty between both predictions, approves the method of combining the uncertainty maps in our case study.

Furthermore, Collard et al. (2014) sampled a legacy soil map for calibrating a regression model and improved the class purity by 10%. Other studies showed an accuracy improvement of 6% to 19%, using DSM approaches to upgrade legacy soil maps (Kempen et al., 2009; Rad et al., 2014; Yang et al., 2011). Our results show accuracy increases of 14% for the silt predictions and 12% for the clay, comparing the LD to LD_{Unc} approach. Generally in DSM, accuracies with $R^2 > 70\%$ are unusual, while $R^2 < 50\%$ are common (Malone et al., 2009). The accuracy results of our best performing RF approach, calibrated with LD_{Unc}, show explained variances of $R^2 = 0.59$ for silt and $R^2 = 0.56$ for clay. The successful application of the spatial uncertainty measure, thus, improving the quality of initial DSM products by an uncertainty guided sampling, approves the practicability and validity of the method.

5. Conclusion

Within the framework of a DSM approach using the widely applied Random Forest regression model, we present a method to straightforwardly derive reliable information on spatial

uncertainties. We use prediction intervals based on the multiple randomized decision trees of the Random Forest model to obtain a compound uncertainty measure for each location.

Furthermore, we apply the uncertainty measure to improve the quality of initial DSM products, which are based on legacy samples. This was accomplished by combining the legacy sample set with additional samples, obtained by sampling in areas of high uncertainties and for two soil properties in one purposive sampling design.

The target soil properties of our case study were topsoil silt and clay contents within a small catchment in the Three Gorges Reservoir area, Central China. We approved the method for its validity, showing convincing quality improvements referring to the proposed spatial uncertainty and conventional accuracy measures for both DSM products. The successful application approves the method as a reliable tool to support decision-making in context of soil management.

Acknowledgements

This study was conducted within the framework of the Sino-German joint research project YANGTZE GEO. The funding by the German Federal Ministry for Education and Research. (BMBF, grant no. 03G 0827A) is highly acknowledged. We particularly thank all students from the China University of Geosciences in Wuhan (P.R. China) that were involved in field campaigns and laboratory analyzes.

References

Behrens, T., Schmidt, K., Zhu, A.X., Scholten, T., 2010a. The ConMap approach for terrain-based digital soil mapping. Eur. J. Soil Sci. 61, 133-143.

Behrens, T., Zhu, A.X., Schmidt, K., Scholten, T., 2010b. Multi-scale digital terrain analysis and feature selection in Digital Soil Mapping. Geoderma 155, 175-185.

Behrens, T., Scholten, T., 2006. Digital soil mapping in Germany – a review. J. Plant Nutr. Soil Sci. 169, 434-443.

Bishop, T.F.A., Horta, A., Karunaratne, S.B., 2015. Validation of digital soil maps at different spatial support. Geoderma 241, 238-249.

Bishop, T.F.A., Minasny, B., McBratney, A.B., 2006. Uncertainty analysis for soil-terrain models. Int. J. Geog. Inf. Sci. 20, 117-134.

Bishop, T.F.A., McBratney, A.B, Whelan, B.M, 2001. Measuring the quality of digital soil maps using information criteria. Geoderma 103, 95-111.

Borra, S., Di Ciaccio, A., 2010. Measuring the prediction error. A comparison of cross-validation, bootstrap and covariate penalty methods. Comput. Stat. Data An. 54, 2976-2989.

Bourennane, H., King, D., Couturier, A., Nicoullaud, B., Mary, B., Richard, G., 2007. Uncertainty assessment of soil water content spatial patterns using geostatistical simulations: an empirical comparison of simulation accounting for single attribute and a simulation for secondary information. Ecol. Model 205, 323-335.

Breiman, L., 2001. Random Forests. Mach. Learn. 45, 5-32.

Brungard, C.W., Boettinger, J.L., 2010. Conditioned Latin Hypercube Sampling: Optimal sample size for Digital Soil Mapping of arid rangelands in Utah, USA, in: Boettinger, J., Howell, D., Moore, A., Hartemink, E., Kienast-Brown, S. (Eds.): Digital Soil Mapping Bridging Research, Environmental Application, and Operation. Springer, pp. 67-75.

Brus, D.J., Kempen, B., Heuvelink, G.B.M., 2011. Sampling for validation. Eur. J. Soil Sci. 62, 394-407.

Bui, E.N., Moran, C.J., 2003. A strategy to fill gaps in soil survey over large spatial extends: an example from the Murray-Darling basin of Australia. Geoderma 111, 21-44.

Burgess, T.M., Webster, R., 1980. Optimal interpolation and isarithmic mapping of soil properties. The semi-variogram and punctual kriging. J. Soil Sci. 31, 315-331.

Cambule, A.H., Rossiter, D.G., Stoorvogel, J.J., 2013. A methodology for digital soil mapping in poorly-accessible areas. Geoderma 192, 341-353.

Carré, F., McBratney, A.B., Minasny, B., 2007. Estimation and potential improvement of the quality of legacy soil samples for digital soil mapping. Geoderma 141, 1-14.

Carré, F., Girard, M.C., 2002. Quantitative mapping of soil types based on regression kriging of taxonomic distances with landform and land cover attributes. Geoderma 110, 241-263.

Clifford, D., Payne, J.E., Pringle, M.J., Searle, R., Butler, N., 2014. Pragmatic soil survey design using flexible Latin hypercube sampling. Comput. Geosci. 67, 62-68.

Collard, F., Kempen, B., Heuvelink, G.B.M., Saby, N.P.A., Richer de Forges, A.C., Lehmann, S., Nehlig, P., Arrouays, D., 2014. Refining a reconnaissance soil map by calibrating regression models with data from the same map (Normandy, France). Geoderma Regional 1, 21-30.

Díaz-Uriarte, R., De Andrés, S., 2006. Gene selection and classification of microarray data using random forest. BMC Bioinformatics 7, 3.

Diodato, N., Ceccarelli, M., 2006. Computational uncertainty analysis of groundwater recharge in catchment. Ecol. Inform.1, 377-389.

Efron, B., Tibshirani, R., 1993. An introduction to the bootstrap. NY monographs on statistics and applied probability, 57. Chapman and Hall, London.

Everitt, B., 2002. The Cambridge dictionary of statistics. Cambridge University Press, Cambridge.

FAO, 2006. Food and Agricultural Organization of the United Nations: Guidelines for Soil Description: ftp://ftp.fao.org/agl/agll/docs/guidel_soil_descr.pdf (accessed at May 14th, 2014).

Finke, P.A., 2007. Quality assessment of digital soil maps: Producers and users perspectives, in: Lagacherie, P., McBratney A.B., Voltz, M. (Eds.), Chapter 39: Digital Soil Mapping, an introductory perspective. Developments in Soil Science, Vol. 31. Elsevier, pp. 523-541.

Fisher, P.F., 1999. Models of uncertainty in spatial data, in: Longley, P., Goodchild, M., Maguire, D., Rhind, D. (Eds.), Geographical information systems: Principles, techniques, management and application. Wiley, pp. 191-205.

Good, P.I., 2006. Resampling methods - A practical guide to data analysis, 3rd edition. Birkhauser, Boston.

Goovaerts, P., 2001. Geostatistical modelling of uncertainty in soil science. Geoderma 103, 3-26.

Goovaerts, P., 1999. Geostatistics in soil science: state-of-the-art and perspectives. Geoderma 89, 1-45.

Grimm, R., Behrens, T., 2010. Uncertainty analysis of sample locations within Digital Soil Mapping approaches. Geoderma 155, 154-163.

Grimm, R., Behrens, T., 2009. Uncertainty analysis of sample locations within digital soil mapping approaches. Geoderma 155, 154-163.

Grimm, R., Behrens, T., Märker, M., Elsenbeer, H., 2008. Soil organic carbon concentrations and stocks on Barro Colorado Island - Digital Soil Mapping using Random Forests analysis. Geoderma 146, 102-113.

Goovaerts, P., 2001. Geostatistical modelling of uncertainty in soil science. Geoderma 103, 3-26.

Grunwald, S., 2009. Multi-criteria characterization of recent digital soil mapping and modelling approaches. Geoderma 152, 195-207.

Grün, B., Leisch, F., 2008. Felxmix Version 2: Finite mixtures with concomitant variables and varying and constant parameters. J. Stat. Softw. 28, 1-35.

Hansen, L.K., Salamon, P., 1990. Neural network ensembles. IEEE Trans. Pattern Anal. Mach. Intell. 12, 993-1001.

Hengl, T., Husnjak, S., 2006. Evaluating adequacy and usability of soil maps in Croatia. Soil Sci. Soc. Am. J. 70, 920-929.

Heung, B., Bulmer, C.E., Schmidt, M.G., 2014. Predictive soil parent material mapping at a regional-scale: A Random Forest approach. Geoderma 214, 141-154.

Kempen, B., Brus, D.J., Heuvelink, G.B.M., Stoorvogel, J.J., 2009. Updating the 1:50,000 Dutch soil map using legacy soil data: a multinominal logistic regression approach. Geoderma 151, 311-326.

Kim, J.H., 2009. Estimating classification error rate: Repeated cross-validation, repeated hold-out and bootstrap. Comput. Stat. Data An. 53, 3735-3745.

Knotters, M., Brus, D.J., Oude Voshaar, J.H., 1995. A comparison of kriging, co-kriging and kriging combined with regression for spatial interpolation of horizon depth with censored observations. Geoderma 67, 227-246.

Kuhn, M., 2009. The caret package: URL http://cran.r-project.org/web/packages/caret/index.html (accessed at October 2nd, 2014).

Kullback, S., Leibler, R.A., 1951. On information and sufficiency. Ann. Math. Stat. 22, 79-86.

Krol, B., 2008. Towards a data quality management framework for digital soil mapping with limited data, in: Hartemink, A.E., McBratney, A.B., Mendonça-Santos, M.L. (Eds.), Chapter 11: Digital Soil Mapping with Limited Data. Springer, pp. 136-149.

Lagacherie, P., 2008. Digital Soil Mapping: A State of the Art, in: Hartemink, A.E., McBratney, A.B., Mendonça-Santos, M.L. (Eds.), Chapter 1: Digital Soil Mapping with Limited Data. Springer, pp. 3-14.

Lagacherie, P., McBratney, A.B., 2007. Spatial soil information systems and digital soil inference systems: perspectives for Digital Soil Mapping, in: Lagacherie, P., McBratney A.B., Voltz, M. (Eds.), Chapter 1: Digital Soil Mapping, an introductory perspective. Developments in Soil Science, Vol. 31. Elsevier, pp. 3-24.

Lagacherie, P., Legros, J., Burrough, P., 1995. A soil survey procedure using the knowledge of soil pattern established on a previously mapped reference area. Geoderma 65, 283-301.

Lark., R.M., Lapworth, D.J., 2012. Quality measures for soil surveys by lognormal kriging. Geoderma 173, 231-240.

Li, J., Heap, A.D., 2011. A review of comparative studies of spatial interpolation methods in environmental sciences: performance and impact factors. Ecol. Inform. 6, 228-241.

Liaw, A., Wiener, M., 2002. Classification and Regression by Random Forest. R News 2, 18-22.

Ließ, M., Glaser, B., Huwe, B., 2012. Uncertainty in the spatial prediction of soil texture. Comparison of regression tree and Random Forest models. Geoderma 170, 70-79.

Malone, B.P., McBratney, A.B., Minasny, B., 2011. Empirical estimates of uncertainty for mapping continuous depth functions of soil attributes. Geoderma 160, 614-626.

Malone, B.P., McBratney, A.B., Minasny, B., Laslett, G.M., 2009. Mapping continuous depth functions of soil carbon storage and available water capacity. Geoderma 154, 138-152.

McBratney, A.B., Minasny, B., Viscarra Rossel, R., 2006. Spectral soil analysis and inference systems: a powerful combination for solving the soil data crisis. Geoderma 136, 272-278.

McBratney, A.B., Mendonça-Santos, M.L., Minasny, B., 2003. On digital soil mapping. Geoderma 117, 3-52.

McBratney, A.B., Inakwu O.A.,, Bishop, T.F.A., Dunbar, M.S., Shatar, T.M., 2000. An overview of pedometric techniques for use in soil survey. Geoderma 97, 293-327.

McMillan, R.A., 2008. Experiences with Applied DSM: Protocol, Availability, Quality and Capacity Building, in: Hartemink, A.E., McBratney, A.B., Mendonça-Santos, M.L. (Eds.), Chapter 1: Digital Soil Mapping with Limited Data. Springer, pp. 113-135.

Mendonça-Santos, M.L., Santos, H.G., Dart, R.O., Pares, J.G., 2008. Digital mapping of soil classes in Rio de Janeiro State, Brazil: Data, modelling and prediction, in: Hartemink, A.E., McBratney, A.B., Mendonç-Santos, M.L. (Eds.), Chapter 34: Digital Soil Mapping with Limited Data. Springer, pp. 381-396.

Minasny, B., Bishop, T.F.A., 2008. Analysing uncertainty, in: McKenzie, N., Grundy, M., Webster, R., Ringrose-Voase, A. (Eds.), Chapter 24: Guidelines for surveying soil and land resources. CSRO Publishing, pp. 383-393.

Minasny, B., McBratney, A.B., 2006. A conditioned Latin hypercube method for sampling in presence of ancillary data. Comput. Geosci. 32, 1378-1288.

Molinaro, A.M., Simon, R., Pfeiffer, R.M., 2005. Prediction error estimation: A comparison of resampling methods. Bioinformatics 21, 3301-3307.

Nelson, M.A., Bishop, T.F.A., Triantafilis, J., Odeh, I.O.A., 2011. An error budget for different sources of error in digital soil mapping. Eur. J. Soil Sci. 62, 417-430.

Parr, J.F., Papendick, R.I., Hornick, S.B., Meyer, R.E., 1992. Soil quality: Attributes and relationship to alternative and sustainable agriculture. Am. J. Alternative Agr. 7, 5-11.

Peters, J., De Baets, B., Verhoest, N.E.C., Samson, R., Degroeve, S., De Becker, P., Huybrechts, W., 2007. Random Forests as a tool for ecohydrological distribution modelling. Ecol. Model. 207, 304-318.

Prasad, A.M., Iverson, L.R., Liaw, A., 2006. Newer classification and regression tree techniques: Bagging and random forests for ecological prediction. Ecosystems 9, 181-199.

Qu, M., Li, W., Zhang, C., 2013. Assessing the spatial uncertainty in soil nitrogen mapping through stochastic simulations with categorial land use information. Ecol. Inform. 16, 1-9.

Quinlan, J.R., 1986. Induction of decision trees. Mach. Learn. 1, 81-106.

Rad, M.R.P., Toomanian, N., Khormali, F., Brungard, C.W., Komaki, C.B., Bogaert, P., 2014. Updating soil survey maps by using random forest and conditioned Latin hypercube sampling in the loess derived soils of northern Iran. Geoderma 232, 97-106.

R Core Team, 2014. R: A language and environment for statistical computing. R Foundation for Statistical Computing, Vienna, Austria. URL http://www.R-project.org (accessed May 5th, 2014).

Roudier, P., 2011. Clhs: a R package for conditioned Latin hypercube sampling. URL http://cran.r-project.org/web/packages/clhs/index.html (accessed March 2nd, 2014).

SAGA GIS, 2011. SAGA GIS (System for Automated Geoscientific Analyses): Version 2.0.6: URL https://www.saga-gis.org (accessed August 8th, 2014).

Schmidt, K., Behrens, T., Daumann, J., Ramirez-Lopez, L., Werban, U., Dietrich, P., Scholten, T., 2014. A comparison of calibration sampling schemes at the field scale. Geoderma 232, 243-256.

Schmidt, K., Behrens, T., Friedrich, K., Scholten, T., 2010. A method to generate soilscapes from soil maps. J. Plant. Nutri. Soil Sci. 173, 163-172.

Schönbrodt-Stitt, S., Behrens, T., Schmidt, K., Scholten, T., 2013. Degradation of cultivated bench terraces in the Three Gorges Area – field mapping and data mining. Ecol. Indic. 34, 478-493.

Scull, P., Franklin, J., Chadwick, O.A., McArthur, D., 2003. Predictive soil mapping: a review. Prog. Phys. Geog. 27, 171-197.

Shrestha, D.L., Solomatine, D.P., 2006. Machine learning approaches for estimation of prediction interval for model output. Neural Networks 19, 225-235.

Strehmel, A., Schönbrodt-Stitt, S., Buzzo, G., Dumperth, C., Stumpf, F., Zimmermann, K., Bieger, K., Behrens, T., Schmidt, K., Bi, R., Rohn, J., Hill, J., Udelhoven, T., Xiang, W., Shi, X., Cai, Q., Jiang, T., Fohrer, N., Scholten, T., 2015. Assessment of Geo-Hazards in a rapidly changing landscape: The Three Gorges Reservoir region in China. Environ. Earth Sci.: doi: 10.1007/s12665-015-4503-7.

Stumpf, F., Schmidt, K., Behrens, T., Schönbrodt-Stitt, S., Buzzo, G., Dumperth, C., Wadoux, A., Wei, X., Scholten, T., 2015. Incorporating legacy soil samples and field operability using a conditioned Latin hypercube sampling design. (revised May 26th, 2015)

Sun, X.L., Wu, S.C., Wang, H.L., Zhao, Y.G., Zhang, G.L., Man, Y.B., Wong, M.H., 2013. Dealing with spatial outliers and mapping uncertainty for evaluating the effects of urbanization on soil: A case study of soil pH and particle fractions in Hong Kong. Geoderma 195-196, 220-233.

Svetnik, V., Liaw, A., Tong, C., Culberson, C.J., Sheridan, R.P., Feuston, B.P., 2003. Random forest: a classification and regression tool for compound classification and QSAR modeling. J. Chem. Inf. Comp. Sci. 43, 1947-1958.

Tutmez, B., Hatipoglu, Z., 2010. Comparing two data driven interpolation methods for modeling nitrate distribution in aquifer. Ecol. Inform. 5, 311-315.

Viscarra Rossel, R.A., McBratney, A.B., 1998. Soil chemical analytical accuracy and costs: implications from precision agriculture. Aust. J. Exp. Agr. 38, 765-775.

Webster, R., Oliver, M.A., 2006. Modeling spatial variation of soil as random functions, in: Grunwald, S. (Eds.), Chapter 9: Environmental soil-landscape modeling: Geographic information technologies and Pedometrics. CRC, pp. 241-287.

Wellmann, F.J., 2013. Information theory for correlation analysis and estimation of uncertainty reduction in maps and models. Entropy 15, 1464-1485.

Wiesmeier, M., Barthold, F., Blank, B., Kögel-Knabner, I., 2011. Digital mapping of soil organic matter stocks using random forest modeling in semi-arid steppe ecosystems. Plant Soil 340, 7-24.

Yang, L., Jiao, Y., Fahmy, S., Zhu, A.X., Hann, S., Burt, J.E., Qi, F., 2011. Updating conventional soil maps through digital soil mapping. Soil Sci. Soc. Am. J. 75, 1044-1053.

Manuscript 4

Sediment Reallocations due to erosive rainfall events in the Three Gorges Reservoir Area, Central China

Land Degradation & Development, under review (2015)

Felix Stumpf*[1]), Philipp Goebes[1]), Karsten Schmidt[1]), Marcus Schindelwolf[2]), Sarah Schönbrodt-Stitt[1]), Alexandre Wadoux[3]), Wei Xiang[4]), Thomas Scholten[1])

[1]) University of Tübingen, Department of Geosciences, Chair of Soil Science and Geomorphology, Germany,
[2]) Technical University Freiberg, Soil and Water Conservation Unit, Germany,
[3]) Wageningen UR, University & Research Centre, Wageningen, Netherlands,
[4]) China University of Geosciences Wuhan, Department of Geotechnical Engineering and Engineering Technology, China
*Corresponding author: University of Tübingen, Department of Geoscience, Chair of Soil Science and Geomorphology, Rümelinstraße 19-23, Tübingen, Germany, Phone: +49 7071 29 73942, e-mail: felix.stumpf@uni-tuebingen.de

Abstract

Soil erosion by water outlines a major threat to the Three Gorges Reservoir Area in China. A detailed assessment of soil conservation measures requires a tool that spatially identifies sediment reallocations due to rainfall-runoff events in catchments. We applied EROSION 3D as a physically based soil erosion and deposition model in a small mountainous catchment. Generally, we aim to provide a methodological frame that facilitates the model parametrization in a data scarce environment and to identify sediment sources and deposits. We used Digital Soil Mapping techniques to generate spatially distributed soil property information for parametrization. For model calibration and validation, we continuously

monitored the catchment on rainfall, runoff, and sediment yield for a period of 12 months. The model performed well for large events (sediment yield > 1 Mg) with an averaged individual model error of 7.5%, while small events showed an average error of 36.2%. We focused on the large events to evaluate reallocation patterns. Erosion occurred in 11.1% of the study area with an average erosion rate of 49.9 Mg ha^{-1}. Erosion mainly occurred on crop rotation areas with a spatial proportion of 69.2% for 'corn-rapeseed' and 69.1% for 'potato-cabbage'. Deposition occurred on 11.0%. Forested areas (9.7%), infrastructure (41.0%), cropland (corn-rapeseed: 13.6%, potato-cabbage: 11.3%), and grassland (18.4%) were affected by deposition. Since the vast majority of annual sediment yields (80.3%) were associated to a few large erosive events, the modelling approach provides a useful tool to spatially assess soil erosion control and conservation measures.

Keywords

Sediment sources and deposits, EROSION 3D-model, rainfall-runoff event, catchment scale, Three Gorges Reservoir Area

1 Introduction

Soils are the foundation of all terrestrial ecosystems and develop at the intersection of atmosphere, biosphere, hydrosphere, and lithosphere (Brevik *et al.*, 2015). In this context, soils inhere ecosystem functions that have direct impact on human societies (Berendse *et al.*, 2015). Examples of these soil functions include water purification by filtration, food production by forming a support system for plants, stabilizing climate change by carbon sequestration, and the provision of a physical basis for human activities (Keesstra *et al.*, 2012; Goebes *et al.*, 2015). However, soil erosion and the accompanied loss of topsoil results in soil quality degradation, and therefore in a declining capacity of soils to provide the ecosystem functions (Lal, 2003; Morgan, 2005; Boardman, 2006). This implies reduced crop productivity and confined water quality due to the reallocation of nutrients and pollutants into the reservoirs (Zhang & Lou, 2011; Zhao et al., 2013). Moreover, sediment depositions in reservoirs result in a declined water storage capacity and a therefore impaired water and energy supply (Palazón *et al.*, 2014; Ferreira *et al.*, 2015; Slimane *et al.*, 2015). The negative

impacts of soil erosion are reinforced when adverse physio-geographic conditions, such as erosion-prone soils, steep sloping terrain, and abundant rainfall meet inappropriate agricultural practices, deforestation and construction activities (Onyando *et al*., 2005; Park *et al*., 2011; Wu *et al*., 2011; Shi *et al*., 2012; Schönbrodt-Stitt *et al*., 2013a). Considering that rates of soil erosion exceed rates of soil formation by several orders of magnitude, soil erosion outlines a major threat to ecosystem sustainability worldwide (Verheijen *et al*., 2009; Zhao *et al*., 2013). Under these circumstances soil erosion becomes potentially hazardous for human livelihood and requires erosion control measures and conservation planning (Shi *et al*., 2004; Zhao *et al*., 2013).

Especially the Three Gorges Reservoir Area (TGRA) in China shows high susceptibility to hazardous soil erosion due to intense anthropogenic activities and unfavorable environmental conditions (Zhang *et al*., 2009; Schönbrodt-Stitt *et al*., 2010; Peng *et al*., 2011; Wu *et al*., 2011; Kepa Brian Morgan *et al*., 2012; Shi *et al*., 2012; Strehmel *et al*., 2015). The TGRA covers an area of 57,802 km². At the maximum pool level of 175 m, the reservoir expands approximately 660 km westwards from Three Gorges Dam (TGD; Xu *et al*., 2011). The TGD project outlines the world`s largest hydroelectric scheme and was designed to increase energy supply, control seasonal floods, and improve navigation on the Yangtze river (Zhang & Lou, 2011). Accompanied by the construction of TGD and the impoundment of the reservoir, 1.3 million people were resettled due to the inundation of 431 km² agricultural land and 35 km² residential areas (Xu *et al*., 2011, 2013). About 42% of the resettlers were moved uphill to previously forested and steep mountainous sites for small scale crop cultivation (Cai *et al*., 2005; Tan & Yao, 2006; Wu *et al*., 2011; Zhang & Lou, 2011). In total, 96% of the TGRA exhibits mountainous and hilly terrain with steep slopes (Zhang *et al*., 2009; Wu *et al*., 2011; Fang *et al*., 2013). It shows a humid subtropical climate with a unimodal rainfall regime, governed by the East-Asian monsoon. The long-term average annual precipitation is 1,146 mm, of which approximately 70% occurs from May to September (CMA, 2012). Purple soils and yellow to yellow-brown soils are dominant in the TGRA and are considered to be highly vulnerable to soil erosion (Zhang *et al*., 2009; Peng *et al*., 2011; Schönbrodt-Stitt *et al*., 2013b). Estimations on the long-term annual soil losses based on empirical modelling amount to 157 million Mg (Lu & Higgitt, 2000). The soil erosion induces sedimentation of the reservoir and hence an attenuated ecological functioning of the Yangtze basin, reduced lifespan of the dam, and a declined capacity to control floods (Shi *et al*., 2004; Zhang & Lou,

2011; Xu *et al*., 2013). Since the 1990s, conservation measures were established to mitigate the hazardous effects. The measures include programs to implement conservation farming practices and to stabilize steep sloping surfaces mainly by reforestation and the construction of cropland terraces (Xu *et al*., 2013).

For a detailed assessment of the conservation measures, an efficient tool is required that spatially identifies patterns of sediment reallocations in a mountainous and highly dynamic region (Shi *et al*., 2012). In the TGRA, the major sediment yield caused by soil erosion is attributable to only very few heavy storm events each year (Fang *et al*., 2013). Thus, event-based estimations on sediment reallocations are of major concern for regional authorities (Peng *et al*., 2011). Consequently, there is a demand for an event-based approach that spatially quantifies soil erosion and deposition at catchment scale (Cai *et al*., 2005; Shi *et al*., 2012). This is addressed by the concept of sediment connectivity, which describes transfer characteristics of sediment through a landscape system at various scales (Hooke, 2003; Fryirs, 2013). Several studies conducted a detailed analysis of sediment connectivity, while identifying sediment sources, deposits, and pathways using combinations of mapping, and modelling techniques (Keesstra *et al.*, 2009; Lexartza-Artza & Wainwright, 2011; Marchamalo *et al.*, 2015). In the TGRA, the demand was only partially addressed in recent attempts of soil erosion modelling (Shi *et al*., 2012).

Empirical soil erosion models, such as the Universal Soil Loss Equation (USLE; Wischmeier & Smith, 1981) and the Revised Universal Soil Loss Equation (RUSLE; Renard *et al*., 1997) were extensively applied in the TGRA (Shi *et al*., 2004; Zhang, 2008; Strehmel *et al.*, 2015). The USLE/RUSLE establishes relationships between rainfall, topography, conservation practices, soil, and vegetation to estimate long-term annual averages of sheet and rill erosion (Zhou *et al*., 2008). Soil loss is calculated from the product of environmental coefficients, which were derived from field observations in 37 U.S. states at plot scale (Zhang *et al*., 1996; Shen *et al*., 2009; Terranova *et al*., 2009). The USLE/RUSLE predicts an average soil loss for an extended time period, provided that the application remains within the range of conditions for which the model was developed (Grønsten & Lundekvam, 2006). However, erosive effects of complex topography are not included, since the influence of flow convergence and divergence is not adequately regarded (Mitasova *et al*., 1996; Tarboton, 1997; Capolongo *et*

al., 2008). Beyond, these approaches are incapable to provide estimations of spatial erosion structures, while deposition is disregarded at all (Zhang *et al*., 1996).

A few studies applied physically-based erosion and sediment transport models in the TGRA, such as the European Soil Erosion Model (EUROSEM), the Water Erosion Prediction Project (WEPP) or the Water and Tillage Erosion Model (WaTEM; Cai *et al*., 2005; Shen *et al*., 2010; Shi *et al*., 2012). These models include the spatial variability of the erosion processes and provide spatially distributed outputs of erosion and deposition. They are based on simulating the individual components of the erosion processes by solving the corresponding mass equations (Zhang *et al*., 1996; Aksoy & Kavvas, 2005). Thus, a variety of spatially distributed input data with respect to soil conditions, terrain, and land use is required. The application and performance of physically-based models is primarily determined by the quality of the input data. In this context, an inadequate resolution or consistency may not represent the erosion-related heterogeneity of the study area (Jetten *et al*., 2003; Jordan *et al*., 2005). Thus, the models underperform if the complexity of the model is not in agreement with the data quality (Van Rompaey & Govers, 2002). Moreover, physically-based models can be distinguished between event-based models to simulate sediment reallocations of single erosive events and continuous models, addressing a series of events (Nearing *et al*., 2005). Input data requirements for continuous models are less restrictive compared to event-based models, since an event-specific parametrization is avoided. However, event-based models are preferable to investigate erosive responses in areas with few but high intensity rainfall such as the TGRA (Cai *et al*., 2005). Recent erosion studies in the TGRA, using physically-based erosion and deposition models, produced acceptable results (Cai *et al*., 2005; Shen *et al*., 2009, 2010; Shi *et al*., 2012). However, most of the studies applied continuous models due to limited data availability at the catchment scale (Shen *et al*., 2009, 2010; Shi *et al*., 2012). By contrast, Cai *et al*. (2005) applied an event- and physically-based model at the plot scale that facilitates parametrization, but is inadequate to assess spatial organization of conservation measures in the catchment (Shi *et al*., 2012).

This study aims to provide a methodological framework that enables a detailed assessment of sediment reallocations due to erosive rainfall events in a data scarce and small mountainous catchment within the TGRA. To identify and characterize erosive events, we continuously monitored the catchment on rainfall, runoff, and sediment yield in temporal resolution of 10

min for a period of 12 months. The reliability of the monitoring data was evaluated by a comparison to long-term observations. Erosive events were determined based on the cause-effect relationship between rainfall, runoff, and sediment yield. We applied EROSION 3D that represents an event- and physically-based erosion and deposition model (Schmidt, 1991, 1992). Digital Soil Mapping (DSM) techniques were used to generate spatially distributed soil property information, therefore facilitating the model parametrization in an area of general data scarcity. Thus, the objective of the study is the spatial identification and characterization of sediment sources and deposits within the catchment.

2 Material and Methods

2.1 Study area

The study was conducted in the Upper Badong catchment (Figure 1), located approximately 74 km upstream of the TGD in western Hubei Province (31°1′24″N, 110°20′35″E). The area covers 428.7 ha of which 72% are exposed to the north. Elevation ranges from 469 m to 1,483 m with an average of 1,053 m. The average slope angle amounts to 26° and ranges between 0° and 53°. The lithology of the southern study area exhibits clayed siltstone linked to the middle Triassic formation, while dolomite and microcrystalline limestone from the lower Triassic is dominant in the north. According to the Chinese Soil Taxonomic system, dominant soil groups are purple soils in the south and yellow to yellow-brown soils in the north. Following the World Reference Base for Soil Resources (WRB, 2014), these soils refer to Cambisols and Alisols, respectively. The climate is humid subtropical with an average temperature of 12.9 C° and an average annual precipitation of 1,082 mm. The rainfall regime of the study area shows a unimodal distribution with 68% of rainfall occurring from May to September. Land use is dominated by secondary forest vegetation (79.4 %) in the steep hillslopes of the mountainous study area. Small agricultural plots (< 0.5 ha) are scattered in the study area, but concentrate to unconsolidated farmland patches in the north at elevations between 500 m and 700 m, in the middle-east from 850 m to 1050 m, and in the south from 1150 m to 1250 m. Since the climate allows two crops per year, the main patterns of crop rotation show corn and sweet potato in summer, followed by rapeseed and cabbage in winter. Conservation farming practices, such as contour tillage, furrow-ridge tillage or mulching with crop residues after harvest are increasingly implemented.

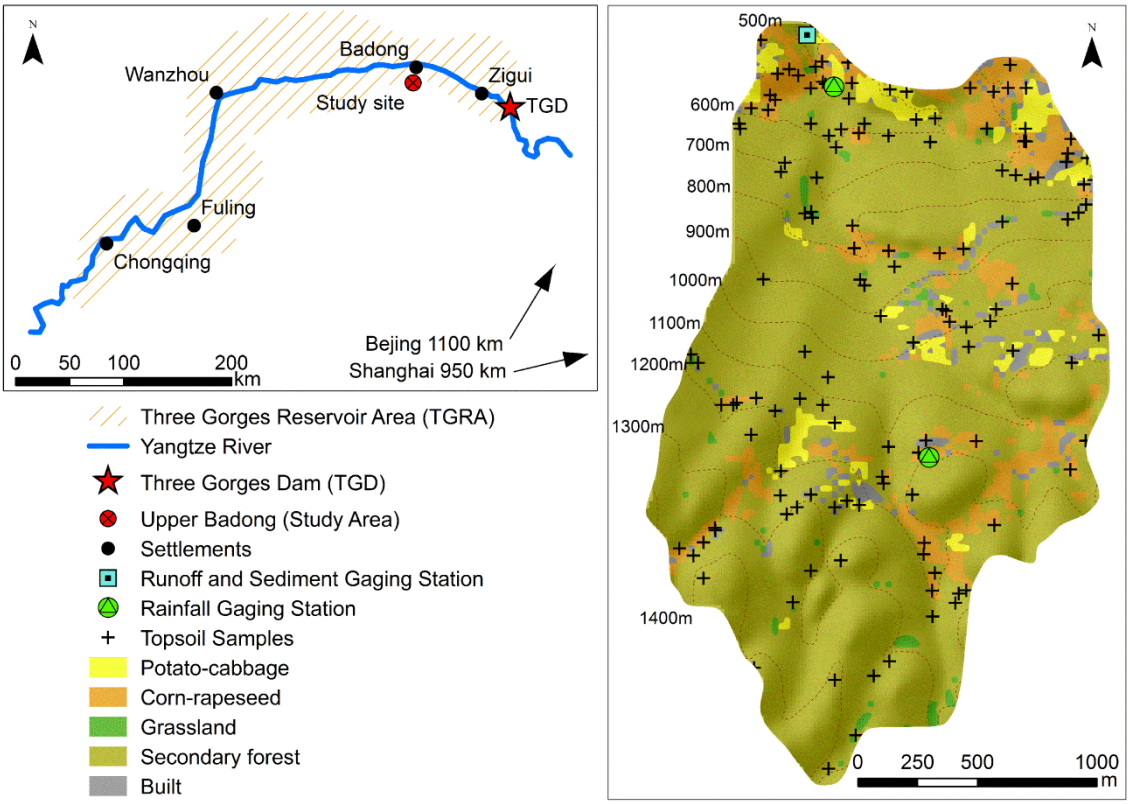

Figure 1: Study area (right) and its location within the Three Gorges Reservoir Area (left).

2.2 Data acquisition and preparation

We established a monitoring network to continuously record data on rainfall, runoff, and sediment yields (Figure 1). The data was logged in a temporal resolution of 10 minutes for a period of twelve months, starting in June 2013.

Rainfall data was obtained by two self-emptying tipping bucket raingauges using the Vantage Pro 2 system by Davis Instruments with a single impulse capacity of 0.2 mm. The calibrated raingauges were installed at elevations of 501 m and 1193 m within the study area (Figure 1). The orifices were positioned at 1.5 m above ground to avoid disturbance by vegetation and wind. For further processing, data from both raingauges were averaged. We compared the measured short-term data to long-term monthly records to evaluate their representativeness.

The long-term records were obtained between 1960 and 2009 by the China Meteorological Administration (CMA, 2012) at a climate station (ID 57355) in distance of approximately 7 km from the study area. The analysis was accomplished by comparing the distributions of the data regimes using descriptive statistics.

Runoff data was obtained using a water pressure sensor (PTM/N/SDI-12 by STS-Sensors) that was positioned at the outlet of the catchment (Figure 1). Primarily, the water level was derived based on the water pressure and the geometry of the flow cross-section, which was measured in-situ. Subsequently, we applied the standard flow rate equation to determine the runoff (Kirkby, 1978):

$$Q = A * V_q, \quad (1)$$

where Q is the runoff [m^3s^{-1}], A is the flow cross-section [m^2], and V_q is the average flow velocity [ms^{-1}]. V_q was calculated according to the empirical Manning equation for gravity flow in open channels (Kirkby, 1978):

$$V_q = \frac{1}{n} * \delta^{2/3} s^{1/2}, \quad (2)$$

where n is the Manning coefficient for the hydraulic surface roughness [$sm^{-1/3}$], s is the slope gradient [-], and δ is the flow depth [m].

We obtained sediment yield data from the outlet using a turbidity sensor (SN-PNEPA by PONSEL).The sensor measures the light intensity with an infrared beam that is scattered due to suspended particles. The measure is expressed in nephelometric turbidity units (NTU) and indicates the clarity of the water, which is mainly influenced by suspended sediments from eroding soil (Satterland & Adams, 1992; Anderson, 2005). Since the NTU measure depends on the properties of the suspended sediment, a conversion into mass units [mgl^{-1}] requires a site-specific calibration. Thus, we progressively added 250 composite sediment samples from the entire study area to a defined water volume of 5 l. By stepwise NTU measurements, we derived a calibration curve to convert NTU values to suspended sediment load in mass units.

During three field campaigns between 2012 and 2014, we conducted singular topsoil (0-20 cm depth) moisture measurements (TDR-sensor ML3 Thetakit by Delta-T Devices) at 235

sites randomly distributed over the entire study area. We further collected 140 topsoil samples (0-25 cm depth) according to statistical sampling designs, which adequately enable the generation of soil property maps by DSM techniques (Stumpf *et al*., 2015a, b). The samples were analyzed for organic carbon content, particle size distribution, and bulk density, since these parameters outline relevant soil information for the application of EROSION 3D. At each sampling location we pooled five sub samples from the corners and the center of a 40 cm x 40 cm square to obtain composite samples. In addition, we pooled three sub samples, which were randomly obtained within this square, using a cylindrical core cutter with a defined volume of 100 cm^3. We used aliquots (50 g) of the homogenized and dried (40°C) composite samples to determine the soil organic carbon content (elemental analyzer Vario EL III). The remains of the composite samples were used for particle size analysis. The samples were sieved (< 0.63 mm) to separate sand contents, while silt and clay contents were separated using the Sedigraph III 5120 by micromeritics GmbH. The bulk density was derived from the dry weight (105°C) of the volume defined samples.

Land use information was based on a RapidEye satellite image from September 28th 2012, providing five spectral bands in a spatial resolution of 5 m x 5 m (RapidEye, 2012). We derived six land use classes according to 'cropland', 'grassland', 'broadleaf', 'conifer', 'shrub', 'woods', and 'built up' (Liu *et al*., 2005). During the field campaigns in 2013 and 2014, we further refined the land use class 'cropland' according to occurring crop rotations into 'corn-rapeseed' and 'potato-cabbage' based on in-situ observations. Moreover, we generated a digital elevation model (DEM) based on digitizing a topographical map of the catchment with contour lines at 10 m intervals. The data was rasterized and resampled to a cell size of 25 m x 25 m to buffer potential uncertainties.

2.3 Determination of erosive events

We used monitoring data on rainfall, runoff, and sediment yield to determine rainfall-runoff events and their associated erosive response. In a first step, we disaggregated the rainfall record according to a minimum inter-event time of six hours using the R-package 'hydromad' (Andrews & Guillaume, 2015). This threshold is commonly applied in event-based erosion studies (Wischmeier & Smith, 1981; Xie *et al*., 2002; Bagarello *et al*., 2008; Soulis *et al*., 2009; Taguas *et al*., 2011) to identify independent rainfall events with similar initial soil

moisture conditions that control runoff generation (Bracken *et al*., 2008; Todisco, 2014). In a second step, we determined the direct runoff associated with each rainfall event. Direct runoff originates from rainfall that contributes immediately to the streamflow, while baseflow reaches the streamflow with a substantial delay (Merz *et al*., 2006). We applied a recursive digital filter technique on the runoff record to separate baseflow from direct runoff (Nathan & McMahon, 1990; Arnold *et al*., 1995). Using the R-package 'Ecohydrology' (Fuka *et al*., 2014), the following filter equation was applied:

$$q_t = \beta * q_{t-1} + \frac{1+\beta}{2} * (Q_t - Q_{t-1}), \quad (3)$$

where q_t [m^3s^{-1}] is the filtered direct runoff at the time step t [min], Q_t [m^3s^{-1}] is the original streamflow, and β [-] is the filter parameter.

While an initial rainfall impulse defined the start of a rainfall-runoff event, the end was indicated when no longer associated direct runoff occurred. Using this event distinction, we attributed the respective sediment yield to each rainfall-runoff event to identify their erosive response. The adequacy of this procedure depends on the strength of the cause-effect relationship between rainfall, runoff, and sediment yields within the specific catchment (Todisco et al., 2014). This was evaluated by comparing the regimes of the monitoring data over the measuring period, using a correlation matrix.

For further analyses, we selected these events, which exhibit direct runoff and an associated erosive response. In contrast, we rejected those events where a distinct attribution of direct runoff to a rainfall event was impossible due to inadequate separation between direct runoff and baseflow (Blume *et al*., 2007).

Each of the erosive rainfall-runoff events was characterized according to the event-triggering rainfall properties (Table 2), such as total rainfall amount P [mm], the duration of occurring rainfall t_p [h], the maximum rainfall intensity in 30 minutes I_{30} [$mm*h^{-1}$], the maximum rainfall intensity in 60 minutes I_{60} [$mm*h^{-1}$], and the erosivity EI_{30} calculated as (Brown & Foster, 1987),

$$EI_{30} = \sum_{r=1}^{0} E * I_{30}, \quad (4)$$

where E [MJ ha^{-1}] is the rainfall kinetic energy for a time interval r that can be estimated by

$$E = 0.29 * [1 - 0.72 * \exp(-0.05 i_r)] * P_r. \quad (5)$$

2.4 Modelling sediment reallocation

2.4.1 Model description

We applied EROSION 3D (Schmidt, 1991, 1992), a raster- and physically based erosion and deposition model that calculates soil losses and deposition, initiated by single rainfall events or event sequences in small watersheds. The model includes the erosional processes of direct runoff, detachment of soil particles by rainfall splash and runoff, transport of detached particles by runoff, routing of runoff and sediment, and sediment deposition. The mathematical incorporation of these processes is based on two subroutines, addressing runoff and more explicitly erosion.

The runoff subroutine calculates the rainfall excess according to a modified Green and Ampt infiltration equation (Green & Ampt, 1911; Weigert & Schmidt, 2005; Schindewolf & Schmidt, 2012):

$$i = k_s * g + k_s * \frac{\Psi_{m0}}{\sqrt{\frac{2 k_s * \Psi_{m0} * t}{P_f * (\Theta_s - \Theta_0)}}}, \quad (6)$$

where i is the infiltration rate [kg/(m²s)], k_s is the saturated hydraulic conductivity [(kg s) m^{-3}], g is the gravity [m s^{-2}], Ψ_{m0} is the matric potential [N m kg^{-1}] related to the initial water content Θ_0 [N m kg^{-1}], t is time [s], P_f is fluid density [kg m^{-3}], and Θ_s is the saturated water content [m^3 m^{-3}]. The saturated hydraulic conductivity k_s is estimated using the pedotransfer functions according to Campbell (1991):

$$k_s = 4 * 10^{-3} * \left(1.3 * \frac{10^{-3}}{P_b}\right)^{1.3 * b} * \exp(-0.069 * T - 0.037 * U, \quad (7)$$

with

$$b = (10^{-3} * D)^{-0.5} + 0.2 * \delta_p, \quad (8)$$

where P_b is the bulk density [kg m^{-3}], T is the clay content [kg kg^{-1}], U is the silt content [kg kg^{-1}], b is parameter [-], D is the average diameter of soil particles [m], and δ_p is the standard deviation of the average diameter of soil particles [-].

Since the pedotransfer function assumes a rigid soil matrix, the temporal variability of the soil structure is disregarded. Therefore, the saturated hydraulic conductivity k_s is corrected by a multiplication with an empirically derived so-called skinfactor to adjust the infiltration rates (Schindewolf & Schmidt, 2012).

The erosion subroutine, thus the spatial quantification of particle detachment, transport and deposition, is based on the momentum-flux approach (Schmidt, 1991). Basically, this approach follows the assumption that the erosive impact of direct runoff and rainfall splash is proportional to their exerted momentum fluxes (Schindewolf & Schmidt, 2012). Where the momentum flux of the direct runoff flow ϕ_q is defined by

$$\phi_q = \frac{W_q * V_q}{\Delta X}, \tag{9}$$

the momentum flux of the rainfall splash $\varphi_{r,\alpha}$ follows the equation

$$\varphi_{r,\alpha} = W_r * V_r * \sin\alpha * (1 - CL), \tag{10}$$

where W_q and W_r are the mass rate of direct runoff flow respectively rainfall splash, V_q and V_r are the average flow velocity respectively velocity of the rainfall droplets, Δx is the length of the slope segment, α is the slope angle, and CL the soil cover.

Since an observable rate of erosion requires a minimum rate of direct runoff q_{crit}, the erosion resistance of the soil is defined as the critical momentum flux ϕ_{crit}, following the equation (Schindewolf & Schmidt, 2012),

$$\phi_{crit} = \frac{q_{crit} * P_q * V_q}{\Delta X}, \tag{11}$$

where q_{crit} is the volume rate of flow [m³ (ms)$^{-1}$] at initial erosion, P_q is the fluid density [kg m^{-3}], Δx is the slope segment width [m], and V_q is the flow velocity [m s^{-1}] that we derived according to equation (2).

2.4.2 Model application

Besides the obtained rainfall records and the DEM, EROSION 3D requires a set of raster-based soil property maps that represent their spatial heterogeneity at catchment scale as good as possible. The parameters of particle size distributions according to textural classes [%], bulk density [kg m^{-3}], and organic carbon content [%] were assumed to be steady over the period of interest. In contrast, the parameters soil cover [%], erosion resistance [N m^{-2}], hydraulic roughness according to Manning`s n [N $m^{-1/3}$], skinfactor [-] to correct infiltration rates, and the initial soil moisture [vol.-%] were adjusted for each event (Schmidt *et al*., 1999; Schindewolf & Schmidt, 2012).

DSM was applied to derive the steady soil parameters, since DSM techniques are cost-efficient and provide soil property maps in high resolution (McBratney *et al*., 2003; Behrens *et al*., 2010; Behrens *et al*., 2014; Zhu *et al*., 2015). We set up Random Forest (RF) regression models (Breiman, 2001) to link the soil property samples with terrain covariates (SAGA, 2012). The models were applied to estimate the spatial distribution of the soil properties. RF was selected since it includes an internal error estimation and has been successfully applied in the field of DSM (Peters *et al*., 2007; Heung *et al*., 2014; Stumpf *et al*., 2015b). For processing, we used the R-package 'randomForest' (Liaw & Wiener, 2002; Table 1).

Table 1: Summary statistics (min: minimum; max: maximum; average; sd: standard deviation) and accuracy (coefficient of determination:R^2; root mean squared error: RMSE) of steady soil parameters.

Parameter	Minimum	Maximum	Average	sd	RMSE	R^2
Clay content [%]	18.6	44.8	32.6	3.7	5.1	0.58
Silt content [%]	43.5	69.0	62.3	3.9	5.0	0.57
Sand content [%]	1.4	30.8	4.9	5.2	3.9	0.79
Bulk density [kg m^{-3}]	700	2,000	1,200	100	100	0.36
Organic carbon [%]	1.0	3.2	2.1	0.4	0.5	0.45

The soil cover was estimated by interpreting the refined land use map in combination with crop rotation patterns and the seasonally occurring grow stages. The input parameters erosion resistance, hydraulic roughness, and skinfactor were estimated using a parameter catalogue (Michael, 2000). This catalogue contains a progressively updated compilation of empirically

obtained parameter values for different soils and crops, considering seasonal variations and management practices (Schmidt *et al*., 1999; Schindewolf & Schmidt, 2012). The parameter soil moisture is most sensitive and highly variable in time and space (Schmidt, 1992; Starkloff & Stolte, 2014). Thus, we initially used the average soil moisture values from the parameter catalogue. Then, we iteratively ran the model with varying soil moisture values and selected the best fit between observed and predicted direct runoff (Jetten *et al*., 1999; Schmidt *et al*., 1999). Since the average moisture values of the test variations were only allowed to deviate by 20% from the average observed data, we ensured that the final data set remained in realistic limits.

For the EROSION 3D model runs, all input parameter were harmonized to a cell size of 25 m x 25 m. We validated the model output of each event individually by comparing the predicted sediment yield at the catchment outlet with the observed sediment yield. To express the discrepancy, we used the proportional deviation (ERR) of the prediction from the respective observation. Moreover, we assessed the average model performance for the sequence of erosive events using the averaged individual prediction error ($ERR_{average}$), the root mean square error (RMSE; Willmott & Matsuura, 2005) and the Nash-Sutcliff coefficient (NS; Nash & Sutcliff, 1970; Krause *et al*., 2005). The equations of the quality measures are defined as follows:

$$ERR = \frac{|SY_{obs} - SY_{sim}|}{SY_{obs}}, \tag{12}$$

$$RMSE = \sqrt{\frac{\sum_{i=1}^{n}(SY_{sim,i} - SY_{obs,i})^2}{n}}, \tag{13}$$

$$NS = 1 - \frac{\sum_{i=1}^{n}(SY_{obs,i} - SY_{sim,i})^2}{\sum_{i=1}^{n}(SY_{obs,i} - SY_{ave,obs,i})^2}, \tag{14}$$

where SY_{obs} [Mg] is the observed sediment yield of an event *i*, SY_{sim} [Mg] is the predicted sediment yield, and $SY_{ave,obs}$ [Mg] is the average observed sediment yield. For model validation we used the R-package 'hydroGOF' by Zambrano-Bigiarini (2014).

Finally, we mapped the erosion and deposition patterns as a budget over the erosive events to spatially identify sediment sources and deposits. We interpreted the results in context of the

occurring land use and topography. The model results of each pixel were separated according to four classes (severe: > 50 t ha^{-1}; high: 20-50 t ha^{-1}; moderate: 10-20 t ha^{-1}; low: 0-10 t ha^{-1}) for erosion and deposition respectively. This classification is based on thresholds that are commonly applied in the TGRA with respect to erosion studies (Shi *et al*., 2004; Shi *et al*., 2012).

3. Results

3.1 Evaluation of the monitoring data

We compared the monitored rainfall data (June 213 to May 2014) to the long-term records from Badong climate station (January 1960 to December 2009; Figure 2 above). With 895 mm, the total rainfall amount of the short-term records is less compared to the long-term annual average of 1,082 mm, revealing relatively dry conditions during the monitoring period. This decline is attributable to the months of May, July, and October, showing a reduced rainfall amount between 54 mm and 68 mm. The deviations of the remaining months range between 1 mm in January and 20 mm in June with a positive budget of 11 mm. Furthermore, we compared the short-term amounts per month to the long-term average maxima and minima per month. The results show that the obtained records were all within the range of the long-term records (Figure 2, above). Both, short- and long-term records exhibit a unimodal distribution with 67% and 68% of the annual rainfall amounts occurring during the wet season from May to September. The analogy between the rainfall records reveal that the short-term record is representative for the area.

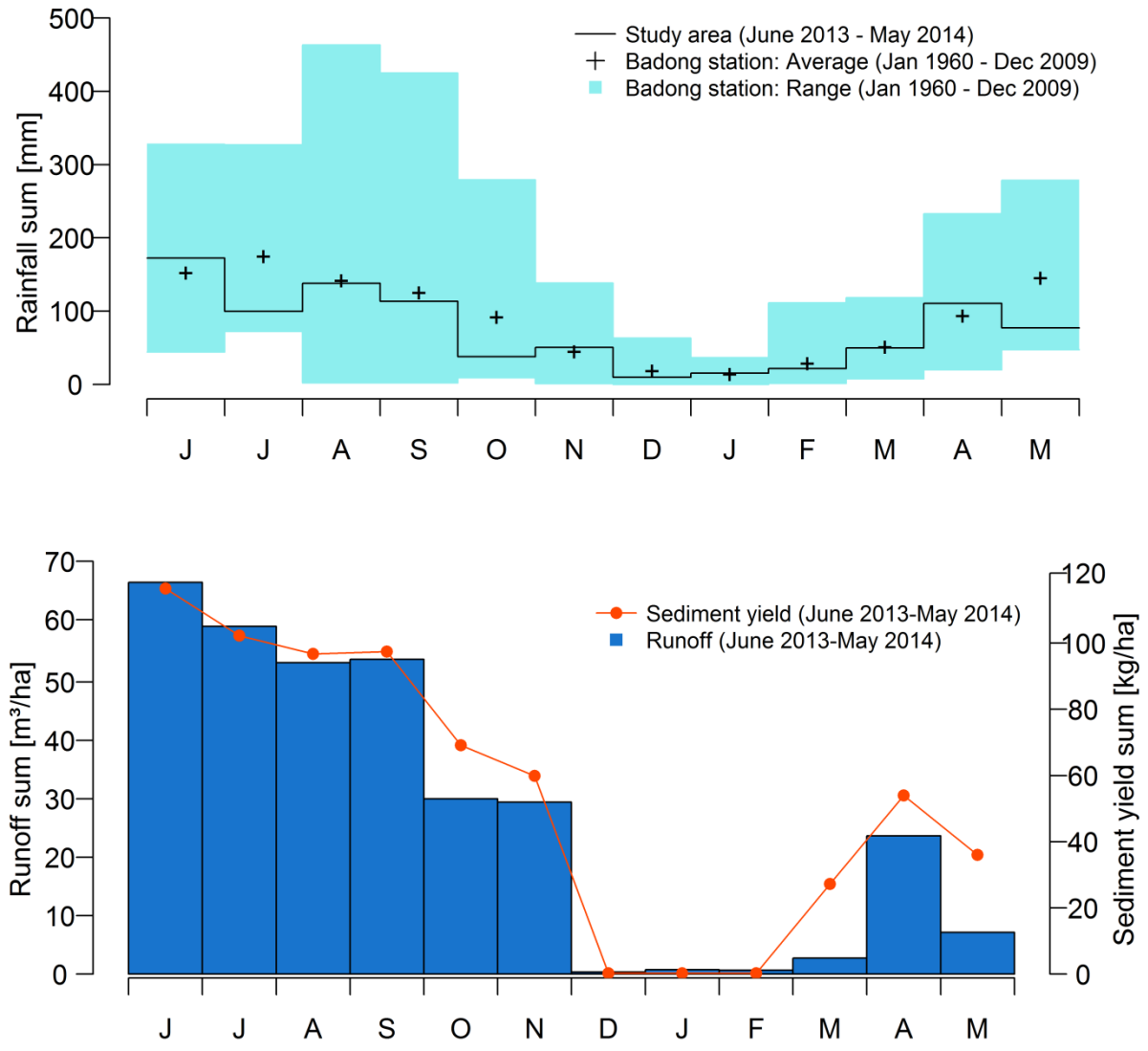

Figure 2: Regimes of monthly rainfall, runoff, and sediment yield data in the monitoring period. Rainfall records are compared to ranges and averages of long-term records from Badong station (above). Regimes of runoff and sediment yield are compared among each other (below).

Moreover, we evaluated the interrelation between the monitored rainfall, runoff, and sediment records within the study area (Figure 2). The annual distribution of the obtained runoff sums and sediment yields per month corresponds to the recorded rainfall regime. With a total annual runoff of 324 m^3 ha^{-1}, 80% occurs in the wet season from May to September. We

found the maximum runoff in June with 66 m^3 ha^{-1}, while from December to January less than 1 m^3 ha^{-1} runoff was recorded. Similarly, the total annual sediment yield adds up to 666 kg ha^{-1}, of which 71% occurs in the wet season. June shows the maximum yield with 116 kg ha^{-1}, while minima occur from December to February with less than 3 kg ha^{-1} (Figure 2, below). We further calculated the relation of rainfall, runoff, and sediment yield by using the correlation coefficient. With a resolution of 10 minutes, rainfall data exhibit an r of 0.94 to runoff and 0.89 to sediment yield data, while the latter two are correlated with r = 0.84. The similar regimes of the recorded data and the associated r-values (>0.80) approve a strong cause-effect relationship between rainfall, runoff, and sediment yield.

3.2 Properties of erosive rainfall events

During the monitoring period we identified 19 erosive events, of which we excluded five from further analyses (Table 2). Compared to the selected events and referring to the average properties, the excluded events show an increase in duration D and total rainfall amount P of 1,140 min and 19.4 mm, respectively. The average peak intensities I_{60}, I_{30} are lower by 4.6 mm $60min^{-1}$ and 4.5 mm $30min^{-1}$, respectively, and the average erosivity EI_{30} are lower by 273.9 MJ ha^{-1} mm h^{-1}. Moreover, the excluded events show intra-event periods of no rainfall close to the inter-event time of 6 h. Summarizing, the excluded events generally exhibit increased durations with decreased intensities of discontinuous rainfall. These patterns result in temporally variable runoff generation, thus, preventing an adequate separation between direct runoff and baseflow.

Table 2: Properties of selected and excluded events. The duration (D), the rainfall amount (P), the peak intensity of 60 and 30 minutes intervals (I_{60}, I_{30}), the erosivity (EI_{30}), and the observed sediment yield (SY_{obs}) are applied to characterize the events.

		Time	D [min]	P [mm]	I_{60} [mm/60min]	I_{30} [mm/30min]	EI_{30} [MJ ha^{-1}*I_{30}]	SY_{obs} [Mg]
Selected for further analysis	SY < 1 Mg	20.06.2013	100	13.2	12.6	11.6	88.1	0.43
		29.07.2013	220	17.2	9.2	7.8	52.2	0.92
		18.08.2013	100	6.8	6.4	6.4	23.4	0.34
		25.08.2013	340	11.2	7.4	6.8	19.9	0.88
		27.03.2014	50	9.8	9.8	8.0	26.4	0.18
		28.03.2014	200	19.8	13.0	7.6	53.8	0.79
		01.05.2014	530	14.6	7.8	5.2	8.8	0.73
		24.05.2014	310	11.8	7.0	4.4	5.9	0.62
	SY > 1 Mg	22.06.2013	170	28.6	22.2	16.4	501.7	4.21
		30.06.2013	100	14.2	13.6	13.6	154.5	1.03
		05.07.2013	530	39.4	26.0	17.6	516.5	3.88
		21.07.2013	270	19.8	14.2	12	116.9	2.58
		03.08.2013	400	22.0	21.6	15.2	286	1.19
		28.08.2013	720	42.6	34.8	32.4	2,789.9	7.03
Excluded		05.06.2013	1,158	49.2	13.6	9.6	120.2	-
		24.06.2013	1,458	36.4	7.0	4.6	22.5	-
		23.08.2013	2,368	25.0	8.0	5.6	17.0	-
		09.09.2013	1,692	41.2	9.0	7.4	48.4	-
		20.04.2014	1,422	42.0	13.8	9.4	81.1	-

The average properties of the 14 selected events show a duration D of 276 min, a total rainfall of 19.4 mm, peak intensities I_{60} and I_{30} of 14.7 and 11.8, and an erosivity EI_{30} of 331.7 MJ ha^{-1} mm h^{-1}. These event properties resulted in sediment yields SY_{obs} ranging between 0.18 Mg and 7.03 Mg with an average of 1.77 Mg and a total sediment yield of 24.8 Mg. Eight events show a sediment yield less than 1 Mg with an average of 0.61 Mg (small events). Six events show sediment yields above 1 Mg with an average of 3.32 Mg (large events; Table 2). The large events account for 80.3% of the sediment yield and 61% of the total rainfall amounts over all events.

3.3 Model performance

To evaluate the model performance for each event, we derived the individual model error (ERR). We compared the ERR-values to the observed sediment yields (Figure 3, above). Generally, small events with SY below 1 Mg exhibit increased model errors compared to events with sediment yields above 1 Mg. The average model error ($ERR_{average}$) of the eight small events amounts to 36.2%, ranging between 15.1% and 62%. Except for one event, the ERR refer to severe underprediction. In contrast, the six large events show an average model error of 7.5%, ranging from 0.1 to 14.7%. Those values mainly result from overprediction. The simulated SY for all events amounts 24.2 Mg and deviates by 2.3% from the observed sediment yield of 24.8 Mg. The $ERR_{average}$ of all events results in 23.9%. Comparing the observed versus the predicted sediment yields across all events show a NS-value of 0.98 and a RMSE of 0.27 (Figure 3, below). Thus, the average model quality is high. However, the evaluation of the individual model errors reveals ambiguous patterns. While the model results for large events (>1 Mg) show low ERR-errors, the model runs for the small events (<1 Mg) result in increased ERR-errors.

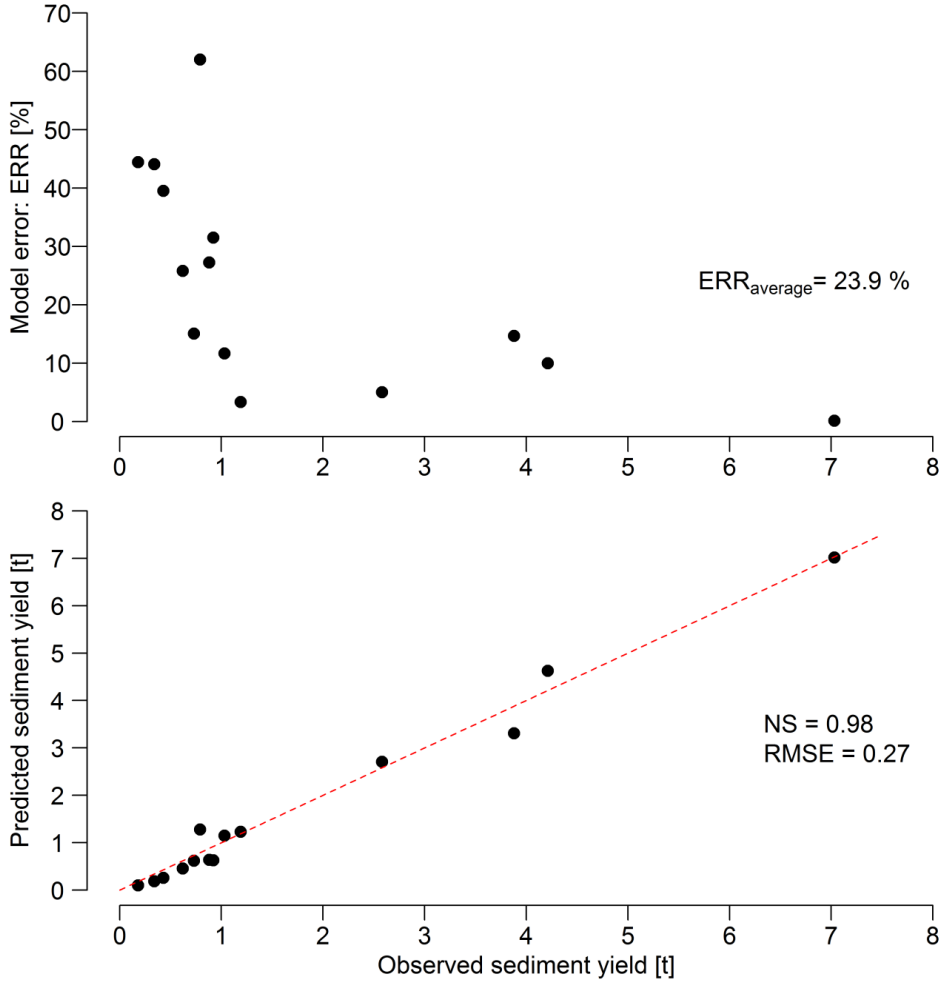

Figure 3: Individual and average model performance for all erosive events (black dots). Performance variability is expressed by comparing the individual prediction error (ERR) to the observed sediment yields (above). Average model performance is revealed by the averaged individual prediction error ($ERR_{average}$, above) and by comparing observed to predicted sediment yields, applying the Nash-Sutcliffe coefficient (NS) and the root mean square error (RMSE; below).

3.4 Characteristics of sediment reallocations

We mapped the model results according to four classes of 'severe' (>50 Mg ha^{-1}), 'high' (20-50 Mg ha^{-1}), 'moderate' (10-20 Mg ha^{-1}), and 'low' (<10 Mg ha^{-1}) erosion and deposition respectively (Figure 4). Moreover, we evaluated the spatial extent of erosion and deposition

zones (Table 3) according to land use patterns (Table 4). Since the large events with a SY > Mg account for the vast majority of all events (80.3%) and uncertainties of the small events (<1 Mg) are high ($ERR_{average}$=36.2%), we excluded the latter from the spatial analysis.

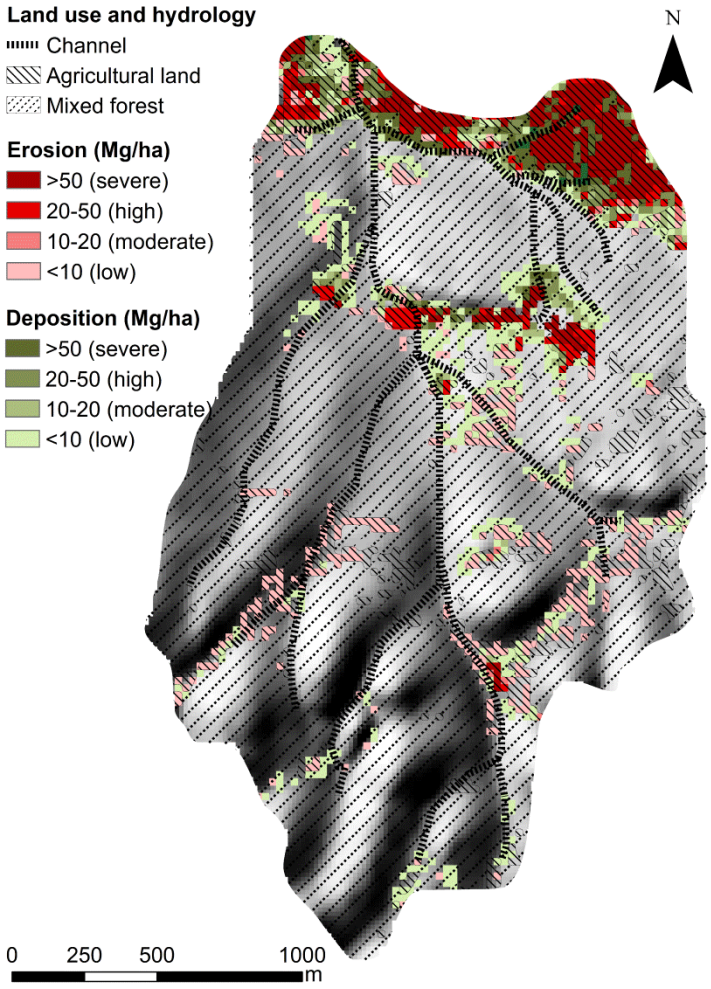

Figure 4: Sediment sources and deposits as budget across erosive events with sediment yields higher than 1 t. Depression channels and land use classes according to agricultural land (composed of the classes 'cropland' and 'grassland') and mixed forest (composed of 'broadleaf', 'conifer' , 'woods', and 'shrub') are indicated.

Agricultural land (land use classes: 'corn-rapeseed', 'potato-cabbage', 'grassland') presents 17% (73.2 ha) of the total study area (428.7 ha). In 79.4% (340.4 ha) of the area 'mixed

forest', composed of the land use classes 'broadleaf', 'conifer', 'woods', and 'shrub' occurs. A small proportion of 3.5% (15.1 ha) is dedicated to small farm buildings.

Table 3: Area of erosion and deposition (ha) and the erosion rate according to classes (severe: > 50 Mg ha^{-1}, high: 20-50 Mg ha^{-1}, moderate: 10-20 Mg ha^{-1}, low: <10 Mg ha^{-1}).

Soil erosion process	Total area [ha]	Severe [%]	High [%]	Moderate [%]	Low [%]
Soil loss	47.5	37.5	13.8	3.6	45.1
Deposition	47.3	15.8	13.4	9.3	61.5

Corresponding to the largest coherent agricultural area, 'severe' and 'high' erosion is predominantly located in the lowlands of the north, where the elevation ranges between 500 m and 650 m. A further band of 'severe' and 'high' erosion extends south of the major agricultural area at elevations between 800 m and 900 m. 'Low' erosion mainly occurs on the agricultural areas in the south at elevations between 900 m and 1400 m. Average slope inclinations of the erosion area amount to 21.5°, ranging between 4.3° and 39.4°. The mapping shows erosion on an area of 47.5 ha, accounting for 11.1% of the entire study area (Figure 4). The simulated erosion rate ranges between 0.01 and 527 Mg ha^{-1} with an average of 49.9 Mg ha^{-1} referring to the erosion area. A proportion of 37.5% (17.8 ha) of the erosion area is classified as 'severe' and 45.1% (21.4 ha) as 'low' (Table 3). In terms of land use, erosion mainly occurs on 'corn-rapeseed' and 'potato-cabbage' with approximately 69% of the respective area (Table 4).

Table 4: Erosion (Ero.) and deposition (Dep.) rates according classes (severe: > 50 Mg ha^{-1}, high: 20-50 Mg ha^{-1}, moderate: 10-20 Mg ha^{-1}, low: <10 Mg ha^{-1}) for different land uses (ha).

Land use	Area [ha]	loss (dep.) [%]	loss (dep.) severe [%]	loss (dep.) high [%]	loss (dep.) moderate [%]	loss (dep.) low [%]
Corn-rapeseed	47.8	69.2 (13.6)	26.1 (1.3)	10.3 (3.6)	2.3 (3.2)	30.5 (5.5)
Potato-cabbage	19.4	69.1 (11.3)	29.9 (0.5)	8.8 (4.6)	3.1 (2.1)	27.3 (4.1)
Grassland	6.0	5.0 (18.4)	- (8.3)	- (1.7)	- (1.7)	5.0 (6.7)
Mixed forest	340.4	0.5 (9.7)	- (1.4)	- (0.8)	- (0.6)	0.5 (6.9)
Built	15.1	- (41.7)	- (10.6)	- (6.6)	- (4.0)	- (20.5)

‘Severe’ and ‘high’ sediment depositions mainly occur in the two major erosive areas in the north. Depositions are concentrated lateral of topographical depression channels, at field borders with high vegetation cover, and in infrastructural areas. In the south of the study area, at an elevation between 900 m and 1400 m, depositions are located adjacent to erosive areas and mainly classified as ‘low’. The total deposition area outlines an average slope inclination of 19.8°, ranging from 1.1° to 35.5°, therefore showing a marginal decline compared to the erosion area. Deposition occurs on 47.3 ha, thus 11% of the study area (Figure 4). The deposition rate ranges between 0.01 and 499.5 Mg ha^{-1} with an average of 40.3 Mg ha^{-1}. A proportion of 61.5% (29.1 ha) of the deposition area is classified as ‘low’, while the remaining classes occupy areal proportions between 9.3% (4.4 ha) and 15.8% (7.5 ha; Table 3). Referring to land use, deposition occurs on each class, while ‘built’ is occupied by 41.7% (6.3 ha) of the area. The proportional deposition area of the remaining land use classes range between 9.7% (33.0 ha) for ‘mixed forest’ and 18.4% (1.1 ha) for ‘grassland’ (Table 4).

4 Discussion

4.1 Erosive events and data quality

In this study, rainfall-runoff events were delimited by an initial rainfall impulse and the remission of the associated direct runoff. This procedure is in accordance with other studies on rainfall-runoff events (Baltas *et al.*, 2007; Blume *et al.*, 2007). Subsequently, observed

sediment yields were attributed to identify the respective erosive response. However, the event properties that determine the erosive response highly depend on methodological settings for data acquisition, event exclusion, event classification rules, and the inter-event time to disaggregate a rainfall record (Dunkerley, 2008). Todisco *et al*. (2014) argued that the event properties change in time and space and can be referred to as arbitrary due to customized settings for individual applications and environments. This limits the comparability in terms of event-based erosion studies.

In addition, high quality monitoring data on erosion become increasingly important to enable an evaluation of the site-specific cause-effect relationship and to address the requirements of complex model structures (Aksoy & Kavvas, 2005; Fang *et al*., 2013). Commonly, continuous and high resolution data on rainfall and runoff are available. Contrary, continuous data on sediment loads are often difficult to obtain due to required maintenance and operating personnel (Rickemann & McArdell, 2007).

Within the TGRA, Fang *et al*. (2013) investigated erosive events in a small catchment of 1,670 ha. Rainfall and runoff data were continuously measured in a resolution of 15 min. Data on sediment loads were manually obtained only during rainfall events. From a total of 205 rainfall-runoff events between 1989 and 2004, 10 were classified as extreme according to a qualitative assessment of surface damage due to erosion. These events caused 83.3% of the sediment load. This supports Cai *et al*. (2005), who stated that most erosion in the TGRA is associated with very few heavy rainfall events each year.

In contrast, we continuously derived data on rainfall, runoff, and sediment yield in a 10 min resolution over a period of 12 months within a catchment of 429 ha (Figure 1). The rainfall data was approved to be representative for the region, since the amounts per months were within the range of averaged daily long-term records (Figure 2). Similar to Fang *et al*. (2013) a few large events caused the major proportion of the total sediment yield. We identified 14 events of which six showed sediment yields above 1 Mg, accounting for 80.3% of the total sediment yield. Moreover, we detected high correlations between the regimes of rainfall, runoff, and sediment yields with r-values above 0.8, while all regimes outline peak values during the wet season and minimum values in winter. Both, the high correlations and similar distributions indicate a strong cause-effect relationship between the monitoring data.

4.2 Erosion modelling in the Three Gorges Reservoir Area

The performance of physically-based erosion models depends on the model capability to deal with the natural complexity of the erosion process and the spatial heterogeneity of the study area (De Vente & Poesen, 2005). Furthermore, the availability and quality of the input data needs to be in agreement with the complexity of the model routines (Van Rompaey & Govers, 2002; De Vente *et al.*, 2013). Thus, the combined criteria of the model design, environmental conditions, and data infrastructure determine the adequacy of a model for a specific research question (Boardman, 2006). In the TGRA, a few physically-based model attempts have been conducted to test model performances and to assess erosion control measures at catchment scale (Shen *et al*., 2010; Shi *et al*., 2012).

Shi *et al*. (2012) applied WaTEM/SEDEM in catchment of 1,670 ha. This model uses the empirical RUSLE to calculate annual water erosion on hillslopes, and a sediment routing along the runoff channels by incorporating local sediment transport capacity (Van Rompaey *et al*., 2001). Shen *et al*. (2010) applied the WEPP model in a catchment of 162 ha. WEPP uses the Green-Ampt infiltration approach to simulate runoff and a steady-state sub-routine to solve a sediment continuity equation at a peak runoff rate (Flanagan & Nearing, 2000). We applied EROSION 3D in a catchment of 429 ha, a model that also uses the Green-Ampt infiltration equation for the runoff routine. However, the erosion routine is based on the momentum flux approach that relates the erosive impact of runoff and rainfall to their exerted momentum flux (Schmidt *et al*., 1999; Schindewolf & Schmidt, 2012).

Both, WaTEM/SEDEM and WEPP present continuous model approaches producing average values for erosion and deposition. In contrast, EROSION 3D is an event-based model and therefore capable to assess the variability of erosive responses due to singular rainfall-runoff events. Event-based models require event-specific parametrization due to a high sensitivity to initial conditions. Thus, requirements for data quality in terms of accuracy and continuity are higher (Jetten *et al*. 2003; Aksoy & Kavvas 2005; Boardman, 2006). This especially accounts for the parameters that control infiltration, such as soil moisture and hydraulic conductivity (Schmidt *et al*. 1999; Jetten *et al*., 2003; Shen *et al*., 2010). Particularly in the TGRA, where major sediment reallocations are due to very few extreme events, the event-based assessment is of substantial interest in context of implementing erosion control measures to prevent hazardous impacts (Cai *et al*., 2005; Fang *et al*., 2013).

Continuous runoff data and discontinuous sediment yield data from the outlet were available for both model attempts by Shen *et al*. (2010) and Shi *et al*. (2012). The data was used to calibrate the WEPP model, while WaTEM/SEDEM was parametrized by available RUSLE data. Both studies were validated by the outlet data. In the present study we used continuous data on runoff and sediment yield, therefore providing an increased data consistency. Model calibration was enabled by using DSM techniques to calculate high resolution soil property information. Thus, DSM provided a solution to enable the parametrization of a physically- and event-based erosion and deposition model at catchment scale in a generally data scarce environment (Stumpf *et al*., 2015a). Further model parameters were based on land use data derived from satellite images and an empirically compiled parameter catalogue (Michael, 2000). Only the sensitive soil moisture parameter was adjusted using observed and predicted runoff data, a procedure that is commonly applied in event-based erosion modelling (Schmidt *et al*., 1999; Jetten *et al*., 2003). Similar to the WaTEM/SEDEM and WEPP approach in the TGRA (Shen *et al*., 2010; Shi *et al*., 2012), model performance of the presented approach was assessed using outlet data on sediment yield. However, due to the variability in the sediment delivery ratio with changing temporal and spatial scale, sediment yield data have been criticized for field erosion measurements (Boardman, 2006). Nevertheless, the assumption of a stable and high sediment delivery ratio is reasonable, since the cause-effect relationship between the monitoring data (rainfall, runoff, sediment yield) is strong ($r > 0.8$) and erosive events are mainly due to high intensity rainfall events that are reported to cause high sediment connectivity (Lexartza-Artza & Wainwright, 2011; Baartman *et al.*, 2013; Todisco, 2014; Marchamalo *et al.*, 2015).

Both physically-based model attempts in the TGRA (Shen *et al*., 2010, Shi *et al*., 2012) showed acceptable average model accuracies with NS=0.65 for the WaTEM/SEDEM approach and NS=0.84 (average deviation: 3.9%) for the WEPP modelling. Contrary, the presented study, using EROSION 3D, exhibited an increased average accuracy of NS=0.98 and an decreased average deviation of 2.3 over all modelled events. Moreover, since EROSION 3D is event-based, we also derived event-specific accuracies. We detected ambiguous model performances between small events (< 1 Mg; $ERR_{average}$=36.2%) and large events (> 1 Mg; $ERR_{average}$=7.5%).The increasing model performance for large events is in agreement with other event-based model attempts (Zhang *et al.*, 1996; Nearing *et al*., 1999; Nearing, 2000; Gumiere *et al.*, 2011; Lee *et al.*, 2013). In this context, Jetten et al. (2003)

argued that small-scale events are generally difficult to simulate since the deterministic character of erosion models is incapable to deal with the random component of measured data. Boardman (2006) relates the low accuracy of small-scale events to oversimplified runoff routines, which solely simulate runoff by infiltration excess and thereby underrating the erosive power of low intensity rainfall on saturated soil. Moreover, the decreased sediment connectivity of low intensity rainfall could cause variability in the outlet data, and therefore leading to biased estimation (Marchamalo *et al.*, 2015).

For the WaTEM/SEDEM approach 'severe' and 'high' erosion occurred on 10.5% of the study area with an average erosion rate of 13 Mg ha^{-1}. Deposition was detected on 20.5%, while no classification on magnitude was conducted (Shi *et al.*, 2012). For the WEPP approach the average erosion rate ranged between 2 and 38 Mg ha^{-1}, while quantitative information on proportional areas of erosion and deposition was not provided. In the presented study, 'severe' and 'high' erosion was found on 5.7% of the study area, while 11% were occupied by deposition. The average erosion rate is 49.9 Mg ha^{-1}, calculated over the erosion area and using the budget of the modelled events that account for 80.3% of the total sediment yield (Table 5).

Table 5: Model-based erosion studies in the Three Gorges Reservoir Area, based on physical (EROSION 3D, WaTEM/SEDEM, WEPP), semi-empirical (SWAT), empirical (USLE/RUSLE), and radionuclide inventory (C^{137}) methods.

Method	Area [ha]	Average soil loss rate [Mg $ha^{-1}a^{-1}$]	Reference
EROSION 3D	429	49.9	present study
WaTEM/SEDEM	1,670	13.2	Shi *et al.*[2012]
WEPP	162	2 - 38	Shen *et al.* [2010]
SWAT	162	27.0	Shen *et al.* [2009]
USLE	$2.3*10^6$	32.8	Zhang [2008]
RUSLE	$3.2*10^5$	52 - 76	Strehmel *et al.* [2015]
RUSLE	162	26 - 52	Shi *et al.* [2004]
^{137}Cs	70	45.0	Lu & Higgit [2000]
^{137}Cs	0.21	51.5	Quine *et al.* [1999]
^{137}Cs	$1.1*10^8$	24.2	He *et al.* [2007]

Other model-based erosion studies within the TGRA applied the empirical RUSLE, the semi-empirical SWAT model, or radionuclide inventories of (C^{137}) in various scales (Quine *et al.*, 1999; Lu & Higgit, 2000; Shi *et al.*, 2004; He *et al.*, 2007; Zhang, 2008; Strehmel *et al.*, 2015). The estimated erosion rates ranged between 26 Mg ha^{-1} a^{-1} and 76 Mg ha^{-1} a^{-1}. Since the average erosion rate of the presented study lies within the range of other erosion studies in this region, the applied approach can therefore be considered as reliable. However, the comparability of erosion rates is limited due to scale-dependency in terms of space and time, a variety of measurement methods, and the complex relationship between environmental factors and erosion (Boardman, 2006; De Vente et al., 2007; Cantón *et al.*, 2011; Vanmaercke *et al.*, 2011; García-Ruiz *et al.*, 2015). In this context, García-Ruiz *et al.* (2015) compiled a data base of erosion rate studies from more than 4000 sites worldwide, and analyzed the data on their relation to (non-) environmental factors. The meta-analysis revealed general trends of positive relations to factors such as slope, annual precipitation, and land use. However, the results showed high variability since the included studies comprised various spatial scales, durations of the experiments, and methods. Moreover, García-Ruiz *et al.* (2015) argued that insufficient descriptions of study areas, methods, and results, further exacerbate the comparability of erosion studies.

4.3 Sediment reallocation and landuse

This study investigates rainfall-triggered sediment reallocations to enable sustainable land management at catchment scale. However, the sedimentological response of a landscape is complex, since it depends on a variety of interacting physical processes, which are related to topography, climate, soil, and vegetation among others (Martínez-Mena *et al.*, 1998; Cammeraat, 2004; Puigdefábregas, 2005; Bracken & Croke, 2007; Bautista *et al.*, 2007; Kröpfl *et al.*, 2013; Marchamalo *et al.*, 2015).

The quantification of the landscape response is increasingly achieved using the concept of landscape connectivity, which describes the water-mediated sediment fluxes within a catchment (Bracken & Croke, 2007; Lexartza-Artza & Wainwright, 2011; Fryirs, 2013). Marchamalo *et al.* (2015) presented a method to identify hotspots of sediment sources, deposits, and their linkages by repeatedly mapping after rainfall events. Keesstra *et al.* (2009) combined field surveys, site-specific expert knowledge, and a sediment delivery model to

establish a detailed sediment budget. However, the aforementioned approaches are accompanied by extensive field work, since detailed landscape features, related to connectivity are difficult to derive from DEMs and remote sensing images (Marchamalo *et al.*, 2015; Lesschen *et al.*, 2009)

In contrast, the presented approach outlines a modelling framework of automated field monitoring and DSM techniques to calibrate a physically- and event based erosion model. The framework reduces efforts for field work and is applicable in data scarce and highly dynamic environments. However, the validation by outlet data only addresses overall model accuracy, while an uncertainty assessment of quantified sediment reallocations is limited (Jetten *et al.*, 1999; Boardman, 2006).

Nevertheless, the spatial results of the modelling approach are in agreement with average soil loss rates of main land use types in southern China (Hill & Peart, 1998; Huang *et al*., 1998; Xiang *et al*., 2001; Gao *et al*., 2004; Zheng & Zhang, 2006; Guo *et al*., 2015). The data is based on plot-scale studies, from which an average soil loss rate of 0.38 Mg ha^{-1} a^{-1} for the land use type 'forest', 5.5 Mg ha^{-1} a^{-1} for 'grassland', and 35.4 t ha^{-1} a^{-1} for 'cropland' were identified. According to a review of Hill & Peart (1998), average soil loss in southern China amounts to 0.1 Mg ha^{-1} a^{-1} for 'forest', 2.4 Mg ha^{-1} a^{-1} for 'grassland', and 62.4 Mg ha^{-1} a^{-1} for 'cropland'. In the present study, we found erosion on the land use classes 'corn-rapeseed' and 'potato-cabbage', while both land use classes were classified as 'severe'(> 50 Mg ha^{-1}) for approximately one third of the specific land use area (Table 4).

In addition, Takken *et al*. (1999) mapped erosion patterns and calculated the erosion rate after an extreme rainfall event for different land use types in a small catchment in Belgium. The results confirm the aforementioned erosion rates with no erosion for 'forest', 0.2 Mg ha^{-1} for 'grassland', 53.0 Mg ha^{-1} for 'potato', and 76.0 Mg ha^{-1} for 'corn'. Moreover, Takken *et al.* (1999) found deposition on 3.5% of the study area, while major deposition zones were concentrated along the topographical depression lines, at field borders with high vegetation, and on roads. These results are generally confirmed by the present study, while deposition occurred on each land use class, but concentrated in topographic depression lines and on infrastructure (Figure 4; Table 4).

5 Conclusion

In this study we analyzed sediment reallocations due to erosive rainfall events in a data scarce and small catchment of the Three Gorges Reservoir area in China. Thus, we set up a methodological workflow to parametrize EROSION 3D and tested the model as a tool to spatially identify sediment sources and deposits. We accomplished the complex model parametrization using Digital Soil Mapping techniques, land use maps based on satellite data, and a parameter catalogue that contains empirically derived values for various conditions. The continuous model calibration data on rainfall, runoff, and sediment yields were representative for the region and showed a strong cause-effect relationship, facilitating to derive erosive events. The majority of the total sediment yield (80.3%) were attributed to only six large erosive events. Erosion 3D performed well for large events, while small events showed high uncertainties. We detected an average erosion rate of 49.9 Mg ha^{-1} within the erosion area that covered 11.1% of the study area. The major proportions of the erosion area were classified as 'severe' (37.5%) and 'low' (45.1%) erosion. Primarily, erosion occurred on cropland, concentrated on the land use classes 'corn-rapeseed' and 'potato-cabbage'. Deposition occurred on 11% of the study area, mainly classified as 'low' deposition (61.5%). Contrary to the erosion area, each land use class was affected by deposition, while the major areal proportions were attributed to the classes 'built' (47.1%) and 'grassland' (18.4%). In summary, we presented an efficient methodological outline to meet the complex data requirements of a physically- and event-based erosion model. Moreover, considering that the major sediment yields in the region are associated to a few large events, EROSION 3D can be recommended to identify sediment reallocations in small catchments.

Acknowledgements

We thankfully acknowledge funding from the German Ministry of Education and Research (BMBF, grant No. 03 G 0827A) for the German-Sino research collaboration YANGTZE GEO. We thank Bi Renneng from the University of Erlangen-Nuremberg, Giovanni Buzzo from the University of Trier, and Alexander Strehmel from the Christian-Albrechts-University of Kiel for data sharing. We thank all students from the China University of Geosciences (CUG) in Wuhan that were involved in field campaigns and laboratory analyzes. We are also very grateful for the general support of the whole YANGTZE GEO research group.

References

Aksoy H, Kavvas ML. 2005. A review of hillslope and watershed scale erosion and sediment transport models. *Catena* **64**: 247–271.

Anderson CW. 2005. Turbidity: U.S. Geological Survey (USGS) Techniques of Water-Resources Investigations. [http://pubs.water.usgs.gov/twri9A; accessed: September 2014]

Andrews F, Guillaume J. 2015. 'hydromad': Hydrological Model Assessment and Development. R package version 0.9-22. [http://hydromad.catchment.org/; accessed: May 2014]

Arnold JG, Allen PM, Muttiah R, Bernhardt G. 1995. Automated Base Flow Separation and Recession Analysis Techniques. *Ground Water* **33**: 1010–1018.

Baartman JEM, Masselink R, Keesstra SD, Temme AJAM. 2013. Linking landscape morphological complexity and sediment connectivity. *Earth Surface Processes And Landforms* **38**: 1457–1471.

Bagarello V, Di Piazza GV, Ferro V, Giordano G. 2008. Predicting unit plot soil loss in Sicily, south Italy. *Hydrological Processes* **22**: 586–595.

Baltas EA, Dervos NA, Mimikou MA. 2007. Technical Note: Determination of the SCS initial abstraction ratio in an experimental watershed in Greece. *Hydrological Earth System Sciences* **11**: 1825–1829.

Bautista S, Mayor AG, Bourakhouadar J, Bellot J. 2007. Plant spatial pattern predicts hillslope runoff and erosion in a semiarid Mediterranean landscape. *Ecosystem* **10**: 987–998.

Behrens T, Zhu AX, Schmidt K, Scholten T. 2010. Multi-scale digital terrain analysis and feature selection for digital soil mapping. *Geoderma* **155**: 175–185.

Behrens T, Schmidt K, Ramirez-Lopez L, Gallant J, Zhu AX, Scholten T. 2014. Hyper-scale digital soil mapping and soil formation analysis. Geoderma **213**: 578–588.

Berendse F, Van Ruijven J, Jongejans E, Keesstra S. 2015. Loss of plant species diversity reduces soil erosion resistance. *Ecosystems* **18**: 881–888.

Blume T, Zehe E, Bronstert A. 2007. Rainfall-runoff response, event-based runoff coefficients and hydrograph separation. *Hydrological Sciences Journal* **52**: 843–862.

Boardman J. 2006. Soil erosion science: Reflections on the limitations of current approaches. *Catena* **68**: 73–86.

Bracken LJ, Cox NJ, Shannon J. 2008. The relationship between rainfall inputs and flood generation in south–east Spain. *Hydrological Processes* **22**: 683–696.

Bracken LJ, Croke J. 2007. The concept of hydrological connectivity and its contribution for understanding sediment transfer at multiple scales. *Earth Surface Processes and Landforms* **21**: 1749–1763.

Breiman L. 2001. Random Forests. *Machine Learning* **45**: 5–32.

Brevik EC, Cerdà A, Mataix-Solera J, Pereg L, Quinton JN, Six J, Van Oost K. 2015. The interdisciplinary nature of soil. *Soil* **1**: 117–129.

Brown L, Foster G. 1987. Storm erosivity using idealized intensity distribution. *American Society of Agricultural Engineers* **30**: 379–386.

Cai QG, Wang H, Curtin D, Zhu Y. 2005. Evaluation of the EUROSEM model with single event data on steeplands in the Three Gorges Reservoir Areas, China. *Catena* **59**: 19–23.

Cammeraat LH. 2004. Scale dependent thresholds in hydrological erosion response of a semi-arid catchment in southeast Spain. *Agricultural Ecosystems and Environment* **104**: 317–332.

Campbell GB. 1991. Soil Physics with Basic Transport Models for Soil–Plant Systems, 1st edition. Elsevier, Amsterdam.

Cantón Y, Solé-Benet A, De Vente J, Boix-Fayos C, Calvo-Cases A, Asensio C, Puigdefábregas J. 2011. A review of soil erosion across scales in semi-arid south-eastern Spain. *Journal of Arid Environments* **75**: 1254–1261.

Capolongo D, Pennetta L, Piccarreta M, Fallacara G, Boenzi F. 2008. Spatial and temporal variations in soil erosion and deposition due to land-levelling in a semi-arid area of Basilicata (Southern Italy). *Earth Surface Processes and Landforms* **33**: 364–379.

CMA. 2012. Chinese Meteorological Administration, Beijing: Climate Data. [http://2011.cma.gov.cn/en/; accessed: February 2014]

De Vente J, Poesen J, Verstraeten G, Govers G, Vanmaercke M, Van Rompaey A, Arabkhedri M, Boix-Fayos C. 2013. Predicting soil erosion and sediment yield at regional scales: Where do we stand? *Earth-Science Reviews* **127**: 16–29.

De Vente J, Poesen J. 2005. Predicting soil erosion and sediment yield at the basin scale: scale issues and semi-quantitative models. *Earth-Science Reviews* **71**: 95–125.

De Vente J, Poesen J, Arabkhedri M, Verstraeten G. 2007. The sediment yield problem revisited. *Progress in Physical Geography* **31**: 155–178.

Dunkerley D. 2008. Rain event properties in nature and in rainfall simulation experiments: a comparative review with recommendations for increasingly systematic study and reporting. *Hydrological Processes* **22**: 4415–4435.

Fang NF, Shi ZH, Yue BJ, Wang L. 2013. The Characteristics of Extreme Erosion Events in a Small Mountainous Watershed. *PLoS One* **8**: 1–10.

Ferreira V, Panagopoulos T, Andrade R, Guerrero C, Loures L. 2015. Spatial variability of soil properties and soil erodibility in the Alqueva reservoir watershed. *Solid Earth* **6**: 383–392.

Flanagan DC, Nearing MA. 2000. Sediment particle sorting on hillslope profiles in the WEPP model. *American Society of Agricultural Engineers* **43**: 576–583.

Fryirs K. 2013. (Dis) Connectivity in catchment sediment cascades: a fresh look at the sediment delivery problem. *Earth Surface Processes and Landforms* **38**: 30–46.

Fuka DR, Walter MT, Archibald JA, Steenhuis TS, Easton ZM. 2014. 'EcoHydRology': community modeling foundation for Eco-Hydrology. R package version 04-12. [http://cran.r-project.org/package=EcoHydRology; accessed: April 2014]

Gao ZQ, Zhang HJ, Shi YH. 2004. Study on soil erosion rate in different land use types in the granite area of Three Gorges. *Journal of Soil Water Conservation* **2**: 26–29.

García-Ruiz JM, Beguería S, Nadal-Romero E, Gonzáles-Hidalgo JC, Lana-Renault N, Sanjuán Y. 2015. A meta-analysis of soil erosion rates across the world. *Geomorphology* **239**: 160–173.

Goebes P, Schmidt K, Seitz S, Stumpf F, Scholten T. 2015. Rule-based analysis of throughfall kinetic energy to evaluate leaf and tree architectural trait thresholds to mitigate erosive power. [accepted for publication in *Progress in Physical Geography*]

Green WH, Ampt GA. 1911. Studies on soil physics: I. The flow of air and water through soils. *Journal of Agricultural Sciences* **4**: 1–24.

Grønsten HA, Lundekvam H. 2006. Prediction of surface runoff and soil loss in southeastern Norway using the WEPP Hillslope model. *Soil &Tillage Research* **85**: 186–199.

Gumiere SJ, Raclot D, Cheviron B, Davy G, Louchart X, Fabre J, Moussa R, Le Bissonais Y. 2011. MHYDAS-Erosion: a distributed single-storm water erosion model for agricultural catchments. *Hydrological Processes* **25**: 1717–1728.

Guo Q, Hao Y, Liu B. 2015. Catena Rates of soil erosion in China : A study based on runoff plot data. *Catena* **124**: 68–76.

He X, Xu Y, Zhang X. 2007. Traditional farming system for soil conservation on slope farmland in southwestern China. *Soil & Tillage Research* **94**: 193–200.

Heung B, Bulmer CE, Schmidt MG. 2014. Predictive soil parent material mapping at a regional-scale: A Random Forest approach. *Geoderma* **214**: 141–154.

Hill RD, Peart MR. 1998. Land use, runoff, erosion and their control: a review for southern China. *Hydrological Processes* **12**: 2029–2042.

Hooke J. 2003. Coarse sediment connectivity in river channel systems; a conceptual framework and methodology. *Geomorphology* **56**: 79–94.

Huang L, Ding SW, Zhang G, Peng YX. 1998. Preliminary estimation of soil and water conservation under different tillages on purple soil slope land in the Three Gorges Reservoir area. *Journal of Huazhong Agricultural University* **17**: 45–49. [in Chinese]

Jetten VG, de Roo APJ, Favis-Mortlock D. 1999. Evaluation of field - scale and catchment - scale soil erosion models. *Catena* **3**: 521–541.

Jetten V, Govers G, Hessel R. 2003. Erosion models: Quality of spatial predictions. *Hydrological Processes* **17**: 887–900.

Jordan G, Van Rompaey A, Szilassi P, Csillag G, Mannaerts C, Woldai T. 2005. Historical land use changes and their impact on sediment fluxes in the Balaton basin (Hungary). *Agriculture, Ecosystems & Environment* **108**: 119–133.

Kepa Brian Morgan TK, Sardelic DN, Waretini AF. 2012. The Three Gorges Project: How sustainable? *Journal of Hydrology* **460**: 1–12.

Keesstra SD, Geissen V, Van Schaik L, Mosse K, Piiranen S. 2012. Soil as a filter for groundwater quality. *Current Opinions in Environmental Sustainability* **4**: 507–516.

Keesstra SD, Bruijnzeel LA, Van Huissteden J. 2009. Meso-scale catchment sediment budgets: combining field surveys and modeling in the Dragonja catchment, southwest Slovenia. *Earth Surface Processes and Landforms* **34**: 1547–1561.

Kirkby, M.J., 1978. Hillslope hydrology. Wiley & Sons Ltd, Chichester.

Krause P, Boyle DP, Bäse F. 2005. Comparison of different efficiency criteria for hydrological model assessment. *Advances in Geosciences* **5**: 89–97.

Kröpfl AI, Cecchi GA, Villasuso NM, Distel RA. 2013. Degradation and recovery processes in semi-arid patchy rangelands of northern Patagonia, Argentinia. *Land Degradation & Development* **24**: 393–399.

Lal R. 2003. Soil erosion and the global carbon budget. *Environment International* **29**: 437–450.

Lee G, Yu W, Jung K. 2013. Catchment-scale soil erosion and sediment yield simulation using a spatially distributed erosion model. *Environmental Earth Sciences* **70**: 33–47.

Lesschen JP, Schoorl JM, Cammeraat LH. 2009. Modelling runoff and erosion for semi-arid catchment using a multi-scale approach based on hydrological connectivity. *Geomorphology* **109**: 174–183.

Lexartza-Artza I, Wainwright J. 2011. Making connections: changing sediment sources and sinks in an upland catchment. *Earth Surface Processes and Landforms* **36**: 1090–1104.

Liaw A, Wiener M. 2002. Classification and Regression by Random Forest. *R News* **2**: 18–22.

Liu J, Liu M, Tian H, Zhuang D, Zhang Z, Zhang W, Tang X, Deng X. 2005. Spatial and temporal patterns of China's cropland during 1990-2000: An analysis based on Landsat TM data. *Remote Sensing Environment* **98**: 442–456.

Lu XX, Higgitt DL. 2000. Estimating erosion rates on sloping agricultural land in the Yangtze Three Gorges, China, from caesium-137 measurements. *Catena* **39**: 33–51.

Marchamalo M, Hooke JM, Sandercock PJ. 2015. Flow and sediment connectivity in semi-arid landscapes in SE Spain: Patterns and control. Land Degradation & Development. DOI: 10.1002/ldr.2352

Martínez-Mena M, Albaladejo J, Castillo VM. 1998. Factors influencing surface runoff generation in a Mediterranean semi-arid environment. *Hydrological Processes* **12**: 74 –754.

McBratney AB, Mendonça Santos ML, Minasny B. 2003. On digital soil mapping. *Geoderma* **117**: 3–52.

Merz J, Dangol PM, Dhakal MP, Dongol BS, Nakarmi G, Weingartner R. 2006. Rainfall-runoff events in a middle mountain catchment of Nepal. *Journal of Hydrology* **331**: 446–458.

Michael A. 2000. Anwendung des physikalisch begründeten Erosionsprognosemodells EROSION 2D/3D - Empirische Ansätze zur Ableitung der Modellparameter. Technical University Freiberg, Germany. [Dissertation]

Mitasova H, Hofierka J, Zlocha M, Iverson LR. 1996. Modeling topographic potential for erosion and deposition using GIS. *International Journal of Geographic Information Systems* **10**: 629–641.

Morgan RPC. 2005. Soil erosion and conservation. Blackwell Publishing, Oxford.

Nash JE, Sutcliff JV. 1970. River flow forecasting through conceptual model. Part 1: A discussion of principles. *Journal of Hydrology* **10**: 282–290.

Nathan RJ, McMahon TA. 1990. Evaluation of automated techniques for base flow and recession analysis. *Water Resources Research* **26**: 1465–1473.

Nearing MA, Govers G, Darrell NL. 1999. Variability in soil erosion data from replicated plots. *Soil Science Society of America Journal* **63**: 1829–1835.

Nearing MA. 2000. Evaluating soil erosion models using measured plot data: accounting for variability in the data. *Earth Surface Processes and Landforms* **25**: 1035–1043.

Nearing MA, Jetten V, Baffaut C, Cerdan O, Couturier A, Hernandez M, Le Bissonnais Y, Nichols MH, Nunes JP, Renschler CS, Souchère V, Van Oost K. 2005. Modeling response of soil erosion and runoff to changes in precipitation and cover. *Catena* **61**: 131–154.

Onyando JO, Kisoyan P, Chemelil MC. 2005. Estimation of potential soil erosion for river Perkerra catchment in Kenya. *Water Resources Management* **19**: 133–143.

Palazón L, Gaspar L, Latorre B, Blake WH, Navas A. 2014. Evaluating the importance of surface soil contributions to reservoir sediment in alpine environments: a combined modelling and fingerprinting approach in the Posets-Maladeta Natural Park. *Solid Earth* **5**: 963–978.

Park S, Oh C, Jeon S, Jung H, Choi C. 2011. Soil erosion risk in Korean watersheds, assessed using the revised universal soil loss equation. *Journal of Hydrology* **399**: 263–273.

Peng CUI, Yonggang GE, Yongming LIN. 2011. Soil Erosion and Sediment Control Effects in the Three Gorges Reservoir Region , China. *Journal of Resources and Ecology* **2**: 289–297.

Peters J, Baets BD, Verhoest NEC, Samson R, Degroeve S, Becker PD, Huybrechts W. 2007. Random forests as a tool for ecohydrological distribution modelling. *Ecological Modelling* **207**: 304–318.

Puigdefábregas J. 2005. The role of vegetation patterns in structuring runoff and sediment fluxes in drylands. *Earth Surface Processes and Landforms* **30**: 133–148.

Quine TA, Walling DE, Chakela QK, Mandiringana OT, Zhang X. 1999. Rates and patterns of tillage and water erosion on terraces and contour strips: evidence from caesium-137 measurements. *Catena* **36**: 115–142.

RapidEye. 2012. Satellite Imagery Product Specifications—version 4.1. [http://www.rapideye.com/upload; accessed: February 2013]

Renard K, Foster G, Weesies G, McCool D, Yoder D. 1997. Predicting soil erosion by water: a guide to conservation planning with the Revised Universal Soil Loss Equation (RUSLE). USDA Agricultural Handbook No. 703. [http://www.osmre.gov/resources/library/ghm/USDA_AH703.pdf; accessed: May 2014]

Rickemann D, McArdell BW. 2007. Continuous measurement of sediment transport in the Erlenbach stream using piezoelectric bedload impact sensors. *Earth Surface Processes and Landforms* **32**: 1362–1378.

SAGA, 2012. System for Automated Geoscientific Analyses -Version 2.0.6. [http//:www.saga-gis.org; accessed: January 2013]

Satterland DR, Adams PW. 1992. Wildland watershed management. Wiley & Sons Ltd, New Jersey.

Schindewolf M, Schmidt J. 2012. Parameterization of the EROSION 2D/3D soil erosion model using a small-scale rainfall simulator and upstream runoff simulation. *Catena* **91**: 47–55.

Schmidt J. 1991. A mathematical model to simulate rainfall erosion. *Catena Supplememt* **19**: 101–109.

Schmidt J. 1992. Modeling long term soil loss and landform change. In: Parson AJ, Abrahams AD (Eds.). Overland Flow — Hydraulics and Erosion Mechanics. UCL Press, London.

Schmidt J, Werner MV, Michael A. 1999. Application of the EROSION 3D model to the CATSOP watershed, the Netherlands. *Catena* **37**: 449–456.

Schönbrodt S, Saumer P, Behrens T, Seeber C, Scholten T. 2010. Assessing the USLE Crop and Management Factor C for Soil Erosion Modelling in a Large Mountainous Watershed in Central China. Journal of Earth Science **21**: 835–845.

Schönbrodt-Stitt S, Bosch A, Behrens T, Hartmann H, Shi X., Scholten T. 2013 a. Approximation and spatial regionalization of rainfall erosivity based on sparse data in a mountainous catchment of the Yangtze river in central China. Environmental Science and Pollution Research **20**: 6917–6933.

Schönbrodt-Stitt S, Behrens T, Schmidt K, Shi X, Scholten T. 2013 b. Degradation of cultivated bench terraces in the Three Gorges Area: Field mapping and data mining. *Ecological Indicators* **34**: 478–493.

Shen ZY, Gong YW, Li YH, Hong Q, Xu L, Liu RM. 2009. A comparison of WEPP and SWAT for modeling soil erosion of the Zhangjiachong Watershed in the Three Gorges Reservoir Area. *Agricultural Water Management* **96**: 1435–1442.

Shen ZY, Gong YW, Li YH, Liu RM. 2010. Analysis and modeling of soil conservation measures in the Three Gorges Reservoir Area in China. *Catena* **81**: 104–112.

Shi ZH, Cai CF, Ding SW, Wang TW, Chow TL. 2004. Soil conservation planning at the small watershed level using RUSLE with GIS: A case study in the Three Gorge Area of China. *Catena* **55**: 33–48.

Shi ZH, Ai L, Fang NF, Zhu HD. 2012. Modeling the impacts of integrated small watershed management on soil erosion and sediment delivery: A case study in the Three Gorges Area, China. *Journal of Hydrology* **438**: 156–167.

Slimane AB, Raclot D, Evrad O, Sanaa M, Lefevre I, Bissonais YL. 2015. Relative contributions of rill/interrill and gully/channel erosion to small reservoir siltation in Mediterranean environments. *Land Degradation & Development* (DOI: 10.1002/ldr.2387).

Soulis KX, Valiantzas JD, Dercas N, Londra PA. 2009. Analysis of the runoff generation mechanism for the investigation of the SCS-CN method applicability to a partial area experimental watershed. *Hydrological Earth System Sciences* **6**: 373–400.

Starkloff T, Stolte J. 2014. Applied comparison of the erosion risk models EROSION 3D and LISEM for a small catchment in Norway. *Catena* **118**: 154–167.

Strehmel A, Schönbrodt-Stitt S, Buzzo G, Dumperth C, Stumpf F, Zimmermann K, Bieger K, Behrens T, Schmidt K, Bi R, Rohn J, Hill J, Udelhoven T, Xiang W, Shi X, Cai Q, Jiang T, Fohrer N, Scholten T. 2015. Assessment of geo-hazards in a rapidly changing landscape: the three Gorges Reservoir Region in China. Environmental Earth Sciences 74: 4939–4960.

Stumpf F, Schmidt K, Behrens T, Schönbrodt-Stitt S, Buzzo G, Dumperth C, Wadoux A, Xiang W, Scholten T. 2015a. Incorporating Limited Field Operability and Legacy Soil Samples in a Hypercube Sampling Design for Digital Soil Mapping. [under review]

Stumpf F, Schmidt K, Goebes P, Behrens T, Schönbrodt-Stitt S, Wadoux A, Xiang W, Scholten T. 2015b. Spatial Uncertainty-Guided Sampling to Improve Digital Soil Maps. [under review]

Taguas EV, Moral C, Ayuso JL, Pérez R, Gómez JA. 2011. Modeling the spatial distribution of water erosion within a Spanish olive orchard microcatchment using the SEDD model. *Geomorphology* **133**: 47–56.

Takken I, Beuselinck L, Nachtergaele J, Govers G, Poesen J, Degraer G. 1999. Spatial evaluation of a physically-based distributed erosion model (LISEM). *Catena* **37**: 431–447.

Tan Y, Yao F. 2006. Three Gorges Project: Effects of resettlement on the Environment in the reservoir area and countermeasures. Population and Environment 27: 351–371.

Tarboton DG. 1997. A new method for the determination of flow directions and upslope areas in grid digital elevation models. *Water Resources Research* **33**: 309–319.

Terranova O, Antronico L, Coscarelli R, Iaquinta P. 2009. Soil erosion risk scenarios in the Mediterranean environment using RUSLE and GIS: An application model for Calabria (southern Italy). *Geomorphology* **112**: 228–245.

Todisco F. 2014. The internal structure of erosive and non-erosive storm events for interpretation of erosive processes and rainfall simulation. *Journal of Hydrology* **519**: 3651–3663.

Verheijen FGA, Jones RJA, Rickson RJ, Smith CJ. 2009. Tolerable versus actual soil erosion rates in Europe. *Earth-Science Reviews* **94**: 23–38.

Vanmaercke M, Poesen J, Verstraeten G, De Vente J, Ocakoglu F. 2011. Sediment yield in Europe: spatial patterns and scale dependency. *Geomorphology* **130**: 142–161.

Van Rompaey A, Verstraeten G, Van Oost K, Govers G, Poesen J. 2001. Modelling mean annual sediment yield using a distributed approach. *Earth Surface Processes and Landforms* **26**: 1221–1236.

Van Rompaey A, Govers G. 2002. Data quality and model complexity for continental scale soil erosion modelling. *International Journal of Geographical Information Science* 16: 663–680.

Weigert A, Schmidt J. 2005. Water transport under winter conditions. *Catena* **64**: 193–208.

Willmott CJ, Matsuura K. 2005. Advantages of the mean absolute error (MAE) over the root mean square error (RMSE) in assessing average model performance. *Climate Research* **30**: 79–82.

Wischmeier WH, Smith DD. 1981. Predicting rainfall erosion losses – a guide to conservation planning. U.S. Department of Agriculture, Handbook 537. [http://naldc.nal.usda.gov/download/CAT79706928/PDF; accessed: April 2014]

WRB. 2014. World Reference Base for Soil Resources. [http://www.fao.org/soils-portal/soil-survey/soil-classification/world-reference-base/en/; accessed: March 2015]

Wu DM, Yu YC, Xia LZ, Yin SX, Yang LZ. 2011. Soil fertility indices of citrus orchard land along topographic gradients in the three gorges area of China. *Pedosphere* **21**: 782–792.

Xiang WS, Liang CF, Li WH. 2001. Soil and water loss from cultivated slope land derived from granite under different cropping systems in the Three Gorges Reservoir area. *Chinese Journal of Applied Ecology* **12**: 47–50. [in Chinese]

Xie Y, Liu B, Nearing MA. 2002. Practical thresholds for separating erosive and non-erosive events. *American Society of Agricultural Engineers* **45**: 1843–1847.

Xu X, Tan Y, Yang G, Li H, Su W. 2011. Impacts of China's Three Gorges Dam Project on net primary productivity in the reservoir area. *Science of the Total Environment* **409**: 4656–4662.

Xu X, Tan Y, Yang G. 2013. Environmental impact assessments of the Three Gorges Project in China: Issues and interventions. *Earth-Science Reviews* **124**: 115–125.

Zambrano-Bigiarini M. 2014. 'hydroGOF': Goodness-of-fit functions for comparison of simulated and observed hydrological time series. R package version 0.3-8. [https://cran.r-project.org/web/packages/hydroGOF/index.html; accessed: July 2015].

Zhao G, Mu X, Wen Z, Wang F, Gao P. 2013. Soil erosion, conservation, and eco-environment changes in the Loess Plateau of China. *Land Degradation & Development* **24**: 499–510.

Zhang B. 2008. Impact on mountainous agricultural development in the Three Gorges Reservoir Area forced by migrants of the Three Gorges Project. *Chinese Journal of Population Resources and Environment* **6**: 83–89.

Zhang L, O'Neill AL, Lacey S. 1996. Modelling approaches to the prediction of soil erosion in catchments. *Environmental Software* **11**: 123–133.

Zhang J, Zhengjun L, Xiaoxia S. 2009. Changing landscape in the Three Gorges Reservoir Area of Yangtze River from 1977 to 2005: Land use/land cover, vegetation cover changes estimated using multi-source satellite data. *International Journal of Applied Earth Observation and Geoinformation* **11**: 403–412.

Zhang Q, Lou Z. 2011. The environmental changes and mitigation actions in the Three Gorges Reservoir region, China. *Environmental Science & Policy* **14**: 1132–1138.

Zheng WW, Zhang CL. 2006. Soil conservation benefit analysis for citrus orchard in the reservoir basin of Three Gorges. *Subtropical Soil Water Conservation* **18**: 15–18.

Zhou P, Luukkanen O, Tokola T, Nieminen J. 2008. Effect of vegetation cover on soil erosion in a mountainous watershed. *Catena* **75**: 319–325.

Zhu AX, Liu J, Du F, Zhang SJ, Qin CZ, Burt J, Behrens T, Scholten T. 2015. Predictive soil mapping with limited sample data. European Journal of Soil Science **66**: 535–547.

Manuscript 5

Rule-based analysis of throughfall kinetic energy to evaluate biotic and abiotic factor thresholds to mitigate erosive power

Progress in Physical Geography, accepted (2015)

Philipp Goebes[1], Karsten Schmidt[1], Werner Härdtle[2], Steffen Seitz[1], Felix Stumpf[1], Goddert von Oheimb[3] and Thomas Scholten[1]

[1] Department of Geosciences, University of Tübingen, Germany
[2] Faculty of Sustainability, Leuphana University Lüneburg, Germany
[3] Department of Forest Sciences, Technische Universität Dresden, Germany
Corresponding author: Philipp Goebes, Department of Geosciences, University of Tübingen, Rümelinstraße 19-23, 72070 Tübingen, Germany.

Abstract

Below vegetation, throughfall kinetic energy (TKE) is an important factor to express the potential of rainfall to detach soil particles and thus for predicting soil erosion rates. TKE is affected by many biotic (e.g. tree height, leaf area index) and abiotic factors (e.g. throughfall amount) due to changes in rain drop size and velocity. However, studies modelling TKE with a high number of those factors are lacking.

This study presents a new approach to model TKE. We used 20 biotic and abiotic factors to evaluate thresholds of those factors that can mitigate TKE and thus decrease soil erosion. Using these thresholds, an optimal set of biotic and abiotic factors was identified to minimize TKE. The model approach combined recursive feature elimination, Random Forest variable importance and Classification and Regression Trees. TKE was determined using 1405 splash cup measurements during five rainfall events in a subtropical Chinese tree plantation with five-year-old trees in 2013.

Our results showed that leaf area, tree height, leaf area index and crown area are the most prominent vegetation traits to model TKE. To reduce TKE, the optimal set of biotic and abiotic factors was a leaf area lower than 6700 mm2, a tree height lower than 290 cm combined with a crown base height lower than 60 cm, a leaf area index smaller than 1, more than 47 branches per tree and using single tree species neighbourhoods. Rainfall characteristics like amount and duration further classified high or low TKE. These findings are important for the establishment of forest plantations which aim to minimize soil erosion in young succession stages using TKE modelling.

Keywords

Soil erosion, BEF China, modelling, Random Forest, CART, tree architecture, leaf traits, rainfall.

I Introduction

Soil erosion by water is a major threat to natural ecosystems and agricultural land in many regions of the world (Cao et al., 2013; Cerdá et al., 2009; Lieskovský and Kenderessy, 2014; Seutloali and Beckedahl, 2015). Besides slope, slope length, soil erodibility and vegetation, rainfall erosivity is another important driver in predicting soil erosion rates by empirical (Renard et al., 1997) or process-based models (Morgan et al., 1998). Higher rainfall and rainfall erosivity are negatively related to soil conservation and thus soils can lose important ecosystem services, e.g. filtering water (Keesstra et al., 2012), secure food production and plant diversity (Brevik et al., 2015), while conversely plant diversity can also affect soil conservation (Berendse et al., 2015). Rainfall erosivity is most commonly expressed by the EI_{30} which combines rainfall energy (E) and rainfall intensity per 30 minute interval (I_{30}). While there are numerous studies investigating rainfall intensity and related processes (van Dijk et al., 2002), research on the determining processes of rainfall energy is limited. Few studies deal with the discussion of a proper erosivity index of rainfall energy (Goebes et al., 2014), while others investigate seasonal and temporal trends of rainfall energy (Nunes et al., 2014; Taguas et al., 2013). This lack of studies is particularly true when rainfall energy is examined below tree canopies as throughfall kinetic energy (TKE). Here, the size distribution

of rain drops is changed due to biotic factors (e.g. leaf traits), potentially resulting in higher TKE than rainfall energy at open field sites (Geißler et al., 2010; Geißler et al., 2012; Nanko et al., 2004; Nanko et al., 2015). In addition, rain drop size is positively related to rainfall intensity (Cerdá, 1997). This strengthens the influence of TKE on inducing soil erosion processes below tree canopies. Hence, if a litter cover at the soil surface is missing, TKE is directly influencing soil erosion (Seitz et al., 2015) indicating the definite role of vegetation for soil erosion control (Cerdá, 1998).

Reflecting the relevance of TKE for soil erosion, TKE has been measured in different regions, under different rainfall conditions and below different vegetation in the past 15 years (Nanko, 2007; Nanko et al., 2008, 2011; Sanchez-Moreno et al., 2012; Zhou et al., 2002). In addition, several studies investigated the influence of biotic (single leaf and tree architectural traits) and abiotic factors (rainfall characteristics) on TKE separately. For instance, a positive effect on TKE has been reported for leaf area (Goebes et al., 2015a), tree height (Foot and Morgan, 2005; Geißler et al., 2013), crown area (Brandt, 1988; Nanko et al., 2008), crown base height (Brandt, 1990; Nanko et al., 2008) and throughfall amount (Brandt, 1988; Geißler et al., 2012; Scholten et al., 2011). TKE is negatively influenced by leaf area index (LAI) (Nanko et al., 2006; Nanko et al., 2008) and the number of branches (Herwitz, 1987). In addition, TKE shows spatial variability (Finney, 1984; Nanko et al., 2011). Furthermore, deciduous tree species can cause higher TKE than evergreens (Goebes et al., 2015a).

There are some studies that modelled TKE with biotic and abiotic factors to evaluate its role in erosion processes. However, these studies are limited in their number of biotic and abiotic factors. For instance, Moss and Green (1987) reported a maximum crown base height of 30 cm below which TKE is non-erosive. Brandt (1990) developed a model incorporating tree height as the most important vegetation variable while Calder (1996) used interception processes to model TKE by evaluating the drop size distribution. Foot and Morgan (2005) suggested to model TKE by only using tree height and canopy area. Type and intensity of a rainfall event determine whether TKE is erosive or not (Brandt, 1989; Zhou et al., 2002). Furthermore, several studies used modelling approaches to determine the role of rainfall kinetic energy in soil erosion at open sites in different regions of the world (Assouline, 2009; Assouline and Mualem, 1989; Salles and Poesen, 2000; van Dijk et al., 2002).

As a consequence, literature on modelling TKE patterns and potential thresholds for a variety of biotic and abiotic factors in the context of erosivity remain scarce. It remains unclear if thresholds exist for biotic and abiotic factors that lead to a specific TKE. This motivates to model TKE by using a variety of biotic and abiotic predictor variables to clarify their influence, interaction and importance. This, in turn, helps to better understand mechanisms that underlie and mediate soil erosion processes.

In the past decades, statistical and machine-learning methodologies made a huge progress. Random Forest (RF) is such a machine-learning technique, representing an ensemble of randomized classification and regression trees (CART) (Breiman, 2001). The final estimation is derived by aggregating the individual trees. A single CART uses a set of binary rules to compute a target variable. The binary rules are based on independent variables and the observed response variable (Breiman et al., 1984). In RF, estimations are derived from multiple CART-like trees, adapted by using randomized subsets of the input data (Grimm et al., 2008). As a consequence, RF is increasingly applied in ecological studies. Peters et al. (2007) estimated the occurrence of vegetation types, while Kuz'min et al. (2011) estimated aquatic toxicity. With regard to soil erosion research, Märker et al. (2011) used Random Forest to model erosional response units and to identify major controlling factors of soil erosion. While RF provides a variable importance measure, the estimations exhibit limited interpretability. Since in RF the final estimation is derived from aggregated results of multiple decision tree models, the relation between predictors and estimations cannot be easily assessed. This in turn can be accomplished by single CART models (Breiman et al., 1984; Cutler et al., 2007).

In this study we propose a step-wise decision tree approach to establish a rule-based system for estimating TKE. We combined the RF feature importance measure and recursive feature elimination (RFE) to determine a feature subset as input for estimating TKE using a single CART modelling approach. Subsequently, we analysed the CART with regard to biotic and abiotic factors to detect erosion-relevant thresholds of those factors in the context of TKE. We used this methodological frame to evaluate three objectives:

i) to describe and model TKE with a distinct set of biotic and abiotic factors
ii) to identify relevant biotic and abiotic factor thresholds for predicting TKE in order to find an optimal predictor subset that minimizes TKE

iii) to evaluate those predictions using a literature comparison

II Data collection and modelling

1 Study site and experimental design

The study was conducted within the framework of the large-scale biodiversity-ecosystem functioning experiment "BEF-China" (Bruelheide et al., 2014) at Xingangshan, Jiangxi Province, PR China (N29°08-11, E117°90-93). The climate in Xingangshan is typical of subtropical summer monsoon regions with a mean annual temperature of 17.4 °C and an average annual rainfall of 1635 mm. The experimental area holds 70 ha with a plot-based tree diversity treatment including 24 tree species on 261 plots. Tree individuals were planted after harvest of the previous stand in 2009 and they were five years old at the time of TKE measurements. For this study, 40 plots were selected by random, including 17 monocultures, 10 2-species mixtures, six 4-species mixtures, four 8 species-mixtures, one 16-species mixtures and two 24-species mixtures to cover a wide range of different species richness levels and compositions. Within one plot, eight measurements were realized by selecting eight different positions in order to cover a wide range of spatial variability (Goebes et al., 2015b). Positions (1), (4), (6) and (8) were influenced by one tree individual (1, 15 cm from the stem; 4, 45 cm from the stem; 6, first branch; 8, 30 cm from the stem), (2), (5) and (7) were influenced by two tree individuals (2, middle of two; 5, 45 x 120 cm intersection; 7, 75 x 75 cm intersection) and (3) was influenced by four tree individuals (3, middle of four).

2 Measurement of TKE and rainfall

TKE was measured using Tübingen Splash Cups (Scholten et al., 2011) filled with uniform fine sand (diameter 0.125 mm). Sand loss in grams (ds) in splash cups (sc) was used to calculate TKE (standardized by gross rainfall; J m^{-2} mm^{-1}) by the function given by Scholten et al. (2011) with a modified slope, a correction to 1 m^2 and the gross rainfall amount in mm (rf) of each rainfall event:

$$KE_{rainfall}[\frac{J}{m^2 mm}] = \frac{ds_{sc}[g] * 0.1455 * (\frac{10{,}000 cm^2}{\pi {r_{sc}}^2})}{rf_{event}}$$

In total, 1600 splash cups were measured during five rainfall events (see Table 1 for rainfall characteristics) from May to July 2013. These rainfall events covered a broad range of all rainfall events. In 2013, our climate station registered 33 erosive events (Renard et al., 1997; Wischmeier and Smith, 1978) ranging from 13 mm to 185 mm with a total rainfall amount of 1205 mm. In 2012, 49 erosive events ranging from 13 mm to 211 mm were measured. Mean rainfall amount per event was 40 mm in 2012 and 30 mm in 2013.

Table 1: Rainfall characteristics of five rainfall events. Rainfall amount (R_A), intensity (I) and duration (D) were measured at the climate station of BEF-China using a tipping bucket. Mean throughfall (TF) was measured at each TKE measurement position using rainfall gauges.

Rainfall events	R_A (mm)	D (h)	I (5 min peak intensity, mm h^{-1})	I (total event, mm h^{-1})	TF (mm)	Mean TKE [J m^{-2} mm^{-1}] (standard deviation)
Event 1	23.3	10.16	12.1	2.29	28.3	11.00 (7.90)
Event 2	39.3	11.5	22.8	3.42	47.9	9.02 (7.66)
Event 3	61.2	14.5	44.4	4.25	73.8	9.05 (5.15)
Event 4	6.6	2.33	25.2	2.83	5	11.93 (8.36)
Event 5	185.7	30.58	127.2	6.07	192.7	6.96 (3.23)

By reviewing literature on TKE measurements (measured in J m^{-2} mm^{-1}) of the past 30 years (Table 2) and classifying those results into four different categories using k-means clustering with 1000 iterations (MacQueen, 1967), we evaluated our TKE measurements according to these categories. The cluster means appeared in a multiplicative way using standard deviations (SD) from the mean TKE across all studies. (20.7 J m^{-2} mm^{-1}, Table 2). Thus, category 1 was calculated by subtracting 2 SD from mean (hereafter referred to as low TKE, range = 0 – 11.3 and mean = 7.5), category 2 by subtracting 1 SD from mean (moderate TKE, range = 11.3 – 17.4 and mean = 14.1), category 3 by representing the mean (average TKE,

range = 17.5 – 24.0 and mean = 20.7) and category 4 by adding 1 SD to the mean (high TKE, range = 24.1 – 70 and mean = 27.3). The studies cover a wide range of rainfall amounts (300 – 2478 mm a^{-1}) and intensities (0.4 – 372 mm h^{-1}). They confirm that rainfall characteristics of our study (rainfall amount of 1635 mm a^{-1} and intensities of 12 - 127 mm h^{-1}) are close to the mean of the literature review and thus can be considered representative. This allows comparing and categorizing our TKE measurements to the categories resulting from the literature review.

Table 2: Mean, minimum and maximum throughfall kinetic energy (TKE in J m^{-2} mm^{-1}) measured in different studies. Rainfall characteristics show amount of annual precipitation or simulated rainfall intensity and type of rainfall. Abbreviations: TF=throughfall, FF=freefall, art=artificial, SD=standard deviation.

Study	Rainfall characteristics of either study site or experiment	Mean TKE	Min TKE	Max TKE
(Sanchez-Moreno et al., 2012)	300-500 mm a^{-1}, FF	~21	4	70
(Nanko, 2007)	2300 mm a^{-1}, TF+(FF)	27 (11)	23.8	31.2
(Finney, 1984)	61 mm h^{-1} (art.), TF	7	0.4	10.5
(Brandt, 1987)	n/a mm, TF	21.8	3	40
(Nanko et al., 2008)	39.8 mm h^{-1} (art.), TF+(FF)	17.5 (12.7)	15.9	20.7
(Nanko et al., 2011)	40 and 85 mm h^{-1} (art.), TF	16.2	11.8	21.2
(van Dijk et al., 2002)	0.4 - 372 mm h^{-1}, FF	21	3.4	36.8
(Brandt, 1988)	2478 mm a^{-1}, TF+(FF)	27 (18)	13.6	40.2
(Zhou et al., 2002)	1454 mm a^{-1}, TF	28	21	33
All 9 studies combined		20.7 (SD 6.6)	0.4	70
Present study	1635 mm a^{-1}, TF	9.6	0.3	54.8

3 Measurement of biotic and abiotic factors

With regard to biotic factors, plot-level diversity was evaluated based on the experimental design. Neighbourhood diversity was specified by the composition of direct neighbouring tree individuals of a measurement position. In addition, we used the binary contrast mono-mixture

to differ between monoculture plots and mixture plots. Tree height, LAI, crown area, ground coverage, number of branches, ground diameter, crown base height, leaf habit (deciduous, evergreen and in mixtures both), leaf area (mean leaf area per one leaf of one species) and specific leaf area (Goebes et al., 2015b; Kröber et al., 2014; Kröber and Bruelheide, 2014; Li et al., 2014) were measured as biotic factors.

As abiotic factors, we measured throughfall at each TKE measurement position using rainfall gauges. The number of individuals was determined by counting direct tree neighbours that were influencing one splash cup. Spatial variability was assessed using the different positions of the sampling design. All splash cup positions were covered by vegetation. If a splash cup was influenced by more than one tree individual, mean values of biotic factors of the respective tree individuals were used. Tree species richness and number of individuals were included as categorical and continuous predictors to avoid underparameterisation of categorical predictors. Altogether we used a set of 5 categorical and 15 continuous predictors to model TKE (Table 3).

Table 3. *Predictors used as independent variables in the CART models. Mean values (and standard deviation; SD) were calculated using all five rainfall events. c = categorical variable and n = numerical variable.*

	Indicators	Abbr.	Mean (SD)	Min	Max	Unit
Biotic factors	Tree species richness (c and n)	A, B	4.00 (5.63)	1	24	-
	Neighbourhood tree species richness	C	1.24 (0.55)	1	4	-
	Mono-Mixture contrast	D	-			-
	Tree height	E	271.60 (156.42)	30	831	cm
	Leaf area index (LAI)	F	1.43 (1.07)	0.02	4.56	-
	Crown area	G	24,132 (26,462)	192	173,590	cm^2
	Ground coverage	H	0.62 (0.28)	0.01	0.99	-
	Number of branches	I	21 (16)	1	110	-
	Ground diameter	J	3.92 (2.03)	0.65	12.6	cm
	Crown base height	K	56.74 (75.10)	0.5	603.5	cm
	Leaf habit (deciduous vs. evergreen)	L	-			-
	Leaf area	M	13,898 (13,214)	1121	37,038	mm^2
	Specific leaf area	N	11.61 (1.27)	8.61	15.23	$g\ mm^{-2}$
Abiotic factors	Throughfall amount	O	69.55 (73.97)	0.8	303.5	mm
	Position	P	-			-
	Number of individuals (c and n)	Q, R	1.73	1	4	-
	Rainfall event intensity	S	46.3 (46.7)	12.1	127.2	$mm\ h^{-1}$
	Rainfall event duration	T	13.8 (10.4)	2.3	30.6	h

4 Data modelling

Leaf and tree architectural thresholds on which TKE was evaluated were finally derived by using CART. Instead of pruning the final CART, we decided to use RFE followed by variable importance selection of Random Forest to decrease the number of input variables before the construction of the final CART. This (i) allows us to reduce noise in the CART if we exclude less important features prior to the CART, (ii) enables a rule-based interpretation of the constructed trees and (iii) limits over-fitting. For instance, noise can be reduced due to exclusion of unimportant input variables if a very large number of uninformative predictors were collected and one such predictor would randomly correlate with the outcome.

a Recursive feature elimination. RFE with incorporated resampling was used to identify model performance related to the numbers of input variables (Kuhn, 2014). The model approach is based on the following steps: (1) Split data in training and validation set, (2) Train the model on the training set using all predictors, (3) Calculate model performance, (4) Calculate variable importance, (5) For each subset size Si, i = 1…S do, (6) Keep the Si most important variables, (7) Train the model on the training set using Si predictors, (8) Calculate model performance, (9) Calculate the performance profile over all Si, (10) Determine the appropriate number of predictors, (11) Determine the final ranks of each predictor, and (12) Fit the final model based on the optimal Si (Kuhn, 2014). Variables occurring after the optimal input variable number were dismissed in the subsequent RF models.

This approach leads to a distinct number of input variables for CART. Therefore, it limits input variables in the final CART and simplifies sub-sequent rule-based model interpretation. However, RFE cannot give information on what the most important variables have been and thus a second approach is needed.

b Variable importance using Random Forests. The variable importance of RF was used to detect the most important variables. RF are optimal suited to identify relevant features (Breiman, 2001) based on mean increased modelling performance (%IncMSE) via randomized feature and instance sampling. This is calculated by using the inherent structure of the RF approach as an ensemble of multiple decision trees where each individual tree is based on a bootstrap sample (random sampling with replacement; Efron and Tibshirani

(1994)) of the data. Additionally, at each split only a random subset of all features is tested to find the parameter, which is best suited to further split the node (see 2.4.3).

All single trees are evaluated using the out-of-the-bag data. OOB is the portion of the data, which is left out in each bootstrap replicate to build one tree of the ensemble. For the mean increased modelling performance each feature is randomly permuted at each split and the rate of change of the mean square error, compared with the original feature, is used as an indicator for its importance (Breiman, 2001; Grimm et al., 2008). This measure does not over-fit because it is tested against the independent OOB data (Prasad et al., 2006).

As a consequence, RF allows for analysis of non-parametric and non-linear effects and gives no need to transform data before modelling. They provide high prediction accuracy by fitting an ensemble of CARTs to a data set and combining the predictions from all CARTs (Cutler et al., 2007). The major drawback is that the resulting models are often black boxes and not able to obtain leaf and tree architectural thresholds for specific TKE measurements.

Therefore, the variable importance of RF was only used to dismiss all input variables that do not lead to a better model performance based on the results of the RFE.

c Rule construction using CART. Classification rules to evaluate biotic and abiotic factor thresholds on TKE were constructed using CART. CARTs build rules by splitting the continuous response into two groups (resulting into nodes which are the sample means of each group) by using an optimal threshold of a predictor (splitting) variable. The optimal split (threshold) is defined as the largest drop to reduce the residual sum of squares between the two groups of the target variable fitted with an ANOVA to the predictor evaluated at this split. The splitting process is iterated in a recursive way for each of the two sub-regions and for each of the predictor variables (Breiman et al., 1984). Vertical location of a predictor defines its importance in predicting the target variable TKE. CARTs were constructed using the ANOVA method. Due to the simplification of the model structure by dismissing none/or less relevant input variables, no tree pruning was applied.

d Modelling setups and validation. We used TKE as dependent target variable and the variables listed in Table 3 as independent variables according to RFE and RF results. Six models were constructed for each approach: one model of each single rainfall event to obtain

rainfall-specific TKE models and one model of all rainfall events to obtain rainfall-independent TKE models. Rainfall event was used as input variable only in the models constructed out of all rainfall events. Model performance of the RFE was evaluated using the root mean square error (RMSE) and the explained variance (R2). To evaluate the optimal number of input variables based on RFE, we calculated weighted mean of all six models (model combining all rainfall events was double-weighted). We only used one number of dismissed variables so that every rainfall event is treated identically with the same number of input variables resulting in equal CART starting positions considering tree growth and importance evaluation. This equal number of input variables allows a comparison between different models. Mean increased modelling performance (%IncMSE) was used to obtain the most important variables within the Random Forests. The number of randomly selected predictors to test at each node (mtry) and the number of instances/data points in the final node (nnodesize) were tested with 1, 2, 3 and 4 and finally set to 3. We constructed 1500 trees per model using regression. Fivefold repeated 10-fold cross-validation was used to validate the CARTs by RMSE and R^2, as well as the model stability/robustness. All models were analysed using R 2.15.3 (R Core Team, 2013) with the packages randomForest (Liaw and Wiener, 2002) and rpart (Therneau, T., Atkinson, B., Ripley, B., 2013) and were validated using the caret package (Kuhn, 2014).

III Results

RFE resulted in dismissing the least important four variables (mean of dismissed variables of the six models; Figure 1).

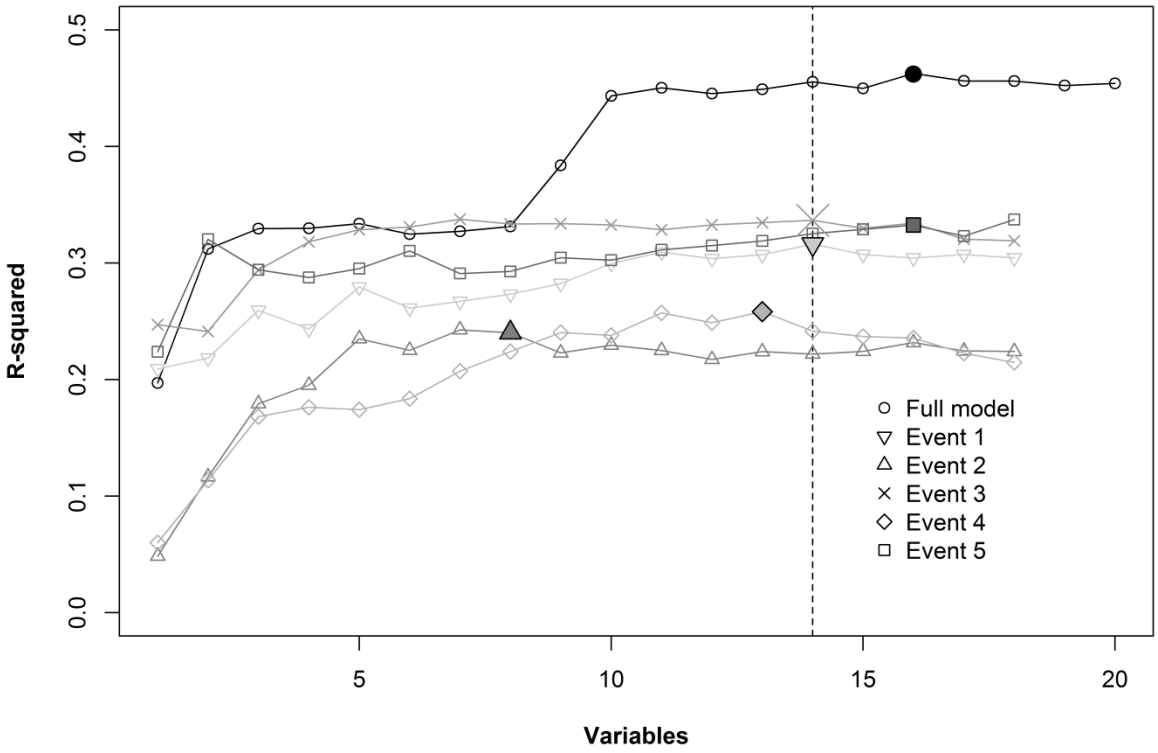

Figure 1: Results of the recursive feature elimination (RFE) with data from each event and combining all events (full model, which had two additional variables characterizing the rainfall event). Large symbols indicate the best variable set for each subset (5 single events and 1 combining all events). Dashed line indicates the best variable set by calculating the weighted mean of all subsets.

Variable importance of all input predictors of all single rainfall events and the model combining all rainfall events is shown in Figure 2. The least five important variables of each model were dismissed in further analysis. A detailed list of the dismissed variables may be found in Table A1.

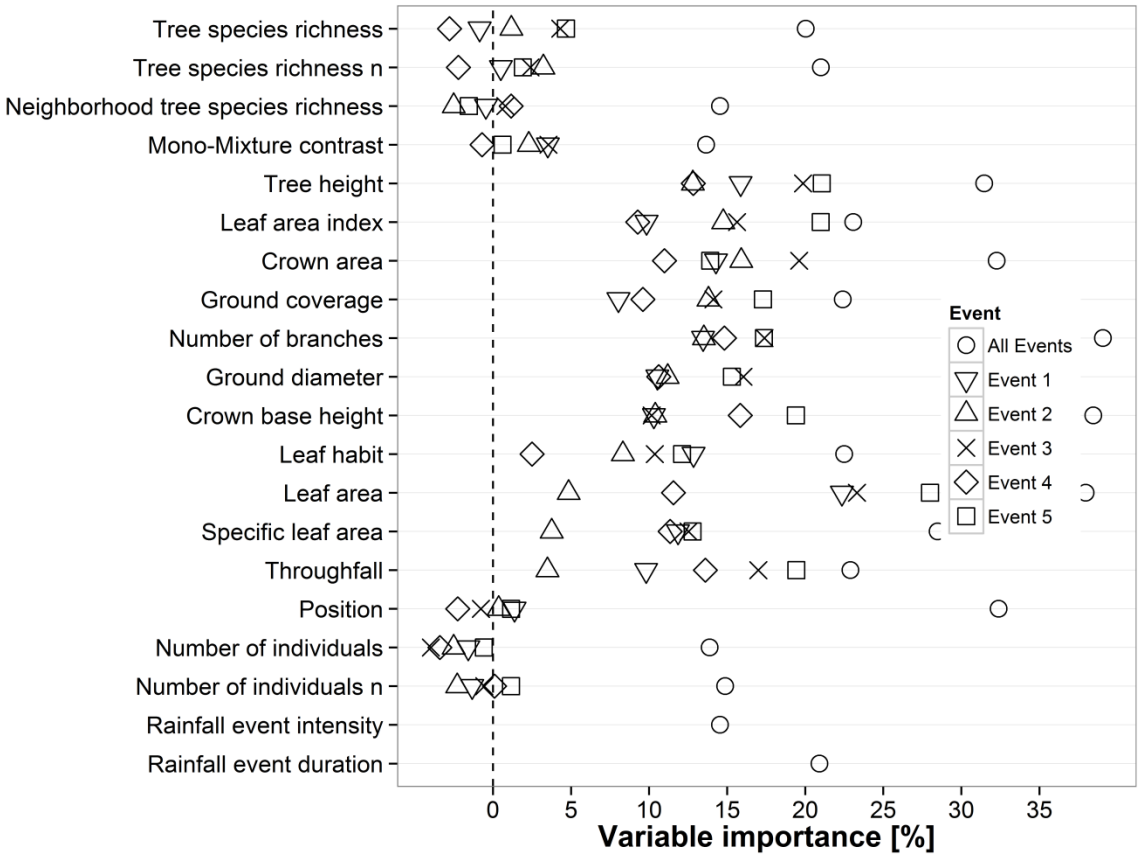

Figure 2: Variable importance (% Inc MSE) of 20 biotic and abiotic factors on throughfall kinetic energy for six rainfall event models. For statistical descriptions of the factors, see Table 3.

The final CART model including all rainfall events is displayed in Figure 3 (Figures A1, A2, A3, A4 and A5 of rainfall event 1, 2, 3, 4 and 5, respectively; see Appendix). Considering non-standardized TKE, CART model performance was R^2 = 0.65, 0.45, 0.37, 0.46, 0.41, and 0.43 and RMSE = 32.0, 16.0, 25.7, 26.5, 4.9, and 52.7 for the model including all rainfall events and single rainfall events 1, 2, 3, 4 and 5, respectively. Considering standardized TKE, CART model performance was R^2 = 0.30, 0.27, 0.21, 0.32, 0.25, and 0.31 and RMSE = 6.09, 7.31, 7.30, 4.64, 7.85, and 2.83 for the model including all rainfall events and single rainfall events 1, 2, 3, 4 and 5, respectively.

Leaf area and throughfall amount occurred in all six CARTs. Tree height and LAI were second prominent with five times occurrence. Ground coverage, specific leaf area, ground

diameter and neighbourhood diversity occurred only once though. Leaf area was the most prominent variable in first splits. Throughfall amount, tree height and LAI were most prominent in second splits, while leaf area, throughfall amount, LAI, number of branches and crown base height were most prominent in third splits.

The thresholds of each biotic and abiotic predictor varied slightly between different rainfall events. Summarizing biotic and abiotic thresholds of CARTs of all single rainfall events and the CART including all rainfall events (for details see Figures 3, A1-A5), leaf area showed prominent thresholds of approximately 35,000 mm^2 and 6,700 mm^2. Throughfall amount splits were found at 2.8 mm, 24 mm, 70 mm and 220 mm. Tree height showed prominent thresholds at 289 and 330 cm. Crown base height showed the most prominent thresholds at 60 cm. Thresholds for the number of branches were found at 14 and 47. LAI showed prominent thresholds at 1 and 1.8, while crown area splits were found at 37,000 cm^2.

To monitor low TKE, thresholds were set by leaf area, throughfall and tree height as the most prominent variables. Leaf area, throughfall, LAI and crown area were most prominent in building splits to yield moderate TKE, while thresholds of leaf area, throughfall, crown area, number of branches and crown base height led to average TKE. High TKE was monitored with splits occurring by leaf area, throughfall, and LAI.

The CART model including all rainfall events showed six different predictor variables, five split levels and 12 terminal nodes (Figure 3). Similarly, the CARTs of rainfall event 2 and 4 showed eight different variables, five split levels and 13 and 12 terminal nodes, respectively.

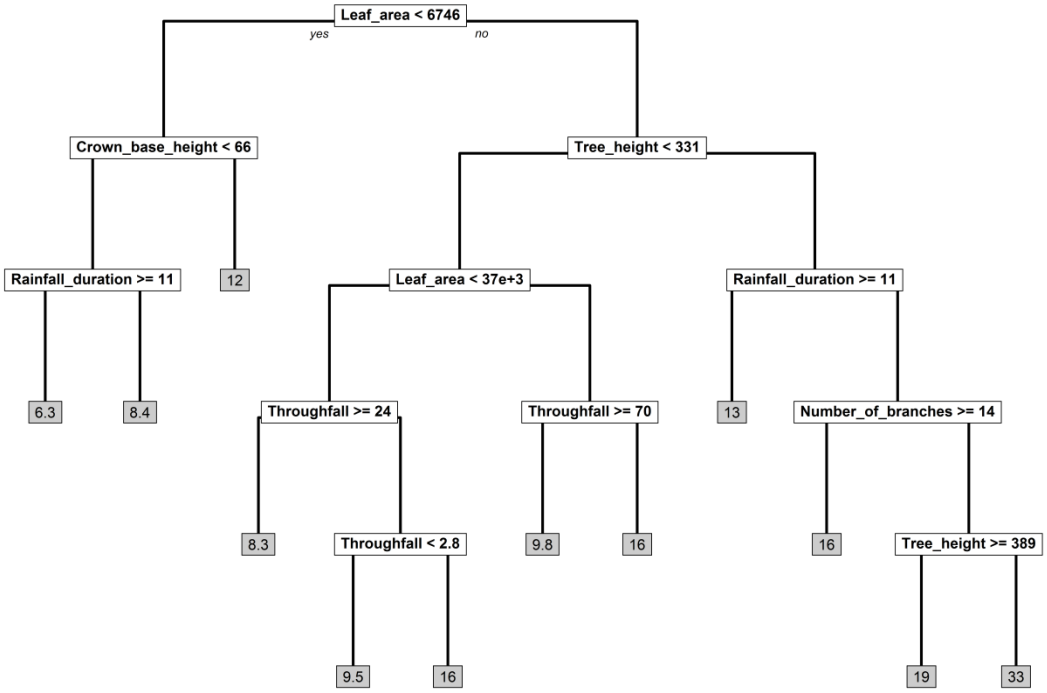

Figure 3: CART across all events. Target variable was throughfall kinetic energy (TKE) and predictor variables are listed in Table 3. TKE was measured as J m^2 mm^{-1} (n=1405).

IV Discussion

We investigated the influence of 20 biotic and abiotic factors on TKE using a step-wise approach of RF and CART. We showed rules induced by those factors to obtain low, moderate, average or high TKE compared to nine studies which investigated TKE in different regions. Leaf area, throughfall, tree height and LAI affected TKE as most prominent variables in the CART models.

1 Ensemble approach using Random Forest variable importance and CART to predict TKE

We detected effects of biotic and abiotic factors on TKE that are consistent with previous studies (objective 1). CARTs showed the influence of leaf area (Goebes et al., 2015a),

throughfall amount (Brandt, 1988; Geißler et al., 2012; Scholten et al., 2011), tree height (Foot and Morgan, 2005; Geißler et al., 2013), LAI (Nanko et al., 2006; Nanko et al., 2008), crown area (Brandt, 1988; Nanko et al., 2008), number of branches (Herwitz, 1987), crown base height (Brandt, 1990; Nanko et al., 2008), spatial variability (Finney, 1984; Nanko et al., 2011) and duration as well as intensity of rainfall event (Brandt, 1989; Zhou et al., 2002) on TKE. Furthermore, feature elimination and selection before using CART left no need for pruning or modifying the final trees. A typical pruned CART has three to 12 terminal nodes (Cutler et al., 2007), which was in the range of 9 to 14 terminal nodes in this study. Prediction results of R^2 =0.68 for the non-standardized models emphasized the suitability of this approach. In addition, the approach was able to detect a non-linear effect of throughfall on TKE due to the interaction with biotic factors such as leaf area.

2 Thresholds of biotic and abiotic factors to model TKE

In general, results obtained from data across all rainfall events can be found in the results of each rainfall event, though in less detail (Figures A1-A5). Thus, we used the CART that combined all rainfall events as major source of interpretation in the following discussion. Since TKE was standardized using rainfall amount, rainfall duration was the major rainfall event characteristic that changed the optimal set of biotic and abiotic factors and their thresholds.

Leaf area was the most important predictor in our CARTs to describe different TKE. Leaf area was of major importance to yield low, moderate, average or high TKE. Leaf areas beyond 35,000 mm^2 caused average to high TKE whereas leaf areas below 6,700 mm^2 led to low TKE (Figures 3, A1, A2, A3, A5). The latter size was most prominent for all species and showed that species with large leaf area cannot function as erosion inhibitors. A higher leaf area might create a larger surface for rain drop gathering as well as confluence, and hence a release of larger rain drops (Herwitz, 1987). For instance, leaves of *Schima superba* (38,090 mm^2) increased sand loss in splash cups by 30 % compared to leaves of *Castanopsis eyrei* (12,920 mm^2), which led to TKE (converted out of sand loss with a linear function by

Scholten et al. (2011)) within the range of 1 SD of natural rainfall (Geißler et al., 2012). This shows that the erosion potential below vegetation can be distinctly reduced compared to that of natural rainfall using small leaf sizes.

Our study showed a non-linear effect of throughfall on TKE and thus contradicts a positive linear effect reported in previous studies (Brandt, 1988; Levia and Frost, 2006; Scholten et al., 2011). Throughfall amount as abiotic factor was second prominent to describe TKE differences, but with a positive and negative effect on TKE (Figure 3). Our approach was particularly dedicated to investigate non-linear relationships which can be caused by interaction with other factors. In this case, throughfall mainly interacted with leaf area (Figure 3). Throughfall amounts (Figure A5) below 229 mm led to moderate TKE, whereas throughfall amounts higher or lower than 185 mm led to low TKE during high rainfall amounts per event. However, low throughfall amounts such as 2.8 mm can also lead to high, average or moderate TKE. It is likely that biotic factors emerged due to the standardization of TKE by rainfall amount at each event, suggesting the importance of interaction effects between biotic and abiotic factors with regard to TKE. The non-linear effect of throughfall on TKE was especially visible when data of all events entered the analyses (Figure 2).

A tree height below 290 cm resulted in low to moderate TKE (7.5 – 14.1 J m^{-2} mm^{-1}, Figure 3 and A3) due to shorter falling heights and hence, reduced rain drop velocities (Gunn and Kinzer, 1949). This threshold led to TKE of about 2 J m^{-2-} mm^{-1}, which is below values reported by Brandt (1990) and Nanko et al. (2008). Brandt (1990) emphasized in her model that effects on TKE were more pronounced for tree height shifts of small trees. Figure 3 indicates that only tree heights above 389 cm led to high TKE, while slightly lower heights (of about 60 cm) led to low to moderate TKE. This suggests that there is a "critical tree height" approximately at 330 cm, above which TKE becomes highly erosive. However, this height is close to the mean of all species and indicates that young tree individuals in particular are non-erosive.

Crown base height was the fourth most important predictor of TKE. Rain drops falling from trees with crown base heights below 60 cm had a low to moderate TKE (Figures 3, A2 and A4). Moss and Green (1987) showed that the height-velocity relationship for rain drops increased rapidly over the first two meters, and that under drop heights of 30 cm no soil erosion takes place. This threshold represented the mean crown base height of trees in the

present study, and is a further argument to consider slow- and low-growing tree species in plantations that aim to minimize soil erosion.

The importance of the number of branches in affecting TKE was moderate. While less than 14 branches at low rainfall amounts (event 3 and 4) led to average or high TKE, more than 47 branches led to low and moderate TKE. We ascribe this negative effect to the higher probability for raindrops to split up at branches and thus decreasing drop size and velocity resulting in low TKE (Herwitz, 1987).

A LAI larger than 1 led to average or high TKE, whereas a lower LAI caused a low or moderate TKE (Figures A2, A4 and A5). This threshold resulted in a positive effect of LAI on TKE which is contrary to previous studies (Geißler et al., 2013; Nanko et al., 2008). However, these studies dealt with LAI ranging from 1.5 to 11. Therefore, the positive effect of LAI might occur only for low LAI, when values are closely related to canopy openness or crown area. Within these low values, a higher LAI represents a higher coverage and throughfall creation without creating more rainfall interception and breaking points by different canopy layers. LAI did not influence TKE variation across all rainfall events.

A crown area below 37,000 cm^2 always led to low or moderate TKE and thus indicates an upper threshold below which TKE can be seen as less-erosive (Figures A2 and A3). We ascribe this positive effect on TKE by rain drop gathering and creating a higher area at which throughfall occurred. However, low rainfall intensities (rainfall event 1) counteract this effect when TKE is analysed at distances of 15 cm, 30 cm and 60 cm from the tree stem (Figure A1). Nanko et al. (2008) showed this negative effect of crown area on TKE by investigating crown areas larger than 85,000 cm^2. Nevertheless, the effect shift remains non-predictable and crown area did not influence TKE variation across all rainfall events.

The effect of spatial variability on TKE remains inconclusive as its importance in the CART was low and effects became evident only in combination with crown area. Thus, it remains unclear below which spatial positions low or moderate TKE appeared. This absence of a spatial variability of TKE is in agreement with findings of Nanko et al. (2011). Nevertheless, at a stem-distance of 30 cm high TKE may appear below or at margins of the canopy (Finney, 1984).

If all neighbouring trees belong to one species, low TKE occurred. Species-mixtures, however, led to moderate TKE. A diverse neighbourhood might lead to more complex tree structures which can positively affect throughfall by creating different canopy layer height at which drops can confluence (Getzin et al., 2008; Schröter et al., 2012). Nevertheless, a classification by neighbourhood tree diversity as well as ground diameter and specific leaf area was not prominent (low importance in CART and not occurring in CART of all rainfall events).

3 TKE comparisons with previous studies

In this study, TKE was twofold lower compared to the mean of other studies investigating rainfall kinetic energy in open fields and below vegetation (Table 2). The age of the subtropical tree plantation can be considered as the main reason for this finding. Many tree individuals have not yet reached full tree height which leads to low fall velocities and thus lower TKE (Gunn and Kinzer, 1949). Furthermore, a dense and thick crown cover was not developed in some plots in the previous six years this plantation existed. LAI and number of branches as major predictors for high TKE emphasized the importance of a dense crown cover (Figure A3). To our knowledge, only one study measured similar TKE (Finney, 1984). Comparable to our study, the relatively low vegetation heights prevented that rain drops achieved their terminal velocity. In contrast, Nanko et al. (2008), Nanko et al. (2011) and Sanchez-Moreno et al. (2012) measured average to high TKE which might be caused by high-intensity rainfall above 40 mm h^{-1}. These intensities exceed those of four events measured in our study. Since throughfall amounts are similar to or lower than our measurements, rainfall intensity might function as the major abiotic factor leading to high TKE throughout all studies (Levia and Frost, 2006). However, TKE can be stable among different rainfall intensities ranging from 1 to 46 mm h^{-1} (Zhou et al., 2002). In this case, throughfall amount might be a better predictor for TKE differences.

V Conclusions

The present study linked biotic and abiotic factors to TKE and set thresholds below which low TKE and above which high TKE occurred (Figure 4). Planting new forests or plantations, these factors should be considered as they constrain the extent of soil erosion. With the set of

species, biotic and abiotic factors used in this study, the erosive potential of TKE can be mitigated by a smaller leaf area than 6,700 mm^2, a lower tree height than 290 cm combined with a crown base height lower than 60 cm, a LAI smaller than 1, more than 47 branches and by using single tree species neighbourhood, while the amount of throughfall can vary. Although these models have been calibrated with data of a young tree plantation, they are, nevertheless, another step towards identifying the importance of biotic and abiotic factors and most of all, setting thresholds for erosion occurrence based on TKE. However, further research is needed in mature forests.

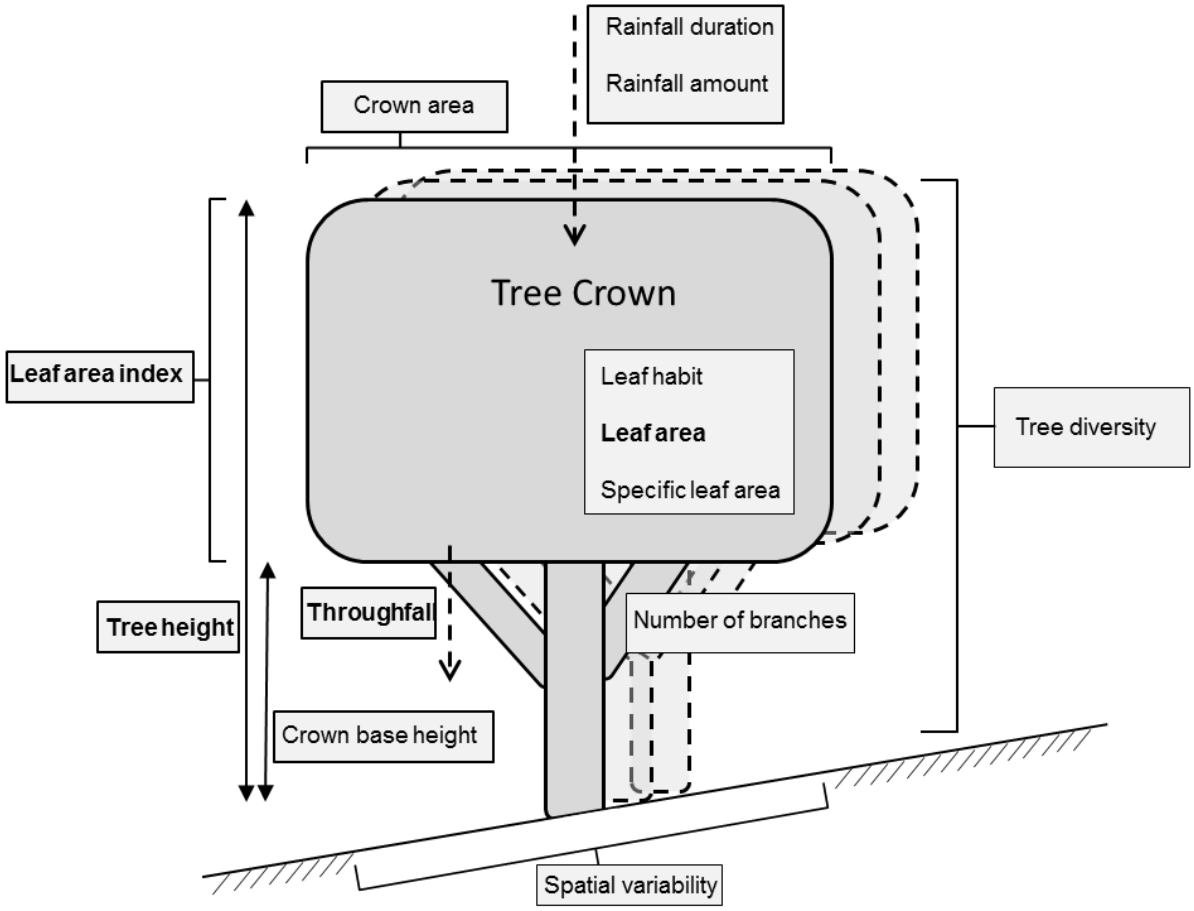

Figure 4: Graphical compilation of relevant biotic and abiotic factors that affect TKE based on Classification and Regression Trees. Bolded factors were most important in explaining TKE.

Appendix

Table A1. Results of the Random Forest feature importance. "Variables selected" mark the variables on which final Classification and Regression Trees were built, and "Variables dismissed" mark variables that have been dismissed after recursive feature elimination combined with Random Forests feature importance. Abbreviations of variables are defined in Table 3.

Model	Variables selected	Variables dismissed
Complete	A, B, E, F, G, H, I, J, K, L, M, N, O, S, T	C, D, P, Q, R
Event 1	D, E, F, G, H, I, J, K, L, M, N, O, P	A, B, C, Q, R
Event 2	A, D, E, F, G, H, I, J, K, L, M, N, O	B, C, P, Q, R
Event 3	A, D, E, F, G, H, I, J, K, L, M, N, O	B, C, P, Q, R
Event 4	C, E, F, G, H, I, J, K, L, M, N, O, Q	A, B, D, P, R
Event 5	A, B, E, F, G, H, I, J, K, L, M, N, O	C, D, P, Q, R

References

Assouline S and Mualem Y (1989) The similarity of regional rainfall: a dimensionless model of drop size distribution. Transaction of the ASAE(32): 1216–1222.

Assouline S (2009) Drop size distributions and kinetic energy rates in variable intensity rainfall. Water Resources Research 45(11): W11501.

Berendse F, van Ruijven J, Jongejans E and Keesstra S (2015) Loss of Plant Species Diversity Reduces Soil Erosion Resistance. Ecosystems 18(5): 881–888. DOI: 10.1007/s10021-015-9869-6.

Brandt J (1987) The effect of different types of forest management on the transformation of rainfall energy by the canopy in relation to soil erosion. Forest hydrology and watershed management/edited by RH Swanson, PY Bernier & PD Woodard.

Brandt J (1988) The transformation of rainfall energy by a tropical rain forest canopy in relation to soil erosion. Journal of Biogeography: 41–48.

Brandt J (1989) The size distribution of throughfall drops under vegetation canopies. Selected papers of the Fourth Benelux Colloquium on Geomorphological Processes 16(4–5): 507–524. DOI: 10.1016/0341-8162(89)90032-5.

Brandt J (1990) Simulation of the size distribution and erosivity of raindrops and throughfall drops. Earth Surface Processes and Landforms 15(8): 687–698. DOI: 10.1002/esp.3290150803.

Breiman L, Friedman J, Stone CJ and Olshen RA (1984) Classification and regression trees: CRC press.

Breiman L (2001) Random Forests. Machine Learning 45(1): 5-32. DOI: 10.1023/A:1010933404324.

Brevik EC, Cerdà A, Mataix-Solera J, Pereg L, Quinton JN, Six J, et al. (2015) The interdisciplinary nature of SOIL. SOIL 1(1): 117–129. DOI: 10.5194/soil-1-117-2015.

Bruelheide H, Nadrowski K, Assmann T, Bauhus J, Both S, Buscot F, et al. (2014) Designing forest biodiversity experiments: general considerations illustrated by a new large experiment in subtropical China. Methods in Ecology and Evolution 5(1): 74–89. DOI: 10.1111/2041-210X.12126.

Calder IR (1996) Dependence of rainfall interception on drop size: 1. Development of the two-layer stochastic model. Journal of Hydrology 185(1–4): 363–378. DOI: 10.1016/0022-1694(95)02998-2.

Cao L, Zhang K, Dai H and Liang Y (2013) MODELING INTERRILL EROSION ON UNPAVED ROADS IN THE LOESS PLATEAU OF CHINA. Land Degradation & Development: n/a. DOI: 10.1002/ldr.2253.

Cerdá A (1997) Rainfall drop size distribution in the Western Mediterranean basin, València, Spain. CATENA 30(2–3): 169–182. DOI: 10.1016/S0341-8162(97)00019-2.

Cerdá A (1998) The influence of geomorphological position and vegetation cover on the erosional and hydrological processes on a Mediterranean hillslope. Hydrological Processes 12(4): 661–671.

Cerdá A, Morera AG and Bodí MB (2009) Soil and water losses from new citrus orchards growing on sloped soils in the western Mediterranean basin. Earth Surface Processes and Landforms 34(13): 1822–1830. DOI: 10.1002/esp.1889.

Cutler DR, Edwards Jr, Thomas C, Beard KH, Cutler A, Hess KT, Gibson J, et al. (2007) Random forests for classification in ecology. Ecology 88(11): 2783–2792.

Efron B and Tibshirani RJ (1994) An introduction to the bootstrap. New York: CRC press.

Finney HJ (1984) The effect of crop covers on rainfall characteristics and splash detachment. Journal of Agricultural Engineering Research 29(4): 337–343. DOI: 10.1016/0021-8634(84)90089-1.

Foot K and Morgan R (2005) The role of leaf inclination, leaf orientation and plant canopy architecture in soil particle detachment by raindrops. Earth Surface Processes and Landforms 30(12): 1509–1520. DOI: 10.1002/esp.1207.

Geißler C, Kühn P, Böhnke M, Bruelheide H, Shi X and Scholten T (2012) Splash erosion potential under tree canopies in subtropical SE China. CATENA 91(0): 85–93. DOI: 10.1016/j.catena.2010.10.009.

Geißler C, Kühn P, Shi X and Scholten T (2010) Estimation of throughfall erosivity in a highly diverse forest ecosystem using sand-filled splash cups. Journal of Earth Science 21(6): 897-900. DOI: 10.1007/s12583-010-0132-y.

Geißler C, Nadrowski K, Kühn P, Baruffol M, Bruelheide H, Schmid B, et al. (2013) Kinetic Energy of Throughfall in Subtropical Forests of SE China – Effects of Tree Canopy Structure, Functional Traits, and Biodiversity. PLoS ONE 8(2): e49618 EP -. DOI: 10.1371/journal.pone.0049618.

Getzin S, Wiegand K, Schumacher J and Gougeon FA (2008) Scale-dependent competition at the stand level assessed from crown areas. Large-scale experimentation and oak regeneration 255(7): 2478–2485. DOI: 10.1016/j.foreco.2008.01.007.

Goebes P, Bruelheide H, Härdtle W, Kröber W, Kühn P, Li Y, et al. (2015a) Species-specific effects on throughfall kinetic energy in subtropical forest plantations are related to leaf traits and tree architecture: accepted. PLoS ONE. DOI: 10.1371/journal.pone.0128084.

Goebes P, Seitz S, Geißler C, Lassu T, Peters P, Seeger M, et al. (2014) Momentum or kinetic energy – How do substrate properties influence the calculation of rainfall erosivity? Journal of Hydrology 517(0): 310–316. DOI: 10.1016/j.jhydrol.2014.05.031.

Goebes P, Seitz S, Kühn P, Li Y, Niklaus PA, Oheimb G von, et al. (2015b) Throughfall kinetic energy in young subtropical forests: Investigation on tree species richness effects and spatial variability. Agricultural and Forest Meteorology: 148–159. DOI: 10.1016/j.agrformet.2015.06.019.

Grimm R, Behrens T, Märker M and Elsenbeer H (2008) Soil organic carbon concentrations and stocks on Barro Colorado Island — Digital soil mapping using Random Forests analysis. Geoderma 146(1–2): 102–113. DOI: 10.1016/j.geoderma.2008.05.008.

Gunn R and Kinzer GD (1949) The terminal velocity of fall for water droplets in stagnant air. J. Meteor. 6(4): 243–248. DOI: 10.1175/1520-0469(1949)006<0243:TTVOFF>2.0.CO;2.

Herwitz SR (1987) Raindrop impact and water flow on the vegetative surfaces of trees and the effects on stemflow and throughfall generation. Earth Surface Processes and Landforms 12(4): 425–432. DOI: 10.1002/esp.3290120408.

Keesstra SD, Geissen V, Mosse K, Piiranen S, Scudiero E, Leistra M, et al. (2012) Soil as a filter for groundwater quality. Current Opinion in Environmental Sustainability 4(5): 507–516. DOI: 10.1016/j.cosust.2012.10.007.

Kröber W and Bruelheide H (2014) Transpiration and stomatal control: a cross-species study of leaf traits in 39 evergreen and deciduous broadleaved subtropical tree species. Trees 28(3): 901-914. DOI: 10.1007/s00468-014-1004-3.

Kröber W, Heklau H and Bruelheide H (2014) Leaf morphology of 40 evergreen and deciduous broadleaved subtropical tree species and relationships to functional ecophysiological traits. Plant Biology: n/a. DOI: 10.1111/plb.12250.

Kuhn M (2014) caret: Classification and Regression Training. Contributions from Jed Wing, Steve Weston, Andre Williams, Chris Keefer, Allan Engelharrdt, Tony Cooper, Zachary Mayer and the R Core Team.

Kuz'min VE, Polishchuk PG, Artemenko AG and Andronati SA (2011) Interpretation of QSAR Models Based on Random Forest Methods. Molecular Informatics 30(6-7): 593–603. DOI: 10.1002/minf.201000173.

Levia DF and Frost EE (2006) Variability of throughfall volume and solute inputs in wooded ecosystems. Progress in Physical Geography 30(5): 605–632. DOI: 10.1177/0309133306071145.

Li Y, Härdtle W, Bruelheide H, Nadrowski K, Scholten T, Wehrden H von, et al. (2014) Site and neighborhood effects on growth of tree saplings in subtropical plantations (China). Forest Ecology and Management 327(0): 118–127. DOI: 10.1016/j.foreco.2014.04.039.

Liaw A and Wiener M (2002) Classification and Regression by randomForest: R News 2(3), 18-22.

Lieskovský J and Kenderessy P (2014) MODELLING THE EFFECT OF VEGETATION COVER AND DIFFERENT TILLAGE PRACTICES ON SOIL EROSION IN VINEYARDS: A CASE STUDY IN VRÁBLE (SLOVAKIA) USING WATEM/SEDEM. Land Degradation & Development 25(3): 288–296. DOI: 10.1002/ldr.2162.

MacQueen J (1967) Some methods for classification and analysis of multivariate observations: Oakland, CA, USA.

Märker M, Pelacani S and Schröder B (2011) A functional entity approach to predict soil erosion processes in a small Plio-Pleistocene Mediterranean catchment in Northern Chianti, Italy. Geomorphology 125(4): 530–540. DOI: 10.1016/j.geomorph.2010.10.022.

Morgan RP, Quinton JN, Smith RE, Govers G, Poesen JW, Auerswald K, et al. (1998) The European Soil Erosion Model (EUROSEM): a dynamic approach for predicting sediment transport from fields and small catchments. Earth surface processes and landforms 23(6): 527–544.

Moss AJ and Green TW (1987) Erosive effects of the large water drops (gravity drops) that fall from plants. Soil Res 25(1): 9–20.

Nanko K (2007) Studies on the process of throughfall drop generation in forest canopies: PhD thesis.

Nanko K, Giambelluca TW, Sutherland RA, Mudd RG, Nullet MA and Ziegler AD (2015) Erosion Potential under Miconia calvescens Stands on the Island of Hawai‘i. Land Degradation & Development 26(3): 218–226. DOI: 10.1002/ldr.2200.

Nanko K, Hotta N and Suzuki M (2004) Assessing raindrop impact energy at the forest floor in a mature Japanese cypress plantation using continuous raindrop-sizing instruments. Journal of Forest Research 9(2): 157-164. DOI: 10.1007/s10310-003-0067-6.

Nanko K, Hotta N and Suzuki M (2006) Evaluating the influence of canopy species and meteorological factors on throughfall drop size distribution. Journal of Hydrology 329(3–4): 422–431. DOI: 10.1016/j.jhydrol.2006.02.036.

Nanko K, Onda Y, Ito A and Moriwaki H (2008) Effect of canopy thickness and canopy saturation on the amount and kinetic energy of throughfall: An experimental approach. Geophysical Research Letters 35(5): L05401. DOI: 10.1029/2007GL033010.

Nanko K, Onda Y, Ito A and Moriwaki H (2011) Spatial variability of throughfall under a single tree: Experimental study of rainfall amount, raindrops, and kinetic energy. Agricultural and Forest Meteorology 151(9): 1173–1182. DOI: 10.1016/j.agrformet.2011.04.006.

Nunes AN, Lourenço L, Vieira A and Bento-Gonçalves A (2014) PRECIPITATION AND EROSIVITY IN SOUTHERN PORTUGAL: SEASONAL VARIABILITY AND TRENDS (1950-2008). Land Degradation & Development: n/a. DOI: 10.1002/ldr.2265.

Peters J, Baets BD, Verhoest, Niko E. C., Samson R, Degroeve S, Becker PD, et al. (2007) Random forests as a tool for ecohydrological distribution modelling. Ecological Modelling 207(2–4): 304–318. DOI: 10.1016/j.ecolmodel.2007.05.011.

Prasad A, Iverson L and Liaw A (2006) Newer Classification and Regression Tree Techniques: Bagging and Random Forests for Ecological Prediction. Ecosystems 9(2): 181-199. DOI: 10.1007/s10021-005-0054-1.

R Core Team (2013) R: A Language and Environment for Statistical Computing: R Foundation for Statistical Computing.

Renard KG, Foster GR, Weesies GMD and Yoder DC (1997) Prediciting soil erosion by water: a guide to conservation planning with the Revised Universal Soil Loss Equation (RUSLE). USDA Agriculture Handbook(703): 384.

Salles C and Poesen J (2000) Rain properties controlling soil splash detachment. Hydrological Processes 14(2): 271–282.

Sanchez-Moreno JF, Mannaerts CM, Jetten V and Löffler-Mang M (2012) Rainfall kinetic energy–intensity and rainfall momentum–intensity relationships for Cape Verde. Journal of Hydrology: 131–140. DOI: 10.1016/j.jhydrol.2012.06.007.

Scholten T, Geißler C, Goc J, Kühn P and Wiegand C (2011) A new splash cup to measure the kinetic energy of rainfall. Journal of Plant Nutrition and Soil Science 174(4): 596–601. DOI: 10.1002/jpln.201000349.

Schröter M, Härdtle W and Oheimb G von (2012) Crown plasticity and neighborhood interactions of European beech (Fagus sylvatica L.) in an old-growth forest. European Journal of Forest Research 131(3): 787-798. DOI: 10.1007/s10342-011-0552-y.

Seitz S, Goebes P, Zumstein P, Assmann T, Kühn P, Niklaus PA, et al. (2015) The influence of leaf litter diversity and soil fauna on initial soil erosion in subtropical forests. Earth Surface Processes and Landforms: n/a. DOI: 10.1002/esp.3726.

Seutloali KE and Beckedahl HR (2015) Understanding the factors influencing rill erosion on roadcuts in the south eastern region of South Africa. Solid Earth 6(2): 633–641. DOI: 10.5194/se-6-633-2015.

Taguas EV, Carpintero E and Ayuso JL (2013) ASSESSING LAND DEGRADATION RISK THROUGH THE LONG-TERM ANALYSIS OF EROSIVITY: A CASE STUDY IN SOUTHERN SPAIN. Land Degradation & Development 24(2): 179–187. DOI: 10.1002/ldr.1119.

Therneau, T., Atkinson, B., Ripley, B. (2013) rpart: Recursive Partitioning.

van Dijk A, Bruijnzeel L and Rosewell C (2002) Rainfall intensity–kinetic energy relationships: a critical literature appraisal. Journal of Hydrology 261(1-4): 1–23. DOI: 10.1016/S0022-1694(02)00020-3.

Wischmeier WH and Smith DD (1978) Predicting rainfall erosion losses-A guide to conservation planning. Predicting rainfall erosion losses-A guide to conservation planning.

Zhou G, Wei X and Yan J (2002) Impacts of eucalyptus (Eucalyptus exserta) plantation on sediment yield in Guangdong Province, Southern China—a kinetic energy approach. CATENA 49(3): 231–251. DOI: 10.1016/S0341-8162(02)00030-9.

CurriculumVitae

Personal Information

Name:	Felix Stumpf
Date of birth:	September 5th, 1984
Place of birth:	Eberbach, Germany

Education

Since 2012:	*PhD studies [Dr. rer. nat.]*, Eberhard Karls University Tübingen (Germany): Studies in Soil-Landscape-Modelling, Spatial Statistics, Data Mining, and Machine Learning (YangtzeGEO-project, funded by German Ministry of Education and Research BMBF, grant No. 03 G 0827A, link: http://www.yangtze-project.de/).
2009 – 2012:	*Master studies [M.Sc.]*, Brandenburg Technical University Cottbus (Germany): Studies in Landscape Ecology, Environmental Modelling, and Soil Science.
2004 – 2009:	*Bachelor studies [B.Sc.]*, University of Innsbruck (Austria): Studies in Physical Geography, Geographic Information Systems (GIS), Geomorphology, Hydrology, Climatology, and Pedology.
1995 – 2004:	*Abitur (matriculation standard)*, Hildegardis Gymnasium Kempten (Germany): Fields of examination: Physics, English, Geography, Sport.

Working Experience

Since 2012:	*Research Assistant*, Eberhard Karls University Tübingen (Germany): Research on Soil-Landscape-Modelling, Spatial Statistics, Data Mining, and Machine Learning techniques; publications in various scientific journals (peer-reviewed) and at international conferences in China, Spain, Italy, Austria, and Germany; lectures for undergraduate students in General Statistics, Statistics with R, Soil-Landscape-Modelling, and Geographic Information Systems (GIS); field work and project meetings in Germany, Central and Western China; organization of research trips with student assistance to Central China; installation and maintenance of hydrological and pedological monitoring systems in Central China.
5/2012 – 8/2012:	*Internship*, GFA Consulting Group Hamburg: EU-/GIZ-/KFW-projects in Europe, Middle East, and North Africa: Evaluation, Aquise in context of the following projects: ENPI Climate East, Water Macedonia, and National Park Azerbaijan.

2/2009 – 8/2010:	*Student assistant*, University of Innsbruck (Austria), Institute for Geography: Supervising tutor for General Statistics.

Languages

German:	Native Speaker
English:	Business fluent
French:	Basic skills
Spanish:	Basic skills

Computer skills (selection)

Microsoft Office:	Excellent skills
GNU R:	Excellent skills (programming language: statistics and graphics, open source)
ArcGIS:	Excellent skills (Geographical Information System)
SAGA GIS:	Excellent skills (Geographical Information System, open source)

Interests

Sport:	Mountain sports, ball sports
Nature Sciences:	Physical and human Geography, Ecology, Physics
Humanities:	Philosophy, Anthropology, Policy
Membership:	International Union of Soil Science (IUSS), Geographic Society of Innsbruck (Austria), Germans Soil Science Society (DBG)/ Working Group: Digital Soil Mapping.

Scientific Publications and Conference Contributions

Publications - peer reviewed:

2015:

Strehmel, A., Schönbrodt-Stitt, S., Buzzo, G., Dumperth, C., **Stumpf, F.**, Zimmermann, K., Bieger, K., Behrens, T., Schmidt, K., Bi, R., Rohn, J., Hill, J., Udelhoven, T., Wei, X., Shi, XZ., Cai, Q., Jiang, T., Fohrer, N., Scholten, T., 2015. Assessment of Geo-Hazards in a Rapidly Changing Landscape: The Three Gorges Reservoir Region in China. *Environmental Earth Sciences* 74 (2015): 4939 – 4960.

Stumpf, F., Schmidt, K., Behrens, T., Schönbrodt-Stitt, S., Buzzo, G., Dumperth, C., Wadoux, A., Wei, X., Scholten, T., 2015. Incorporating Limited Field Operability and legacy Samples in a Hypercube Sampling Design for Digital Soil Mapping. (Journal of Plant Nutrition and Soil Science, accepted with major revision).

Stumpf, F., Schmidt, K., Goebes, P., Behrens, T., Schönbrodt-Stitt, S., Wadoux, A., Wei, X., Scholten, T., 2015. Spatial Uncertainty-Guided Sampling to Improve Digital Soil Maps. (Catena, under review).

Goebes, P., Schmidt, K., Seitz, S., **Stumpf, F.**, Scholten, T., 2015. Rule-based analysis of throughfall kinetic energy to evaluate leaf and tree architectural trait thresholds to mitigate erosive power. (Progress in Physical Geography, accepted).

Stumpf, F., Schmidt, K., Goebes, P., Schindewolf, M., Schönbrodt-Stitt, S., Wadoux, A., Scholten, T., 2015. Sediment reallocation due to erosive rainfall events in the Three Gorges Reservoir Area, Central China. (Land Degradation & Development, under review).

Dumperth, C., Fleer, A., Rohn, R., **Stumpf, F.**, Xiang, W., Zimmermann, K., 2015. Terrestrial radar interferometry measurements in a densely populated area. Result correction and verification by using finite element analyses and ArcGIS. A case study on Huangtupo landslide (P.R. China). (in preparation).

Schönbrodt-Stitt, S., Hartmann, H., Schmidt, K., Behrens, T., **Stumpf, F.**, Scholten, T., et al., 2015. Spatial prediction of the rainfall erosivity in the Three Gorges Reservoir Area, Central China. (in preparation).

Schönbrodt-Stitt, S., Schmidt, K., Behrens, T., **Stumpf, F.**, Scholten, T., et al., The effect of the spatial variability of bench terraces on the soil erosion in a heterogeneous terraced landscape in China. (in preparation).

Other articles:

2013:

Schönbrodt-Stitt, S., **Stumpf, F.**, Schmidt, K., Scholten, T., 2013. Tübinger Forscher koordinieren geowissenschaftliche Forschungen am Yangtze. Forum der Geoökologie (VGöD) 24, 23-24.

Publications - conference contributions:

2015:

Stumpf, F., Schmidt, K., Behrens, T., Schönbrodt-Stitt, S., Xiang, W., Scholten, S., 2015. Integration von Zusatzstichproben zur Qualitätssteigerung von digitalen Bodeneigenschaftskarten. 5. Digital Soil Mapping Workshop, 30. März bis 01. April 2015, Tübingen, Deutschland. [Talk]

Wadoux, A., Ramirez-Lopez, L., **Stumpf, F.**, Schmidt, K., Scholten, T., 2015. Mid-Infrared spectroscopy as a tool for the study of soil-landscape relationships. 5. Digital Soil Mapping Workshop, 30. März - 01. April 2015, Tübingen, Deutschland. [Talk]

Schönbrodt-Stitt, S., Schmidt, K., Hartmann, H., **Stumpf, F.**, Behrens, T., Scholten, T., 2015. Räumliche Prognose der Regenerosivität unter Berücksichtigung der geringen Datenverfügbarkeit anhand des Beispiels des Drei-Schluchten-Reservoirs in China. 5. Digital Soil Mapping Workshop, 30. März bis 01. April 2015, Tübingen. [Talk]

Stumpf, F., Schindewolf, M., Schönbrodt-Stitt, S., Schmidt, K., Scholten, T., 2015. Prozess-basierte Erosionsmodellierung in einem Kleineinzugsgebiet in Zentralchina. Jahrestagung der Deutschen Bodenkundlichen Gesellschaft 2013, Kommission VI /Bodenerosion, 05.-10. September 2015, München, Deutschland. [Talk]

Schönbrodt-Stitt, S., Schmidt, K., Behrens, T., **Stumpf, F.**, Scholten, T., 2015. Der Einfluss von Bankterrassen auf die Bodenerosion in einer heterogenen Terrassenlandschaft in China. Jahrestagung der Deutschen Bodenkundlichen Gesellschaft 2015, Kommission VI /Bodenerosion, 05.-10. September 2015, München, Deutschland. [Talk]

Schmidt, K., Wadoux, A., Ramirez-Lopez, L., **Stumpf, F.**, Schmidt, K., Scholten, T., Behrens, T., 2015. Mid-Infrared spectroscopy as a tool to analyze soil-landscape relationships. Jahrestagung der Deutschen Bodenkundlichen Gesellschaft 2013, Kommission V /Digital Soil Mapping, 05.-10. September 2015, München, Deutschland. [Talk]

Stumpf, F., Schmidt, K., Behrens, T., Schönbrodt-Stitt, S., Wadoux, A., Scholten, S., 2015. Spatial uncertainty-guided sampling to improve digital soil maps. Pedometrics 2015, 14-18 September, Cordoba, Spain. [Poster]

2014:

Stumpf, F., Schmidt, K., Behrens, T., Schönbrodt-Stitt, S., Scholten, T., 2014. Erosionsmodellierung in Zentralchina - Digital Soil Mapping auf Basis eines modifizierten Latin Hypercube Samplings und Random Forest zur Parameterabschätzung. Arbeitskreis Theorie und Quantitative Methoden in der Geographie Tübingen 2014, Theorie - Modell - Anwendung, 27.02.-01.03.2014, Universität Tübingen, Deutschland.[Talk]

Stumpf, F., Schönbrodt-Stitt, S., Schmidt, K., Behrens, T., Scholten, T., 2014. Erosion modeling in Central China: Digital Soil Mapping based on a modified conditioned Latin Hypercube Sampling and Random Forest. Digital Soil Mapping Workshop, 9-11 April 2014, Tübingen, Germany. [Talk]

Stumpf, F., Schmidt, K., Behrens, T., Schönbrodt-Stitt, S., Buzzo, G., Dumperth, C., Wadoux, A., Scholten, T., 2014. Integrating legacy soil information in a Digital Soil Mapping approach based on a modified conditioned Latin Hypercube Sampling design. EGU General Assembly 2014, 27 April-02 May 2014, Vienna, Austria. [Talk]

Stumpf, F., Schmidt, K., Behrens, T., Schönbrodt-Stitt, S., Buzzo, G., Dumperth, C., Wadoux, A., Scholten, T., 2014. Integrating legacy soil information in a Digital Soil Mapping approach based on a modified conditioned Latin Hypercube Sampling design. EGU - SSS

Conference ELS 2014 The Earth Living Skin: Soil, Life and Climate Changes, 22-25 September 2014, Bari, Italy. [Talk]

Stumpf, F., Schönbrodt-Stitt, S., Schmidt, K., Behrens, T., Scholten, T., 2014. Uncertainty analysis and guided resampling for Digital Soil Mapping – A case study in Central China. 6th Global Workshop on Digital Soil Mapping 2014, 11-14 November, Nanjing, China. [Talk]

Wadoux, A., Ramirez-Lopez, L., **Stumpf, F.**, Schmidt, K., Scholten, T., 2014. Mid-Infrared spectroscopy as a tool for the study of soil-landscape relationships. 6th Global Workshop on Digital Soil Mapping 2014, 11-14 November, Nanjing, China. [Poster]

2013:

Schönbrodt-Stitt, S., **Stumpf, F.**, Schmidt, K., Behrens, T., Scholten, T., 2013. Bodenerosionsmodellierung in einem kleinen Gebirgseinzugsgebiet im Reservoir des Drei-Schluchten-Staudamms. Workshop der Deutschen Bodenkundlichen Gesellschaft "Möglichkeiten modellgestützter Bodenerosionsermittlung - Anwendung des Modells Erosion 3D", 13.-15. März 2013, Berlin-Spandau, Deutschland. [Talk]

Schönbrodt-Stitt, S., **Stumpf, F.**, Schmidt, K., Althaus, P., Renneng Bi, Bieger, K., Buzzo, G., Dumperth, C., Fohrer, N., Rohn, J., Strehmel, A., Udelhoven, T., Xiang, W. Zimmermann, K., Scholten, T., 2013. Studying and understanding the environmental impacts of the Three Gorges Dam in China. EGU General Assembly 2013, Geophysical Research Abstracts 15, EGU General Assembly 2013, 07-12 April 2013, Vienna, Austria. [Talk]

Schönbrodt-Stitt, S., **Stumpf, F.**, Schmidt, K., Behrens, T., Xiang, W., Scholten, T., 2013. Ökologische Implikationen des Drei-Schluchten-Staudamms in China. Deutscher Geographentag 2013, Passau, Deutschland. [Talk]

Stumpf, F., Schönbrodt-Stitt, S., Schmidt, K., Behrens, T., Scholten, T., 2013. Erosion modeling in Central China: soil data acquisition by conditioned Latin Hypercube sampling and incorporation of legacy data. EGU General Assembly 2013, Geophysical Research Abstracts 15, EGU General Assembly 2013, 07-12 April 2013, Vienna, Austria. [Talk]

Stumpf, F., Schönbrodt-Stitt, S., Schmidt, K., Behrens, T., Scholten, T., 2013. Erosion modeling in Central China: soil data acquisition by conditioned Latin Hypercube sampling

and incorporation of legacy data. Digital Soil Mapping Workshop, 11-12 April 2013, Tübingen, Germany. [Talk]

Stumpf, F., Schönbrodt-Stitt, S., Schmidt, K., Behrens, T., Scholten, T., 2013. Erosionsmodellierung in Zentralchina: Conditioned Latin Hypercube Sampling als Grundlage für eine Bodenlandschaftsmodellierung. Jahrestagung der Deutschen Bodenkundlichen Gesellschaft 2013, Kommission V / Thema 7 (Digital Soil Mapping), 07.-12. September 2013, Rostock, Deutschland. [Talk]

2012:

Schönbrodt-Stitt, S., Schmidt, K., **Stumpf, F.**, Althaus, P., Bi, R., Bieger, K., Dumperth, C., Fohrer, N., Rohn, J., Strehmel, A., Subklew, G., Udelhoven, T., Xiang Wei, Zimmermann, K., Scholten, T., 2012. YANGTZE GEO: The Three Gorges Dam - Environmental research at the Yangtze River. IALE-D Jahrestagung 2012, 24-26 October 2012, Eberswalde, Germany. [Talk]

Acknowledgements

First of all I want thank Prof. Dr. Thomas Scholten for offering me the exciting and challenging opportunity to work in his group and to be part of the YANGTZE GEO project. During the past three years he was constantly bestowing patience, scientific advice, and confidence on me and my work. I am very grateful for him being my supervisor and mentor.

I am very grateful to Prof. Dr. Volker Hochschild for evaluating this thesis.

I wish to sincerely express my gratitude to Dr. Karsten Schmidt and Dr. Thorsten Behrens for their academic guidance and their amicable support in all kinds of situations. Their trust and sincerity was an imprinting experience. Thank you very much.

Special thanks goes to Dr. Sarah Schönbrodt-Stitt, who provided me with constant support in academic problems and an all time friendly ear. Her benignity to share experiences in China and her courage to dispute adversities are inspiring.

I thank Alexandre Wadoux for his exceptional commitment in the field, at the desk, and in the laboratory. I also want to thank him for being a friend.

Special thanks goes to my colleagues and friends Michael Müller, Philipp Goebes, Steffen Seitz, Zhengshan Song, and Philipp Gries. Their unconditional support and help made our work a pleasant, exciting, and entertaining venture.

I want to thank my colleagues from the YANGTZE GEO research group for sharing data, knowledge, and pleasant times in Germany and abroad. Special thanks goes to Giovanni Buzzo, Alexander Strehmel, Renneng Bi, and Christian Dumperth for their helping hands and distractions during the field trips in China. My warmest thanks extent to the students of the Department of Geotechnical Engineering and Engineering Geology at the China University of Geosciences in Wuhan for their organizational and physical help in the field.

I am indebted to Prof. Dr. Xiang Wei for his organizational and friendly support in China. Moreover, I very much thank Dr. Peter Kühn, Sabine Flaiz, and Lisa Funke for their helping hands in the laboratory.

In the end, peerless thanks to Katerina Bobrovova, our little boy Oscar, and my family for their patience and never-ending support. Thank you so much for your confidence and love.

Declaration by the candidate

I hereby declare that this dissertation is the product of my own work and effort and that it has not been submitted anywhere for any award. I further declare that all the sources I have used or quoted have been indicated and acknowledged as complete references.

Hiermit erkläre ich, dass ich die vorliegende Dissertation, abgesehen von der Beratung durch meine Betreuer, selbstständig verfasst habe und keine weiteren Quellen und Hilfsmittel als die hier angegebenen verwendet habe. Diese Arbeit hat weder ganz noch in Teilen bereits an anderer Stelle einer Prüfungskommission zur Erlangung des Doktorgrades vorgelegen. Ich erkläre, dass die vorliegende Arbeit gemäß der Grundsätze zur Sicherung guter wissenschaftlicher Praxis der Deutschen Forschungsgemeinschaft erstellt wurde.

I certify that the above statement is correct.

Date, Signature of the candidate